

**USING TOMOGRAPHY, CFD, AND DYNAMIC TESTS TO STUDY THE
CONTINUOUS-FLOW MIXING OF YIELD-PSEUDOPLASTIC FLUIDS**

By

Dineshkumar Patel

Master of Science, Sardar Patel University, V.V. Nagar, Gujarat, India, 1999

Bachelor of Science, Sardar Patel University, V.V. Nagar, Gujarat, India, 1997

A Dissertation

Presented to Ryerson University

in Partial Fulfillment of the Requirements for the Degree of

Doctor of Philosophy

in the Program of Chemical Engineering

Toronto, Ontario, Canada, 2014

© Dineshkumar Patel, 2014

Author's Declaration

I hereby declare that I am the sole author of this dissertation. This is a true copy of the dissertation, including any required final revisions, as accepted by my examiners.

I authorize Ryerson University to lend this dissertation to other institutions or individuals for the purpose of scholarly research.

I further authorize Ryerson University to reproduce this dissertation by photocopying or by other means, in total or in part, at the request of other institutions or individuals for the purpose of scholarly research.

I understand that my dissertation may be made electronically available to the public.

Dineshkumar Patel

ABSTRACT

Dineshkumar Patel

Using tomography, CFD, and dynamic tests to study the continuous-flow mixing of yield-pseudoplastic fluids

PhD, Chemical Engineering, Ryerson University, Toronto, 2014

The major technological challenges faced by modern chemical industries are non-ideal flows such as dead zones and channeling encountered in the mixing of fluids with complex rheology. These cause sub-optimal mixing and lead to low quality products and high costs of raw materials. Therefore, the core objectives of this study were to develop methodology and tools to design an efficient continuous-flow mixing system for the fluids with complex rheology using electrical resistance tomography (ERT), computational fluid dynamics (CFD), and dynamic tests. The xanthan gum solution, which is a pseudoplastic fluid with yield stress, was used to study the dynamic behavior of the continuous-flow mixing process. The power consumption, cavern size, mixing time, and the extents of channelling and the fraction of fully mixed volume were successfully determined using dynamic tests, ERT tests, and CFD simulations and used as mixing quality criteria.

A novel and efficient method was developed for flow visualization in the continuous-flow mixing of opaque fluids using 2D and 3D tomograms. A unique study on identifying the sources of flow non-ideality in non-Newtonian fluids with yield stress was done by visualizing the flow pattern inside the continuous-flow mixing vessel using 2D and 3D tomograms. The deformation of the cavern was analyzed and quantified in the continuous-flow mixing system for yield-pseudoplastic fluids using ERT. Moreover, the cavern volume was compared with the

fully mixed volume and it was found that the latter was higher due to the extra momentum induced by the inlet-outlet flow. A novel study on exploring the effect of the rheological parameters of the pseudoplastic fluids with yield stress on the non ideal flows in a continuous-flow mixing system was performed using CFD. The CFD results revealed that the mixing quality was improved when the degree of the shear thinning was increased. The ratio of the residence time to the batch mixing time was evaluated to achieve ideal mixing for the continuous-flow mixing of yield-pseudoplastic fluids using dynamic tests and ERT. It was found that the ratio of residence time to the batch mixing time should be at least 8.2 or higher to achieve ideal mixing.

Acknowledgements

First of all, I acknowledge the invaluable advice and funding from my PhD supervisors Dr. Farhad Ein-Mozaffari and Dr. Mehrab Mehrvar. I found Dr. Ein-Mozaffari very kind, honest, professional, and having a depth and advance knowledge in the mixing area. He helped me greatly improve my research and English skills by guiding me in write research papers and offering me the opportunity to present research work at international conferences. Besides regular meetings, he also gave priority to any urgent meeting that I requested to discuss my research and career. I am grateful for the freedom I felt to investigate almost anything that I found interesting. I also acknowledge Dr. Mehrvar as my co-supervisor and for his funding and guidance in academic and nonacademic issues. I also found Dr. Mehrvar very kind and helpful and always available when I needed to discuss my research and career development.

I am thankful to Professor Simant R. Upreti (Chair of the Department of Chemical Engineering, Ryerson University) for his invaluable suggestions and support for my research and career development during my PhD program. I also extend my warm thanks to my examination committee members, Professor Ali Elkamel (external examiner, Department of Chemical Engineering, University of Waterloo), Professor Krishna Dev Kumar (Department of Aerospace Engineering, Ryerson University), Professor Simant R. Upreti, and Professor Jiangning Wu for their time and consideration.

I acknowledge the help of administration staff, Mrs. Leah Rogan, Mrs. Isabella Fernandes, and Mrs. Louise Lichacz, and also engineering staff, Mr. Ali Hemmati, Mr. Daniel Boothe, and Mr. Tondar Tajrobekar, in the Chemical Engineering Department at Ryerson University. Sincere thanks to all my friends in the Chemical Engineering Department at Ryerson University for their kind help.

I acknowledge Natural Sciences and Engineering Research Council of Canada (NSERC-PGS-D2), Ontario Graduate Scholarships (OGS), Ontario Graduate Scholarships in Science and Technology (OGSST), Ryerson Graduate Scholarship (RGS), Ryerson Graduate Award (RGA), SMCC scholarship, NAMF competition award, and Chemical Engineering Departmental Awards for excellence in research as well as academics for the financial support

during this work. I also acknowledge the HPCVL (High Performance Computing Virtual Laboratory) for providing the high performance computing facilities.

Special thanks to my parents and my wife for their infinite support and unconditional love. Finally, thanks to my little son, Vedant, for being so good and patient during my PhD program.

Dedicated to

my father **Nathalal** and my wife **Vimu**

for their love, support, and encouragement in pursuit of excellence and success in my
life.

Table of Contents

AUTHOR'S DECLARATION	ii
ABSTRACT.....	iii
ACKNOWLEDGEMENTS	v
LIST OF TABLES	xvii
LIST OF FIGURES	xviii
NOMENCLATURE.....	xxviii
1. INTRODUCTION.....	1
2. LITERATURE REVIEW	6
2.1 Power Consumption	7
2.1.1 Power Consumption for Newtonian Fluids	7
2.1.2 Power Consumption for Non-Newtonian Fluids.....	9
2.1.2.1 The Metzner and Otto Approach.....	9
2.2 Mixing Time in a Batch Mode.....	11
2.3 Cavern	12

2.4	Continuous-Flow Mixing	14
2.4.1	Close-Clearance Impellers in the Continuous-Flow Mixing.....	15
2.4.1.1	The Double Helical Ribbon (DHR) Impeller	15
2.4.1.2	The Maxblend Impeller	16
2.4.2	Dynamic Modeling of Continuous-Flow Mixing System	18
2.4.3	Literature Review on Continuous-Flow Mixing	22
2.5	Research Objectives	25
3.	EXPERIMENTAL SETUP AND METHODOLOGY	27
3.1	Experimental Setup for Dynamic tests	27
3.1.1	Design of Input Signal and Dynamic Model Validation	30
3.2	Experimental Setup for ERT tests	35
3.2.1	ERT System.....	36
3.2.1.1	Electrodes	37
3.2.1.2	Data Acquisition System	37
3.2.1.3	Host Computer or Image Reconstruction System	38
3.3	Fluid Rheology	39
3.4	Experimental Procedure	40
3.4.1	Solution Preparation	40
3.4.2	Power Measurements	40
3.4.3	Mixing Time Measurements	43

3.4.4	Cavern and Flow Visualization	45
3.4.5	The Ratio of Residence to Mixing Time	48
3.5	Error Analysis.....	48
3.5.1	Evaluation of Torque Sensor Precision	48
3.5.2	Evaluation of ERT Measurements Precision.....	49
3.6	Experimental Conditions	49
4.	CFD MODEL DEVELOPMENT	51
4.1	Introduction to CFD Modeling	51
4.1.1	Governing Equations	51
4.1.2	Continuity Equation	52
4.1.3	Momentum Equation	52
4.1.4	Boundary Conditions.....	54
4.1.5	CFD Modeling of Mixing Tanks.....	55
4.1.5.1	The Multi Reference Frame (MRF) Approach.....	55
4.1.5.2	The Sliding Mesh (SM) Approach	56
4.2	Model Description	56
4.2.1	Geometry	57
4.2.2	Grid Generation	57
4.2.2.1	Grid Independence Study through Velocity Profile	58

4.2.3	Impeller Model, Flow Model, Physical Properties, Boundary Conditions, and Convergence	60
4.2.4	Modeling Tracer Injection to a Continuous-Flow Mixer and Model Validation	62
4.2.4.1	Model Validation.....	64
4.2.5	Modeling Tracer Injection for Mixing Time in a Batch Mode	66
4.2.6	Cavern region in CFD	67
5.	RESULTS AND DISCUSSION	69
5.1	Dynamic Performance of Continuous-Flow Mixing of Pseudoplastic Fluids Exhibiting Yield Stress in Stirred Reactors (Patel et al., 2011)	71
5.1.1	Introduction	71
5.1.2	Results and Discussion.....	72
5.1.2.1	Effect of Impeller Speed.....	72
5.1.2.2	Effect of Impeller Type	74
5.1.2.3	Effect of Impeller Diameter.....	77
5.1.2.4	Effect of Impeller Clearance	79
5.1.2.5	Effect of Inlet and Outlet Locations	81
5.1.2.6	Effect of Pumping Directions of an Axial-Flow Impeller.....	84
5.1.2.7	Effect of Fluid Height in a Vessel	86
5.1.2.8	Effect of Residence Time	88
5.1.2.9	Effect of Jet Velocity.....	89
5.1.3	Conclusions	94

5.2	Effect of Impeller Type on Continuous-Flow Mixing of Non-Newtonian Fluids in Stirred Vessels through Dynamic Tests (Patel et al., 2012b).....	96
5.2.1	Introduction	96
5.2.2	Results and Discussion.....	97
5.2.2.1	Effect of Power Input	97
5.2.2.2	Effect of Type of Impellers	98
5.2.2.3	Effect of Pumping Direction of the DHR Impeller	99
5.2.2.4	Effect of Fluid Rheology	101
5.2.2.5	Effect of Feed Flow Rate.....	102
5.2.2.6	Effect of Input Locations.....	104
5.2.3	Conclusions	105
5.3	Improving the Dynamic Performance of Continuous-Flow Mixing of Pseudoplastic Fluids Possessing Yield Stress Using Maxblend Impeller (Patel et al., 2012a).....	107
5.3.1	Introduction	107
5.3.2	Results and Discussion.....	108
5.3.2.1	Effect of Power Input	108
5.3.2.2	Effect of Type of Impeller.....	110
5.3.2.3	Effect of Baffles	112
5.3.2.4	Effect of Fluid Rheology	114
5.3.2.5	Effect of Feed Flow Rate.....	115
5.3.2.6	Effect of Inlet and Outlet Locations	117
5.3.3	Conclusions	119

5.4 Characterization of the Continuous-Flow Mixing of Non-Newtonian Fluids Using the Ratio of Residence Time to Batch Mixing Time (Patel et al., 2013c) 120

5.4.1 Introduction 120

5.4.2 Results and Discussion 121

5.4.2.1 Effect of Impeller Speed 121

5.4.2.2 Effect of Fluid Rheology 122

5.4.2.3 Effect of Type of Impeller 124

5.4.2.4 Effect of Pumping Direction of an Axial-flow Impeller 125

5.4.2.5 Effect Inlet and Outlet Locations 126

5.4.2.6 Effect of Impeller Off-bottom Clearance 128

5.4.2.7 Effect of Jet Velocity 129

5.4.2.8 Effect of Fluid Height in the Vessel 130

5.4.2.9 Effect of Fluid Residence Time 131

5.4.3 Conclusions 132

5.5 Tomography Images to Analyze the Deformation of the Cavern in the Continuous-Flow Mixing of Non-Newtonian Fluids (Patel et al., 2014a) 134

5.5.1 Introduction 134

5.5.2 Results and Discussion 135

5.5.2.1 Dimensionless Cavern Diameter 135

5.5.2.2 Ratio of Cavern Height to Cavern Diameter 136

5.5.2.3 Effect of Fluid Rheology on Cavern Volume 137

5.5.2.4 Effect of Impeller Type on Cavern Volume 138

5.5.2.5 Comparison of Cavern Volume and Fully Mixed Volume 139

5.5.2.6	Deformation of the Cavern Using Tomography Images	142
5.5.2.7	Effect of Inlet and Outlet Locations on Cavern Deformation	143
5.5.2.8	Effect of Fluid Rheology on Cavern Deformation	149
5.5.2.9	Effect of Jet Velocity on Cavern Deformation.....	150
5.5.2.10	Effect of Fluid Flow Rate on Cavern Deformation	151
5.5.3	Conclusions	154
5.6	Using Tomography to Visualize the Continuous-Flow Mixing of Biopolymer	
	Solutions inside a Stirred Tank Reactor (Patel et al., 2014b).....	156
5.6.1	Introduction	156
5.6.2	Results and Discussion.....	157
5.6.2.1	Effect of Inlet and Outlet Locations on Flow Pattern.....	158
5.6.2.2	Effect of Jet Velocity on Flow Pattern	165
5.6.2.3	Effect of Feed Flow Rate on Flow Pattern	166
5.6.2.4	Effect of Fluid Rheology on Flow Pattern	169
5.6.2.5	Effect of Type of Impeller on Flow Pattern	171
5.6.2.6	Effect of Impeller Speed on Flow Pattern	174
5.6.3	Conclusions	177
5.7	Effect of Rheological Parameters on the Continuous-Flow Mixing of Biopolymer	
	Solutions	180
5.7.1	Introduction	180
5.7.2	Results and Discussion.....	181
5.7.2.1	Effect of Power Input	181

5.7.2.2	Effect of Fluid Rheology	182
5.7.2.3	Effect of Feed Flow Rate.....	184
5.7.2.4	Effect of Power Law Index.....	185
5.7.2.5	Effect of Fluid Yield Stress	187
5.7.2.6	Effect of Fluid Consistency Index	187
5.7.3	Conclusions	189
5.8	Using CFD to Study the Effect of Rheological Parameters on Mixing Time for the Shear Thinning Fluids with Yield Stress.....	191
5.8.1	Introduction	191
5.8.2	Results and Discussion.....	192
5.8.2.1	CFD and Experimental Cavern Diameter.....	192
5.8.2.2	Effect of Fluid Rheology on Cavern Volume	193
5.8.2.3	Comparison between Cavern and Fully Mixed Volume	194
5.8.2.4	Effect of Impeller Speed on Mixing Time	196
5.8.2.5	Effect of Fluid Rheology on Mixing Time.....	196
5.8.2.6	Dimensionless Mixing Time	197
5.8.2.7	Effect of Power Law Index on Mixing Time	199
5.8.2.8	Effect of Fluid Yield stress on Mixing Time.....	201
5.8.2.9	Effect of Consistency Index on Mixing Time	201
5.8.3	Conclusions	202
5.9	Using Tomography to Characterize the Mixing of Non-Newtonian Fluids with a Maxblend Impeller (Patel et al., 2013b)	204

5.9.1	Introduction	204
5.9.2	Results and Discussion.....	205
5.9.2.1	Effect of Impeller Speed.....	205
5.9.2.2	Effect of Fluid Rheology	206
5.9.2.3	Dimensionless Mixing Time	207
5.9.2.4	Effect of Type of Impeller.....	209
5.9.2.5	Effect of Baffles	211
5.9.3	Conclusions	212
6.	OVERALL CONCLUSIONS	213
6.1	Recommendations for Future Work.....	217
	<i>Publications</i>	218
	<i>Bibliography</i>	224

List of Tables

Table (3.1-1). Geometrical details of close-clearance impellers .	28
Table (3.1-2). Dynamic model parameters obtained from two different input signals.	34
Table (3.3-1). Rheological properties of xanthan gum solutions (Saeed et al., 2008).	39
Table (3.6-1). Experimental conditions.	50
Table (4.2-1). Fluid rheological parameters applied in CFD modeling	62
Table (5.8-1). Coefficients of the mixing time correlation using Equation (2.2–2).	199
Table (5.9-1). Coefficients of the mixing time correlation [Equation (2.2–2)] for the Maxblend impeller as a function of the xanthan gum concentration.	208
Table (5.9-2). Coefficients of the mixing time correlation using Equation (2.2–2).	210

List of Figures

Figure (2.4-1). Continuous-time dynamic model for continuous-flow mixers (Ein-Mozaffari, 2002).	20
Figure (3.1-1). Schematic diagram of the continuous-flow mixing process: (1) feed tank, (2) progressing cavity pump, (3) tracer tank, (4) metering pump, (5) solenoid valve, (6) conductivity sensor, (7) electric motor, (8) torque meter, (9) mixing tank, (10) data acquisition system, and (11) discharge tank.	28
Figure (3.1-2). Axial-flow and radial-flow impellers: (1) HG 3AH, (2) Lightnin A315, (3) Lightnin A320, (4) Lightnin A200, (5) Lightnin R500 (sawtooth), (6) Scaba 6 SRGT, (7) HG 3AM, (8) Lightnin A100, (9) Lightnin A310, (10) RSB (retreat swept-back), and (11) RT (Rushton turbine).....	29
Figure (3.1-3). Close-clearance impellers: (a) Anchor (b) Maxblend (c) Double helical ribbon (DHR).....	30
Figure (3.1-4). System excitation using a rectangular pulse: input and output signals in black lines and model output in white line. (3AH, $Q = 9.65 \text{ L min}^{-1}$, 251 rpm, 0.5% xanthan gum, $D = T/2.1$, $C = H/2.7$, $H = T/0.93$).	31
Figure (3.1-5). Procedure for designing a frequency-modulated random binary input signal. .	32
Figure (3.1-6). The magnitude of the Bode plot for the partial derivatives of the approximate model.....	33
Figure (3.1-7). System excitation using a frequency-modulated random binary input signal: experimental input and output in black and model output in white. (3AH, $Q = 9.65 \text{ L min}^{-1}$, 251 rpm, 0.5% xanthan gum, $D = T/2.1$, $C = H/2.7$, $H = T/0.93$).	33
Figure (3.1-8). Model validation: new input and output signals (second set of experiment) in black and estimated model output from the first set of data in white (3AH, $Q = 9.65 \text{ L min}^{-1}$, 251 rpm, 0.5% xanthan gum, $D = T/2.1$, $C = H/2.7$, $H = T/0.93$).	34
Figure (3.2-1). Experimental setup with ERT system (dimensions in meter).....	35

Figure (3.4-1). Power number (P_o) versus Reynolds number (Re): (a) axial-flow impellers (b) radial-flow impellers, and (c) close-clearance impellers (1.5% xanthan gum solution).	42
Figure (3.4-2). 2D tomograms recorded after the tracer injection (Maxblend impeller, 1% xanthan gum concentration, $N = 175$ rpm, and with baffles).....	44
Figure (3.4-3). Conductivity versus time for six tomography planes after the injection of the tracer (Maxblend, 1% xanthan gum concentration, $N = 175$ rpm, and with baffles)...	45
Figure (3.4-4). The 3D images generated from the 2D tomograms show the formation of the cavern in the mixing of the 0.5% xanthan gum solution using the RT impeller: (a) 2D tomogram and (b) 3D images generated using the Slicer Dicer software (the 3D images were generated by cutting the vertical plane at the center of the tank and / or the horizontal plane on the impeller surface).....	47
Figure (3.5-1). Error associated with torque measurements (RSB impeller and 1.5% xanthan gum).	49
Figure (4.2-1). Unstructured tetrahedral mesh generated using ANSYS Fluent (v14.5) in Meshing Mode.	58
Figure (4.2-2). Effect of the number of cells on (a) radial velocity and (b) tangential velocity at horizontal line close to the impeller: Position of line (m): $x = 0.09$; $y = -0.09$ to 0.09 ; $z = 0.16$).	59
Figure (4.2-3). Shear stress vs. shear rate according to Equations (4.2-2) and (4.2-3).....	61
Figure (4.2-4). UDF code used to model tracer injection for frequency-modulated random binary input signal.....	64
Figure (4.2-5). Effect of time step on the output response to a frequency-modulated random binary input signal using CFD ($Q = 9.65$ L min ⁻¹ , 1.0% xanthan gum, and $N = 416$ rpm).....	65
Figure (4.2-6). Input/output signals (experimental and CFD) at $Q = 9.65$ L min ⁻¹ , 1.0% xanthan gum, and $N = 416$ rpm.....	65

Figure (4.2-7). Power number (experimental and CFD) versus Reynolds number for 1.5% xanthan gum. 66

Figure (4.2-8). Measurement of mixing time for 1% xanthan gum agitated by RT impeller {monitoring point–1 ($x = -0.09, y = -0.09, z = 0.34$); point–2 ($x = 0.03, y = -0.13, z = 0.28$); point–3 ($x = 0.09, y = 0.09, z = 0.22$); point–4 ($x = 0.11, y = 0.03, z = 0.16$); point–5 ($x = -0.12, y = 0.04, z = 0.10$); point–6 ($x = 0.09, y = -0.07, z = 0.04$). Tracer injection point: ($x = 0.07, y = 0.11, z = 0.34$)}. 67

Figure (4.2-9). Velocity contours showing the formation of cavern in the mixing of 0.5% xanthan gum agitated by the RT impeller. 68

Figure (5.1-1). Axial-flow impellers: Effects of impeller speed and impeller type on the extents of (a) channeling and (b) fully mixed volume ($Q = 9.65 \text{ L min}^{-1}$, 1.0% xanthan gum, $D = T/2.1$, $C = H/2.7$, $H = T/0.93$, $V_j = 0.317 \text{ ms}^{-1}$, residence time = 292 s, input-output locations: TI–BO). 73

Figure (5.1-2). Radial-flow impellers: Effects of impeller speed and impeller type on the extents of (a) channeling and (b) fully mixed volume ($Q = 9.65 \text{ L min}^{-1}$, 1.0% xanthan gum, $D = T/2.1$, $C = H/2.7$, $H = T/0.93$, $V_j = 0.317 \text{ m s}^{-1}$, residence time = 292 s, input-output locations: TI–BO). 75

Figure (5.1-3). Effects of the solidity ratio of the hydrofoil impellers on the extents of channeling and fully mixed volume at the fixed power consumption ($Q = 9.65 \text{ L min}^{-1}$, 1.0% xanthan gum, $D = T/2.1$, $C = H/2.7$, $H = T/0.93$, $V_j = 0.317 \text{ m s}^{-1}$, residence time = 292 s, input-output locations: TI–BO). 76

Figure (5.1-4). Effects of impeller diameter on the extents of (a) channeling, (b) fully mixed volume, and (c) channeling and fully mixed volume at the fixed power consumption as a function of D/T (A200, $Q = 9.65 \text{ L min}^{-1}$, 1.0% xanthan gum, $C = H/2.7$, $H = T/0.93$, $V_j = 0.317 \text{ m s}^{-1}$, residence time = 292 s, input-output locations: TI–BO). 79

Figure (5.1-5). Effects of impeller clearance on the extents of (a) channeling, (b) fully mixed volume, and (c) channeling and fully mixed volume as a function of C/H at 50 rpm (3AH, $Q = 9.65 \text{ L min}^{-1}$, 1.0% xanthan gum, $D = T/2.1$, $H = T/0.93$, $V_j = 0.317 \text{ m s}^{-1}$, residence time = 292 s, input-output locations: TI–BO). 81

Figure (5.1-6). Effects of inlet and outlet locations on the extents of (a) channeling, (b) fully mixed volume, and (c) channeling and fully mixed volume for each configuration at

400 rpm (3AH, $Q = 9.65 \text{ L min}^{-1}$, 1.0% xanthan gum, $D = T/2.1$, $C = H/2.7$, $H = T/0.93$, $V_j = 0.317 \text{ m s}^{-1}$, residence time = 292 s)..... 83

Figure (5.1-7). Effects of impeller pumping direction on the extents of (a) channeling, (b) fully mixed volume, and (c) channeling and fully mixed volume for each pumping direction for the 3AH and the A200 impellers at 400 rpm ($Q = 9.65 \text{ L min}^{-1}$, 1.0% xanthan gum, $D = T/2.1$, $C = H/2.7$, $H = T/0.93$, $V_j = 0.317 \text{ m s}^{-1}$, residence time = 292 s, input-output locations: TI–BO). 85

Figure (5.1-8). Effects of fluid height (H) in the mixing vessel on the extents of (a) channeling and (b) fully mixed volume, and (c) channeling and fully mixed volume as a function of H/T at power 224 W m^{-3} (constant residence time = 292 s but different fluid flow rate $Q = 3.20, 9.65,$ and 14.17 L min^{-1} , 3AH, 1.0% xanthan gum, $D = T/2.1$, $C = H/2.7$, $V_j = 0.317 \text{ m s}^{-1}$, input-output locations: TI–BO). 87

Figure (5.1-9). Effects of fluid residence time in the mixing vessel on the extents of (a) channeling and (b) fully mixed volume, and (c) channeling and fully mixed volume as a function of the residence time at power 16 W m^{-3} (at constant fluid flow rate (Q) = 9.65 L min^{-1} but different fluid height (H) = 36, 41, and 46cm, 3AH, 1.0% xanthan gum, $D = T/2.1$, $C = H/2.7$, $V_j = 0.317 \text{ m s}^{-1}$, input-output locations: TI–BO)..... 89

Figure (5.1-10). Effects of inlet jet velocity on the extents of (a) channeling and (b) fully mixed volume, and (c) channeling and fully mixed volume as a function of the jet velocity at 400rpm (3AH, $Q = 9.65 \text{ L min}^{-1}$, 1.0% xanthan gum, $D = T/2.1$, $C = H/2.7$, $H = T/0.93$, residence time = 292 s, input-output locations: TI–BO). 92

Figure (5.1-11). Effects of the inlet jet velocity on the extents of (a) channeling and (b) fully mixed volume (3AH, $Q = 9.65 \text{ L min}^{-1}$, 1.0% xanthan gum, $D = T/2.1$, $C = H/2.7$, $H = T/0.93$, residence time = 292 s, input-output locations: TI–TO). 93

Figure (5.1-12). Effects of inlet jet velocity on the extents of channeling for different output locations (200 rpm, 3AH, $Q = 9.65 \text{ L min}^{-1}$, 1.0% xanthan gum, $D = T/2.1$, $C = H/2.7$, $H = T/0.93$, residence time = 292 s)..... 93

Figure (5.2-1). Effects of impeller speed and impeller types on the extents of (a) channeling and (b) fully mixed volume ($Q = 9.65 \text{ L min}^{-1}$, 1.0% xanthan gum, input-output locations: TI–BO) 99

Figure (5.2-2). Effects of impeller pumping direction on the extents of (a) channeling and (b) fully mixed volume ($Q = 9.65 \text{ L min}^{-1}$, 1.0% xanthan gum, input-output locations: TI–BO)..... 100

Figure (5.2-3). Effects of fluid rheology on the extents of (a) channeling and (b) fully mixed volume (DHR, $Q = 9.65 \text{ L min}^{-1}$, input-output locations: TI–BO)..... 102

Figure (5.2-4). Effects of fluid flow rate through mixing vessel on the extents of (a) channeling and (b) fully mixed volume (DHR, 1.0% xanthan gum, input-output locations: TI–BO)..... 103

Figure (5.2-5). Effects of the locations of inlet and outlet on the extents of (a) channeling and (b) fully mixed volume (DHR, $Q = 9.65 \text{ L min}^{-1}$, 1.0% xanthan gum). 105

Figure (5.3-1). Effects of impeller power and the type of close-clearance impellers on the extents of (a) channeling and (b) fully mixed volume ($Q = 9.65 \text{ L min}^{-1}$, 1.0% xanthan gum, input-output locations: TI–BO)..... 109

Figure (5.3-2). Effects of impeller type (axial-flow, radial-flow, and close-clearance) on the extents of (a) channeling and (b) fully mixed volume (Maxblend with baffles, $Q = 9.65 \text{ L min}^{-1}$, 1.0% xanthan gum, input-output locations: TI–BO)..... 111

Figure (5.3-3). Effects of baffles on the extents of (a) channeling and (b) fully mixed volume ($Q = 9.65 \text{ L min}^{-1}$, 1.0% xanthan gum, input-output locations: TI–BO). 113

Figure (5.3-4). Effects of fluid rheology on the extents of (a) channeling and (b) fully mixed volume (Maxblend with baffles, $Q = 9.65 \text{ L min}^{-1}$, input-output locations: TI–BO). 115

Figure (5.3-5). Effects of fluid flow rate through mixing vessel on the extents of (a) channeling and (b) fully mixed volume (Maxblend with baffles, 1.0% xanthan gum, input-output locations: TI–BO). 116

Figure (5.3-6). Effects of the inlet and outlet locations on the extents of (a) channeling and (b) fully mixed volume (Maxblend with baffles, $Q = 9.65 \text{ L min}^{-1}$, 1.0% xanthan gum). 118

Figure (5.4-1). Effect of the impeller speed (Reynolds number) on the ratio of the residence time to the mixing time (Scaba 6 SRGT impeller, $Q = 9.65 \text{ L min}^{-1}$, 1.0% xanthan

gum, $C = H/2.7$, $H = T/0.93$, $V_j = 0.317 \text{ m s}^{-1}$, residence time = 292 s, and input-output locations: TI–BO).	122
Figure (5.4-2). Effect of the fluid rheology on the ratio of the residence time to the mixing time (A200 impeller, $Q = 10.05 \text{ L min}^{-1}$, $C = H/2.7$, $H = T/0.93$, residence time = 281 s, and input-output locations: TI–BO).	123
Figure (5.4-3). Effect of the type of (axial-flow and radial-flow) impellers on the ratio of the residence time to the mixing time ($Q = 9.65 \text{ L min}^{-1}$, 1.0% xanthan gum, $C = H/2.7$, $H = T/0.93$, $V_j = 0.317 \text{ m s}^{-1}$, residence time = 292 s, and input-output locations: TI–BO).	125
Figure (5.4-4). Effect of the pumping direction of an axial-flow impeller on the ratio of the residence time to the mixing time (3AH impeller, $Q = 9.65 \text{ L min}^{-1}$, 1.0% xanthan gum, $C = H/2.7$, $H = T/0.93$, $V_j = 0.317 \text{ m s}^{-1}$, residence time = 292 s, and input-output locations: TI–BO).	126
Figure (5.4-5). Effect of the inlet and outlet locations on the ratio of the residence time to the mixing time (3AH impeller, $Q = 9.65 \text{ L min}^{-1}$, 1.0% xanthan gum, $C = H/2.7$, $H = T/0.93$, $V_j = 0.317 \text{ m s}^{-1}$, and residence time = 292 s).	127
Figure (5.4-6). Effect of the impeller off-bottom clearance on the ratio of the residence time to the mixing time (3AH impeller, $Q = 9.65 \text{ L min}^{-1}$, 1.0% xanthan gum, $H = T/0.93$, $V_j = 0.317 \text{ m s}^{-1}$, residence time = 292 s, and input-output locations: TI–BO).	128
Figure (5.4-7). Effect of the jet velocity on the ratio of the residence time to the mixing time (3AH impeller, $Q = 9.65 \text{ L min}^{-1}$, 1.0% xanthan gum, $C = H/2.7$, $H = T/0.93$, residence time = 292 s, and input-output locations: TI–BO).	129
Figure (5.4-8). Effect of the fluid height (H) in the vessel on the ratio of the residence time to the mixing time (3AH impeller, 1.0% xanthan gum, $C = H/2.7$, $V_j = 0.317 \text{ m s}^{-1}$, residence time = 292 s, and input-output locations: TI–BO).	131
Figure (5.4-9). Effect of the fluid residence time in the mixing vessel on the ratio of the residence time to the mixing time (3AH impeller, $Q = 9.65 \text{ L min}^{-1}$, 1.0% xanthan gum, $C = H/2.7$, $H = T/0.93$, $V_j = 0.317 \text{ m s}^{-1}$, and input-output locations: TI–BO).	132
Figure (5.5-1). Dimensionless cavern diameter (D_c/D) vs. dimensionless P_oRe_y for the radial-flow impeller (RT) and axial-flow impellers (A310 and 3AM).	136

Figure (5.5-2). Dimensionless cavern height (H_c/D_c) vs. impeller speed (N) for the radial-flow impeller (RT) and axial-flow impellers (A310 and 3AM)..... 137

Figure (5.5-3). Effect of the fluid rheology on the dimensionless cavern volume for the RT impeller at 0.5, 1.0, and 1.5% xanthan gum solutions. 138

Figure (5.5-4). Effect of the impeller type on the dimensionless cavern volume (A310, RT, and 3AM impellers and 1.0% xanthan gum solution). 139

Figure (5.5-5). Dimensionless cavern volume (V_c/V_{total}), the fraction of fully mixed volume ($V_{fully\ mixed}/V_{total}$), and the extent of channeling (f) as a function of the specific power at 1% xanthan gum solution for the (a) RT impeller, (b) A310 impeller, and (c) 3AM impeller. 142

Figure (5.5-6). Effect of inlet and outlet locations on the deformation of the cavern for four different configurations: (a) TI-BO, (b) BI-BO, (c) TI-TO, and (d) BI-TO (RT impeller, $N = 30$ rpm, $Q = 9.65$ L min⁻¹, 1.0% xanthan gum, and $V_j = 0.317$ m s⁻¹). 144

Figure (5.5-7). Tomography images obtained for the RT impeller at $N = 30$ rpm, $Q = 9.65$ L min⁻¹, 0.5% xanthan gum, $V_j = 0.317$ m s⁻¹, and inlet-outlet locations: TI-BO..... 149

Figure (5.5-8). Tomography images obtained for the RT impeller at $N = 30$ rpm, $Q = 9.65$ L min⁻¹, 1.0% xanthan gum, $V_j = 1.66$ m s⁻¹, and inlet-outlet locations: TI-BO..... 151

Figure (5.5-9). Effect of the feed flow rate on the deformation of the cavern (a) $Q = 3.2$ L min⁻¹ and (b) $Q = 14.17$ L min⁻¹ (RT impeller, $N = 30$ rpm, 1.0% xanthan gum, and inlet-outlet locations: TI-BO). 152

Figure (5.6-1). Effect of the inlet and outlet locations on the fluid flow inside a vessel for the four configurations: (a) TI-BO, (b) BI-TO, (c) BI-BO, and (d) TI-TO (RT impeller, $N = 54$ rpm, $Q = 9.65$ L min⁻¹, 1.0% xanthan gum, and $V_j = 0.317$ m s⁻¹)..... 159

Figure (5.6-2). Effect of the inlet jet velocity on the fluid flow (RT impeller, $N = 54$ rpm, $Q = 9.65$ L min⁻¹, 1.0% xanthan gum, $V_j = 1.66$ m s⁻¹, and input-output locations: TI-BO). 165

Figure (5.6-3). Effect of the feed flow rate on the fluid flow (a) $Q = 3.2 \text{ L min}^{-1}$ and (b) $Q = 14.17 \text{ L min}^{-1}$ (RT impeller, $N = 54 \text{ rpm}$, 1.0% xanthan gum, and input-output locations: TI-BO).	167
Figure (5.6-4). Effect of the fluid rheology on the fluid flow (a) 0.5% xanthan gum and (b) 1.5% xanthan gum (RT impeller, $N = 54 \text{ rpm}$, $Q = 9.65 \text{ L min}^{-1}$, $V_j = 0.317 \text{ m s}^{-1}$, and input-output locations: TI-BO).....	169
Figure (5.6-5). Effect of the impeller type on the fluid flow (Maxblend impeller, $N = 54 \text{ rpm}$, $Q = 9.65 \text{ L min}^{-1}$, 1.0% xanthan gum, $V_j = 0.317 \text{ m s}^{-1}$, and input-output locations: TI-BO).....	172
Figure (5.6-6). Effect of the impeller speed and the impeller type on the extent of (a) channeling and (b) fully mixed volume ($Q = 9.65 \text{ L min}^{-1}$, 1.0% xanthan gum, $V_j = 0.317 \text{ m s}^{-1}$, and input-output locations: TI-BO).	173
Figure (5.6-7). Effect of the impeller speed on the fluid flow (a) $N = 77 \text{ rpm}$, (b) $N = 100 \text{ rpm}$, and (c) $N = 250 \text{ rpm}$ (RT impeller, $Q = 9.65 \text{ L min}^{-1}$, 1.0% xanthan gum, $V_j = 0.317 \text{ m s}^{-1}$, and input-output locations: TI-BO).	175
Figure (5.7-1). Effect of impeller power on the extent of (a) channeling and (b) fully mixed volume ($Q = 9.65 \text{ L min}^{-1}$ and 1.0% xanthan gum).	182
Figure (5.7-2). Effect of fluid rheology on the extent of (a) channeling and (b) fully mixed volume ($Q = 9.65 \text{ L min}^{-1}$).	183
Figure (5.7-3). Effect of fluid flow rate through mixing vessel on the extent of (a) channeling and (b) fully mixed volume (1.0% xanthan gum).	185
Figure (5.7-4). Effect of power law index (n) on the extent of (a) channeling and (b) fully mixed volume ($Q = 9.65 \text{ L min}^{-1}$, $N = 100 \text{ rpm}$, $K = 8 \text{ Pa s}^n$, $\tau_y = 5.25 \text{ Pa}$, and $\mu_o = 22.61 \text{ Pa s}$).	186
Figure (5.7-5). Effect of fluid yield stress (τ_y) on the extent of (a) channeling and (b) fully mixed volume ($Q = 9.65 \text{ L min}^{-1}$, $N = 100 \text{ rpm}$, $K = 8 \text{ Pa s}^n$, and $n = 0.12$).	188

Figure (5.7-6). Effect of consistency index (K) on the extent of (a) channeling and (b) fully mixed volume ($Q = 9.65 \text{ L min}^{-1}$, $N = 100 \text{ rpm}$, $n = 0.12$, $\tau_y = 5.25 \text{ Pa}$, and $\mu_o = 22.61 \text{ Pa s}$).....	189
Figure (5.8-1). Comparison between CFD and experimental data for dimensionless cavern diameter (D_c/D) versus dimensionless $P_o Re_y$ at 0.5, 1.0, and 1.5% xanthan gum solutions.	193
Figure (5.8-2). Effect of the fluid rheology on the dimensionless cavern volume (V_c/V_{total}) at 0.5, 1.0, and 1.5% xanthan gum solutions using CFD and experimental data.....	194
Figure (5.8-3). Dimensionless cavern volume (V_c/V_{total}), the fraction of fully mixed volume ($V_{\text{fully mixed}}/V_{\text{total}}$), and the extent of channeling (f) as a function of the specific power at 1% xanthan gum solution.....	195
Figure (5.8-4). Effect of impeller speed on the mixing time at 0.5, 1.0, and 1.5% xanthan gum solutions using CFD.....	197
Figure (5.8-5). Dimensionless mixing time as a function of Reynolds number using CFD. ..	198
Figure (5.8-6). Effect of the fluid rheology on the mixing time as a function of power per volume.....	199
Figure (5.8-7). Effect of power law index (n) on the mixing time ($N = 900 \text{ rpm}$, $K = 8 \text{ Pa s}^n$, $\tau_y = 5.25 \text{ Pa}$, and $\mu_o = 22.61 \text{ Pa s}$).....	200
Figure (5.8-8). Effect of fluid yield stress (τ_y) on the mixing time ($N = 900 \text{ rpm}$, $K = 8 \text{ Pa s}^n$, and $n = 0.12$).	201
Figure (5.8-9). Effect of consistency index (K) on the mixing time ($N = 900 \text{ rpm}$, $n = 0.12$, $\tau_y = 5.25 \text{ Pa}$, and $\mu_o = 22.61 \text{ Pa s}$).....	202
Figure (5.9-1). Effect of impeller speed on the mixing time as a function of the xanthan gum concentration for the Maxblend impeller (with baffles).	206
Figure (5.9-2). Dimensionless mixing time as a function of Reynolds number for the Maxblend impeller (with baffles).....	207

Figure (5.9-3). Effect of the fluid rheology on the mixing time as a function of power per volume for the Maxblend impeller (with baffles)..... 208

Figure (5.9-4). Effect of the types of impellers on the mixing time at 1% xanthan gum concentration (with baffles). 209

Figure (5.9-5). Effect of the baffles on the mixing time (Maxblend, 1% xanthan gum)..... 211

Nomenclature

a	constant [Equations (2.1–6) and (2.2–1)]
A	cross section area of the inlet pipe (m^2)
A_i	swept area by the impeller (m^2)
b	constant [Equations (2.1–6) and (2.2–1)]
c	constant [Equations (2.1–6) and (2.2–2)]
C	impeller off-bottom clearance (m)
C_m	solution mass concentration (kg m^{-3})
C'_m	deviation in solution mass concentration (kg m^{-3})
$C_{m,in}$	Inlet solution mass concentration (kg m^{-3})
$C_{m,out}$	outlet solution mass concentration (kg m^{-3})
$C_{m,ss}$	Solution mass concentration at steady state conditions (kg m^{-3})
d	constant [Equation (2.2–2)]
d_i	inner diameter of the inlet and outlet (m)
D	impeller diameter (m)
\overline{D}	rate of strain tensor (s^{-1})
D_c	cavern diameter (m)
D_m	molecular diffusivity of the tracer ($\text{m}^2 \text{s}^{-1}$)
e_t	white noise signal
e_t^f	filtered white noise signal
f	percentage of channeling
\vec{F}	external (body) force (N)
Fr	Froude number
G	transfer function [Equation (2.4–7)]
G_1, G_2	transfer function [Figure (2.4-1)]
$\hat{G}(q)$	discrete time domain mixing vessel transfer function
g	gravitational acceleration (m s^{-2})
H	fluid height in the vessel (m)
H_c	cavern height (m)

K	consistency index (Pa.s ⁿ)
K_s	Metzner-Otto constant
M	torque (N.m)
n	power-law index
n	number of nodes in the velocity field [Equation (4.2–1)]
n_e	number of electrodes
N	impeller rotational speed (s ⁻¹)
$N\theta$	Mixing time number
N_Q	dimensionless impeller flow number
P	power (W)
P	pressure (Pa)
P_o	power number
$P1-P6$	plane number
Q	volumetric feed flow rate (m ³ s ⁻¹)
$Q_{impeller}$	impeller pumping rate (m ³ s ⁻¹)
R	percentage of recirculation
Re	Reynolds number
Re_y	yield stress Reynolds number
r, Φ, z	cylindrical coordinates (m, °, m)
T	tank diameter (m)
T	Temperature (°C) [Section (4.1.1)]
T_1, T_2	time delay (s)
t_s	sampling time (s)
u	radial or tangential velocity (m s ⁻¹)
u_i, v_j, w_k	cartesian velocity component normal to face (m s ⁻¹)
u_t^b	frequency modulated, random binary input signal
v	velocity of the fluid passing through the inlet (m s ⁻¹)
\bar{v}	mean velocity (m s ⁻¹)
\vec{v}	velocity (m s ⁻¹)
V_c	cavern volume (m ³)

$V_{fully\ mixed}$	fully mixed volume (m^3)
V_j	jet velocity ($m\ s^{-1}$)
v_n	normal velocity ($m\ s^{-1}$)
v_{tip}	impeller tip velocity ($m\ s^{-1}$)
V_{total}	fluid volume inside the mixing tank (m^3)
w	local mass fraction of the tracer
x, y, z	coordinates (m, m, m) [Section (4.2)]
y_t^b	Frequency modulated, random binary output signal

Greek Letters

ξ	length of data set
θ	mixing time (s)
μ	Newtonian viscosity (Pa.s)
μ_0	yielding viscosity (Pa.s)
$\dot{\gamma}$ and $\dot{\gamma}_{avg}$	shear rate (s^{-1})
η	non-Newtonian viscosity (Pa.s)
ρ	fluid density ($kg\ m^{-3}$)
τ	residence time (s)
τ	viscous stress tensor (Pa)
τ_s	shear stress (Pa)
τ_1 and τ_2	time constant (s)
τ_y	fluid yield stress (Pa)
ω	frequency, Hz

Abbreviations

2D	two-dimensions
3D	three-dimensions
BI	bottom inlet

BO	bottom outlet
CFD	computational fluid dynamics
CSTR	continuous stirred-tank reactor
DAS	data acquisition system
DHR	double helical ribbon
ERT	electrical resistance tomography
HG	Hayward Gordon
LBP	linear back projection
LDV	laser Doppler velocimetry
MRF	multiple reference frames
rpm	revolution per minute
RMS	root-mean-square
RSB	retreat swept back
RT	Rushton turbine
RTD	residence time distribution
TI	top inlet
TO	top outlet
UDF	user-defined function

Chapter 1

1. INTRODUCTION

The key objective of any mixing process is to maximize the degree of homogeneity of a property such as concentration, viscosity, color, and temperature. Mixing is prevalent in several contexts of biotechnology, petrochemical, mineral processing, food, power industries, fine chemicals, glass, polymer processing, pulp and paper, drinking water and wastewater treatment, cosmetic and consumer products, paints and automotive finishes, agrichemicals, and pharmaceuticals because of its vast applications (Oldshue, 1983). Mixing can be operated in a continuous or batch mode in stirred vessels. In the batch processes, materials are charged to the vessel, processed within it, and then discharged, therefore, it could favor for the processing a large number of products in a small-volume. On the other hand, in continuous-flow system, materials flow constantly through the mixing vessel from inlet to outlet. The continuous-flow mixing has several advantages over the batch mixing operation such as it provides high production rates, improves process control, and saves operation time and labor cost by eliminating loading and unloading materials and between-cycle cleaning (Nauman, 2002). Pseudoplastic or shear thinning fluids with yield stress such as paint, biological and polymer suspensions, pigment slurries, radioactive slurries, and paper and pulp suspension are commonly encountered in chemical and allied industries (Etchells et al., 1987).

Due to the complex rheology of non-Newtonian fluids, the design of mixing systems for these types of fluids is more challenging than that for the Newtonian fluids. Mixing of yield stress fluids leads to the formation of a well-mixed zone around the impeller (cavern) surrounded by a stagnant zone far from the impeller, where the impeller-imparted shear stress fails to exceed fluid yield stress (Wichterle and Wein, 1975). Ein-Mozaffari (2002) studied the continuous-flow mixing of non-Newtonian fluids in a pulp suspension chest and identified the non-ideal flows such as channeling, recirculation, and dead volume inside the stirred vessels.

The existence of non-ideal flows within a mixing vessel leads to ineffective heat and mass transfer, which results in the poor quality of end products, product degradation, and production loss. To improve the mixing efficiency of a reactor, it is always beneficial to eradicate such undesired non-ideal flows in the mixing of non-Newtonian fluids with yield stress.

The efficiency of continuous-flow system depends on the system geometry, fluid properties, and operating conditions. Important design parameters such as the impeller types (axial-flow impellers, radial-flow impellers, and close-clearance impeller), fluid rheology, feed flow rate, impeller speed, impeller diameters, impeller off-bottom clearance, locations of inlet and outlet, pumping directions of an axial-flow impeller, fluid height in the vessel, residence time, and jet velocity must be incorporated into the design protocol. Little information is available in the open literature on the effects of non-ideal flow on continuous-flow mixers for shear thinning fluids with yield stress. It is therefore highly desirable to investigate the dynamic behaviour of such vessels under realistic conditions, aiming to incorporate the extent of non-ideal flows (channeling, recirculation and dead zones) into the design criteria.

To investigate the effect of the design parameters on the mixing performances, different experimental techniques can be employed. Dynamic test has been successfully performed to identify non-ideal flows in the continuous-flow mixing of non-Newtonian fluids (Ein-Mozaffari, 2002; Ford et al., 2006; Saeed et al., 2008; Patel et al., 2011, 2012a, 2012b). Moreover, tomography, an efficient non-intrusive technique, is a tool to identify the dynamics characteristics of industrial processes based on real-time measurements. The electrical resistance tomography (ERT) provides new prospect for understanding of mixing processes and also validating CFD model (Bolton et al., 2004; Cullen, 2009; Tahvildarian et al., 2011). The recent and rapid development of the non-intrusive ERT seems to provide a valuable set of tools for the analysis and control of mixing processes especially in the case of non-Newtonian fluids (Patel et al., 2014a, 2014b, 2013a, 2013b, 2013c; Pakzad et al., 2008a).

The experimental techniques are sometimes costly, time-consuming, and not practical to study mixing of the non-Newtonian fluids. To overcome this difficulty, computational fluid dynamics (CFD) simulations can be applied to optimize the design of mixing vessels by developing models that take into account the actual flow fields in a mixing vessel. CFD

technique has been successfully used for mixing of yield-pseudoplastic fluids (Ein-Mozaffari and Upreti, 2009; Ihejirika and Ein-Mozaffari, 2007; Ford et al., 2006; Prajapati and Mozaffari, 2009; Pakzad et al., 2008a; Saeed et al., 2007, 2008), mixing of viscoelastic fluids (Bertrand et al., 1999), mixing of pseudoplastic fluids (Arratia et al., 2006; Montante et al., 2005; Kelly and Gigas, 2003; Murthy and Jayanti, 2003a, and b; Shekhar and Jayanti, 2003; Devals et al., 2008; Iranshahi et al., 2007; Iranshahi et al., 2006; Kelly and Humphrey, 1998), mixing in solid-liquid stirred tanks (Khopkar et al., 2006; Hosseini et al., 2010b; Montante and Magelli, 2005), mixing in gas-liquid stirred tanks (Ekambara and Joshi, 2003; Jahoda et al., 2009), mixing in gas-liquid-solid stirred tanks (Chapman et al., 1983; Murthy et al., 2007), mixing in multiple impeller stirred tanks (Aubin and Xuereb, 2006), mixing in coaxial stirred tanks (Rudolph et al., 2007; Rivera et al., 2009) and mixing of Newtonian fluids in laminar and turbulent regime (Kukukova et al., 2005; Aubin et al., 2004; Patwardhan and Joshi, 1999; Ranade, 1997; Vakili and Nasr Esfahany, 2009; Zadghafari et al., 2009).

The aim of this work was to characterize the continuous-flow mixing of yield-pseudoplastic fluid in a stirred vessel using dynamic tests, ERT and CFD. The objectives of this research were: (i) to investigate effect of impeller type, impeller off-bottom clearance, impeller diameter, impeller speed, pumping directions of an axial-flow impeller, fluid height in the vessel, fluid rheology, feed flow rate, mean residence time, jet velocity, and the locations of input and output on the degree of channeling (f) and the fraction of fully mixed volume ($V_{fully\ mixed}$) in the continuous-flow stirred tanks reactor for yield-pseudoplastic fluid with yield stress through dynamic tests, (ii) to explore the effects of the operating conditions and design parameters on the ratio of the residence time (τ) to the mixing time (θ) for the continuous-flow mixing of non-Newtonian fluids using dynamic tests and ERT, (iii) to visualize the flow pattern (in three dimensions) inside the continuous-flow mixing vessel to identify the dead zones and channeling of non-Newtonian fluids using ERT, (iv) to study the effect of inlet-outlet flows on the deformation of the cavern in a continuous-flow mixing system and to measure the cavern size and mixing time in the batch mode through ERT, (v) to investigate the effects of Herschel-Bulkley model parameters on the extent of channeling (f) and fully mixed volume ($V_{fully\ mixed}$) in the continuous mode, and the mixing time (θ) in the batch mode.

Chapter two is organized in two sections: the first section of this chapter provides comprehensive literature review on cavern, mixing time, and continuous-flow mixing in agitated vessels. The second section is devoted to the research objectives set for this study.

Chapter three will provide details on the experimental setup used for batch and continuous-flow mixing systems (including ERT system), the fluid rheology, and the experimental procedures and conditions.

Chapter four is organized in two sections: the first section provides the general information about CFD such as governing equations and other relevant information and the second section is devoted to the development of the CFD models for the batch and continuous-flow mixing systems employed in this study.

Chapter five provides the experimental and CFD results with the thorough discussions. This chapter is divided into nine sections. Each section is organized in three parts; introduction, results and discussion, and conclusions:

- **Section 5.1** provides details on the effects of various operating conditions and design parameters on performance of the continuous-flow mixing of non-Newtonian fluids using dynamic tests.
- **Section 5.2** focuses on the effect of close-clearance impeller i.e. the double helical ribbon (DHR) on the dynamic performance of the continuous-flow mixing.
- **Section 5.3** provides the hydrodynamic characteristics of the Maxblend impeller in continuous-flow mixing system using dynamic tests.
- **Section 5.4** discusses the characterization of the continuous-flow mixing system using the ratio of residence time to batch mixing time.
- **Section 5.5** mainly deals with the analysis of the deformation of the cavern in the continuous-flow mixing of non-Newtonian fluids using tomography.

- **Section 5.6** demonstrates an efficient method for flow visualization in the continuous-flow mixing of non-Newtonian fluids with yield stress using tomography.
- **Section 5.7** presents the effect of Herschel-Bulkley model parameters on the dynamic performance of the continuous-flow mixing of non-Newtonian fluids using CFD.
- **Section 5.8** explains the effect of the rheological parameters on the mixing time in the batch mode using CFD.
- **Section 5.9** describes the performances of the Maxblend impeller in the batch mode through mixing time.

Chapter 2

2. LITERATURE REVIEW

Mixing operations are multi-faceted and are extensively used in most of the chemical and allied process industries (Paul et al., 2004). It is necessary to properly design the mixing systems since the mixing efficiency has a momentous effect on the product quality. To evaluate the mixing performance, usually the channeling (f), fully mixed volume ($V_{fully\ mixed}$), cavern size (V_c), power consumption (P), and mixing time (θ) are determined. These parameters relies on the fluid properties, operating conditions, and system geometry.

Rheology studies the relation between force and deformation in materials. Viscosity is usually defined as the ratio of shear stress (τ_s) to shear rate ($\dot{\gamma}$). Fluids having a constant viscosity for any shear rate are called Newtonian and their viscosity is called Newtonian viscosity. If the ratio of shear stress to shear rate is not constant, the fluid is called non-Newtonian, and their viscosity is called apparent or non-Newtonian viscosity (Morrison, 2001). Fluids shows a wide variety of rheological behaviour ranging from Newtonian to viscoelastic (Rao, 1999). While the mixing of the Newtonian fluids is well understood, the understanding of the mixing of the non-Newtonian fluids still remains challenging. The viscoplastic fluids, which can be found frequently in food, paint, cosmetic, and pharmaceutical industries, are common class of non-Newtonian fluids (Paul et al., 2004). Mixing of this class of fluids such as the xanthan gum solution results in the formation of a well-mixed zone around the impeller and stagnant region elsewhere (Patel et al., 2014a). Lab scale study on pseudoplastic fluid with yield stress shows that the non-ideal flows such as channeling, recirculation, and dead zones significantly affect the performance of the continuous-flow mixing (Ein-Mozaffari, 2002). Channeling represents the portion of the fluid that is directly bypassed from inlet to outlet without going into mixing zone. This behaviour affects the mixing efficiency, which has a considerable impact on the performance of the industrial processes. It is important to remove

non-ideal flows (channeling and stagnant regions), which lead to the formation of hotspots and poor mass and heat transfer in the industrial reactors, by designing the mixing systems correctly. The present understanding and implementation of the continuous-flow mixing of non-Newtonian fluids is not enough to ensure the better mixing quality in many cases.

Following is a review of the literature pertaining to power consumption in agitated vessels, mixing time in a batch mode, cavern formation, and literature review on continuous-flow mixing in agitated vessels. At the end of this chapter, the objectives of this study are defined and justified.

2.1 Power Consumption

For the design of the mixing vessel, the power (P) is one of the most essential factors considered in the estimation of industrial operating costs. Power signifies the rate of energy dissipated within a fluid from the impeller. To operate an impeller, it is very necessary to have a good knowledge regarding the required power consumption (Chhabra and Richardson, 1999). Because of the very different flow patterns and mixing mechanisms involved, it is important to consider the power consumption for the Newtonian and non-Newtonian fluids separately.

2.1.1 Power Consumption for Newtonian Fluids

The impeller power in a homogeneous liquid depends upon the geometry of the impeller and the tank, the liquid properties such as density and viscosity, the impeller rotational speed and the gravitational force (Tatterson, 1991):

$$P = f(\mu, \rho, N, D, T, g) \quad (2.1-1)$$

where P , μ , ρ , N , D , T , and g are power, fluid viscosity, fluid density, impeller rotational speed, impeller diameter, tank diameter, and gravitational acceleration, respectively. Applying the dimensional analysis, we obtain (Skelland, 1967):

$$\frac{P}{\rho N^3 D^5} = f\left(\frac{\rho N D^2}{\mu}, \frac{N^2 D}{g}\right) = f(\text{Re}, Fr) \quad (2.1-2)$$

This relation shows that the dimensionless power coefficient $P/\rho N^3 D^5$ depends on both Reynolds number and Froude number for a fluid. The dimensionless groups can be presented as follows:

- **Power Number, P_o** is a non-dimensional measure of the power drawn by the impeller:

$$P_o = \frac{P}{\rho N^3 D^5} \quad (2.1-3)$$

- **Froude Number, Fr** represents the ratio of applied forces to gravitational forces. Thus, Fr is only considered when there are significant gravitational effects:

$$Fr = \frac{DN^2}{g} \quad (2.1-4)$$

- **Reynolds Number, Re** indicates the relative importance of the inertial forces to the viscous forces:

$$\text{Re} = \frac{\rho N D^2}{\mu} \quad (2.1-5)$$

For a single-phase fluid, it has been found that the functional relation becomes as:

$$\frac{P}{\rho N^3 D^5} = c \left(\frac{\rho N D^2}{\mu}\right)^a \left(\frac{N^2 D}{g}\right)^b \quad (2.1-6)$$

c , a , and b are the constants and depend on the geometry of the system and on the state of flow. In a baffled tank or in a vessel with an offset impeller to eliminate swirl, the gravitation effect will be negligible due to the elimination of the swirls and thus we can neglect the Froude number in the above relations; and the power number becomes only a function of Reynolds number.

The relation between the power number and the Reynolds number can be divided to three regions (Skelland, 1967): at low Reynolds number region (<10), laminar flow occurs and the slope of the power curve on log-log coordinates is -1. At very high values of Reynolds number ($>10^4$), the flow is fully turbulent. In this region, the power number is almost constant and independent of the Reynolds number. In between the laminar and turbulent zones, there exists a transition zone. No simple mathematical relationship exists between P_o and Re in this flow region (Chhabra and Richardson, 1999). It is generally accepted that laminar flow occurs for $Re < 10$, but for the transitional region, it is strongly dependent on the impeller and vessel geometry.

2.1.2 Power Consumption for Non-Newtonian Fluids

While predicting power number poses no problems for Newtonian fluids, the situation is more complicated for non-Newtonian fluids. The expression for Re has to be modified according to the fluid rheology. The most acceptable approach for the calculation of apparent viscosity at a given impeller speed is Metzner and Otto (Metzner and Otto, 1957) method.

2.1.2.1 The Metzner and Otto Approach

The basis of the Metzner and Otto approach is the determination of the range of the shear rate in the mixing system. To do this, they defined an apparent viscosity (η) as the viscosity of a Newtonian fluid, which requires the same power input under the same conditions in the laminar flow regime. The next step is to relate this viscosity to the shear rate. They considered that the fluid motion in the impeller region could be specified by an average shear rate, which is proportional to the impeller speed as:

$$\dot{\gamma}_{av} = K_S N \quad (2.1-7)$$

where K_S is a function of the impeller type. The xanthan gum solution is a shear-thinning fluid possessing yield stress and its rheological properties can be described by the Herschel-Bulkley model (Herschel and Bulkley, 1926):

$$\tau_s = \tau_y + K(\dot{\gamma})^n \quad (2.1-8)$$

where τ_s is the shear stress, τ_y is the yield stress, K is the consistency index, $\dot{\gamma}$ is the shear rate, and n is the power-law index. The apparent viscosity (η) of the Herschel-Bulkley fluid can be evaluated by (Ahmad et al., 2005):

$$\eta = \frac{\tau_y}{\dot{\gamma}_{av}} + K|\dot{\gamma}_{av}|^{n-1} \quad (2.1-9)$$

For Herschel-Bulkley type fluid, with:

$$\eta = \frac{\tau_s}{\dot{\gamma}_{av}} + \frac{\tau_s}{K_S N} \quad (2.1-10)$$

the Reynolds number is defined as:

$$\text{Re} = \frac{K_S N^2 D^2 \rho}{[\tau_y + K(K_S N)^n]} \quad (2.1-11)$$

where $\dot{\gamma}_{av}$, N , D , and ρ are averaged shear rate, impeller rotational speed, impeller diameter, and fluid density, respectively.

The value of K_S obtained by Metzner and Otto (1957) was 13 for the disk flat-blade turbine. Calderbank and Moo-Young (1959) have repeated and extended this work for a wide variety of sizes and types of impellers. They found the value of K_S as 10 rather than 13 for Bingham and

pseudoplastic fluids, suggested by Metzner and Otto (1957). For dilatants fluids the relative size of the impeller and mixing vessel has an effect on the shear rate and therefore on the effective value of K_S . Skelland (1967) has reported the experimental values for K_S for a variety of impeller, turbines, propeller, paddle, and anchor. For pseudoplastic fluids, K_S lies approximately in the range 10–13 for most impeller types, while slightly larger values 25–30 have been reported for anchors and helical ribbons (Bakker and Gates, 1995).

2.2 Mixing Time in a Batch Mode

To study the effect of various parameters on the performance of batch mixing, the mixing time provides a potent way for the evaluation of mixing effectiveness (Zlokarnik, 2001). The mixing time can be characterized as the time needed to reach a specific degree of homogeneity, and is usually measured by monitoring the dispersion of a small amount of a tracer within the stirred vessel through different experimental techniques. Mixing time is usually defined as the time required the tracer concentration to reach within 98% of the completely mixed value.

To measure the mixing time, different techniques based on the experimental analysis of tracer dispersion have been employed. Over the past few years, several experimental techniques, such as laser-induced fluorescence (Distelhoff et al., 1997), liquid-crystal thermography (Lee and Yianneskis, 1997), dye addition (Ascanio et al., 2003), conductivity probe (Bouaifi and Roustan, 2001), thermocouple-based techniques (Rewatkar and Joshi, 1991) and radioactive liquid tracer (Pant et al., 2001) have been employed to measure the mixing time. Some of these methods are not applicable for the opaque fluids and the probe techniques have the disadvantage of affecting the flow pattern inside the tank. Another disadvantage of some of these techniques is the confinement of the mixing time to a few monitoring points inside the tank. These limitations can be overcome using tomography technique. The capability of the ERT technique to characterize the mixing processes in term of mixing time (Zhao et al., 2008; Pakzad et al., 2008b) have been established.

It is desirable to use computational fluid dynamics (CFD) as a powerful tool for understanding of the mixing processes since the experimental studies have limitations

regarding the range of the variables that can be studied. CFD models enable simulation of the flow field and homogenization of the tracer by the direct solution of their governing equations (Bujalski et al., 2002; Sahu et al., 1999; Iranshahi et al., 2006; Jaworski et al., 2000; Patwardhan and Joshi, 1999; Ranade et al., 1991).

Mixing time is often correlated with the various design parameters using different mathematical models. Many mathematical models have been proposed for the prediction of mixing time. Moo-Young et al. (1972) studied the mixing time of miscible liquids having the same viscosity and density using various types of impellers such as the turbine, helical ribbon, and tubular agitators. They used a decolorization method to measure the mixing time and correlated the results using the following model (Tatterson, 1991):

$$N\theta = aRe^b \quad (2.2-1)$$

where a and b are constants.

Since power consumption is one of the most influential factors when estimating the operating cost in the design of mixing vessels in any industry. Therefore, some researchers attempted to study the efficiency of mixing systems by correlating the mixing time with the power consumption per unit volume (P/V) using the following equation (Moo-Young et al., 1972; Nienow, 1997).

$$\theta = c \left(\frac{P}{V} \right)^d \quad (2.2-2)$$

where c and d are constants.

2.3 Cavern

A main characteristic of the rheology of shear-thinning fluids possessing yield stress is that the viscosity decreases with increasing shear rate. Consequently, fluid flows very easily in high shear regions near the rotating impeller but it is subjected to high shear flow resistance in low shear regions remote from the impeller. In particular, the fluid motion ceases where shear

stresses are below the yield stress of the fluid. This leads to the formation of a well mixed region of fluid around the impeller with the remaining fluid appearing stagnant (Nienow and Elson, 1988; Galindo and Nienow 1993; Nienow, 1998). The term “cavern” was first introduced by Wichterle and Wein (1975 and 1981) to describe this region. In the laminar flow region, the ratio of cavern diameter/impeller diameter is constant (independent of impeller speed) and approximately equal to unity. Thus, mixing of a yield stress fluid in the laminar region requires an impeller which has a diameter equal to that of the tank to avoid stagnant regions (Solomon et al. 1981; Elson et al. 1986; Galindo and Nienow, 1992). In the transition and turbulent region, cavern diameter increases with increasing impeller speed. Cavern diameter becomes constant when the cavern reaches the vessel wall. As impeller speed continues to increase, cavern gains vertical circulation and increases in height until it fills the whole of the vessel (Galindo and Nienow, 1992; Galindo et al., 1996).

Some researchers have developed models to predict the cavern size as a function of mixing conditions and fluid properties. Solomon et al. (1981) assumed a spherical cavern with the torque induced by the impeller acting tangentially at the cavern boundary. Subsequently, Elson and Cheeseman (1986) and Elson (1988) proposed a cylindrical model, which effectively predicted the behavior of the cavern before it reached the vessel walls. This proposed model Equation (2.3–1) specifies that the dimensionless cavern diameter (D_c/D) is proportional to the product of the power (P_o) and the yield stress Reynolds number (Re_y):

$$\left(\frac{D_c}{D}\right)^3 = \left(\frac{1}{\left(\frac{H_c}{D_c} + \frac{1}{3}\right) \pi^2}\right) \left(\frac{N^2 D^2 \rho}{\tau_y}\right) P_o \quad (2.3-1)$$

where D_c , D , H_c , N , ρ , and τ_y are the cavern diameter, impeller diameter, cavern height, impeller rotational speed, fluid density, and fluid yield stress, respectively. The term $N^2 D^2 \rho / \tau_y$ on the right hand side of Equation (2.3–1) is referred to as the yield stress Reynolds number, Re_y . Amanullah et al. (1998) developed an axial force model for a torus-shaped cavern while Wilkens et al. (2005) proposed a model for an elliptical torus-shaped cavern without accounting the axial force. Hirata and Aoshima (1996) also suggested a model based on viscous dissipation

for a cylindrical-shaped cavern. Hui et al. (2009) developed an axial force cavern model, which accounted for interaction between the cavern and vessel walls due to the impeller location. Amanullah et al. (1998) showed that the cylindrical model represents the cavern shape better than the spherical model. In fact, the cylindrical model [Equation (2.3–1)] has been widely used to measure the cavern size (Patel et al., 2014a; Pakzad et al., 2008a; Saeed et al., 2008).

Several experimental methods have been applied to investigate the cavern shape and size such as coloring with dye and taking pictures (Wichterle and Wein, 1975, 1981; Galindo and Neinow, 1992, 1993; Amanullah et al., 1998), traversing hot film anemometer (Solomon et al., 1981), taking X-ray photographs (Elson et al., 1986; Elson, 1988; Nienow and Elson, 1988), using laser Doppler anemometer (Hirata and Aoshima, 1996; Jaworski and Nienow, 1994), and using planar laser induced (Adams and Barigou, 2006; Arratia et al., 2006) and ultraviolet fluorescence (Arratia et al., 2006). In some visualization technique (e.g. colorimetric), the medium must be transparent while most of the non-Newtonian fluids are opaque. However, hot film anemometer has considerable advantages specially compared with laser Doppler anemometers in the case of cost, frequency response, size of sensor, and signal to noise ratio, it has the disadvantage of delicate probes presence which modifies the local flow field. The X-ray technique provides a non-intrusive measurement in opaque fluids (Elson, 1988), a task otherwise impossible for laser Doppler anemometers and hot film anemometer. The penetration depth of X-rays is restricted by the X-ray opacity of the fluids used and the vessel walls (Nienow and Elson, 1999). The electrical resistance tomography (ERT), a non-intrusive technique, can be employed to study the shape and the size of cavern generated around the impeller in the mixing of the opaque fluids possessing yield stress (Pakzad et al., 2008a).

2.4 Continuous-Flow Mixing

As mentioned earlier, the chemicals to be mixed in the batch mixing are loaded into the mixer, the mixer is operated, and the final product is unloaded so that another batch can be loaded into the vessel. On other hand, the continuous-flow mixing allows material to flow steadily from an upstream process into the mixing vessel, is retained in the vessel for a specified residence time,

and is discharged for downstream handling. Compared to batch mixing, continuous mixing is more economical due to consistent mixing quality, improved process control, high capacity, and lower mixing cost (Nauman, 2002). In continuous-flow mixers, the mixing process depends not only upon the type of stirrer and speed of stirring, but also upon mean residence time and vessel geometry, including the input and output location. The outlet may be positioned either at the bottom of the tank to drain vessel contents by gravity, or at the side of the vessel. The inlet position may also vary, with the tip of the inlet pipe located at the top of the vessel or at some place inside the stirred liquid close to the impeller. Although submerged inlets are recommended for efficient mixing, they may generate operational problems such as mechanical vibrations, corrosion, and clogging. Thus, bottom outlet and surface input are often preferred.

The work done in the open literature on mixing in continuous-flow vessels is provided in the rest of this section.

2.4.1 Close-Clearance Impellers in the Continuous-Flow Mixing

2.4.1.1 The Double Helical Ribbon (DHR) Impeller

Close-clearance impellers such as helical ribbon and anchor impellers are also used in the mixing of viscous fluids in stirred vessels. The anchor impeller primarily generates tangential flow (Peters and Smith, 1969); while operating at higher rotational speeds it creates secondary axial and radial flow (Ohta et al., 1985), and it has been used for the mixing of non-Newtonian fluids in a batch mixing vessel (Prajapati and Ein-Mozaffari, 2009). Iranshahi et al. (2006) compared the performance of the Ekato Paravisc with that of the anchor and double helical ribbon (DHR) impellers. The analysis of the flow patterns and chaotic mixing parameters showed that the DHR impeller was the most efficient among the three impellers used in their study. Shervin et al. (1991) employed the flow visualization technique to explore the mixing of viscoelastic fluids in stirred batch vessels. The results showed that the helical impellers provided shorter blend times and more uniform mixing than other types of impeller, such as an axial-flow impeller (pitched blade turbine) and an radial-flow impeller (Rushton turbine). Ihejirika and Ein-Mozaffari (2007) investigated the mixing of pseudoplastic fluids with a helical ribbon impeller in a batch stirred vessel using computational fluid dynamics (CFD) and

ultrasonic velocimetry. The results showed that although the torque and power characteristics remained the same for upward and downward pumping mode of the helical ribbon impeller, the mixing times were considerably longer for the downward pumping mode. Takahashi et al. (1988) studied the mixing of pseudoplastic liquids in a batch stirred vessel equipped with a variety of helical ribbon impellers and showed that the direction of the primary flow of a helical ribbon impeller was reversed by reversing the impeller rotational direction while the effect of the secondary circulation flows was strongly dependent on the impeller geometry. Helical ribbon impellers are also widely used in the mixing of viscous fluids in the agitated vessel and a review of these could be found in Delaplace et al. (2000). These studies on the mixing of viscous fluids in stirred vessels equipped with the helical ribbon and anchor impellers are more related to a batch process. No information is available on the continuous-flow mixing of non-Newtonian fluids with the helical ribbon impeller.

2.4.1.2 The Maxblend Impeller

Apart from the traditional close-clearance impellers, the efficient, versatile, and very rapidly emerging close-clearance impeller, “the Maxblend impeller” was first introduced for mixing of highly viscous culture broths. The Maxblend impeller is efficient in the mixing of viscous fluids over a wide range of Reynolds numbers at lower energy dissipation. Moreover, the Maxblend impeller takes a planar shape as a whole for easy maintenance and cleaning after operations. The unified structure of the Maxblend impeller consists of a bottom paddle mounted by a top grid. The paddle assists in generating an overall flow circulation in a tank while the grid provides capacity for dispersing a second phase. Hence, it is suitable for a variety of applications in liquid-liquid, solid-liquid, and gas-liquid mixing. The diameter of the Maxblend impeller generally falls in a range from 45 to 70% of the inner diameter of the vessel, which allows installing the other internal components such as baffles and heat transfer coils as well (Mishima, 1992; Yokoi et al., 1993).

Very few researchers have investigated the performance of the Maxblend impeller in batch mixing. Yao et al. (2001) explored the mixing of Newtonian fluids in stirred vessels using the Maxblend and double helical ribbons impellers. The numerical results showed that the double helical ribbon impeller was not capable of providing better mixing performance although total

circulation of fluids in the tank was good. The Maxblend impeller showed satisfactory local dispersive mixing performance when operated at moderate Reynolds numbers but could not perform effectively at very low Reynold numbers. Dohi et al. (2004) compared the power consumption and solid suspension performance among the Maxblend, Fullzone, and triple-impeller by mixing the gas-liquid-solid phase in a stirred vessel. The results showed that the Maxblend impeller was the most efficient for solid suspension among the impellers used in their studies.

Takahashi et al. (2006a) measured the mixing time achieved by the Maxblend, Fullzone, and triple-disk turbine. The results showed that in some cases the Maxblend impeller had essentially the same performance as the Fullzone impeller. However, overall the Maxblend impeller gave the best mixing performance in the boiling system among the impellers used in their study. Takahashi et al. (2006b) found that the Maxblend impeller had shorter mixing time than the double helical ribbon impeller for $Re > 10$. Iranshahi et al. (2007) characterized experimentally and numerically the performance of the Maxblend impeller for the mixing of Newtonian fluids in the stirred vessel equipped with baffles and without baffles. They demonstrated that the Maxblend impeller provided superior performance when used with baffles in transition regime and upper laminar regime. The hydrodynamics of an agitated vessel equipped with the Maxblend impeller was experimentally investigated with the viscous Newtonian and shear-thinning fluids by Fradette et al. (2007). The results showed that variation of the off-bottom clearance up to three times of the nominal clearance recommended by suppliers did not affect significantly the mixing efficiency; however, the bottom clearance had a significant influence on the mixing time when it reached five times the nominal value of the bottom clearance. They concluded that the Maxblend impeller provided efficient mixing with lower power consumption.

Devals et al. (2008) characterized numerically the hydrodynamic performance of the Maxblend impeller utilized for the mixing of Newtonian and non-Newtonian fluids in an agitated vessel. They found that the power constant for the Maxblend impeller was smaller than that of impellers like Paravisc, anchor, and helical ribbon. Further, the power constant was slightly higher in the baffled configuration compared to the unbaffled one. It was also

concluded that the impeller off-bottom clearance played a significant role in the power consumption. Guntzburger et al. (2009) studied the mixing of Newtonian fluids in an agitated vessel using the Maxblend impeller and found that the straight Maxblend impeller is less efficient (yields longer mixing times and more power consumption) than the wedge Maxblend impeller. The evidences in the literatures suggest that the Maxblend impeller has been successful and efficient for the mixing of Newtonian and non-Newtonian fluids in the batch vessels. Nevertheless, these studies are absolutely confined to batch mixing. Based on the author's knowledge, no information is available on the continuous-flow mixing of non-Newtonian fluids with the Maxblend impeller.

2.4.2 Dynamic Modeling of Continuous-Flow Mixing System

The continuous-flow mixing vessels have always been designed based on ideal mixing assumptions (Oldshue, 1983): (1) input stream is instantaneously dispersed throughout the vessel, (2) input and output flow rate are equal, (3) composition of outlet stream is equal to the uniform composition throughout the tank, and (4) fully mixed volume is equal to the total volume of solution in the vessel. A mass balance on continuous-flow vessel yields the following:

$$\rho Q C_{m,in} - \rho Q C_{m,out} = \rho V \frac{dC_{m,out}}{dt} \quad (2.4-1)$$

$$C_{m,in} - C_{m,out} = \tau \frac{dC_{m,out}}{dt} \quad (2.4-2)$$

where C_m , t , ρ , Q , V and $\tau = V/Q$, represent solution mass concentration, time, solution density, solution flow rate, solution volume and vessel residence time. At steady state, $C_{m,in,ss} = C_{m,out,ss}$ and Equation (2.4-2) can be written as follows:

$$(C_{m,in} - C_{m,in,ss}) - (C_{m,out} - C_{m,out,ss}) = \tau \frac{dC_{m,out}}{dt} \quad (2.4-3)$$

$$C'_{m,in} - C'_{m,out} = \tau \frac{dC'_{m,out}}{dt} \quad (2.4-4)$$

where $C'_{m,in} = C_{m,in} - C_{m,in,ss}$ and $C'_{m,out} = C_{m,out} - C_{m,out,ss}$ are deviation variables. Taking Laplace transform of both sides of Equation (2.4-4) yields the following:

$$\tau s.C'_{m,out}(s) = C'_{m,in}(s) - C'_{m,out}(s) \quad (2.4-5)$$

$$G(s) = \frac{C'_{m,out}(s)}{C'_{m,in}(s)} = \frac{1}{\tau s + 1} \quad (2.4-6)$$

Equation (2.4-6) indicates the behaviour of a perfectly mixed-flow mixer represented by a first order transfer function.

However, compared to Newtonian fluids, non-Newtonian fluids display a complex rheology which can create considerable deviation from the ideal mixing. It has been shown in open literatures that the non-ideal flows such as channeling, recirculation, and dead zones significantly affect the performance of continuous mixing processes (Ein-Mozaffari et al., 2003a, 2007; Ford et al., 2006; Upreti and Ein-Mozaffari, 2006; Saeed et al., 2007; Saeed and Ein-Mozaffari, 2008; Saeed et al., 2008). Hence, one would set an objective to identify the flow non-ideality encountered in a continuous-flow mixing vessel under different working conditions. For this purpose, a model that describes the dynamics of a mixing vessel, incorporating non-ideal flow parameters, i.e. channeling, recirculation, and dead zones, should be adopted. Ein-Mozaffari (2002) developed such a dynamic model [Figure (2.4-1)] which included a well-mixed zone as well as non-ideal flows for non-Newtonian fluids. This model has been widely useful to describe the behavior of mixing in a continuous-flow vessel.

In Figure (2.4-1), f represents the portion of the fluid that channeled in the mixing tank. A limited amount of mixing can occur in the channeled flow and is presented by a first order transfer function (G_1). On the other hand, $(1-f)$ is the fraction of the fluid that enters the mixing zone and has a first order transfer function of G_2 . A portion of the fluid, R , exiting the mixing

zone can be recirculated within the mixing zone. Parameters τ_1 and τ_2 are the time constants for the channeling and mixing zones, respectively. Parameters T_1 and T_2 are the time delays for the channeling and mixing zones, respectively.

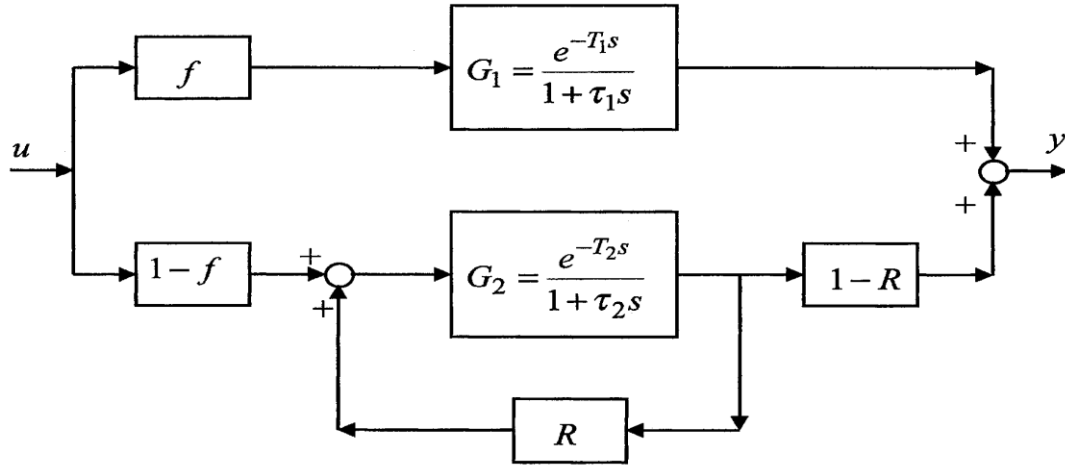


Figure (2.4-1). Continuous-time dynamic model for continuous-flow mixers (Ein-Mozaffari, 2002).

The combined transfer function for the above system in a continuous-time domain can be expressed mathematically as follows (Ein-Mozaffari et al., 2003b, 2004a, 2005, 2007):

$$G = \frac{f e^{-T_1 s}}{1 + \tau_1 s} + \frac{(1-f)(1-R) \frac{e^{-T_2 s}}{1 + \tau_2 s}}{1 - \frac{R e^{-T_2 s}}{1 + \tau_2 s}} \quad (2.4-7)$$

where G is the transfer function of the vessel. To estimate the non-ideal parameters such as channeling, recirculation, and dead zones, the mixing vessel is excited by an input signal in order to observe the system response (output signal). By measuring the input and output responses of the mixing vessel, the dynamic model parameters can be estimated using the numerical method developed by Kammer et al. (2005). No recirculation (R) was observed in the laboratory-scale pulp mixing tank (Ein-Mozaffari et al., 2004b, 2003b), however, it was identified in the industrial mixing vessel (Ein-Mozaffari et al. 2004a, 2005).

Kammer et al. (2005) transformed the continuous-time model Equation (2.4–7) into a simple discrete-time model Equation (2.4–8) using zero-order hold (Seborg et al., 1989). The discrete-time domain transfer function $\hat{G}(q)$ equivalent to Equation (2.4–7) is given as follows (Einz-Mozaffari et al., 2003b, 2005):

$$\hat{G}(q) = \frac{\alpha_1 q^{-d_1} + \alpha_2 q^{-(d_1+1)} + \alpha_3 q^{-d_2} + \alpha_4 q^{-(d_2+1)} + \alpha_5 q^{-(d_1+d_2)}}{1 + \alpha_6 q^{-1} + \alpha_7 q^{-2} + \alpha_8 q^{-d_2} + \alpha_9 q^{-(d_2+1)}} \quad (2.4-8)$$

where

$\alpha_1 = f(1 - a_1),$	$\alpha_7 = a_1 a_2,$
$\alpha_2 = -f(1 - a_1) a_2,$	$\alpha_8 = -R(1 - a_2),$
$\alpha_3 = (1 - f)(1 - R)(1 - a_2),$	$\alpha_9 = R a_1(1 - a_2),$
$\alpha_4 = -(1 - f)(1 - R) a_1(1 - a_2),$	$a = e^{-t_s/\tau_m},$
$\alpha_5 = -fR(1 - a_1)(1 - a_2),$	$d_1 = 1 + T_i / t_s,$
$\alpha_6 = -a_1 - a_2,$	$d_2 \geq d_1.$

where T_i , t_s and q^{-1} are the i^{th} time delay, sampling time, and backward shift operator, respectively. The backward shift operator defined as $q^{-1}f(K)=f(K-1)$. The model parameters (f , R , a_1 , a_2 , d_1 , and d_2) are estimated by minimizing the cost function as follows:

$$J_\xi = \frac{1}{\xi} \sum_{t=1}^{\xi} [y_t^b - \hat{G}(q)u_t^b]^2 \quad (2.4-9)$$

where ξ , y_t^b , and u_t^b are the length of data set, measured output, and measured input, respectively.

Two distinct stages were used during the minimum search process: an efficient but less accurate least squares minimization for the optimal delays, followed by an accurate gradient search for all parameters using sequential quadratic programming (SQP) method (Fletcher, 1987; Edgar et al., 2001). This method uses an optimization technique to solve the constrained nonlinear problems. The parameter R was set to zero as the recirculation of the fluid was not observed in the dynamic responses of the laboratory-scale mixing vessel. Two parameters were used to quantify the flow non-ideality: f , the degree of channeling in the vessel, and $V_{\text{fully mixed}}/V$,

the ratio of the fully mixed volume ($V_{fully\ mixed}$) in the vessel to the total solution volume (V) in the vessel. The fully mixed volume is given by (Ein-Mozaffari et al., 2004b, 2004b, 2005, 2007):

$$\frac{V_{fully\ mixed}}{V} = \frac{Q\tau_2(1-f)}{V} \quad (2.4-10)$$

where Q is the solution flow rate through the mixing vessel. Normally, the nominal fully-mixed volume is calculated using $V_{fully\ mixed} = \tau Q$, where τ and Q are the nominal residence time and total feed flow rate, respectively. However, this equation cannot be used for the continuous-flow mixing of non-Newtonian fluids since the non-ideal flows exist within the mixing tank. Thus, to calculate the actual fully-mixed volume, we should employ the residence time of the mixing zone (τ_2) and the fraction of the feed, which enters to the mixing zone. Since f is the fraction of the feed, which is short-circuited, the flow rate to the mixing zone would be $Q(1-f)$. Therefore, the actual fully-mixed volume is calculated using $V_{fully\ mixed} = Q(1-f)\tau_2$.

2.4.3 Literature Review on Continuous-Flow Mixing

Although continuous-flow stirred tanks have been described by Agricola in 1556, study of the mixing in continuous-flow vessels is relatively limited to few publications. In his state of the art book *De Re Metallica* (1556), Agricola provided drawings of continuous-flow stirred tanks utilized in mining and metallurgical applications. The studies conducted on Newtonian fluids show that continuous-flow mixing systems deviate from perfect mixing (Magelli et al., 1978).

Many researchers have employed the residence time distribution (RTD) technique (Danckwerts, 1953) to identify the non-ideal flows in continuous-flow mixing systems (Paul et al., 2004), while some others have related the mean residence time (τ) in a continuous-flow mixing vessel to the mixing time (θ) for the batch mode (Zannoud et al., 1991). These studies suggest that $\tau/\theta = 10$ should be used as a criterion for ideal mixing in the continuous-flow mixing of Newtonian fluids in stirred vessels. These studies also showed that if the value of τ/θ is less than 10, the mixing system would be prone to the existence of non-ideal flows.

Roussinova and Kresta (2008) studied continuous-flow mixing of Newtonian fluids in a stirred vessel. They found that when the mean residence time (τ) in the tank fell below 10 times the batch blend time (θ), mixing deviated by up to 50% from an ideal continuous stirred-tank reactor (CSTR) model. They also found that for the design of an ideal mixer, a line from the inlet to the outlet should pass through the impeller. Jones et al. (2009) evaluated the performance of the continuous-flow mixing using a momentum ratio (a ratio of impeller discharge momentum to inlet jet momentum) and found that a momentum ratio of above 100 was required to achieve a perfectly mixed CSTR.

Using laser Doppler velocimetry (LDV), Mavros et al. (1997, 2002a, 2000b) studied continuous-flow mixing of Newtonian fluids. They investigated the flow structure generated by a Rushton turbine and a Mixel TT impellers in a vessel. Velocity measurements were obtained for two inlet locations: a surface input located above the impeller and a submerged input facing the impeller. They concluded that the flow disruption caused by incoming liquid stream in both configurations was noticeable only in the first vessel quarter, which followed the plane where the input tube was located. The disruption of the flow gradually attenuated and velocity measurements taken in a plane rotated 90° clockwise from the input indicated a flow pattern similar to that obtained in a batch mixing vessel. They also found that non-ideal flows such as channeling are likely to occur in a mixer if the ratio of residence time to batch mixing time is less than 10.

Using residence time distribution (RTD) and computational fluid dynamics (CFD), Samaras et al. (2006) studied the continuous-flow mixing of Newtonian fluids. They revealed that mixing Newtonian fluids with axial-flow impellers was prone to channeling when the location of the outlet was directly below the impeller discharge; however, such a potential problem was not observed when a radial-flow impeller was used. They concluded that the amount of perfectly mixed volume in the vessel reached only 60-80% of the total vessel volume, and noted that up to 25% of the total vessel volume behaved like dead zones, and up to 14% corresponds to plug flow.

Using CFD, Aubin et al. (2006) studied the effects of pumping directions of an axial flow impeller (a Mixel TT impeller) in the continuous-flow mixing of Newtonian fluids. They

observed that the channeling through a bottom outlet may be reduced when the impeller was employed in the up-pumping mode instead of the down-pumping mode.

Using CFD, Khopkar et al. (2004) simulated the fluid flow of the continuous-flow mixing of Newtonian fluids and found that the locations of the inlet and outlet affect the performance of continuous-flow mixing systems. All these studies were conducted for the Newtonian fluids.

Johnson and Hubbard (1974) obtained response data for negative step changes in input tracer concentration for a continuous-flow mixing vessel under different impeller speeds and polysaccharide dilution rates. Comparing experimental measurements with the ideal residence time distribution, Johnson and Hubbard concluded that using ideal mixing concept in scaling mixing vessels may lead to serious errors because bulk motion does not dominate the mixing vessel.

Using dynamic tests, Ein-Mozaffari et al. (2000, 2003a, 2003b, 2004a, 2004b, 2005, 2007) studied the mixing of pulp suspensions (a non-Newtonian fluid) in an agitated pulp stock chest under controlled conditions of impeller speed, pulp suspension concentration, input pulp suspension flow rate and vessel input and output locations. They attributed the deviations from ideal mixing to a number of factors including channeling, recirculation and the presence of dead zones in the chest. Such zones can arise from the interaction between the circulation patterns generated by the impellers, the suspension flow through the vessel and chest geometry. Dynamic tests conducted on a pilot stock chest by Ein-Mozaffari et al. (2003a, 2003b) showed that the extent of non-ideal flow can be significant. Ein-Mozaffari et al. (2003a) examined the effect of impeller diameter (the ratio of impeller diameter to chest width was 0.25, 0.34, and 0.41) on the performance of an agitated pulp stock chest. It was observed that the impeller with the largest diameter provided the best performance for the mixing of pulp suspension, which indicates that an increase in the diameter of the impeller improves the performance of the mixing system. The performance of a continuous-flow mixing system also depends on the fluid rheology (Ein-Mozaffari et al., 2007).

Using CFD, Ford et al. (2006) studied the fluid flow of pulp suspensions (a non-Newtonian fluid) in an agitated pulp stock chest equipped with a side-entering impeller using CFD. They

found that the extent of non-ideal flows was reduced using the bottom outlet compared to the side outlet while providing the inlet at the top of the vessel.

Using dynamic tests, Saeed et al. (2008) and Saeed and Ein-Mozaffari (2008) studied the continuous flow mixing of xanthan gum (non-Newtonian fluid) using four axial-flow impellers. They reported that Lightnin A200 impeller was the least effective, while Lightnin A320 impeller was the most effective in reducing the effect of channeling and dead volume.

These studies on continuous-flow mixing are more related to Newtonian fluids. Little information is available on the continuous-flow mixing of non-Newtonian fluids possessing yield stress in stirred vessels.

2.5 Research Objectives

In fact, an exhaustive search of the literature suggest that a very limited research has been devoted to study the continuous-flow mixing in stirred vessels. Even within these limited areas of research, more attention has been given to the study of continuous-flow mixing of Newtonian fluids. To develop a design protocol for this type of the mixers, more studies should be conducted to characterize the hydrodynamics of the continuous-flow mixers as a function of operating conditions and design parameters by using the advanced flow visualization techniques such as the electrical resistance tomography (ERT), the advanced numerical methods such as the computational fluid dynamics (CFD), and dynamic tests. Therefore, the core objective of this study is to develop methodology and tool to design the continuous-flow mixing system for the fluids with complex rheology using dynamic tests, ERT, and CFD.

In this study we employed dynamic tests, ERT and CFD to study the continuous-flow mixing of yield-pseudoplastic fluids in the stirred tank reactor. The key objectives of this work are:

- To improve the dynamic performance of the continuous-flow mixing of yield-pseudoplastic fluids by utilizing the Maxblend and Double Helical Ribbon (DHR) impellers. Also to improve the understanding of mixing dynamics in continuous-flow

mixers by investigating the effect of impeller type, impeller off-bottom clearance, impeller diameter, impeller speed, pumping directions of an axial-flow impeller, fluid height in the vessel, fluid rheology, feed flow rate, mean residence time, jet velocity, and the locations of inlet and outlet on the degree of channeling (f) and the fraction of fully mixed volume ($V_{fully\ mixed}$) in the mixing of yield-pseudoplastic fluid with the 3AH (axial-flow) impeller.

- To evaluate the ratio of the residence time (τ) to the batch mixing time (θ) for ideal mixing of the continuous-flow mixing of yield-pseudoplastic fluids through dynamic tests and ERT, and to explore the effects of various operating conditions and design parameters on the ratio of τ to θ .
- To analyze and quantify the deformation of the cavern in the continuous-flow mixing system for yield-pseudoplastic fluids using ERT. Also to measure the cavern size and mixing time in a batch mode using ERT.
- To demonstrate an efficient method for flow visualization in the continuous-flow mixing of opaque fluids using 2D and 3D tomograms. Also to identify the sources of flow non-ideality in yield-pseudoplastic fluids by visualizing the flow pattern inside the continuous-flow mixing vessel using ERT.
- To evaluate the hydrodynamic characteristics of the Maxblend impeller in a batch mode through mixing time (θ) using ERT.
- To develop a CFD model to evaluate the effects of Herschel-Bulkley model parameters, and fluid rheology on the extent of channeling (f) and fully mixed volume ($V_{fully\ mixed}$), and on the mixing time (θ).

Chapter 3

3. EXPERIMENTAL SETUP AND METHODOLOGY

This chapter comprises experimental setup, fluid rheology, experimental procedure, error analysis, and experimental conditions.

3.1 Experimental Setup for Dynamic tests

The experimental setup shown in Figure (3.1-1) was used in this study to perform dynamic tests on a continuous-flow mixing system (Patel et al., 2014). A transparent flat-bottomed cylindrical tank with a diameter (T) of 0.38 m and a height of 0.60 m was used as a mixing vessel. As shown in Figure (3.1-2) and Figure (3.1-3) various axial-flow, radial-flow, and close-clearance impellers were utilized to agitate the xanthan gum solution. The diameter of each axial-flow and radial-flow impeller was a 0.178 m diameter (D). The geometrical details of close-clearance impellers is provided in Table (3.1-1). To avoid creating a vortex, the tank was fitted with four equally spaced baffles (0.04 m wide, 0.012 m thick, and length equal to the tank height) to the vessel wall. The tank was also fitted with inlet and outlet tubes. The inner diameter of the outlet was kept to 0.025 m. However, the inner diameter of the inlets was varied (7.94×10^{-3} to 25.4×10^{-3} m) to explore the effect of jet velocity on the continuous-flow mixing system. To investigate the effects of the inlet and outlet locations on continuous-flow mixing, the inlets were located at the top ($r = 0.13$ m, $\Phi = 90^\circ$, and $z = 0.38$ m) and at the bottom ($r = 0.05$ m, $\Phi = 105^\circ$, and $z = 0.10$ m) of the mixing vessel. The outlets were located at the bottom ($r = 0.13$ m, $\Phi = 315^\circ$, and $z = 0.00$ m) and the top side ($r = 0.19$ m, $\Phi = 315^\circ$, and $z = 0.35$ m) of the mixing vessel. The mixing tank was equipped with a top-entering impeller driven by a 2-hp motor and the impeller speed was set to the desired revolutions per minute (rpm) using a variable frequency drive (VFD).

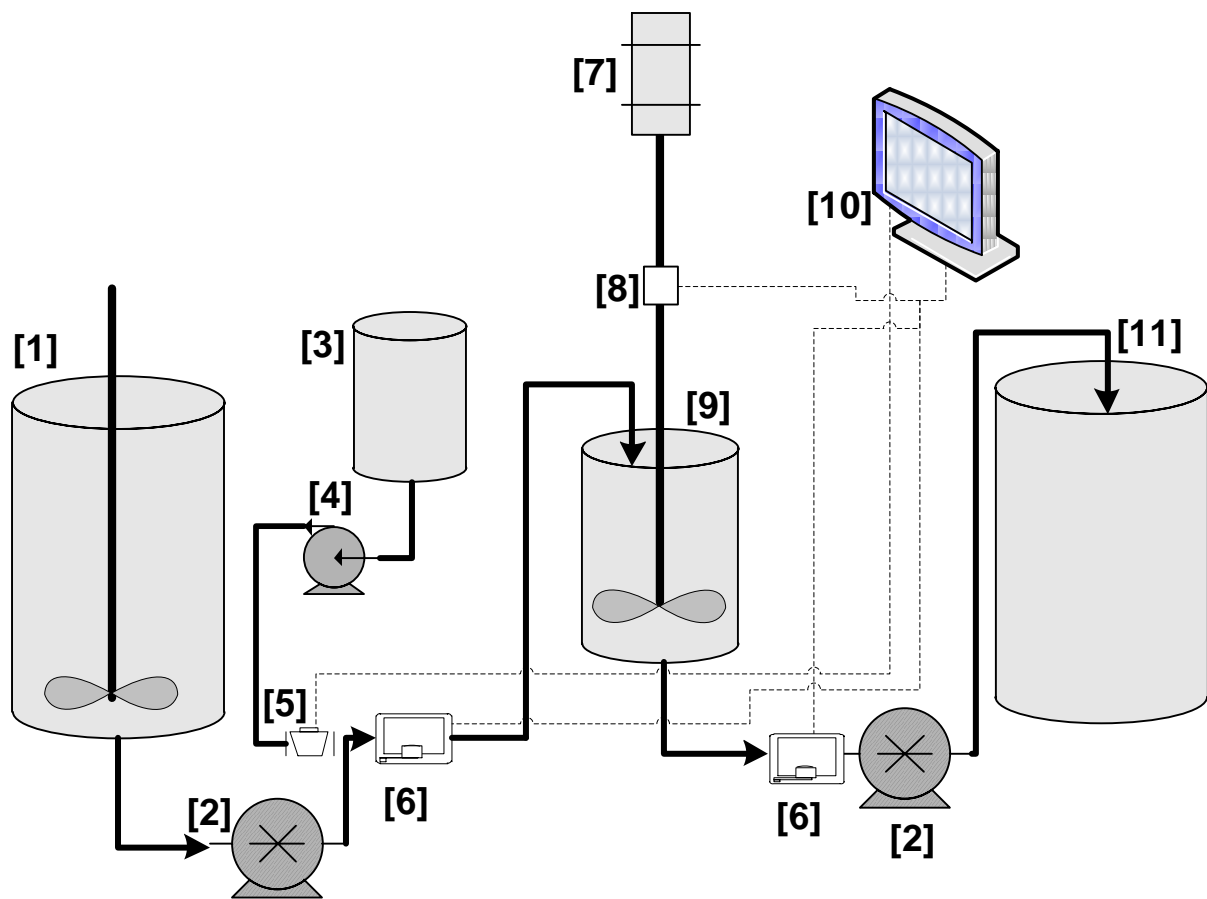


Figure (3.1-1). Schematic diagram of the continuous-flow mixing process: (1) feed tank, (2) progressing cavity pump, (3) tracer tank, (4) metering pump, (5) solenoid valve, (6) conductivity sensor, (7) electric motor, (8) torque meter, (9) mixing tank, (10) data acquisition system, and (11) discharge tank.

Table (3.1-1). Geometrical details of close-clearance impellers .

Descriptions	Off-bottom clearance (m)	Diameter (m)
Double helical Ribbon	0.010	0.367
Maxblend	0.005	0.247
Anchor	0.018	0.343

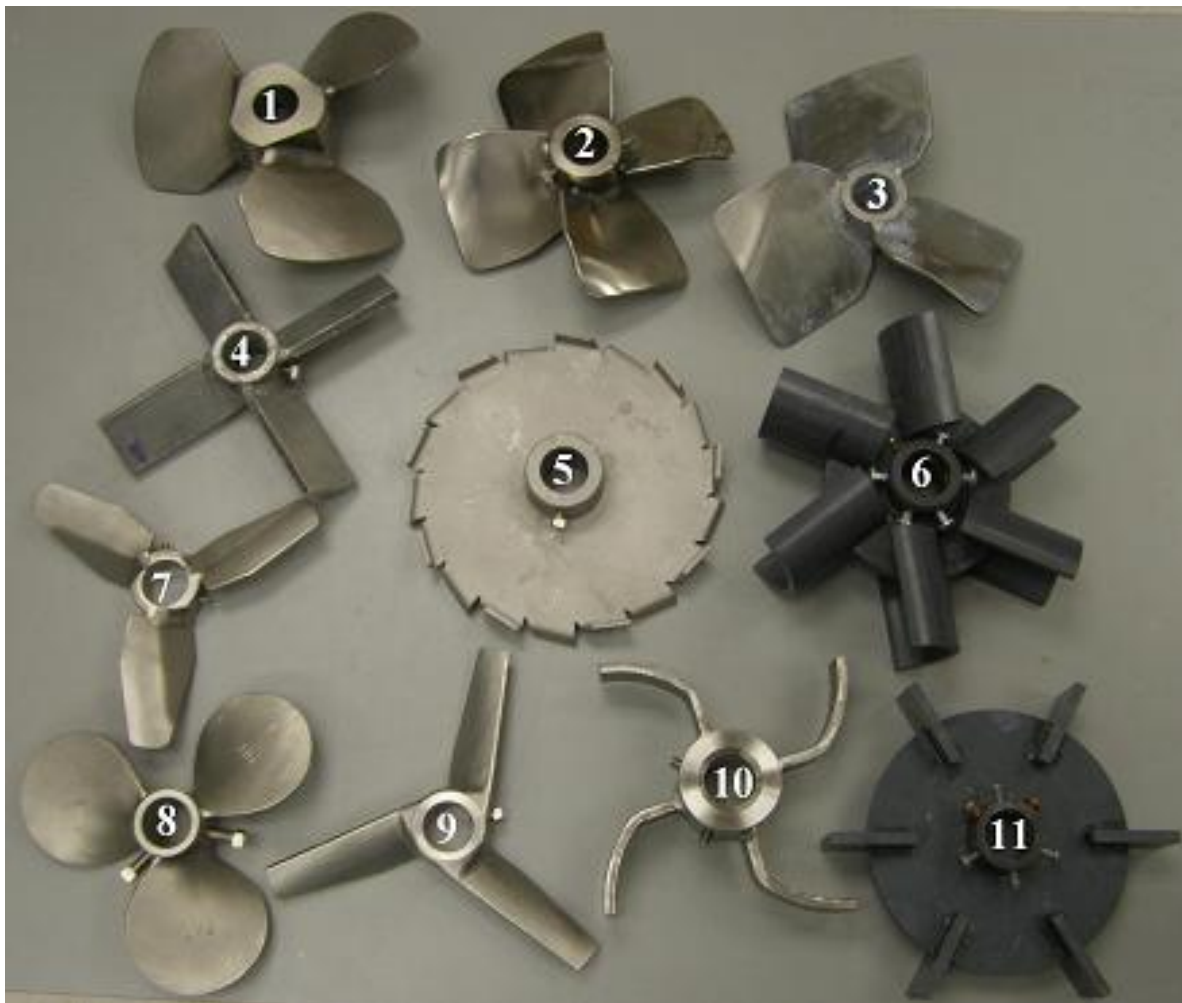


Figure (3.1-2). Axial-flow and radial-flow impellers: (1) HG 3AH, (2) Lightnin A315, (3) Lightnin A320, (4) Lightnin A200, (5) Lightnin R500 (sawtooth), (6) Scaba 6 SRGT, (7) HG 3AM, (8) Lightnin A100, (9) Lightnin A310, (10) RSB (retreat swept-back), and (11) RT (Rushton turbine).

The impeller torque and speed were measured using a rotary torque transducer (Staiger Mohilo, Lorch, Germany) and a tachometer, respectively. During the experiments, the fluid was pumped from the feed tank to the discharge tank through the mixing vessel. Dynamic tests were carried out by injecting a saline solution (NaCl solution as a tracer) into the fresh feed stream prior to being pumped into the mixing vessel using a metering pump (Milton Roy, USA). The injection of the tracer was controlled by a computer-controlled on-off solenoid valve. The

conductivity values of the input and output streams were measured as a function of time using the flow-through conductivity sensors (RoseMount Analytical, Irvine, CA, USA) and these values were recorded using a data acquisition system controlled by LABVIEW software (National Instruments, Austin, TX, USA) to estimate dynamic model parameters. The thermocouples were installed at inlet and outlet of the mixing vessel to measure the fluid temperature. We did not observe any significant variations in temperature while running the experiments for the given range of impeller speeds. All measurements were made at room temperature 22 ± 1 °C.

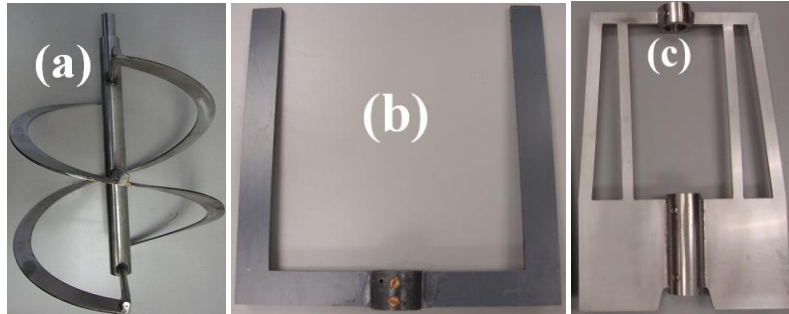


Figure (3.1-3). Close-clearance impellers: (a) Anchor (b) Maxblend (c) Double helical ribbon (DHR).

3.1.1 Design of Input Signal and Dynamic Model Validation

Generally, an identification experiment is performed by exciting a system using some sort of input signal such as a step, a sinusoidal or a random signal. The choice of input signal has a substantial influence on the observed output. The same procedure suggested by Ein-Mozaffari (2002) was used here. This procedure consists of the following steps:

- Exciting the system by a rectangular pulse
- Designing a frequency-modulated random binary exciting signal based on rectangular pulse
- Exciting the system by the frequency-modulated random binary exciting signal, and
- Validating the use of frequency-modulated random binary exciting signal.

An identification experiment was performed by exciting the system and examining the input and output conductivities over a precise time interval (Ein-Mozaffari et al., 2003b). The excitation was performed by injecting the saline solution through a computer controlled solenoid valve into the feed stream. The conductivity variations in input and output streams were measured using the flow-through conductivity sensors. These signals were recorded in a computer using data acquisition system to estimate flow non-ideal parameters.

In the first experiment, the input signal was a rectangular pulse (two steps change). Figure (3.1-4) shows a typical rectangular pulse and the corresponding output signal. The input signal should be persistently exciting, implying that all the modes of the system should be excited (Ljung, 1999). Therefore, an input such as two steps change will not provide enough excitation to identify model parameters (Ein-Mozaffari, 2002). However, the quality of parameter estimation can be improved by using this simple rectangular pulse to design a frequency-modulated random binary exciting signal by concentrating the excitation energy at frequencies where the Bode plot for model parameters is sensitive to parameter variations (Ljung, 1999). The procedure for designing a frequency-modulated random binary input signal is shown in Figure (3.1-5).

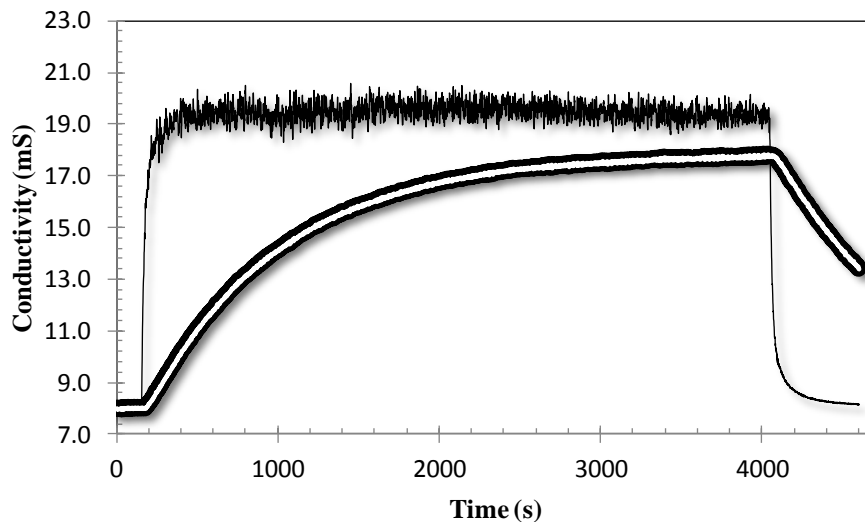


Figure (3.1-4). System excitation using a rectangular pulse: input and output signals in black lines and model output in white line. ($3AH$, $Q = 9.65 \text{ L min}^{-1}$, 251 rpm, 0.5% xanthan gum, $D = T/2.1$, $C = H/2.7$, $H = T/0.93$).

For rectangular pulse input, Bode plot for partial derivatives of transfer function with respect to model parameters (f , R , a_1 , a_2) was obtained. The partial derivatives of the model were calculated using MATLAB to generate Bode plots of these partial derivatives. The result is shown in Figure (3.1-6).

The excitation energy for random exciting signal must be chosen at frequencies where the magnitude of Bode plot is sensitive to model parameter variations (Ljung, 1999). For this intention, the magnitudes of the Bode plot for the partial derivatives of the approximate model with respect to model parameters (f , R , a_1 , and a_2) were calculated. As shown in Figure (3.1-6), the frequencies at the maximum magnitudes were obtained: $\omega_f = 2.0612 \times 10^{-3} \text{ rad s}^{-1}$, $\omega_R = 1.1575 \times 10^{-3} \text{ rad s}^{-1}$, $\omega_{a1} = 10.000 \times 10^{-3} \text{ rad s}^{-1}$, and $\omega_{a2} = 1.5446 \times 10^{-3} \text{ rad s}^{-1}$. Hence, the excitation energy for the second experiment was concentrated at frequencies from $1.1575 \times 10^{-3} \text{ rad s}^{-1}$ to $10.000 \times 10^{-3} \text{ rad s}^{-1}$. A zero-mean white-noise signal (e_t) was filtered by a band-pass filter with cut-off frequencies of $1.1575 \times 10^{-3} \text{ rad s}^{-1}$ and $10.000 \times 10^{-3} \text{ rad s}^{-1}$. Then, the filtered signal was converted into a binary sequence using the following:

$$u_t^b = \begin{cases} 0 & \text{if } e_t^f \leq 0 \\ 1 & \text{if } e_t^f > 0 \end{cases} \quad (3.1-1)$$

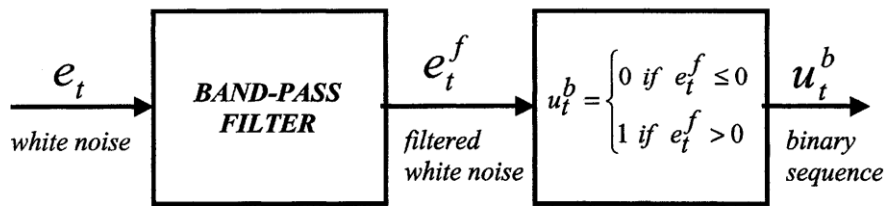


Figure (3.1-5). Procedure for designing a frequency-modulated random binary input signal.

The new input and output signals (black line) are shown in Figure (3.1-7). In this figure the response of the model to the given excitation is in white line. To validate the model the system was excited by a new input signal under the identical operating conditions and the input and output data were recorded. The input signal employed in the second experiment and the model parameters estimated from the first experiment were used to calculate the output signal. These estimated output signals were then compared to the output signals recorded in the second

experiments as shown in Figure (3.1-8). In this figure the measured output is shown by a black line and the estimated output is shown by a white line. It shows that measured output and estimated output are very close to each other.

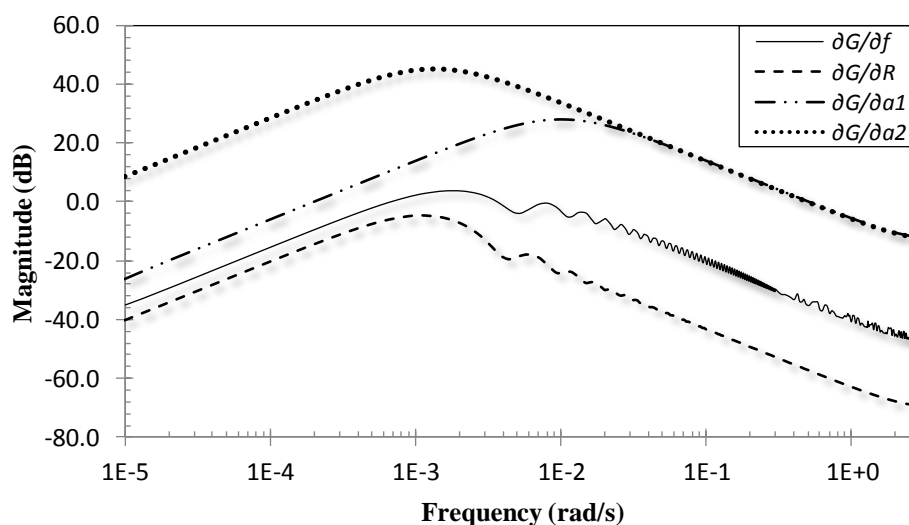


Figure (3.1-6). The magnitude of the Bode plot for the partial derivatives of the approximate model.

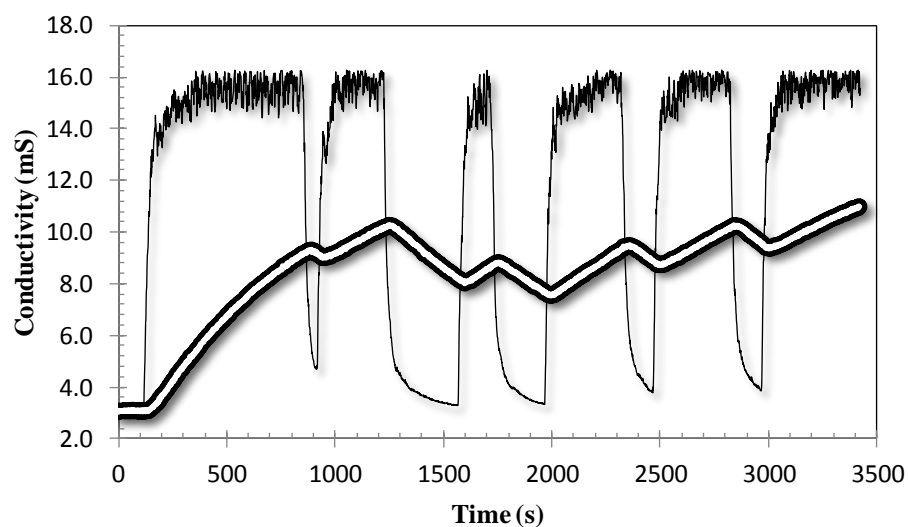


Figure (3.1-7). System excitation using a frequency-modulated random binary input signal: experimental input and output in black and model output in white. (3AH, $Q = 9.65 \text{ L min}^{-1}$, 251 rpm, 0.5% xanthan gum, $D = T/2.1$, $C = H/2.7$, $H = T/0.93$).

Table (3.1-2) shows the model parameters (f and $V_{fully\ mixed}/V_{total}$) obtained from both experiments. It shows that the model parameters obtained from the first input signal [Figure (3.1-7)] completely match with those of the obtained from the new input signal [Figure (3.1-8)]. This implies that the first exciting input signal was able to identify dynamic model parameters and that the estimated parameters are unique characteristics of the system under specified operating conditions. Although the discrete-time transfer function is an approximation of the continuous-time model, it provides an accurate estimation for all parameters.

Table (3.1-2). Dynamic model parameters obtained from two different input signals.

First input signal [Figure (3.1-7)]		Second input signal [Figure (3.1-8)]	
f	$V_{fully\ mixed}/V_{total}$	f	$V_{fully\ mixed}/V_{total}$
0.1047	0.8951	0.1051	0.8946

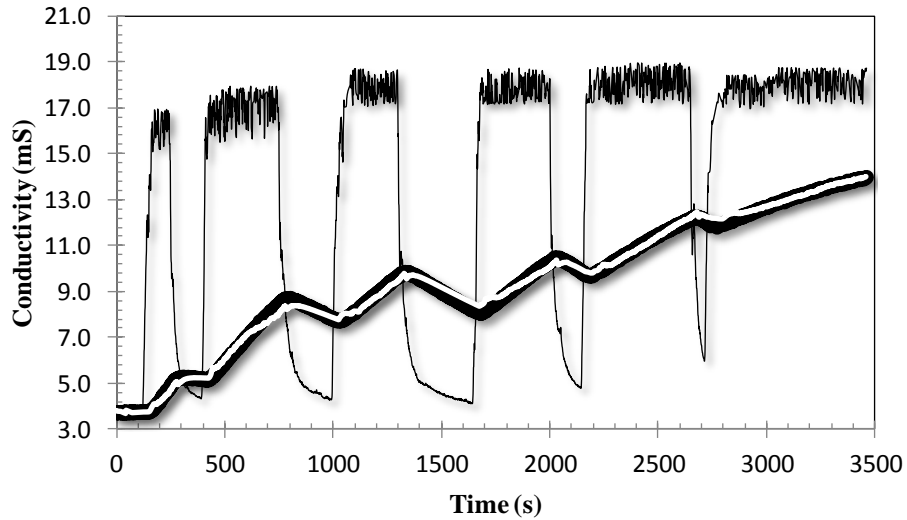


Figure (3.1-8). Model validation: new input and output signals (second set of experiment) in black and estimated model output from the first set of data in white (3AH, $Q = 9.65\text{ L min}^{-1}$, 251 rpm, 0.5% xanthan gum, $D = T/2.1$, $C = H/2.7$, $H = T/0.93$).

3.2 Experimental Setup for ERT tests

The experimental setup depicted in Figure (3.2-1) was utilized in this study to measure the mixing time and cavern size in the batch mode, and to visualize the flow pattern and the deformation of the cavern in the continuous mode using electrical resistance tomography (ERT).

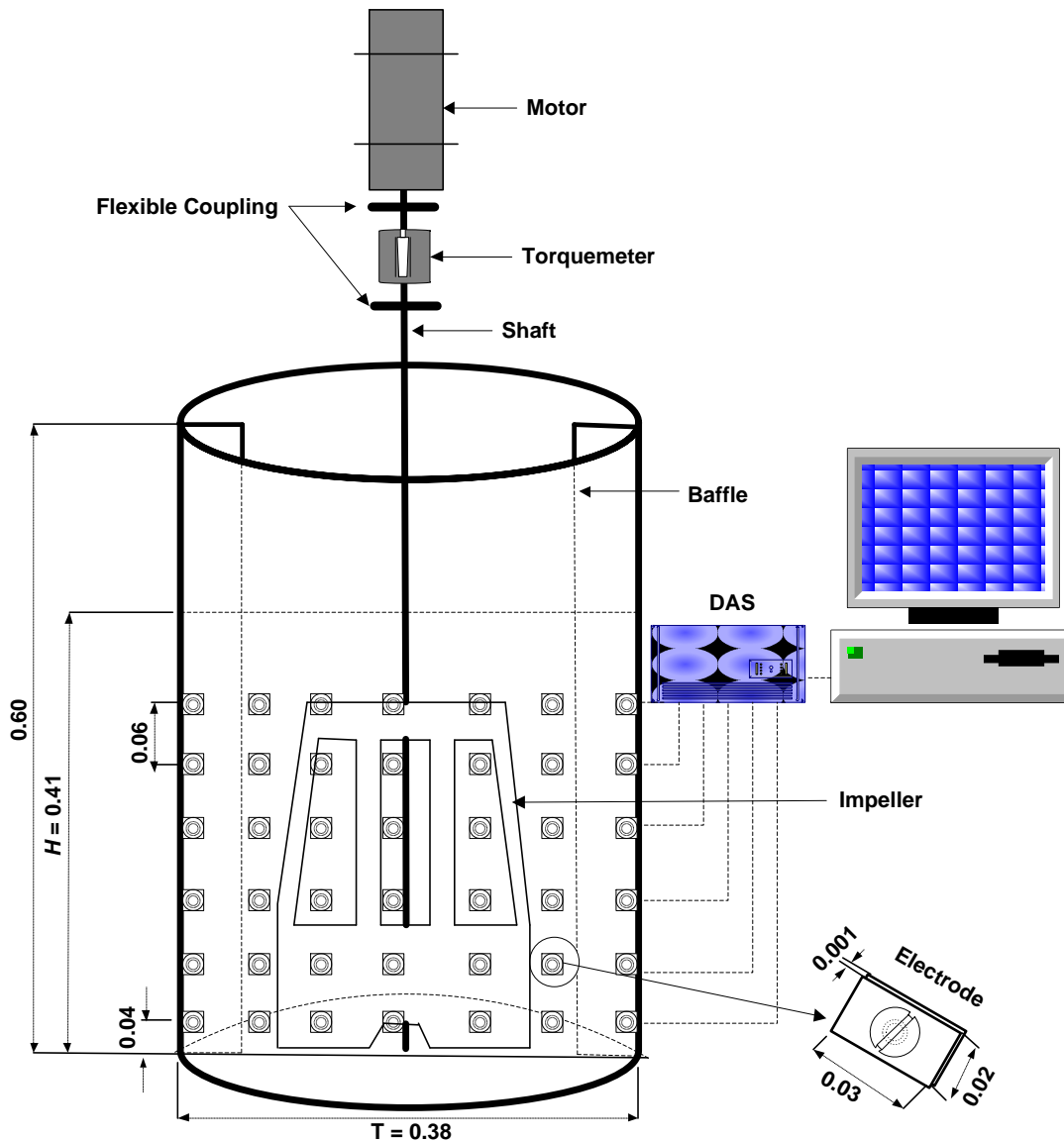


Figure (3.2-1). Experimental setup with ERT system (dimensions in meter).

Six tomography sensor planes were positioned around the circumference of the mixing tank. The planes were 0.06 m apart from each other with the bottom plane 0.04 m from the bottom of the tank. The planes were numbered from top to bottom. Each plane had 16 stainless steel electrodes which were located equidistantly on the periphery of the vessel. The height, width, and thickness of the electrodes were 0.02, 0.03, and 0.001 m, respectively. Each electrode was in direct contact with the working fluid in the tank without invading the flow. The reference for this study was taken based on the single ground electrode installed between planes three and four. All electrodes were connected to the electrical resistance tomography (ERT) system (Industrial Tomography Systems, Manchester, UK). The tomography machine was connected to a computer for the image reconstruction.

3.2.1 ERT System

Electrical resistance tomography (ERT), a non-intrusive technique, is used in a wide range of research and development applications, including monitoring the performance of a hydrocyclone (Williams et al., 1999), measurement and control of bubble columns (Wang et al., 2001), investigating a solid–liquid filtration processes (Vlaev et al., 2000), interrogation of mixing processes (Kim et al., 2006), monitoring stability of reaction in the polymerization reactor (Kaminoyama et al., 2005), and monitoring of multiphase processes such as gas–liquid (Gumery et al., 2011; Hamood-ur-Rehman et al., 2012; Wang et al., 2001), liquid–liquid (Dickin and Wang, 1996), and solid–liquid (Hosseini et al., 2010a, 2010b; Ricard et al., 2005; Lucas et al., 1999; Tahvildarian et al., 2011). The capability of the ERT technique to characterize the different mixing processes in term of mixing time (Zhao et al., 2008; Pakzad et al., 2008b), cavern diameter and height in mixing of yield-pseudoplastic fluids (Pakzad et al., 2008a) have been established,

The aim of the ERT system is to acquire the conductivity distribution in the area of interest. The conductivity distribution in a cross section can be obtained by injecting currents (or applying voltages) on the domain and measuring voltages (or currents) via a number of spaced electrodes mounted non-invasively on its boundary. A standard ERT system consists of three main parts: electrodes, a data acquisition system (DAS), and a host computer, which is an image reconstruction system.

3.2.1.1 Electrodes

Extreme focus could be given to the design of electrodes, as a heart of ERT system, to maximize its efficiency to sense conductivity in the area of interest (Seagar et al., 1987). They must be in continuous contact with the fluid inside the vessel. The electrodes attached on the periphery of the process vessel must have low cost, ease of installation, good conductivity (more conductive than the fluid), and resistance to corrosion/abrasion effects or the process operation environment, such as the temperature, pressure, electrical fire hazards, vessel wall thickness, and material (Williams and Beck, 1995). They can be fabricated from gold, platinum, stainless steel, brass, and silver (Tapp and Williams, 2000). The position of the electrodes is also important since the reconstruction algorithm is based on the electrodes being located at exactly defined intervals in order to outline the maximum amount of information from inside of the vessel (Kaminoyama et al., 2005). The size of the electrodes is another important factor in measuring the electric field distribution (Mann et al., 1996). A large surface area is required for the current-injecting electrodes to ensure that enough current is generated within the vessel (Kaminoyama et al., 2005) while the voltage-measuring electrodes are required to be as small as possible (Paulson et al., 1992). A study conducted a theoretical analysis of the proportion of the boundary, which the electrodes should cover to provide a high signal-to-noise ratio, and recommended that electrodes cover 60–80% of the surface of the region of interest (Pinheiro et al., 1998).

3.2.1.2 Data Acquisition System

The data acquisition system (DAS) is located in a portable unit and it is connected to the electrodes and communicates with the host image reconstruction computer. It receives the quantitative data, which provides the state of the conductivity distribution inside the vessel. DAS co-ordinates the desired measurement protocol or collection strategy. Good data collection strategies are important because misleading images can be rebuilt if a full set of independent measurements is not collected (Kaminoyama et al., 2005). It is necessary to select the scheme that has a good distinguishability and high sensitivity to conductivity changes in the process. There are four main strategies: adjacent strategy, opposite strategy, diagonal strategy, and conducting boundary strategy. In this study, the system makes use of an adjacent

measurement protocol (Barber et al., 1983), applying a current between two adjacent electrodes and measuring the resultant potential difference (voltage) between all other adjacent electrode pairs. The AC drive current then rotates to the next electrode pair and the voltages for all other electrode pairs are measured. This process is then repeated until all possible combinations have been tried, and provides 104 individual voltage measurements according to the equation $N_e(N_e - 3)/2$, where N_e is the number of electrodes per plane, i.e., 16 in this study. The six planes provide 624 interrogative measurements of the given liquid volume. All ERT tests were performed using a P2000 ERT system (Industrial Tomography Systems-ITS, Manchester, UK). The frequency range, injection current range, output voltage range, and voltmeter sensitivity of the DAS used in this study were: 75–153.6 kHz, 0–75 mA (peak–peak), -10 V to +10 V, and 0.0488 mV, respectively. The shortest possible time for the acquisition of one frame for 16 electrodes was 20 ms. The ERT system operates to a spatial resolution around 5% of the vessel diameter, using 16 equispaced electrodes (Holden et al., 1998). The DAS was connected to a computer (Pentium 4, CPU 2 GHz, and 512 MB of Ram) via a nine-pin communication port and recorded the data through ITS “ERTWIN” software (Industrial Tomography Systems-ITS, Manchester, UK) for control, image reconstruction, and data storage.

3.2.1.3 Host Computer or Image Reconstruction System

Ultimately, DAS communicates these quantitative data to host image reconstruction computer where data are processed using a suitable image reconstruction algorithm. Generally, there are two types of algorithms: non-iterative and iterative. A non-iterative image reconstruction algorithm (Linear Back Projection – LBP) is applied to convert raw voltage measurements into a 2D conductivity map of each plane. The linear back projection algorithm (Barber and Brown, 1984) has a low computational requirement compared to an iterative image reconstruction algorithm [Sensitivity Conjugate Gradient Method – SCG (Wang, 2002)]. These algorithms are qualitative ones, as the images depict relative change in conductivity against an initial set of reference data. Each individual tomogram consists of a 20×20 pixel array giving 400 spatial elements. However, some of these pixels lie outside the vessel circumference and the image is therefore formed from pixels inside the vessel. The circular image is constructed using 316

pixels from a 400 pixels square grid. Since the vessel had 6 sensing planes, this resulted in 1,896 non-intrusive conductivity probes.

3.3 Fluid Rheology

The food grade xanthan gum powder (NovaXan, ADM, USA) was used throughout the experiments. Xanthan gum is a natural polysaccharide and one of the important industrial biopolymer (Garcia-Ochoa et al., 2000). Due to its emulsion stabilization, temperature stability, compatibility with food ingredients, and pseudoplastic rheological properties, xanthan gum has been used in food industry (Garcia-Ochoa et al., 2000). Xanthan gum is used in pharmaceutical formulations, cosmetics, and agricultural products due to properties such as thickening the aqueous solutions and stabilizing the emulsions and suspensions, (Rao, 1999). It is also employed in textile printing pastes, ceramic glazes, slurry explosive formulations, and rust removers (Garcia-Ochoa and Casas, 1994).

The rheological data of the xanthan gum solutions measured by Saeed et al. (2008) was used in this study. The rheological properties of the xanthan gum solutions was measured at the bulk fluid temperature (23 ± 0.5 °C) in a Bohlin CVOR Rheometer 150 (Malvern instruments, USA) using a 40 mm 1° cone and 60 mm plate measuring system. The range of the shear rate applied in the controlled shear rate rheometer varied from 0.1 to 150 s^{-1} , which was covered the range of shear rates encountered in the mixing tank. The rheological characteristics of the solutions for 0.5, 1.0, and 1.5% are listed in Table (3.3-1).

Table (3.3-1). Rheological properties of xanthan gum solutions (Saeed et al., 2008).

Concentration (%)	Density, ρ (kg m ⁻³)	Yield Stress, τ_y (Pa)	Consistency Index, K (Pa.s ⁿ)	Power law Index, n
0.5	997.36	1.79	3	0.11
1.0	991.80	5.25	8	0.12
1.5	989.76	7.46	14	0.14

3.4 Experimental Procedure

The experimental procedure involves the preparation of xanthan gum solution and measurements of power, mixing time, and cavern size.

3.4.1 Solution Preparation

Each batch of solution was prepared by adding the appropriate amount of xanthan gum powder to tap water. In this study, xanthan gum solution with 0.5, 1.0, and 1.5% mass concentrations were used. One third of the feed tank was filled with water. The impeller in the feed tank was started first and then xanthan gum powder was added gradually into the water in the feed tank. Each batch was mixed for approximately 5–6 hours. Water was then added to complete the required solution volume, and the whole solution was mixed for an additional 1–2 hours. For all experiments, the solution within the tank was allowed to be sit overnight to reach the desired temperature and eliminate possible air bubbles.

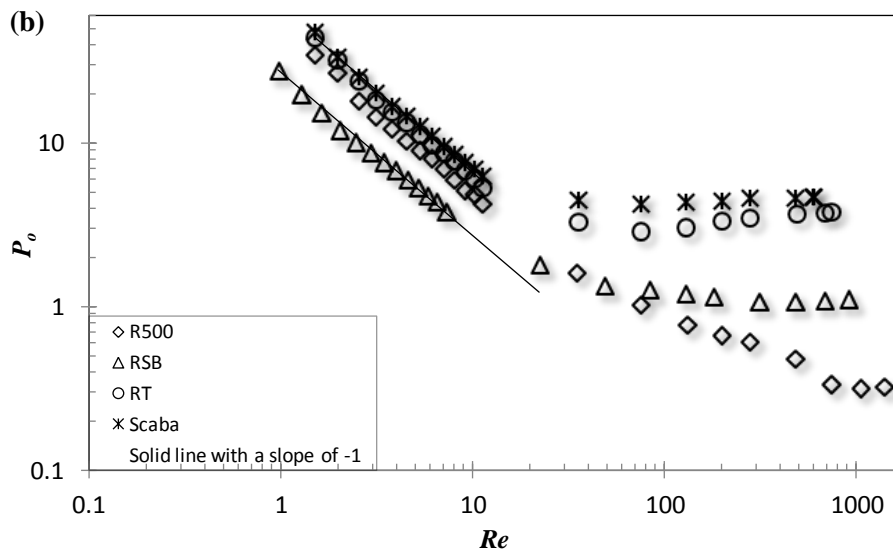
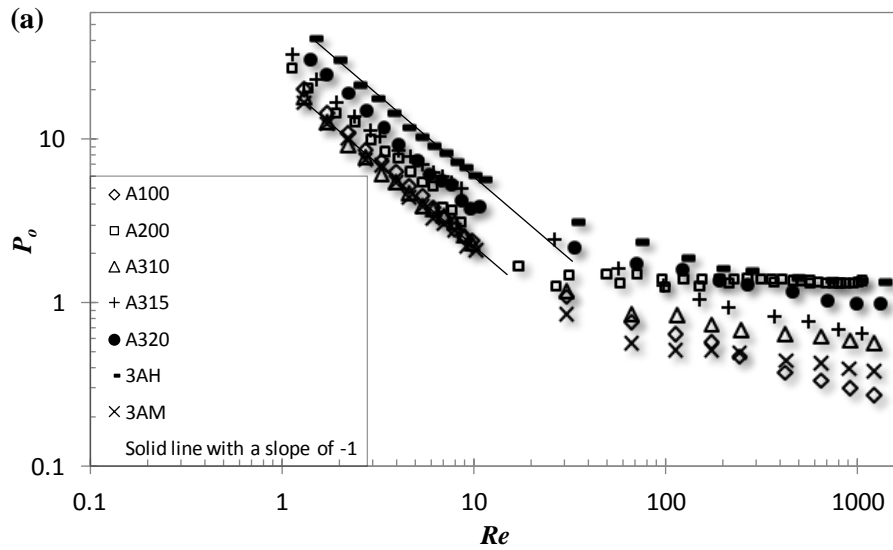
Each batch of prepared xanthan gum was used 1–3 times, until the maximum amount of salt accumulated in the solution reached to approximately 0.17 (wt/wt %). Saline tracer solution was prepared by dissolving table salt in distilled water. The tracer was an aqueous solution of sodium chloride and it did not have the same physical and rheological properties as xanthan gum solution. It was observed that the addition of 0.17% aqueous solution of tracer did not significantly change the rheological properties of the xanthna gum solutions (Saeed and Ein-Mozaffari, 2008) hence, the maximum concentration of the tracer in the xanthan gum solution was 0.17%.

3.4.2 Power Measurements

The power input to the impeller (P) was obtained from torque (M) and impeller rotational speed (N) measurements using:

$$P = 2\pi NM \tag{3.4-1}$$

The bearing friction was measured by operating the system when the vessel was empty. This friction torque was subtracted from all the measured torques. The power number (P_o) and Reynolds number (Re) was calculated using Equations (2.1–3) and (2.1–11), respectively.



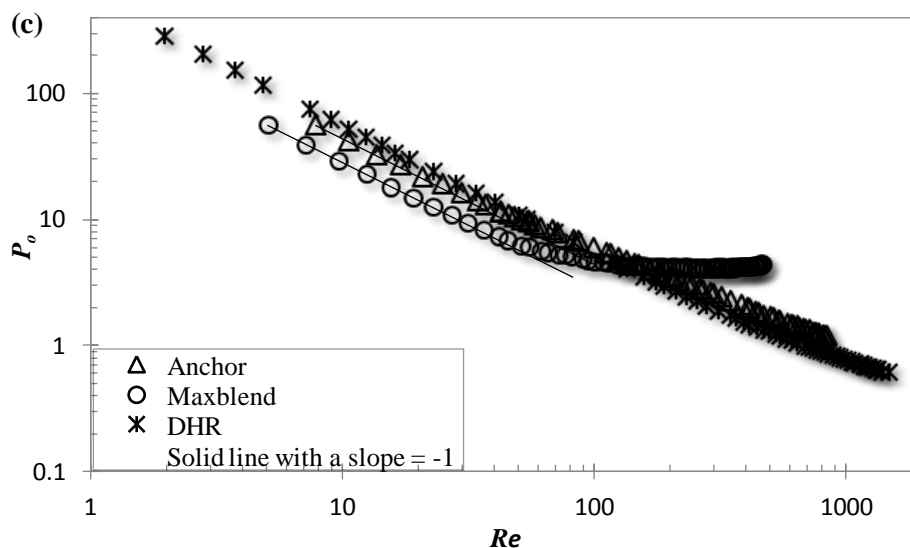


Figure (3.4-1). Power number (P_o) versus Reynolds number (Re): (a) axial-flow impellers (b) radial-flow impellers, and (c) close-clearance impellers (1.5% xanthan gum solution).

Figure (3.4-1) shows the power curve for axial-flow, radial-flow, and close-clearance impellers. The value of Metzner-Otto proportionality constant k_s was selected within a range of 7.1–25 according to the geometry of the impellers (Metzner et al., 1961; Chhabra and Richardson, 2008). The trend in the power number curve illustrated in Figure (3.4-1) is similar to those general trends reported by several researchers (Paul et al., 2004; Kelly and Gigas, 2003; Holland and Chapman, 1966; Nagata, 1975). It has been shown that $P_o \propto Re^{-1}$ in the laminar regime ($Re < 10$), P_o is constant in the turbulent regime ($Re > 10^4$) and P_o changes to some extent in the transitional regime (Re between 10 and 10^4). Figure (3.4-1) shows that at $Re < 10$ the solid line with a slope of -1 fits the data precisely, which implies that $P_o Re$ is constant for the laminar regime. It also shows that in the transitional regime the power number changes slightly with Re . However, in the case of the close clearance impellers (Maxblend, DHR, and anchor), the laminar region ends at about $Re = 40$. The same value was also reported by Fradette et al. (2007) for the Maxblend impeller; however, Iranshahi et al. (2007) found a slightly lower value, $Re = 25$, for the Maxblend impeller. Ihejirika and Ein-Mozaffari (2007) also found a similar result for the DHR impeller where the laminar region ended at approximately $Re = 40$.

3.4.3 Mixing Time Measurements

Mixing time is defined as the time required to achieve a predetermined state of homogeneity by a mixer. In this study, the mixing time (θ) was defined as the time required for the conductivity of the fluid to reach 98% of the steady-state value after the injection of the tracer. Mixing time measurement was carried out by injecting 50 mL of 10% saline solution (NaCl) near shaft on plane 1 ($r = 0.07$ m, $\Phi = 260^\circ$, and $z = 0.34$ m) and monitoring the tracer concentration with time using ERT. Before the injection of the tracer, the reference state was measured to eliminate the effect of the stirrer and other internals within the mixing tank. To determine the conductivity distributions within the mixing system, tomography images were employed. The red color in the tomograms shows the high-conductivity regions, which represents the higher tracer concentration in those regions. The blue color demonstrates the low-conductivity regions, which indicates the lower tracer concentrations. Figure (3.4-2) shows the 2-dimensional (2D) tomograms of the mixing process after the injection of the tracer in which 1% xanthan gum solution was agitated by the Maxblend impeller at $N = 175$ rpm.

The blue color in all planes at $t = 0$ s (before the tracer injection) demonstrates that only low-conductivity xanthan gum solution was present throughout the vessel. At $t = 1$ s, the color changed from blue to red/green in tomograms, which indicates that the tracer was injected on plane 1. After 2 s, the tracer had moved downward and appeared on plane 6. As time proceeded, the tracer was spread in the clockwise direction and dispersed throughout the tank. Since the xanthan gum solution is a shear-thinning fluid, the apparent viscosity of the xanthan gum solution decreases with an increase in the shear rate. Therefore, good mixing was achieved in the impeller region. The size of the Maxblend impeller was larger compared to the axial and radial-flow impellers. Thus, it swept more volume within the tank and provided better mixing quality. The time series of 2D tomograms show that a homogenous mixture was obtained after 21 s.

The ERT data were also used to plot average conductivity as a function of time for six ERT planes. Figure (3.4-3) shows a practical approach to measure the mixing time after the injection of the tracer for six tomography planes. It shows that the average conductivity value for all ERT planes reached within 98% of the steady state value after 21 s.

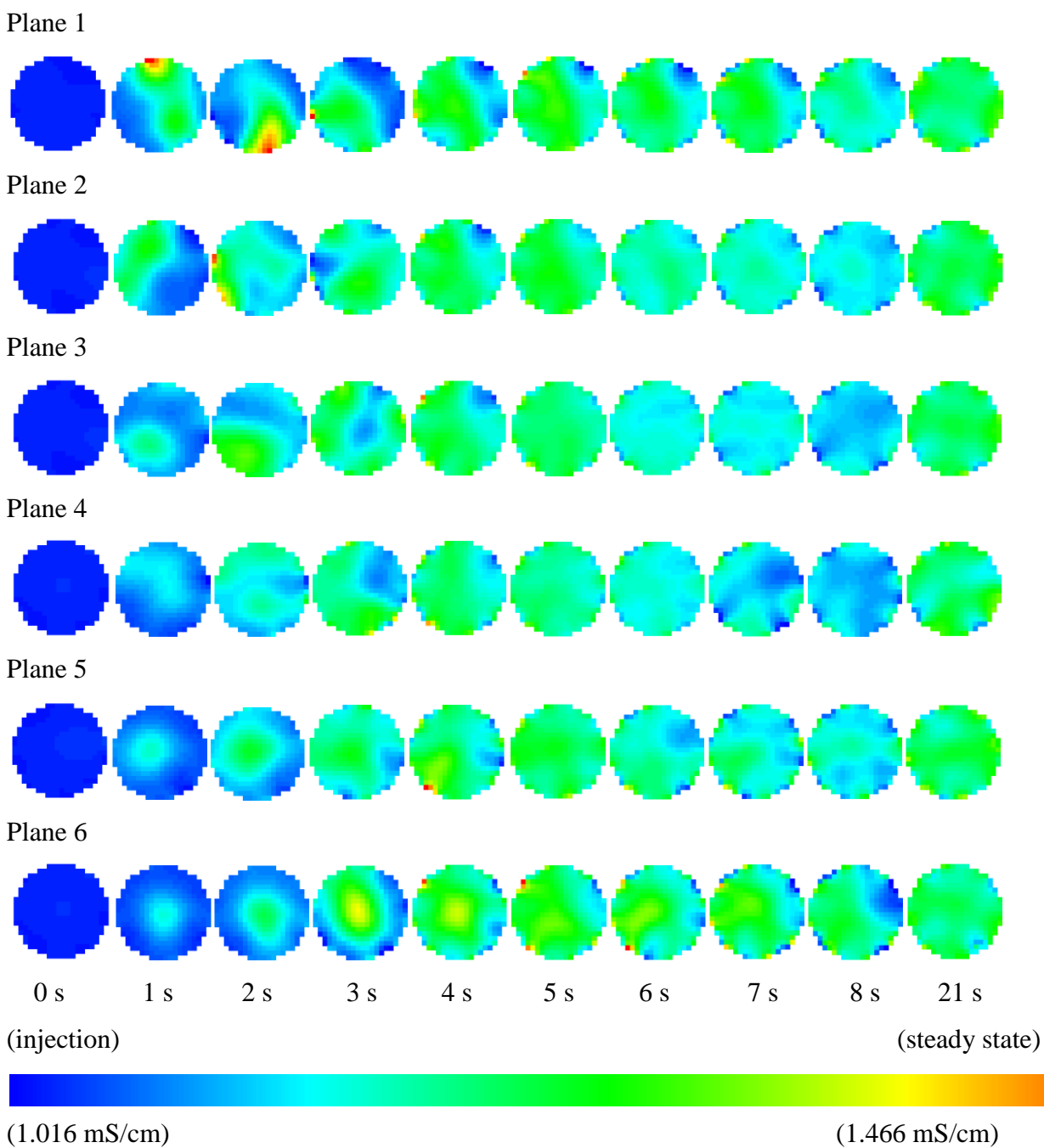


Figure (3.4-2). 2D tomograms recorded after the tracer injection (Maxblend impeller, 1% xanthan gum concentration, $N = 175$ rpm, and with baffles).

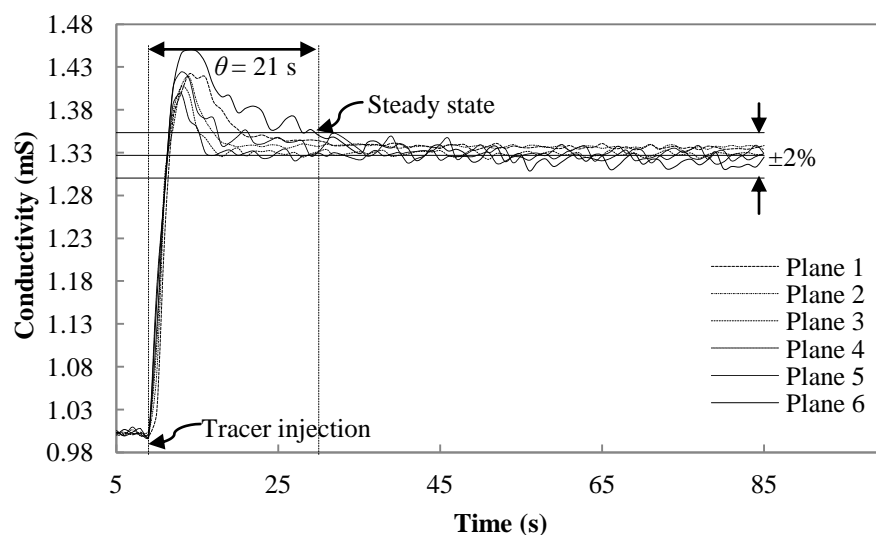


Figure (3.4-3). Conductivity versus time for six tomography planes after the injection of the tracer (Maxblend, 1% xanthan gum concentration, $N = 175$ rpm, and with baffles).

All mixing time measurements were conducted when there were no stagnant regions within the tank. In the ERT experiments, each test was repeated three times for a set of 4 experiments. These data were analyzed for mixing time. In the ERT tests, the maximum standard deviation observed was about 1. To measure the mixing time, 200-500 frames were recorded for each experiment. This approach was employed to measure the mixing time as a function of the operating conditions and design parameters in this study.

3.4.4 Cavern and Flow Visualization

There were three procedures were adopted in this section: (i) to measure the cavern size in the batch mode, (ii) to study the effect of the inlet-outlet flow on the deformation of the cavern and (iii) to visualize the flow pattern generated in the continuous-flow mixing.

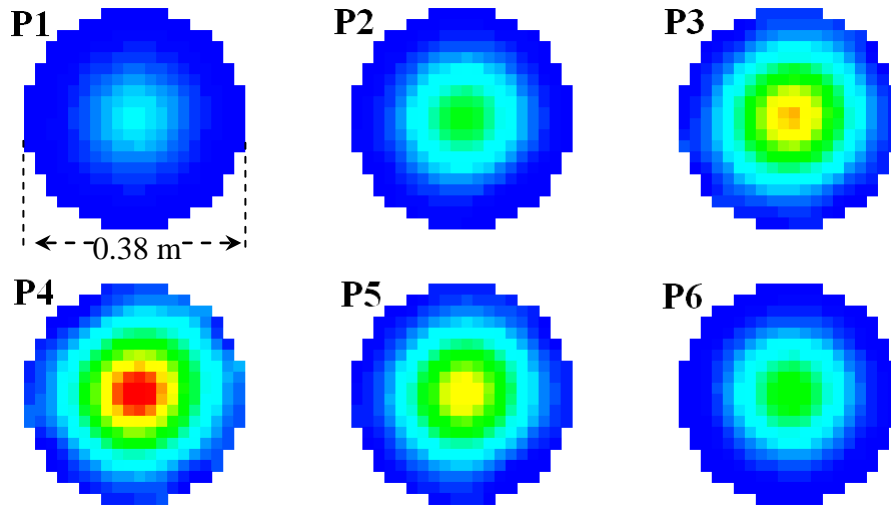
To measure the cavern size in the batch mode, 30 mL of 5% saline solution (tracer) was injected directly into the xanthan gum solution near the impeller hub (Plane P4) using a plastic syringe and the tracer concentration was monitored using ERT. Measurements were collected from six planes of electrodes until the cavern size remained unchanged. Figure (3.4-4a) shows the formation of the cavern visualized using the two dimensional (2D) tomograms generated

after the injection of the tracer in the mixing of the 0.5% xanthan gum solution using the RT impeller. The impeller was located on the plane *P4*. Colors in tomograms display the dispersion of the tracer in the vessel. The blue color in these tomograms demonstrates the low-conductivity zones, and represents the lower tracer concentrations. The red color in the tomograms shows the high-conductivity regions, and indicates the higher tracer concentration in those zones. At the boundary of the cavern, the conductivity of the fluid was equal to the conductivity of the fresh xanthan gum solution which was not zero but was lower than the conductivity of the solution containing salt. The 2D tomogram shows that the tracer injected near the impeller hub remained within the cavern and no tracer was found in the surroundings. Although the 2D tomogram provides good images of the cavern formation, it is difficult to measure the cavern height using the 2D tomogram. Therefore, 2D images were converted into three dimensional (3D) images. Figure (3.4-4b) shows the 3D images generated from the 2D images using Slicer-Dicer software (PIXOTEC, USA). Based on the 3D images, the shape of the cavern was approximated by a right circular cylinder; therefore, the characteristics of the cavern can be described by the diameter and height of this region. The cavern diameter was measured on a horizontal plane passing through the impeller on plane *P4*. The cavern height was measured on a vertical plane along the shaft and perpendicular to the horizontal plane of the impeller. To visualize meticulously how the tracer was dispersed in the opaque fluid (xanthan gum solutions), 3D images were generated by cutting the block in all possible ways on the *x*, *y* and *z*-axes to provide enough information about the cavern. Various 3D images shown in Figure (3.4-4b) were generated by cutting the vertical plane at the center of the tank and/or cutting a horizontal plane passing through the impeller on plane *P4*. The outlines around the cavern volume in Figure (3.4-4b) were generated by the Slicer Dicer software in the default setting. Thus, the 3D images provided a motivating insight to visualize the flow in the mixing of opaque fluids. For each experiment, 50 frames were recorded and the dimension of the cavern was measured once the cavern size remained unchanged.

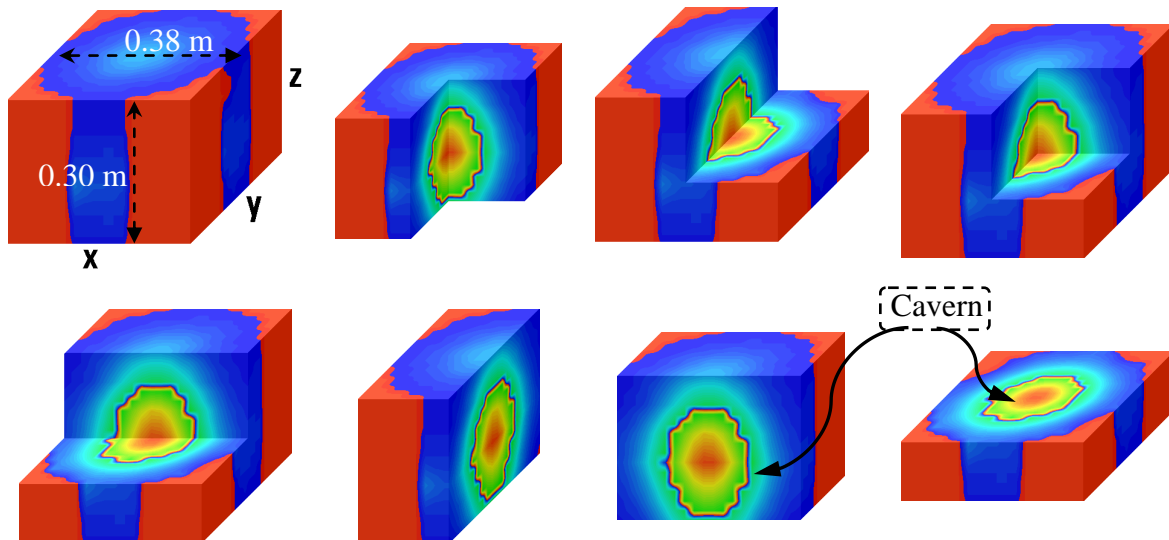
To study the effect of the inlet-outlet flow on the deformation of the cavern (or to visualize the deformation of the cavern) in the continuous-flow mixing system using ERT, first the cavern was fully developed in a batch mode. Once the cavern was fully developed, the feed and discharge pumps were turned on simultaneously while the impeller was still running at the

given speed and the fluid was pumped from the feed tank to the discharge tank through the mixing vessel. ERT images were collected to visualize the flow inside the mixing vessel.

(a)



(b)



(Low-conductivity)

(High-conductivity)

Figure (3.4-4). The 3D images generated from the 2D tomograms show the formation of the cavern in the mixing of the 0.5% xanthan gum solution using the RT impeller: (a) 2D tomogram and (b) 3D images generated using the Slicer Dicer software (the 3D images were generated by cutting the vertical plane at the center of the tank and / or the horizontal plane on the impeller surface).

Finally, to visualize the flow in the continuous-flow mixing system, the feed and discharge pumps were turned on simultaneously and the fluid was pumped from the feed tank to the discharge tank through the mixing vessel. 150 mL of 9% saline solution (tracer) was injected in the feed. Measurements were collected from six planes of electrodes. ERT data were collected and tomography images were reconstructed to visualize the distribution of the tracer concentration inside the mixing vessel. In all procedures, before the injection of the tracer, the reference state was taken to eliminate the effect of the stirrer and other internals within the mixing tank.

3.4.5 The Ratio of Residence to Mixing Time

In this study, the continuous-flow mixing system was considered as an ideal system when channeling (f) approached zero and the fully mixed volume ($V_{fully\ mixed}$) approached the total volume (V_{total}) of the fluid in the vessel. To achieve an ideal mixing for a given condition, impeller speed was gradually increased until the percentage of channeling approached approximately zero and the fully mixed volume approached approximately the total volume of the fluid in the vessel. Under these circumstances, the residence time (τ) was calculated from the ratio of the fluid volume (V_{total}) in the vessel to the feed flow rate (Q). This similar operating condition was then applied (impeller power per volume) to measure the mixing time in the batch mode, which was finally used to find the ratio of the residence time to the mixing time.

3.5 Error Analysis

The errors regarding the torque sensors and ERT system have been analysed as follows:

3.5.1 Evaluation of Torque Sensor Precision

The random error of the torque sensors caused by electronic fluctuations, mechanical play, and friction can be defined using the standard deviation. Each experiment was repeated 3 times and the torque measurements were averaged. Figure (3.5-1) demonstrates that the maximum

standard deviation observed in torque measurement was 0.0042665 N.m which is small enough to accept the torque measurement with negligible error.

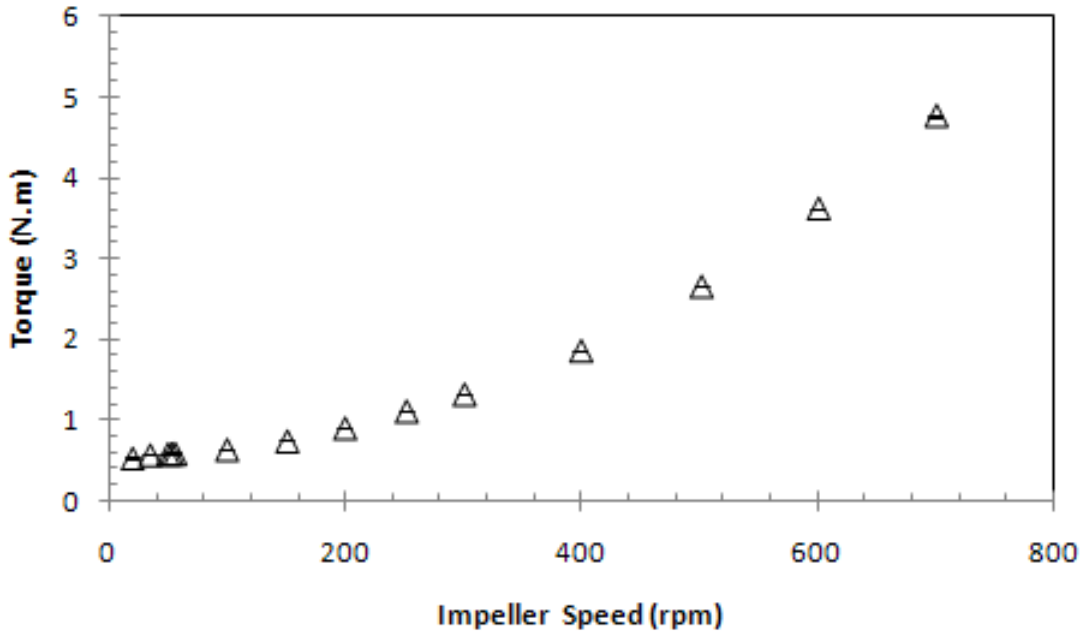


Figure (3.5-1). Error associated with torque measurements (RSB impeller and 1.5% xanthan gum).

3.5.2 Evaluation of ERT Measurements Precision

The ERT system was calibrated for each measurement. In the ERT experiments, each test was repeated three times for a set of 4 experiments. These data were analyzed for mixing time. The maximum standard deviation observed was about 1% confirming a good repeatability and reproducibility of the experiments.

3.6 Experimental Conditions

The effect of operation conditions and design criteria on the performance of the continuous-flow mixing vessel was studied in terms of on the degree of channeling (f), the fraction of fully mixed volume ($V_{fully\ mixed}$), the flow pattern, the cavern size, power consumption, and mixing time by varying the following parameters. The experimental conditions are summarized in Table (3.6-1).

Table (3.6-1). Experimental conditions.

Descriptions	Range and types
Impeller types	Axial-flow: A100, A200, A310, A315, A320, 3AH, and 3AM Radial-flow: R500, RSB, RT, and Scaba Close clearance: Maxblend, DHR, and anchor
Impeller speed (N)	22–800 rpm
Fluid flow rate (Q)	3.20, 8.47, 9.65, 10.81, and 14.17 L min ⁻¹
Fluid rheology	0.5, 1.0, and 1.5 wt/v % xanthan gum solution
Impeller diameter (D) (A200 impeller)	$T/3.2$, $T/2.5$, $T/2.1$, and $T/1.6$
Impeller off-bottom clearance (C) (3AH impeller)	$H/3.4$, $H/2.7$, $H/2.1$, and $H/1.7$
Impeller pumping direction (3AH and A200 impellers)	Down-flow and up-flow pumping directions
Fluid height in the stirred vessel (H) (3AH impeller)	$T/1.06$, $T/0.93$, and $T/0.83$
Mean residence time (3AH impeller)	257, 292, and 328 s
Jet velocity (V_j)	$V_j = 0.317, 1.66, \text{ and } 3.24 \text{ m s}^{-1}$
Inlet locations	TI ($r = 0.13 \text{ m}$, $\Phi = 90^\circ$, and $z = 0.38 \text{ m}$) BI ($r = 0.05 \text{ m}$, $\Phi = 105^\circ$, and $z = 0.10 \text{ m}$) BI ($r = 0.16 \text{ m}$, $\Phi = 105^\circ$, and $z = 0.00 \text{ m}$) –Section 5.3
Outlet locations	TO ($r = 0.19 \text{ m}$, $\Phi = 315^\circ$, and $z = 0.35 \text{ m}$) BO ($r = 0.13 \text{ m}$, $\Phi = 315^\circ$, and $z = 0.00 \text{ m}$)

Chapter 4

4. CFD MODEL DEVELOPMENT

To simulate the 3-D flow field generated by the RT impeller in the mixing of xanthan gum solution, the commercial CFD package ANSYS Fluent (version 14.5) was used in this study. The first section of this chapter provides the general information about governing equations, numerical methods, and methods of discretizing the equations as well as grid generation and other relevant information. The second section of the chapter describes the CFD models developed for the mixing of xanthan gum solution in a stirred vessel.

4.1 Introduction to CFD Modeling

4.1.1 Governing Equations

Computational Fluid Dynamics (CFD) solves transport equations (fluid flow, heat transfer, and mass transfer) numerically using various algorithms. The main equations of fluid dynamics are based on the conservation laws, i.e. mass, momentum, and energy conservations (Blazek, 2005). For the case of three-dimensional domain, the flow field is specified by the velocity vector ($\mathbf{v}=u_i+v_j+w_k$), the pressure p , density ρ , and the temperature T as functions of the space coordinates and time t . It is obvious that these six quantities (u_i, v_j , and w_k, p, ρ , and T) need six equations to be determined. These six equations (Bird et al., 2007) are the continuity equation (conservation of mass), the three equations of motion (conservation of momentum), the energy equation (conservation of energy), and the thermodynamic equation of state $p=p(\rho, T)$.

The flow field can be solved by considering mass conservation (continuity equation) and momentum equations since the mixing process in this study occurs in an isothermal condition.

For incompressible fluids (without density variations), there is no relation between the energy equation and the mass conservation and momentum equations, i.e. there is no need for an equation of state.

4.1.2 Continuity Equation

The conservation of mass applied to a fluid passing through a fixed control volume (Eulerian approach) gives the following equation of continuity for the unsteady flow of a compressible fluid (Patankar, 1980; Ranade, 2002; ANSYS13/Fleunt, 2012):

$$\frac{\partial \rho}{\partial t} + \nabla \cdot (\rho \vec{v}) = \frac{D\rho}{Dt} + \rho(\nabla \cdot \vec{v}) = 0 \quad (4.1-1)$$

The first term in above equation represents the dynamic change of density in the control volume and the second term shows the rate of mass flux passing through the control volume per unit volume. The symbol $D\rho/Dt$ denotes the substantive derivative, which consists of the local contribution in unsteady flow $\partial\rho/\partial t$ and the convective contribution $v \cdot (\nabla \rho)$.

A flow in which the density of each fluid element remains constant is called incompressible (Shyy et al., 1997). Then Equation (4.1-1) reduces to Equation (4.1-3) for steady [referred to Equation (4.1-2)] incompressible flow:

$$\frac{D\rho}{Dt} = 0 \quad (4.1-2)$$

$$\nabla \cdot \vec{v} = \frac{\partial v_i}{\partial x_i} = 0, \quad i = 1, 2, 3 \quad (4.1-3)$$

4.1.3 Momentum Equation

As per Newton's second law, the net force on the fluid element equals its mass times the acceleration of the element. The momentum equation is derived from Newton's second law ($\vec{F} = m\vec{a}$) of motion (Batchelor, 1967). There are two sources for the force: **(i)** forces acting

directly on the mass of the fluid element or volume (e.g., gravitational forces) known as body forces, and **(ii)** forces acting on the surface of the fluid element or volume (e.g., pressure and friction) known as surface forces.

$$\frac{\partial}{\partial t}(\rho \bar{v}) + \nabla \cdot (\rho \bar{v} \bar{v}) = -\nabla p + \nabla \cdot (\bar{\tau}) + \rho \bar{g} + \bar{F} \quad (4.1-4)$$

where p is the static pressure, ρg is the gravitational body force, F is the external body force and $\bar{\tau}$ is the stress tensor which is created from the friction between the fluid and the surface of the fluid element in accordance with ANSYS13.0/ Fluent (2012):

$$\bar{\tau} = \mu \left[(\nabla \bar{v}) + (\nabla \bar{v}^T) - \frac{2}{3} \nabla \cdot \bar{v} I \right] \quad (4.1-5)$$

where μ is the molecular viscosity, I is the unit tensor, and the second term on the right hand side is the effect of volume dilation (Bird et al., 2007). For incompressible fluids, the expression for the stress tensor is given by Equation (4.1-5) with the last term omitted:

$$\bar{\tau} = \mu \left[(\nabla \bar{v}) + (\nabla \bar{v}^T) \right] \quad (4.1-6)$$

$$\mu \left[(\nabla \bar{v}) + (\nabla \bar{v}^T) \right] = \mu \bar{D} \quad (4.1-7)$$

where \bar{D} is the rate-of-strain tensor. The generalized Newtonian fluid model is obtained by simply replacing the constant viscosity μ . The non-Newtonian viscosity η is a function of the shear rate $\dot{\gamma}$, which is related to the second invariant of \bar{D} and is defined as (Bird et al., 2007):

$$\dot{\gamma} = \sqrt{\frac{1}{2} (\bar{D} : \bar{D})} \quad (4.1-8)$$

Therefore, we have governing momentum equation:

$$\rho \left(\frac{\partial v_i}{\partial t} + v_i \frac{\partial v_i}{\partial x_i} \right) = -\frac{\partial p}{\partial x_i} + \frac{\partial}{\partial x_i} \left[\eta \left(\frac{\partial v_i}{\partial x_j} + \frac{\partial v_j}{\partial x_i} \right) \right] + F_i, \quad (i, j = 1, 2, 3) \quad (4.1-9)$$

In Equation (4.1-9), the convection terms are on the left-hand side. The terms on the right-hand side are pressure gradient (source term); the divergence of the stress tensor (diffusion of the momentum); the gravitational force (source term) and other generalized forces (source terms), respectively. These well-known differential equations form the basis of fluid mechanics, and are known as the Navier-Stokes/ Euler equations (Blazek, 2005).

4.1.4 Boundary Conditions

The continuity equation and momentum equations govern the flow of a fluid. The boundary and initial conditions (for unsteady cases) are required to determine the solution. Normally used boundary conditions are specified at the inlet, outlet, wall, and symmetry surface.

- **Inlet;** At inlet boundaries, velocity (or pressure), and composition of the incoming fluid stream are known. The inlet velocity can be calculated from volumetric flow rate specified from experimental condition, i.e., $v = 4Q/\pi d_i^2$ (where Q is the volumetric flow rate and d_i is the pipe inlet diameter). All other scalar, except pressure, can be set equal to input values. When velocity is known, the boundary condition for pressure is not required since the pressure-velocity coupling schemes depend on the pressure gradient and not on the absolute pressure. CFD codes usually fix the absolute pressure at one inlet node (atmospheric pressure for open tanks), and set the pressure correction to zero at that node (Versteeg and Malalasekera, 1995; Ranade, 2002).
- **Outlet;** Output boundary condition implies that gradients normal the outlet boundary are zero for all the variables except pressure. This boundary condition means that the conditions downstream of the outlet boundary should not influence the flow within the solution domain. This condition approached physically in fully developed flows, thus the exit pipe was modeled with a length/diameter ratio = 10 (Versteeg and Malalasekera, 2007). For pressure boundary condition, static pressure (atmospheric pressure for open tanks) is defined. For outflow through the exit, the static pressure is used to calculate the outflow velocities (Ranade, 2002).

- **Wall;** at the wall boundaries of the domain, a ‘no slip’ boundary condition can be used (Patankar, 1980). This means that the transverse fluid velocity is equal to that of the surface of the wall and the normal velocity is zero.
- **Symmetry;** at the symmetry surface, the normal velocity is set to zero (no flow across the symmetry surface) and the normal gradients of all variables except normal velocity are set to zero (no flux across the symmetry surface). It means that there is no convective or diffusive flux across the boundary (Versteeg and Malalaskera, 2007).

The fluid transport properties, such as the density and the viscosity need to be prescribed as constant or selected from a database and can be functions of temperatures, pressure or any other variables of state. Fluids can be modeled as being either compressible or incompressible. The fluid can be either Newtonian or non-Newtonian.

The governing equations are complex partial differential equations for which no analytical solution (applicable only to some simplified flow problems) can be found. A numerical solution of a differential equation consists of a set of numbers from which the distribution of the dependent variable can be formed. On the other hand, the numerical solution requires some discretization of the field into a collection of points or cells which is called discretization of the domain or grid generation.

4.1.5 CFD Modeling of Mixing Tanks

To model the geometry of the impeller in a mixing vessel, fully predictive simulation methodologies were developed to explicitly present impeller rotation in a vessel. ANSYS13/Fluent uses the following two methods to model impeller rotation in a mixing vessel: Multiple Reference Frame (MRF) Model and Sliding Mesh (SM) Model.

4.1.5.1 The Multi Reference Frame (MRF) Approach

A multiple reference frame model (MRF) is a steady state approach allowing for the modeling of baffled tanks with complex (rotating or stationary) internals (Luo et al., 1994). In MRF approach, two regions are created within the mixing tank; one region around the impeller with distance above and below it and one is attached to the tank wall. The impeller grid region is

stationary, but the conservation equations are solved in a rotating frame. The angular velocity of the rotating frame is the same as that of the impeller and shaft. Thus, the velocity of these elements is zero relative to the rotating frame. The second region is attached to the tank walls (including the top surface) as well as the baffles (if exists). The conservation equations in this grid region are solved in the stationary frame. Thus, no motion is applied to the tank wall, the liquid surface, or the baffles. Values of the conserved quantities are matched at the interface between these two grid regions, i.e. rotating and stationary frames.

4.1.5.2 The Sliding Mesh (SM) Approach

In the sliding mesh approach (Luo et al., 1993), the simulations are carried out using two grid zones; one is attached to the tank wall while the other is attached to the rotating impeller. In this approach, the impeller rotates in time relative to the rest of the tank, so does the grid in the impeller region, while the tank region does not move. To evaluate the motion of the grid, the solution method must be time-dependent. As this approach depends on unsteady-state solution in a stirred vessel, computational requirements are greater than those required by the steady-state simulations. Therefore, use of such an approach as a design tool to evaluate the mixing performance becomes time-consuming and costly. On the other hand, the extreme computational requirements make some limitations on number of computational cells that can be used for the simulations. Therefore if the knowledge of the full unsteady-state flow field is not necessary from industrial view of points, the simulations would be performed by steady-state approaches such as multi reference frame (MRF).

4.2 Model Description

In this study, ANSYS¹ workbench platform (ANSYS Inc., 2011) was employed to calculate the 3D flow field generated by RT impeller in the mixing of xanthan gum solutions. In this platform, we applied ANSYS DesignModeler, ANSYS Meshing, and ANSYS Fluent to draw

¹ ANSYS has acquired a number of companies since 2000, including ICEM CFD Engineering, CADOE, CFX (2003), Century Dynamics, Harvard Thermal, Fluent Inc. (2006), Ansoft Corporation (2008), Apache Design Solutions (2011), and Esterel Technologies (2012).

the geometry, mesh, and simulate our cases. In this study, Fluent solves the conservation of mass and momentum equations using a finite volume method via a coupled solver. In order to explain the model development, the continuous-flow mixing system has been selected as a sample of our modeling for this section.

4.2.1 Geometry

A mixing tank with identical geometry to the one used in the experiments was modeled using ANSYS DesignModeler. The same dimensions for tank, baffles, shaft, inlet, outlet, and the impeller (RT impeller) mentioned in section (3.1) were used to model the tank. The simulations were conducted in a flat-bottomed cylindrical tank with a diameter (T) of 0.38 m fitted with baffles. The RT impeller with a diameter (D) of 0.178 m was centrally positioned at an off-bottomed clearance (C) of 0.16 m. The fluid height in the mixing tank was equal to 0.41 m. The inlet was located at the top ($r = 0.13$ m, $\Phi = 90^\circ$, and $z = 0.38$ m) and the outlet was located at the bottom ($r = 0.13$ m, $\Phi = 315^\circ$, and $z = 0.00$ m) of the mixing vessel. The geometry consisted of one rotating grid zones (around the impeller) and one stationary zone (other than around impeller). For grid generation, this geometry was loaded in the “Meshing” application of the workbench.

4.2.2 Grid Generation

Since the density of cells in a computational grid needs to be fine enough to capture the flow details, an increased mesh density was used near the tank wall and the rotating impellers. In order to have an unstructured mesh in the mixing tank, the grids were created on the faces of both impellers using proper size functions to control the mesh growth. This feature allows the mesh elements to grow slowly as a function of the distance from the impellers blades as shown in Figure (4.2-1). The quality of the grid has been checked using a grid histogram for the equiangle skewness (Q). The equiangle skewness is a normalized measure of skewness that is an indication of how close the cell is to a perfect tetrahedral element (for this study). In fact, skewness = 0 describes the perfect tetrahedral element and skewness = 1 indicates a poorly shaped element. In the majority of simulations performed, about 99% of the cells generated

had skewness smaller than 0.6 confirming a good quality of mesh formation. However, the total number of grid cells was determined after conducting a grid independence study.

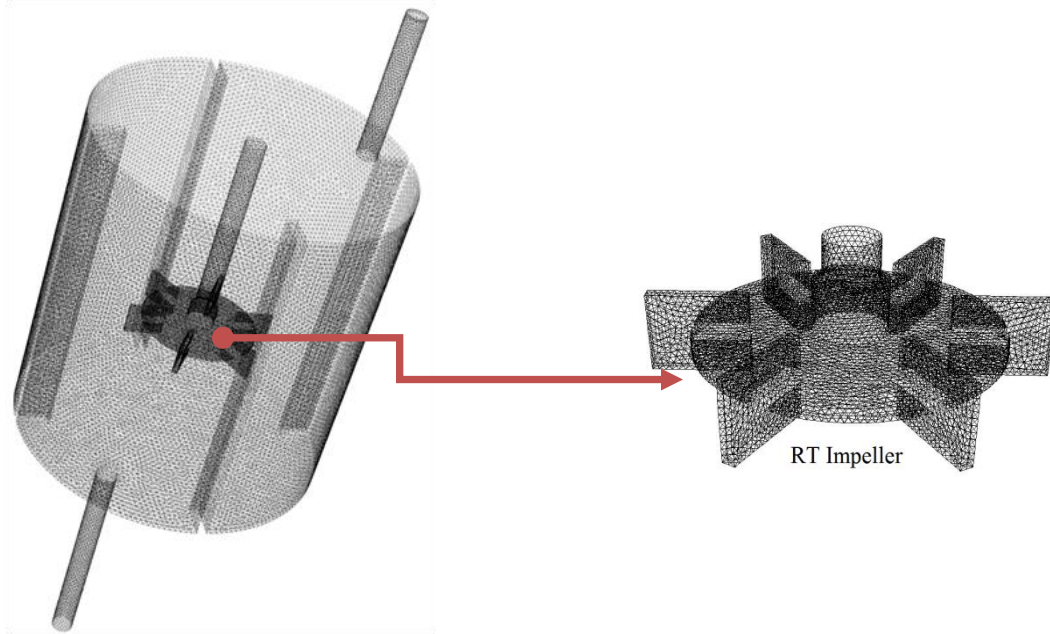


Figure (4.2-1). Unstructured tetrahedral mesh generated using ANSYS Fluent (v14.5) in Meshing Mode.

4.2.2.1 Grid Independence Study through Velocity Profile

In general, the density of cells in a computational grid needs to be fine enough to capture the flow details, but not so fine, since problems described by large numbers of cells require more time to solve. In order to capture the boundary layer flow detail, an increased mesh density was used near the tank wall and the rotating impellers. In order to have a very refined mesh in the vicinity of the blades, the sufficient amount of nodes that properly define the curvature of the blades was created on the impeller edges and a size function was used to control the mesh growth. This feature allows the mesh elements to grow slowly as a function of the distance from the impeller blades. The number of cells used for discretization was determined by conducting a grid independence study. Grid independence was verified by demonstrating that additional cells did not change the calculated velocity magnitude measured in the regions of high velocity gradients around the impeller blades by more than 6%.

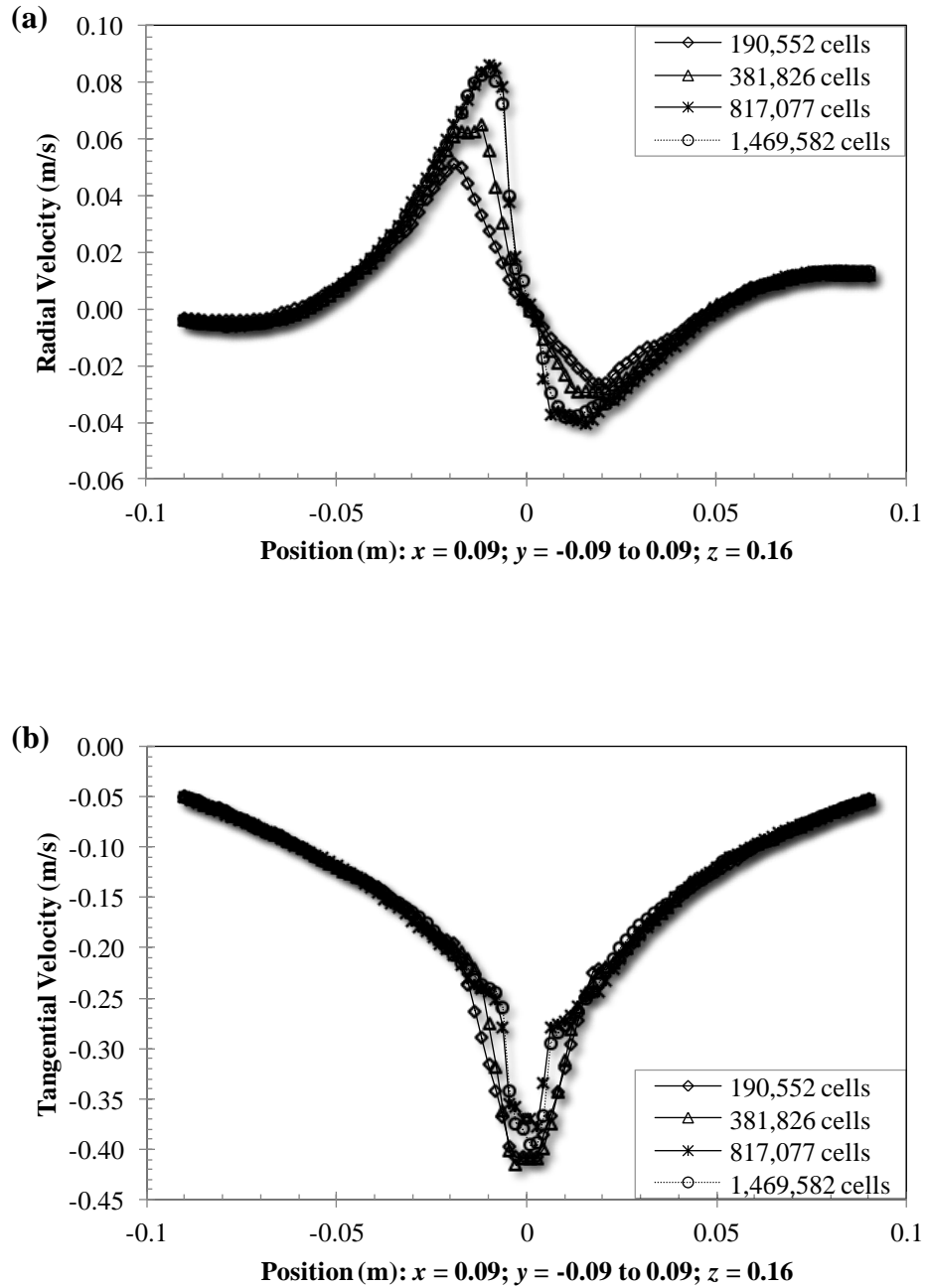


Figure (4.2-2). Effect of the number of cells on (a) radial velocity and (b) tangential velocity at horizontal line close to the impeller: Position of line (m): $x = 0.09$; $y = -0.09$ to 0.09 ; $z = 0.16$).

As demonstrated in Figure (4.2-2), the velocity profile was checked for four grids generated, i.e. 190,552 cells, 381,826 cells, 817,077 cells, and 1,469,582 cells. The results showed that

817,077 cells, and 1,469,582 cells provided similar velocity profiles. Thus, the optimal mesh of the model, which consisted of 817,077 cells, was used in all simulations. The discrepancy between the results obtained for the different grids can be quantified in terms of the root-mean-square (RMS) deviation (Arratia et al., 2006):

$$RMS = \frac{\left[\frac{1}{n} \sum_1^n (u_1 - u_2)^2 \right]^{1/2}}{\left[\frac{1}{n} \sum_1^n (u_2)^2 \right]^{1/2}} \quad (4.2-1)$$

where n is the number of nodes in the velocity field and u is the radial or tangential velocity in this study. The procedure to verify the grid independency was as follows; in fact, the number of cells was first increased from 190,552 cells to 381,826 cells and then from 381,826 cells to 817,077 cells,. In both cases, the additional cells changed the velocity magnitude in the regions of high velocity gradients by more than 5%. Therefore, the number of cells was changed from 817,077 cells to 1,469,582 cells. In this case, the additional cells did not change the velocity magnitude in the regions of high velocity gradients by more than 6%. Thus, the optimal mesh of the model, which consisted of 817,077 cells, was used to simulate the mixing of xanthan gum solution in a stirred vessel.

4.2.3 Impeller Model, Flow Model, Physical Properties, Boundary

Conditions, and Convergence

In this study the MRF technique was employed to model the rotation of the impeller in the mixing tank equipped with the RT impeller (Luo et al., 1994). Since all simulations in this study were conducted in the laminar and transitional regimes, the flow was modeled as laminar.

The xanthan gum solutions in water at 0.5, 1.0, and 1.5% concentrations was used in this study. The relationship between the shear stress and the shear rate was best described using the Herschel–Bulkley non-Newtonian model [Equation (2.1–9)]. In numerical modeling, the Bingham and Herschel-Bulkley models are discontinuous since at small shear rates, the non-Newtonian viscosity becomes unbounded (Ford et al., 2006). This discontinuous behaviour

causes major difficulties in numerical analysis. Therefore, it can be assumed that for low shear rates ($\dot{\gamma} \leq \tau_y / \mu_0$), the solution acts like a very viscous fluid with viscosity μ_0 [Equation (4.2–2)]. As the shear rate is increased and the yield stress (τ_y) is overcome, the fluid behaviour is described by a power-law model [Equation (4.2–3)]. Figure (4.2-3) shows how shear stress (τ_s) varies with shear rate ($\dot{\gamma}$) for the Herschel-Bulkley model. Hence, a two-viscosity model can be used to overcome the discontinuity [Equation (4.2–3)] as follows:

$$\eta = \mu_0 \quad \text{for } \tau_s \leq \tau_y \quad (4.2-2)$$

$$\eta = \frac{\tau_y + K \left[\dot{\gamma}^n - \left(\frac{\tau_y}{\mu_0} \right)^n \right]}{\dot{\gamma}} \quad \text{for } \tau_s > \tau_y \quad (4.2-3)$$

where μ_0 is yielding viscosity. Therefore, the fluid rheology was modeled as a Herschel-Bulkley fluid based on the parameters in Table (4.2-1).

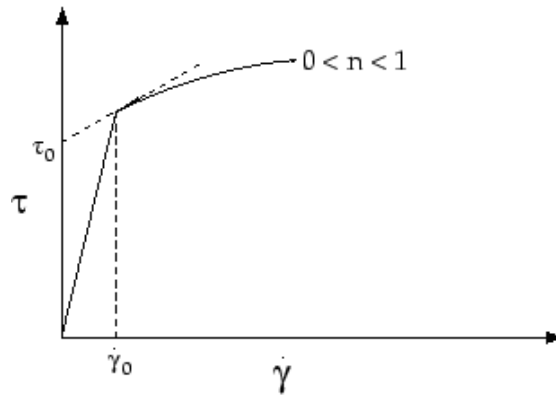


Figure (4.2-3). Shear stress vs. shear rate according to Equations (4.2–2) and (4.2–3).

Boundary conditions applied on the geometry included (i) nonslip at the vessel wall and baffles ($v = 0$), (ii) zero normal velocity ($v_n = 0$) at the free surface, (iii) an inflow boundary condition for the vessel inlet, defining the inlet velocity from the volumetric flow rate of the feed, i.e, $v = 4Q/\pi d_i^2$ (where Q is the volumetric flow rate and d_i is the pipe inlet diameter), and

(iv) an outflow boundary condition for the vessel outlet, implying zero normal diffusive flux for all flow variables ($\partial\phi/\partial n = 0$) (Versteeg and Malalasekera, 2007).

Table (4.2-1). Fluid rheological parameters applied in CFD modeling.

Xanthan concentration (%)	K (Pa.s^{n})	n -	τ_y (Pa)	μ_0 (Pa.s)
0.5	3	0.11	1.789	13.30
1.0	8	0.12	5.254	22.61
1.5	14	0.14	7.455	32.36

The discretized equations were solved using a segregated implicit scheme. CFD simulations were carried out using the followings schemes: (i) second order for pressure interpolation (Versteeg and Malalasekera, 2007), (ii) power law for momentum interpolation (Patankar, 1980), (iii) first order for temporal discretization (Versteeg and Malalasekera, 2007), and (iv) SIMPLEC for pressure-velocity coupling (Van Doormal and Raithby, 1984). The convergence history was monitored for the mass and x , y , and z velocities. Simulations were considered converged when the scaled residuals for each transport equation were below 10^{-7} . Most simulations required more than 6000 iterations for convergence. The simulations were carried out using the supercomputing facilities of HPCVL (High Performance Computing Virtual Laboratory). Each simulation was run in parallel with 12 dual cores SUN Ultra-Spark IV, 1.8GHz Sun Micro-Systems CPUs. The grid was partitioned into 12 parts and one CPU was then assigned to each partition. The convergence for each run was achieved after about 4 hours (depending on the case and the available CPU).

4.2.4 Modeling Tracer Injection to a Continuous-Flow Mixer and Model

Validation

The flow fields obtained using ANSYS FLUENT were used to simulate the system dynamic response to a tracer injection. When a tracer is added to a fluid in a mixing tank, the transient calculation can be exclusive of the flow field simulations, provided that the properties of the tracer and the background flow in the vessel are the same. Once the flow field of the

background fluid is satisfactorily converged, the tracer can be introduced and transient species solution for the tracer can be performed. The properties of background fluid (xanthan gum) will not be changed during tracer addition as the tracer was added in very small amount to the vessel.

To model the dispersion of the tracer, the following species transport equation was solved:

$$\frac{\partial}{\partial t}(\rho w) + \nabla \cdot (\rho \bar{v} w) = \nabla \cdot \rho D_m \nabla w \quad (4.2-4)$$

where w is the local mass fraction of the tracer, \bar{v} is the mean velocity vector, ρ is the fluid density, D_m is the molecular diffusivity of the tracer in the mixture which is assumed to be 10^{-9} ($\text{m}^2 \text{s}^{-1}$) as a typical value for liquids (Montante et al., 2005). In order to simulate transient species transport, species conservation equation must be solved in a time-dependent form and species conservation equation must be discretized in time and space. First order scheme was used for temporal discretization, and second order upwind scheme was used for concentration interpolation. Implicit scheme was used for temporal discretization of species transport equation.

A user-defined function (UDF) written in C programming language as shown in Figure (4.2-4) was linked to the ANSYS Fluent 14.5 solver for simulating the dynamic tests. This UDF defines the time at which the tracer was continuously injected into the mixing vessel. The UDF was linked to the inlet as a boundary condition that specified the tracer concentration in the inlet stream. The outlet concentration was recorded for comparison with experimental data. The mass fraction of the tracer in UDF was set to values similar to the conductivity of the random binary excitation signal used in the experimental work. To verify the effect of the time step, dynamic data were obtained at 0.1 s. This sampling time was then increased to 1 s. As shown in Figure (4.2-5), the predicted dynamic responses overlapped, indicating temporal independency. Therefore, the time step used in simulating the tracer injection was set to 1 s.

4.2.4.1 Model Validation

The CFD model was validated with the experimental data for continuous-flow mixing system. As demonstrated in Figure (4.2-6), the experimental and CFD input/output conductivity curves for the tracer injection were compared against each other in order to evaluate the CFD ability to predict the dynamic behavior of the continuous-flow mixers. The output response predicted by CFD demonstrated good agreement with the experimental response. The CFD model was further validated with the experimental power number. The power number curve for the RT impeller depicted in Figure (4.2-7) showed good agreement between the calculated power numbers through CFD and the experimentally determined values.

```
#include "udf.h"
DEFINE_PROFILE(tracer_mf_profile,t,i)
{
    real flow_time=CURRENT_TIME;
    face_t f;
    begin_f_loop(f,t)
    {
        if(flow_time>1250)
            F_PROFILE(f,t,i)=0.1504;
        else if(flow_time>806)
            F_PROFILE(f,t,i)=0.0598;
        else if(flow_time>425)
            F_PROFILE(f,t,i)= 0.1491;
        else if(flow_time>100)
            F_PROFILE(f,t,i)= 0.0598;
        else if(flow_time>58)
            F_PROFILE(f,t,i)=0.1350;
        else
            F_PROFILE(f,t,i)=0.0442;
    }
    end_f_loop(f,t)
}
```

Figure (4.2-4). UDF code used to model tracer injection for frequency-modulated random binary input signal.

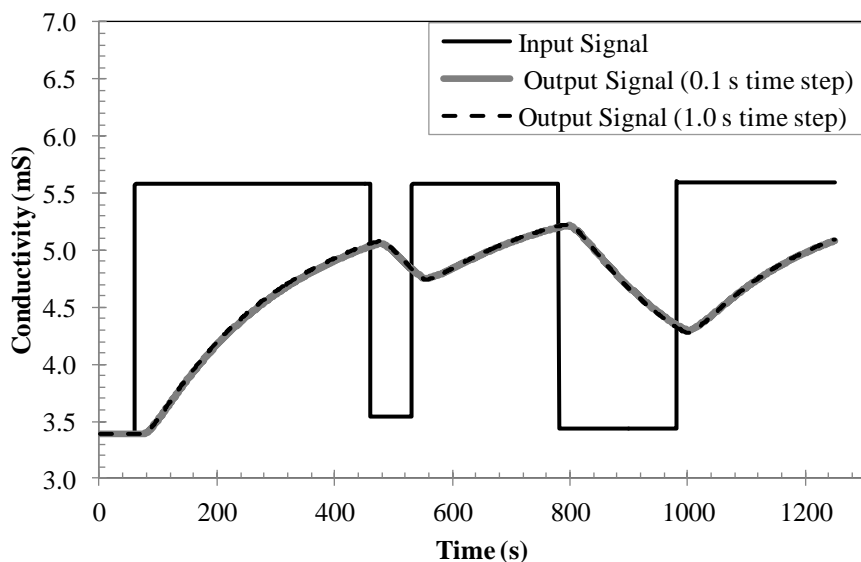


Figure (4.2-5). Effect of time step on the output response to a frequency-modulated random binary input signal using CFD ($Q = 9.65 \text{ L min}^{-1}$, 1.0% xanthan gum, and $N = 416 \text{ rpm}$).

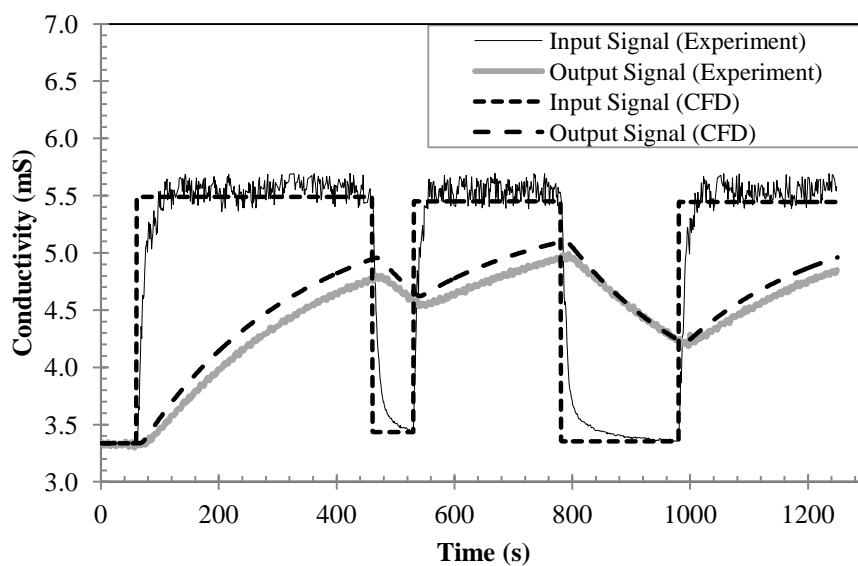


Figure (4.2-6). Input/output signals (experimental and CFD) at $Q = 9.65 \text{ L min}^{-1}$, 1.0% xanthan gum, and $N = 416 \text{ rpm}$.

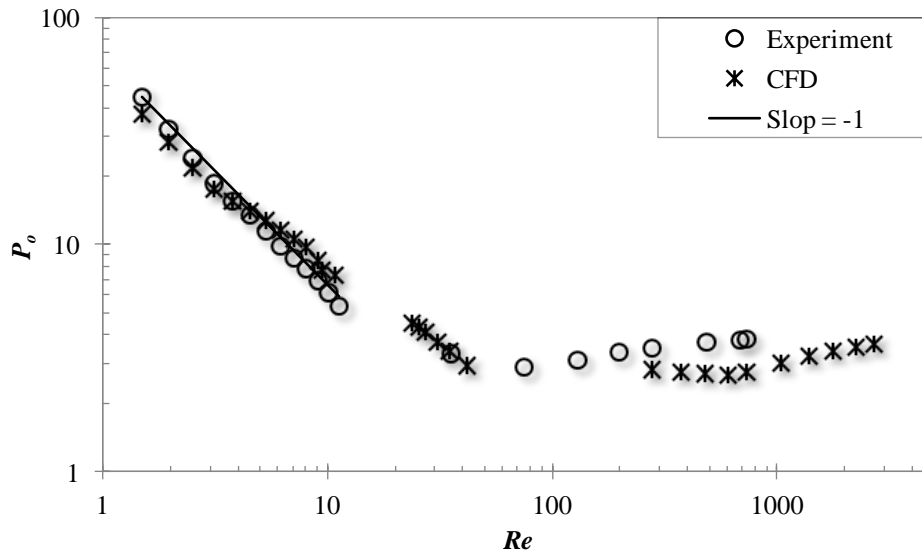


Figure (4.2-7). Power number (experimental and CFD) versus Reynolds number for 1.5% xanthan gum.

4.2.5 Modeling Tracer Injection for Mixing Time in a Batch Mode

After the flow field was calculated in a batch mode, the homogenization of the injected tracer was simulated to calculate the mixing time (θ). To measure the mixing time (θ) using CFD, the tracer having the same physical properties as xantahn gum solution was added below the liquid surface at point ($x = 0.07, y = 0.11, z = 0.34$). In this study, the mixing time (θ) was defined as the time required for the mass concentration of the fluid to reach 98% of the steady-state value after the injection of the tracer. The tracer was monitored at point-1 ($x = -0.09, y = -0.09, z = 0.34$); point-2 ($x = 0.03, y = -0.13, z = 0.28$); point-3 ($x = 0.09, y = 0.09, z = 0.22$); point-4 ($x = 0.11, y = 0.03, z = 0.16$); point-5 ($x = -0.12, y = 0.04, z = 0.10$); and point-6 ($x = 0.09, y = -0.07, z = 0.04$). The vertical position of each monitoring point in CFD model was set identical to that of the ERT planes shown in Figure (3.2-1). In all simulations, the value of mass fraction of the injected tracer was set to 1.

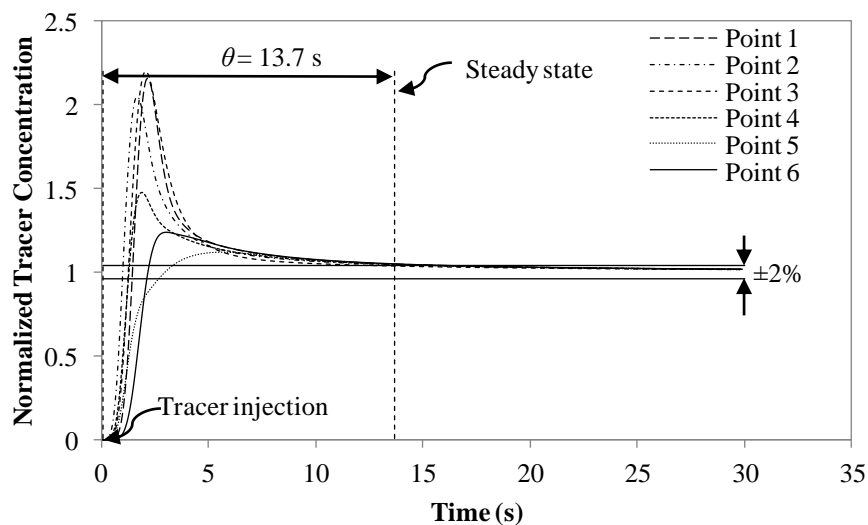


Figure (4.2-8). Measurement of mixing time for 1% xanthan gum agitated by RT impeller {monitoring point–1 ($x = -0.09$, $y = -0.09$, $z = 0.34$); point–2 ($x = 0.03$, $y = -0.13$, $z = 0.28$); point–3 ($x = 0.09$, $y = 0.09$, $z = 0.22$); point–4 ($x = 0.11$, $y = 0.03$, $z = 0.16$); point–5 ($x = -0.12$, $y = 0.04$, $z = 0.10$); point–6 ($x = 0.09$, $y = -0.07$, $z = 0.04$). Tracer injection point: ($x = 0.07$, $y = 0.11$, $z = 0.34$)}.

Figure (4.2-8) shows a practical approach to measure the mixing time after the injection of the tracer for six monitoring points. It shows that the average mass concentration value for all monitoring planes reached within 98% of the steady state value after 13.7 s. This approach was employed to measure the mixing time as a function of the operating conditions and rheological parameters of fluid in this study. The value of species residual for a converged solution was set equal to 10^{-7} . The CPU time varied between 6 and 8 hours

4.2.6 Cavern region in CFD

To measure the cavern size using CFD results, the shape of the cavern was approximated by a right circular cylinder; therefore, the characteristics of the cavern can be described by the diameter and height of this region. The cavern diameter was measured on a horizontal plane passing through the impeller on plane $P4$ (point–4 in Figure (4.2-8)). The cavern height was measured on a vertical plane along the shaft and perpendicular to the horizontal plane of the

impeller. As shown in Figure (4.2-9), the cavern boundary was determined as a position at which the velocity magnitude of xanthan gum solution was zero.

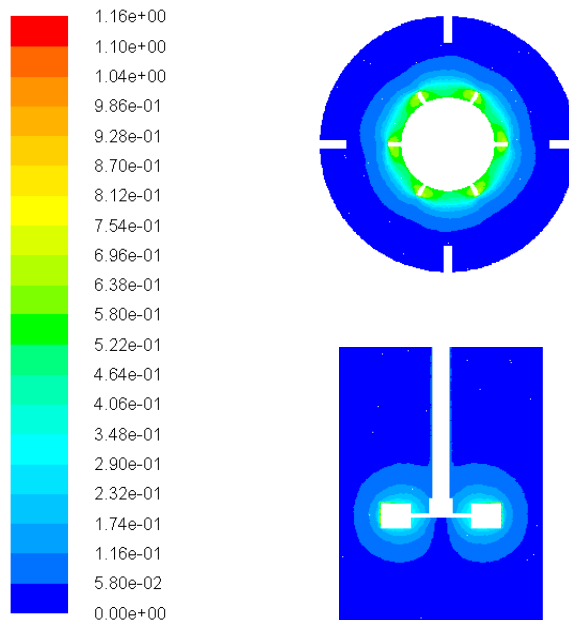


Figure (4.2-9). Velocity contours showing the formation of cavern in the mixing of 0.5% xanthan gum agitated by the RT impeller.

Chapter 5

5. RESULTS AND DISCUSSION

In this study, dynamic tests, electrical resistance tomography (ERT), and computational fluid dynamics (CFD) were used to assess the performances of continuous-flow mixing of non-Newtonian fluids in stirred vessel. To achieve this objective, the effects of various design parameters and operating conditions on the impeller power consumption, the cover size, mixing time (θ), and the extent of channelling (f) and the fully mixed volume ($V_{fully\ mixed}$) were evaluated. In this chapter, we present all results and related discussions in the nine separate sections as below:

Section 5.1 “*Dynamic Performance of Continuous-Flow Mixing of Pseudoplastic Fluids Exhibiting Yield Stress in Stirred Reactors*” is described on page 71. The results presented in this section have been published in a peer-reviewed journal (Patel et al., 2011).

Section 5.2 “*Effect of Impeller Type on Continuous-Flow Mixing of Non-Newtonian Fluids in Stirred Vessels through Dynamic Tests*” is explained on page 96. The results presented in this section have been published in a peer-reviewed journal (Patel et al., 2012b).

Section 5.3 “*Improving the Dynamic Performance of Continuous-Flow Mixing of Pseudoplastic Fluids Possessing Yield Stress Using Maxblend Impeller*” is provided on page 107. The results presented in this section have been published in a peer-reviewed journal (Patel et al., 2012a).

Section 5.4 “*Characterization of the Continuous-Flow Mixing of Non-Newtonian Fluids Using the Ratio of Residence Time to Batch Mixing Time*” is presented on page 120. The results presented in this section have been published in a peer-reviewed journal (Patel et al., 2013c).

Section 5.5 “*Tomography Images to Analyze the Deformation of the Cavern in the Continuous-Flow Mixing of Non-Newtonian Fluids*” is given on page 134. The results presented in this section have been published in a refereed journal (Patel et al., 2014a).

Section 5.6 “*Using Tomography to Visualize the Continuous-Flow Mixing of Biopolymer Solutions inside a Stirred Tank Reactor*” is described on page 156. The results presented in this section have been published in a refereed journal (Patel et al., 2014b).

Section 5.7 “*Effect of Rheological Parameters on the Continuous-Flow Mixing of Biopolymer Solutions*” is explained on page 180. The results presented in this section have been submitted to a peer-reviewed journal.

Section 5.8 “*Using CFD to study the effect of rheological parameters on mixing time for the shear thinning fluids with yield stress*” is provided on page 191. The results presented in this section have been submitted to a peer-reviewed journal.

Section 5.9 “*Using Tomography to Characterize the Mixing of Non-Newtonian Fluids with a Maxblend Impeller*” is described on page 204. The results presented in this section have been published in a refereed journal (Patel et al., 2013b).

5.1 Dynamic Performance of Continuous-Flow Mixing of Pseudoplastic Fluids Exhibiting Yield Stress in Stirred Reactors (Patel et al., 2011)

5.1.1 Introduction

Non-ideal flows such as channelling, recirculation, and dead zones significantly affect the performance of continuous-flow mixing systems (Ein-Mozaffari, 2002; Ford et al., 2006; Saeed et al., 2008). To eradicate non-ideal flows inside stirred vessels, the important parameters such as impeller types, impeller speed, impeller diameters, impeller off-bottom clearance, locations of inlet and outlet, pumping directions of an axial-flow impeller, fluid height in the vessel, residence time, and jet velocity should be considered into design criteria.

A detail literature review discloses that Newtonian fluids have been widely used for the study of continuous-flow mixing in stirred tank reactors and little effort has been devoted to the study of the effects of above parameters on the performance of continuous-flow mixing of pseudoplastic fluids exhibiting yield stress. More work still needs to be done in order to develop a comprehensive methodology to design a continuous-flow mixers for fluid with complex rheology. Therefore, the core objective of this study is to characterize the continuous-flow mixing of pseudoplastic fluids possessing yield stress in stirred reactors using dynamic tests. To achieve this objective, the effects of impeller types (seven axial-flow impellers: A100, A200, A310, A315, A320, 3AH, and 3AM; and four radial-flow impellers: R500, RSB, RT, and Scaba), impeller speed (50–800 rpm), impeller diameters ($T/3.2$ – $T/1.6$, where T is the tank diameter), impeller off-bottom clearance ($H/3.4$ – $H/1.7$, where H is the fluid height in the vessel), locations of inlet and outlet (configurations: top inlet-top outlet, top inlet-bottom outlet, bottom inlet-bottom outlet, and bottom inlet-top outlet), pumping directions of an axial-flow impeller (up-pumping and down-pumping), fluid height in the vessel ($T/1.06$ – $T/0.83$), residence time (257–328 s), and jet velocity (0.317–3.24 m s⁻¹) on the dynamic performance of the mixing vessel were explored.

The experimental setup for continuous-flow mixing system shown in Figure (3.1-1) was used in this study. The extent of non-ideal flows was quantified using a dynamic model [Equation (2.4–7)] that incorporated channelling, recirculation, and dead volume in the mixing vessel. To estimate the dynamic model parameters, the system was excited using a frequency-modulated random binary input by injecting the saline solution (as a tracer) into the fresh feed stream prior to being pumped into the mixing vessel. The extent of channelling (f) and the fully mixed volume ($V_{fully\ mixed}$) were successfully determined and used as mixing quality criteria. The Herschel-Bulkley model [Equation (2.1–9)] was used to describe the rheological behaviour of the xanthan gum solutions.

5.1.2 Results and Discussion

The estimation of power (P) is crucial for the design of mixing vessels in industries. Power represents the rate of energy dissipated within a fluid from the impeller and is a function of the impeller speed (N), fluid rheology, and geometry of the impeller and tank. The power number (P_o) for seven axial-flow impellers: A100, A200, A310, A315, A320, 3AH, and 3AM; and four radial-flow impellers: R500, RSB, RT, and Scaba was calculated using Equation (2.1–3). The Reynolds number (Re) was calculated using Equation (2.1–11). Figure (3.4-1) represents the power curve for axial-flow, and radial-flow. The trend in the power number curve is similar to those general trends reported by several researchers (Paul et al., 2004; Kelly and Gigas, 2003; Holland and Chapman, 1966; Nagata, 1975).

5.1.2.1 Effect of Impeller Speed

The impeller speed is one of the most important parameters which affect the dynamic performance of the continuous-flow mixing system. Figure (5.1-1a and b) shows the extent of channeling and the fraction of fully mixed volume as a function of impeller speed, respectively. As expected, the channeling decreased and the fully mixed volume increased with an increase in impeller speed. At higher impeller speeds, the xanthan gum solution was agitated vigorously and disrupted further away from the impeller, leading to improved mixing by reducing the extent of non-ideal flows. Other researchers also observed similar phenomena (Saeed and Ein-Mozaffari, 2008; Saeed et al., 2008; Ford et al., 2006). The optimum impeller speed at which

the channeling approaches zero and the fully mixed volume approaches the total volume of the fluid within the mixing tank should be preferred, as further increases in the impeller speed will lead to more power consumption for the same extent of the fully mixed volume.

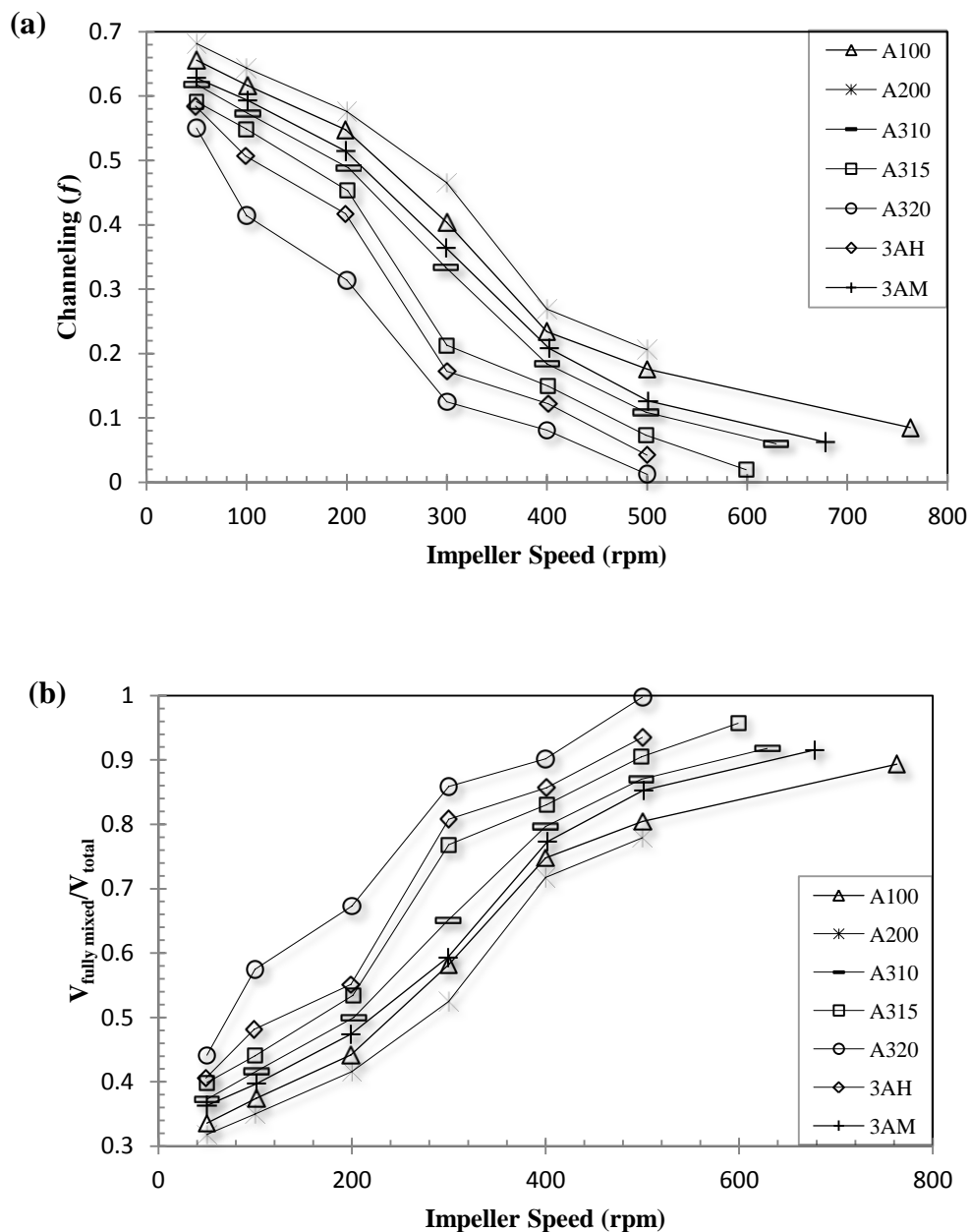


Figure (5.1-1). Axial-flow impellers: Effects of impeller speed and impeller type on the extents of (a) channeling and (b) fully mixed volume ($Q = 9.65 \text{ L min}^{-1}$, 1.0% xanthan gum, $D = T/2.1$, $C = H/2.7$, $H = T/0.93$, $V_j = 0.317 \text{ ms}^{-1}$, residence time = 292 s, input-output locations: TI-BO).

5.1.2.2 Effect of Impeller Type

Besides the impeller speed, the type of impeller also influences the dynamic performance of continuous-flow mixing. Several types of impeller are used in industries; however, the determination of the most effective impeller should be based on an understanding of the process requirements and knowledge of the physical properties. Normally, the axial-flow and radial-flow impellers are utilized for the mixing of fluids with low to medium viscosities. Seven axial-flow impellers (A100, A200, A310, A315, A320, 3AH, and 3AM) and four radial-flow impellers (R500, RSB, RT, and Scaba) were employed in this study and the efficiency of each impeller in terms of the extent of channeling and fully mixed volume is depicted in Figure (5.1-1) and Figure (5.1-2). It can be seen from Figure (5.1-1) that the A200 impeller was the least effective while the A320 impeller was the most effective in reducing the effect of channeling and dead volume among the axial-flow impellers. The hydrofoil impellers with a high solidity ratio have been recommended in the literature for mixing of viscous fluids (Paul et al., 2004; Nienow, 1990; McFarlane and Nienow, 1995). Thus, we measured the solidity ratios of five hydrofoil impellers (A320, 3AH, A315, A310, and 3AM) utilized in this study. The solidity ratios of A320, 3AH, A315, A310, and 3AM were 0.944, 0.902, 0.881, 0.668, and 0.643, respectively. It can be seen that the A320, 3AH, and A315 impellers have higher solidity ratio than the A310 and 3AM impellers. Moreover, the A320 impeller has the highest solidity ratio among all hydrofoil impellers used in this study. Figure (5.1-3) illustrates the effect of solidity ratio of hydrofoil impellers on the extent of channeling and fully mixed volume at the fixed power consumption. The results show that the A320, A315, and 3AH impellers (with a high solidity ratio) were more effective than the A310 and 3AM impellers (with a low solidity ratio) in reducing the effect of non-ideal flows in the continuous-flow mixing of xanthan gum solutions. These results are in good agreement with those reported in the literature regarding the effect of the solidity ratio of hydrofoil impellers on the mixing quality. In Figure (5.1-1), the power consumed per unit volume by the A320 impeller when the channeling approached zero and fully mixed volume approached unity value was the least power consumption among all axial-flow impellers.

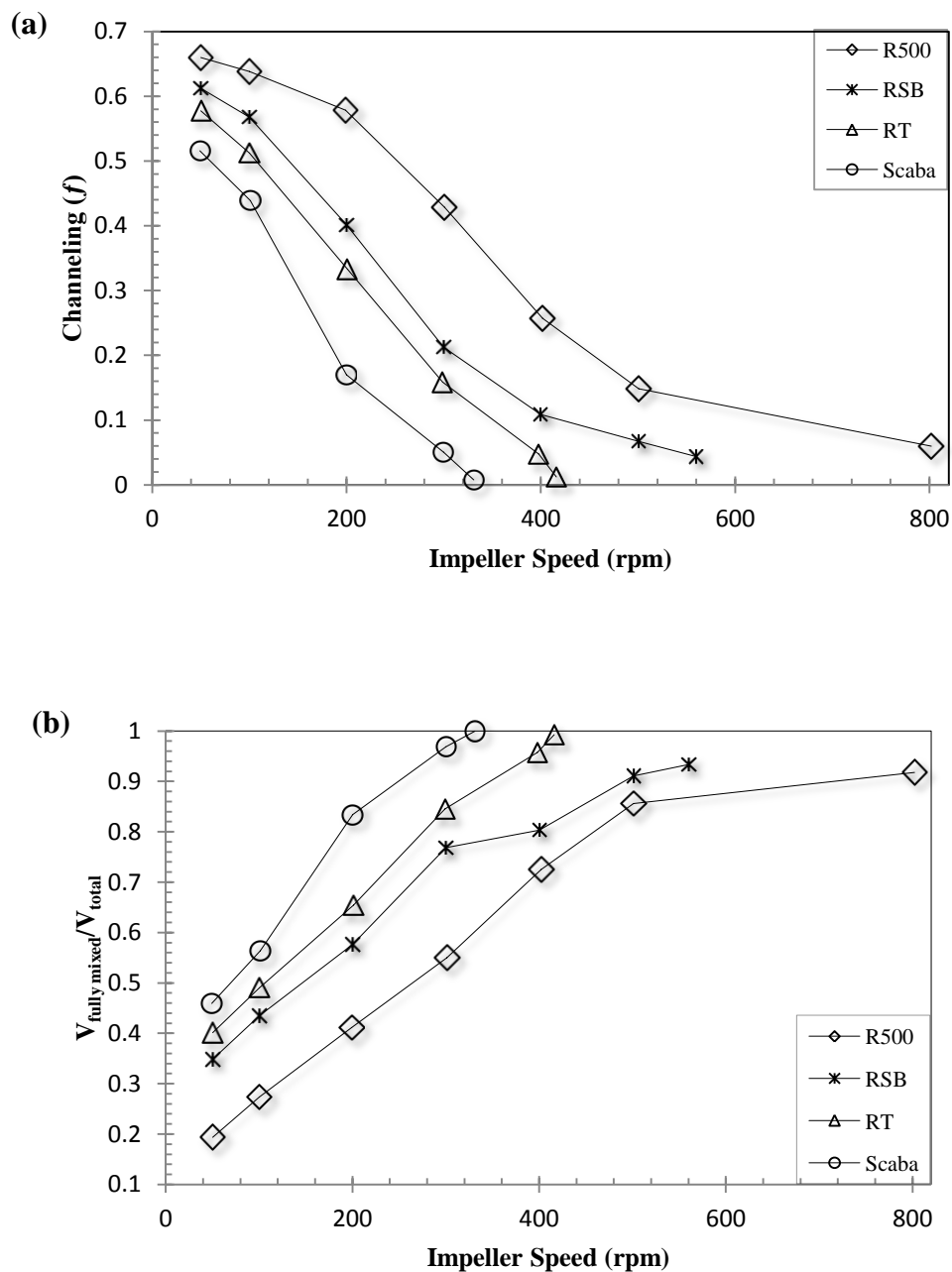


Figure (5.1-2). Radial-flow impellers: Effects of impeller speed and impeller type on the extents of (a) channeling and (b) fully mixed volume ($Q = 9.65 \text{ L min}^{-1}$, 1.0% xanthan gum, $D = T/2.1$, $C = H/2.7$, $H = T/0.93$, $V_j = 0.317 \text{ m s}^{-1}$, residence time = 292 s, input-output locations: TI-BO).

Alternatively, radial-flow impellers produce two circulating loops, one below and one above the impeller. The disk-type radial-flow impellers (Scaba and RT) provide a more

uniform radial flow pattern and draw more power than those without disk radial-flow impellers (RSB). The Scaba impeller is similar to the Rushton turbine except curved blades are substituted for vertical flat blades resulting in a lower power number, while a very high-shear producing R500 impeller consists of a disk with serrations around its circumference (Paul et al., 2004). Figure (5.1-2) shows that the R500 impeller was the least effective, while the Scaba impeller was the most effective in reducing the effect of channeling and dead volume among the radial-flow impellers. The power consumed per unit volume by the Scaba impeller when the channeling approached zero and fully mixed volume approached unity value was the least power consumption among all radial-flow impellers.

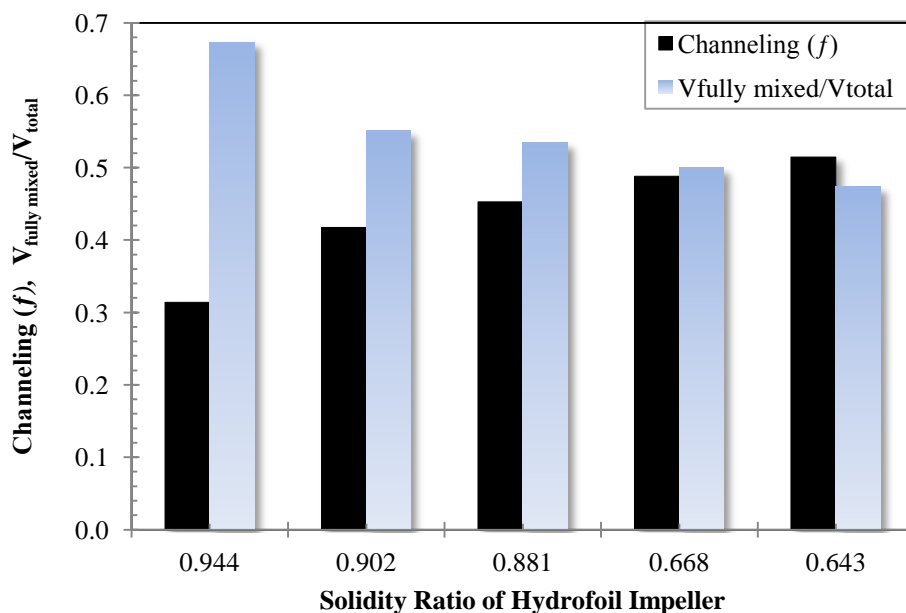


Figure (5.1-3). Effects of the solidity ratio of the hydrofoil impellers on the extents of channeling and fully mixed volume at the fixed power consumption ($Q = 9.65 \text{ L min}^{-1}$, 1.0% xanthan gum, $D = T/2.1$, $C = H/2.7$, $H = T/0.93$, $V_j = 0.317 \text{ m s}^{-1}$, residence time = 292 s, input-output locations: TI–BO).

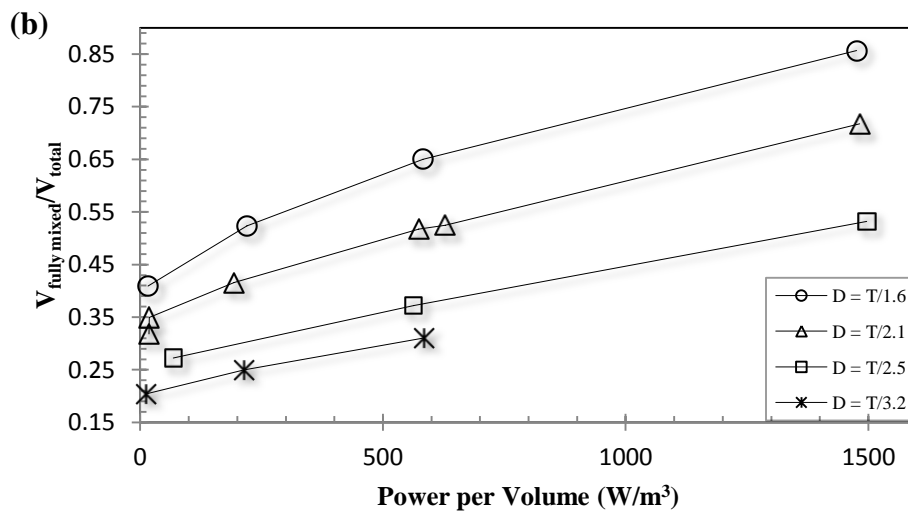
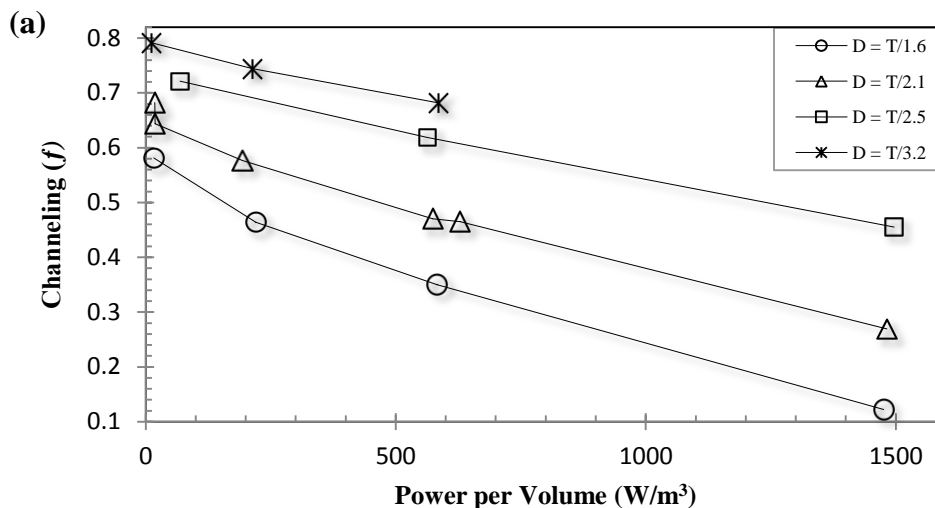
Thus, the results show that the A320 impeller was the most effective among the axial-flow impellers and the Scaba impeller was the most effective among the radial-flow impellers in reducing the effect of non-ideal flows. However, these two most effective impellers would seldom be used in similar conditions. The axial-flow hydrofoil impellers are mostly capable for a high pumping and low shear. Compared to axial-flow impellers, radial-flow impellers provide

higher shear and turbulence levels with lower pumping. Therefore, based on commercial price of each impeller, process requirements, and physical properties of fluids, either an impeller producing high pumping and low shear such as the A320 impeller or a low pumping and high shear impeller such as the Scaba impeller should be chosen. The Scaba impeller provides better gas dispersion and higher gas-holding capacity than the A320 impeller in gas-liquid mixing operations.

5.1.2.3 Effect of Impeller Diameter

In addition to the impeller speed and impeller type, the impeller diameter also influences the dynamic performance of the continuous-flow mixing system. Choosing the optimum ratio of the impeller diameter to the tank diameter (D/T) can drastically reduce the capital cost (impeller, gearbox, and motor) and operating cost (power requirement) of the processing unit. Reducing the impeller diameter cuts down the impeller weight, which leads to a reduction in the shaft's normal frequency and allows an increase in speed, whereas the selection of a smaller gearbox reduces the motor size. Figure (5.1-4a and b) demonstrates the effects of changing the impeller diameter ($D = T/1.6$, $T/2.1$, $T/2.5$ and $T/3.2$) on the extent of channeling and the fraction of fully mixed volume as a function of the power input for the A200 impeller, respectively, while Figure (5.1-4c) shows the channeling and fraction of fully mixed volume as a function of D/T at the constant power input for the A200 impeller. The results show that the impeller with $D = T/3.2$ was the least effective, while the impeller with $D = T/1.6$ was the most effective in reducing the effect of channeling and dead volume. It is clear that with an increase in impeller diameter the extent of channeling decreased and the fully mixed volume increased. An increase of the impeller diameter also increases the value of the average velocity of the circulation flow in the tank, which leads to improved mixing by eliminating channeling and dead volume. Moreover, the flow pattern with the A200 impeller becomes closer to that generated with a radial-flow impeller as the impeller diameter increases (Paul et al., 2004). This radial-flow pattern also reduces the degree of channeling compared to that achieved by an axial-flow pattern. Ein-Mozaffari et al. (2003a) also observed a similar phenomenon, where an impeller with a larger diameter provided better performance than an impeller with a smaller diameter for the continuous-flow mixing of pulp suspension (a non-Newtonian fluid) in a

laboratory chest. The range of the rotational speed for the impellers with $D = T/3.2$ was narrower than that for others because at higher impeller speed the system generated a lot of mechanical vibrations, severe turbulent flow, and surface air entrainment. In such situation, it was almost risky to conduct the experiment at higher impeller speed.



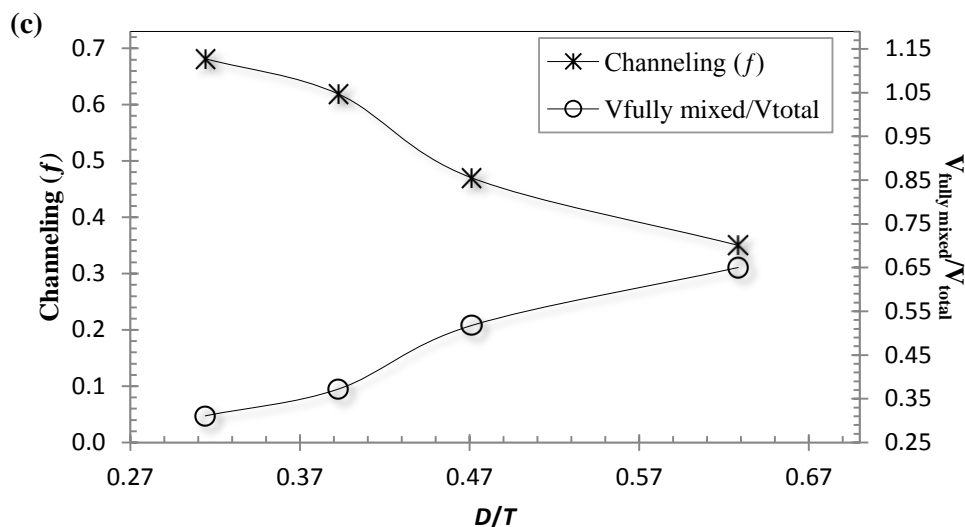
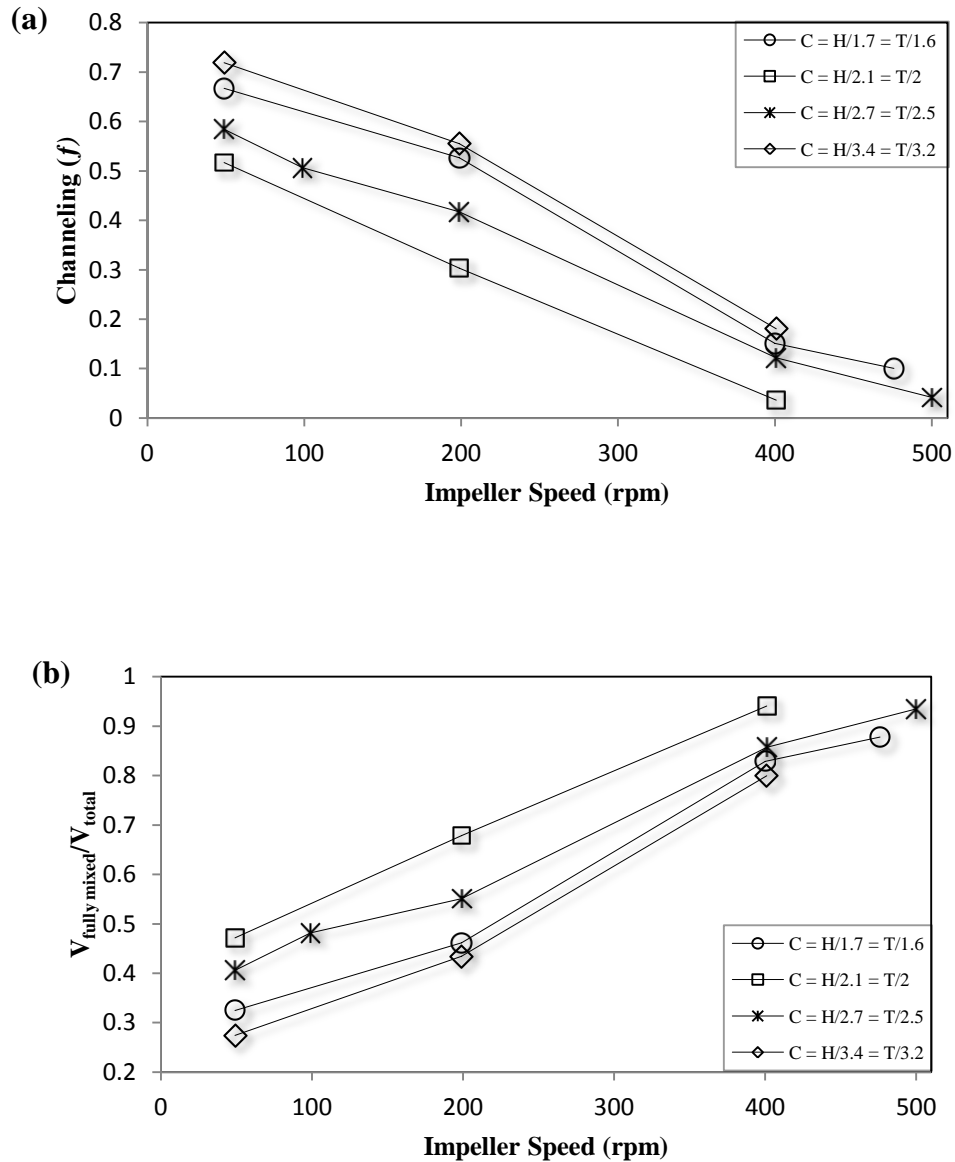


Figure (5.1-4). Effects of impeller diameter on the extents of (a) channeling, (b) fully mixed volume, and (c) channeling and fully mixed volume at the fixed power consumption as a function of D/T (A200, $Q = 9.65 \text{ L min}^{-1}$, 1.0% xanthan gum, $C = H/2.7$, $H = T/0.93$, $V_j = 0.317 \text{ m s}^{-1}$, residence time = 292 s, input-output locations: TI–BO).

5.1.2.4 Effect of Impeller Clearance

The impeller clearance (C) from the bottom of the tank has a significant impact on the dynamic performance of the continuous-flow mixing system. In the mixing of pseudoplastic fluid with yield stress, placing the impeller too low results in the majority of the fluid remaining unmixed on the upper part of the tank. Placing the impeller too high causes a deep vortex, which leads to surface aeration even at the lower impeller speed and also results in the creation of dead zones at the bottom of the tank, especially the bottom corner of the tank. Hence, placing the impeller at an optimum clearance (C) can drastically reduce the channeling and dead zones in the continuous-flow mixing of viscous fluids. The four different impeller positions from the base of the tank $C = H/1.7$, $H/2.1$, $H/2.7$, and $H/3.4$ were tested with the 3AH impeller. Figure (5.1-5a and b) shows the effects of the impeller clearance on the extent of channeling as well as the fraction of fully mixed volumes, respectively. Figure (5.1-5c) demonstrates the channeling and the fraction of fully mixed volume as a function of C/H at the constant power input for the 3AH impeller. These results show that as the clearance of the impeller increased from $H/3.4$ to $H/2.1$, the non ideal flows such as channeling and dead volume decreased and reached a minimum value at $C = H/2.1$. Further increase in the clearance of the impeller ($H/1.7$) had an

adverse effect on the extent of the non ideal flows. This result is similar to those obtained by Ein-Mozaffari and Upreti (2009), who observed a reduction in the mixing time with increasing impeller clearance (from $H/3$ to $H/2$) for a pitched blade turbine in the mixing of a pseudoplastic fluid with yield stress. Houcine et al (2000). also observed identical phenomena in the batch mixing of Newtonian fluids with a pitched blade turbine.



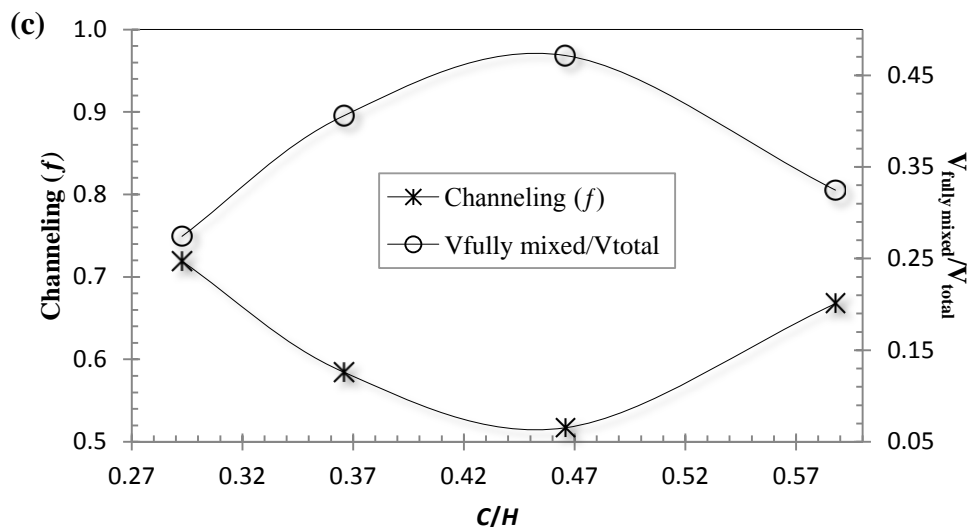


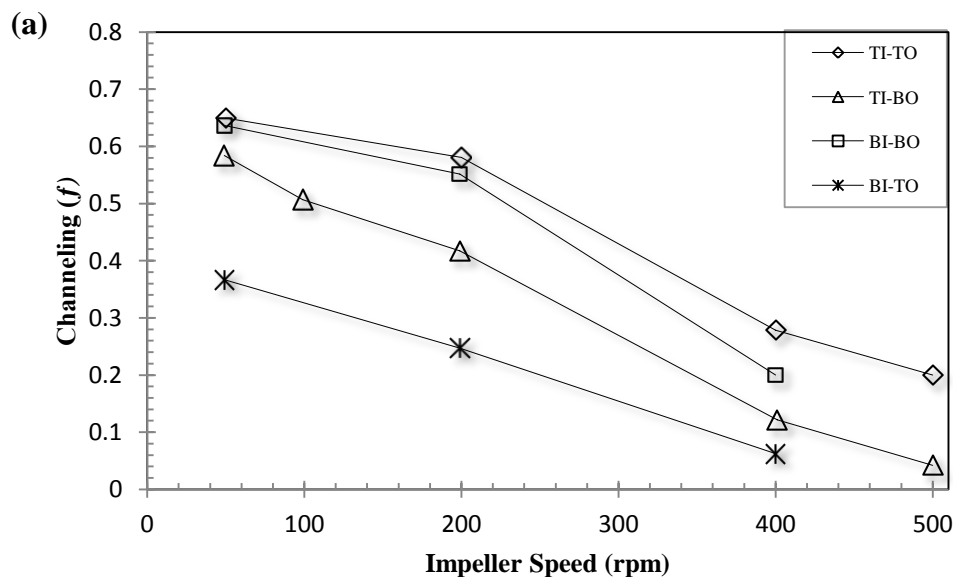
Figure (5.1-5). Effects of impeller clearance on the extents of (a) channeling, (b) fully mixed volume, and (c) channeling and fully mixed volume as a function of C/H at 50 rpm (3AH, $Q = 9.65 \text{ L min}^{-1}$, 1.0% xanthan gum, $D = T/2.1$, $H = T/0.93$, $V_j = 0.317 \text{ m s}^{-1}$, residence time = 292 s, input-output locations: TI–BO).

Amanullah et al (1997). also investigated the effects of impeller clearance on the cavern volume in the mixing of shear thinning viscous fluid for $C/T = 0.24\text{--}0.49$ (0.2% Carbopol, $D/T = 0.49$) and $C/T = 0.17\text{--}0.33$ (0.1% Carbopol, $D/T = 0.33$). In both cases, increasing the impeller clearance from the vessel base was beneficial in generating larger cavern volumes at a given power input.

5.1.2.5 Effect of Inlet and Outlet Locations

The locations of the inlet and outlet, one of the vital geometric parameters of a mixing tank, play a crucial role in the continuous-flow system. Ein-Mozaffari et al. (2004a and 2005) and Saeed and Ein-Mozaffari (2008) found that the locations of the inlet and outlet have a significant effect on the extent of non-ideal flows in the continuous-flow mixing of non-Newtonian fluids. Thus, this study examined the effects of four different configurations; (1) TI–TO (top inlet–top outlet), (2) TI–BO (top inlet–bottom outlet), (3) BI–BO (bottom inlet–bottom outlet), and (4) BI–TO (bottom inlet–top outlet) on the extent of non-ideal flows. The effect of the inlet and outlet locations on the extent of channeling and the fraction of fully mixed volume is depicted in Figure (5.1-6a and b), respectively. Figure (5.1-6c) displays the

degree of channeling and fully mixed volume for each configuration at 400 rpm for the 3AH impeller. It can be seen from the results that for the identical operating conditions, the BI–TO configuration was the most effective in reducing the extent of the non-ideal flows, while the TI–TO configuration was very prone to a high degree of channeling and dead volume. The BI–BO configuration was more susceptible to a high degree of channeling and dead volume than the TI–BO configuration. The TI–TO and BI–BO configurations enabled a large percentage of feed to be conveyed directly to the outlet without being drawn into the mixing zone (or through the impeller). Conversely, in the case of the BI–TO and TI–BO configurations, the feed was forced to flow through the mixing zone before leaving the vessel. Even in the case of BI–TO, the feed had to face the intense fluid discharge from the impeller and pass through the mixing zone in the direction opposite to the gravitational force. Based on the data presented in Figure (5.1-6c), the BI–TO configuration was the optimum inlet/outlet configuration. Overall it seems that the locations of the inlet and outlet should be chosen in such a way that a line drawn from the inlet to the outlet passes through the impeller (or the intense mixing zone). Khopkar et al. (2004). simulated the flow generated by an axial flow impeller to investigate the effect of the inlet and outlet locations on the mixing of Newtonian fluid and reported that the mixing was improved when the inlet was located at the bottom and the outlet as an overflow instead of having the inlet at the top and the outlet at the bottom of the tank.



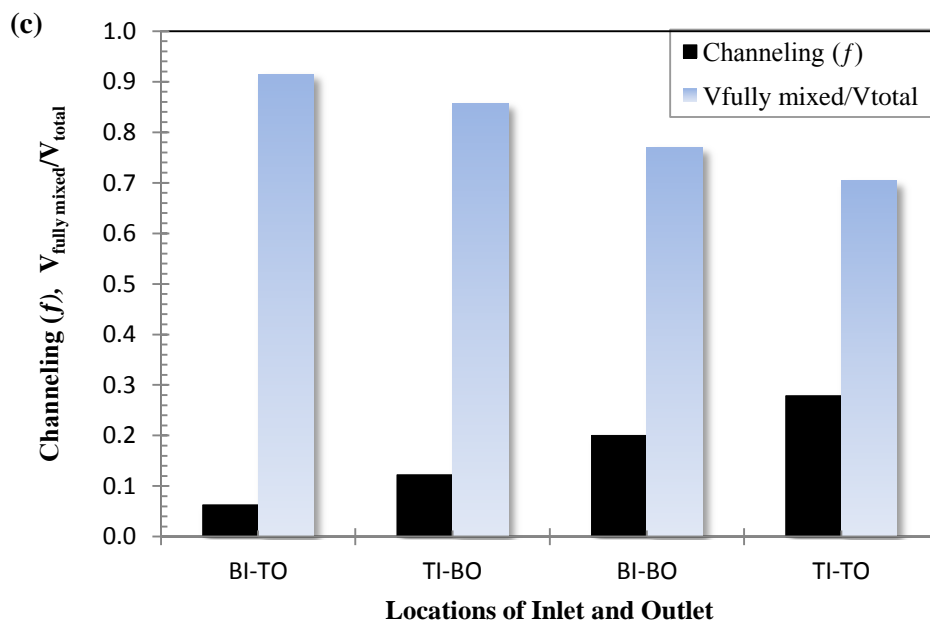
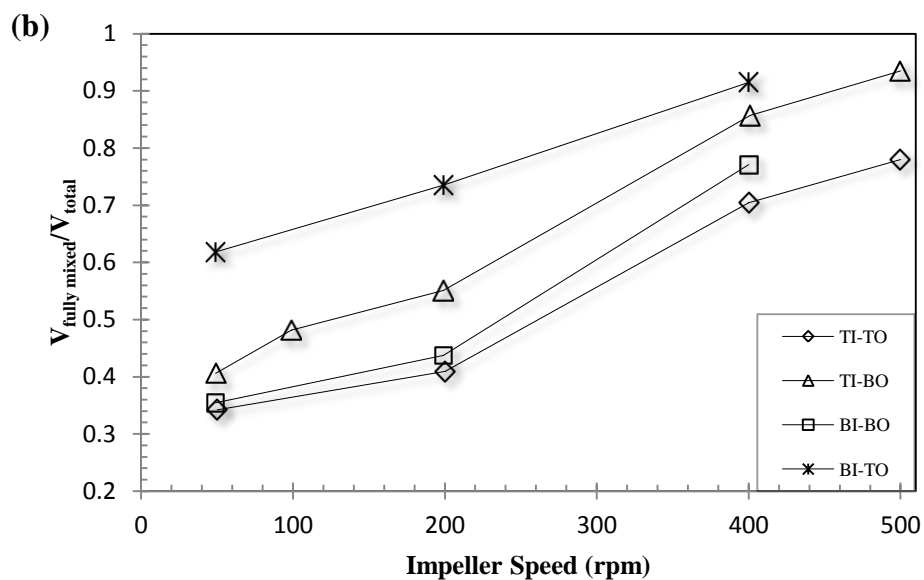
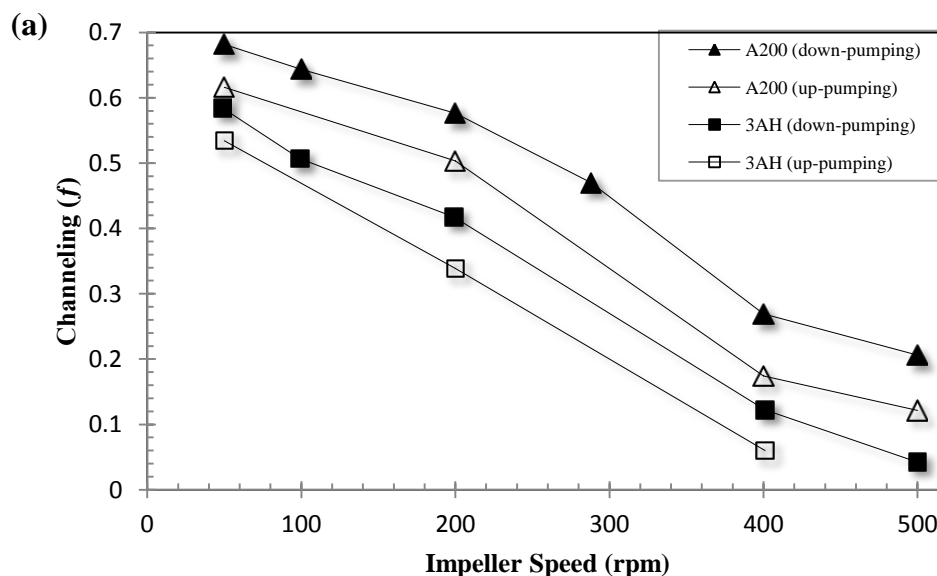


Figure (5.1-6). Effects of inlet and outlet locations on the extents of (a) channeling, (b) fully mixed volume, and (c) channeling and fully mixed volume for each configuration at 400 rpm (3AH, $Q = 9.65 \text{ L min}^{-1}$, 1.0% xanthan gum, $D = T/2.1$, $C = H/2.7$, $H = T/0.93$, $V_j = 0.317 \text{ m s}^{-1}$, residence time = 292 s).

5.1.2.6 Effect of Pumping Directions of an Axial-Flow Impeller

For an axial-flow impeller, the impeller rotational direction or the impeller pumping direction (either up-pumping or down-pumping) also has a momentous effect on the dynamic performance of continuous-flow mixing when the outlet is located at the bottom of the tank. The up-pumping impeller avoids creating a vortex, which can cause air entrainment and mechanical vibration. The effect of pumping directions for the A200 and 3AH impellers on the extent of channeling and the fraction of fully mixed volume is exemplified in Figure (5.1-7a and b), respectively. Figure (5.1-7c) demonstrates the extent of channeling and the fraction of fully mixed volume for each pumping direction at 400 rpm for the A200 and 3AH impellers. The results show that the up-pumping impellers were more effective than the down-pumping impellers in terms of reducing the non-ideal flows such as channeling and dead volumes. The mixing performance in the case of the up-pumping impeller was improved because the feed stream was directly facing the up-pumping stream from the impeller discharge and provided better mixing in the upper part of the tank. Moreover, the outlet was located at the bottom of the tank; therefore, the feed stream had to pass through the intense up-flow from the impeller discharge before reaching the outlet. This feature is particularly useful for the surface feed applications. These results are identical to those reported in the literature.



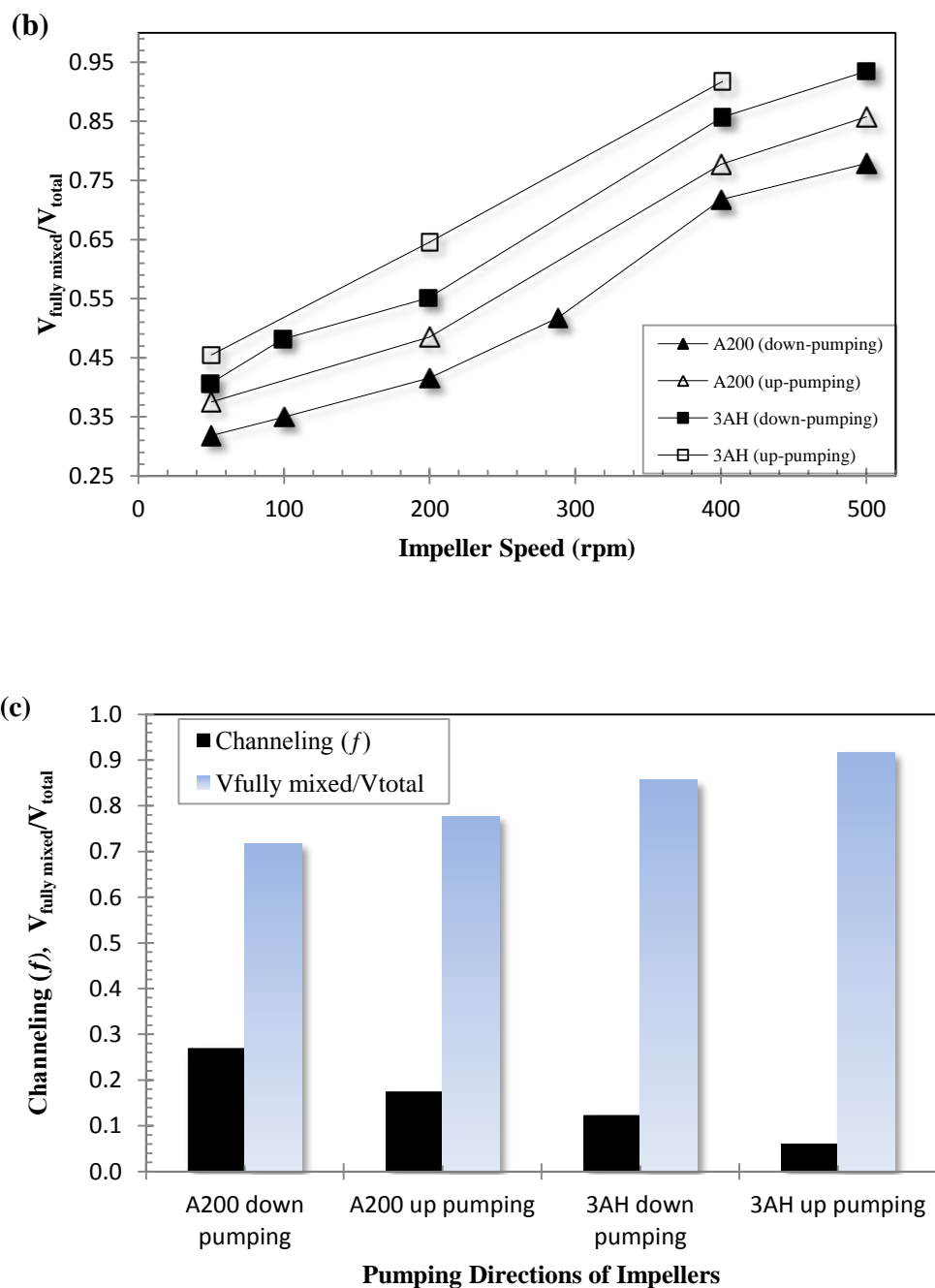


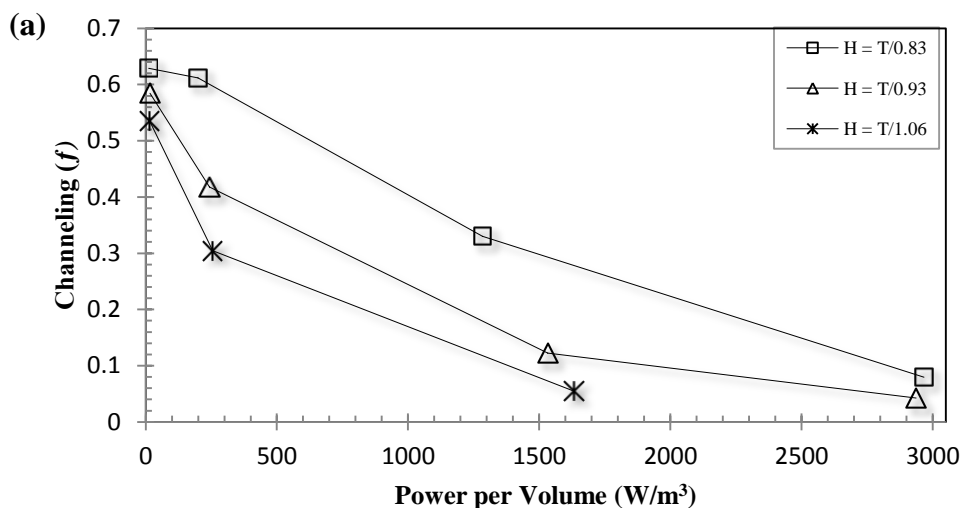
Figure (5.1-7). Effects of impeller pumping direction on the extents of (a) channeling, (b) fully mixed volume, and (c) channeling and fully mixed volume for each pumping direction for the 3AH and the A200 impellers at 400 rpm ($Q = 9.65 \text{ L min}^{-1}$, 1.0% xanthan gum, $D = T/2.1$, $C = H/2.7$, $H = T/0.93$, $V_j = 0.317 \text{ m s}^{-1}$, residence time = 292 s, input-output locations: TI–BO).

For instance, Aubin et al (2006) studied the effects of up-pumping and down-pumping (Mixel TT) impellers on the efficiency of the CSTR using a Newtonian fluid. It was reported that

channeling through a bottom outlet may be reduced in the CSTR when the impeller is employed in the up-pumping mode instead of the down-pumping mode.

5.1.2.7 Effect of Fluid Height in a Vessel

The fluid height (H) in the vessel also affects the dynamic performance of continuous-flow mixing. The actual volume to be agitated in the vessel depends on the height of the fluid, in addition to the vessel diameter (T). Three different fluid heights $H = T/0.83$, $T/0.93$, and $T/1.06$ in the mixing vessel were tested with the 3AH impeller. To maintain the constant residence time of the fluid, the inlet flow rates (Q) were changed accordingly ($Q = 8.47, 9.65$ and 10.81 L min^{-1}). Figure (5.1-8a and b) shows the effects of the fluid height on the extent of channeling and the fraction of fully mixed volume, respectively. Figure (5.1-8c) demonstrates the extent of channeling and the fraction of fully mixed volume as a function of H/T for the 3AH impeller at a constant power input and residence time. The results show that as the fluid height in the vessel was increased, the extent of channeling and dead volume also increased and the fraction of fully mixed volume decreased. This is due to poor mixing above the impeller when the height of the fluid increases while the impeller clearance is constant. However, choosing an optimum ratio of the fluid height (H) to the tank diameter (H/T) is important because the low fluid height in the vessel reduces the production capacity, while an increase in the fluid height increases non-ideal flows.



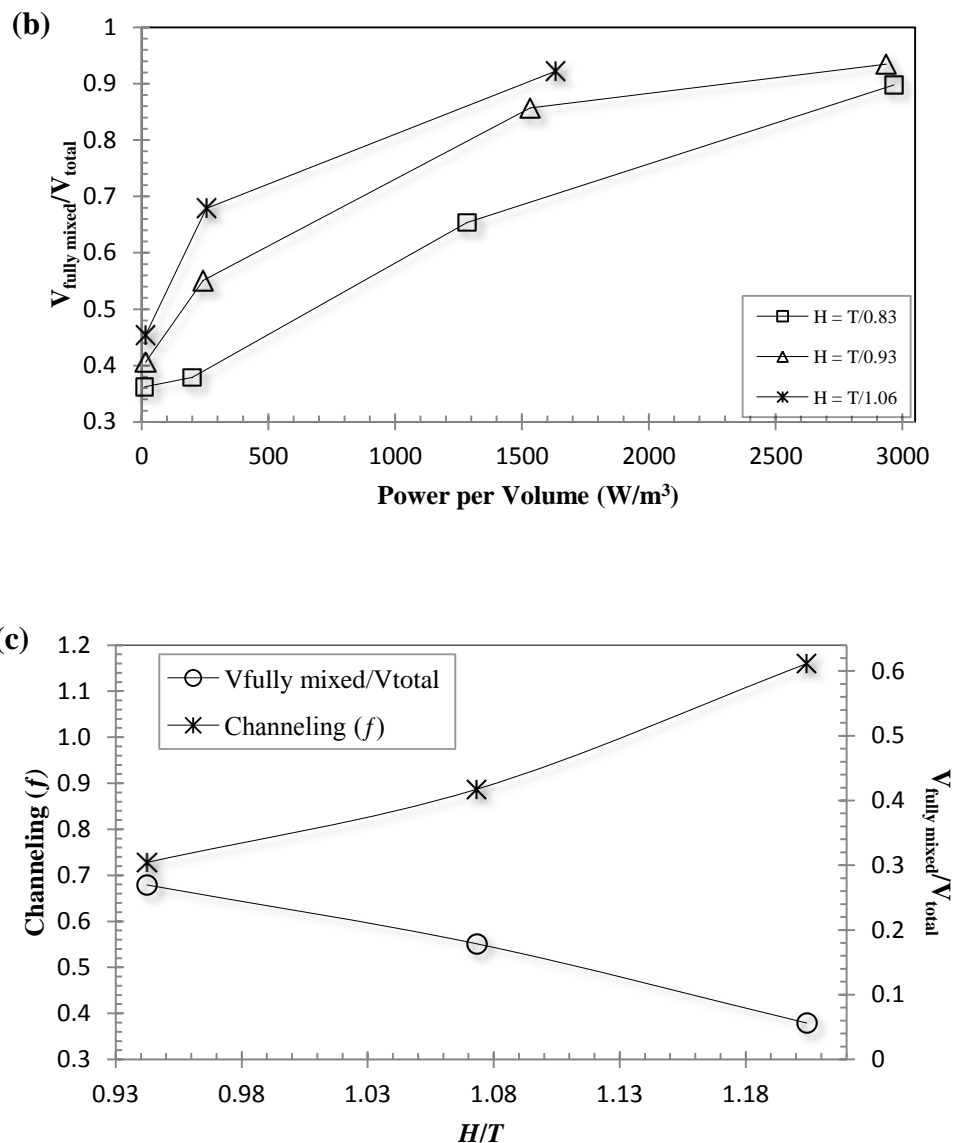
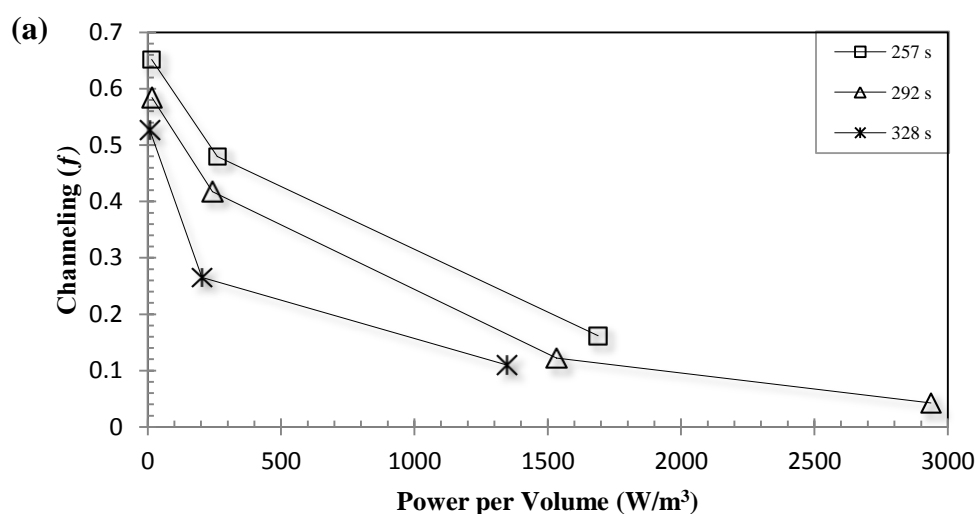


Figure (5.1-8). Effects of fluid height (H) in the mixing vessel on the extents of (a) channeling and (b) fully mixed volume, and (c) channeling and fully mixed volume as a function of H/T at power 224 W m^{-3} (constant residence time = 292 s but different fluid flow rate $Q = 3.20, 9.65,$ and 14.17 L min^{-1} , 3AH, 1.0% xanthan gum, $D = T/2.1$, $C = H/2.7$, $V_j = 0.317 \text{ m s}^{-1}$, input-output locations: TI-BO).

Generally, for any single impeller the aspect ratio fluid height/vessel diameter (H/T) of about 1 is selected and the multiple impellers may be recommended if the aspect ratio is much higher than 1 (Paul *et al.*, 2004).

5.1.2.8 Effect of Residence Time

The residence time also has a significant effect on the dynamic performance of continuous-flow mixing. The total time spent by a molecule within the boundary of the reactor (time taken by a molecule to reach the outlet from the inlet) is known as the residence time, which is calculated from the ratio of fluid volume (V) in the vessel and the feed flow rate (Q). The residence time could be adjusted by changing either the feed flow rate or the fluid volume. In this study three different residence times (257, 292, and 328 s) were tested by changing the fluid height ($H = 36, 41, \text{ and } 46\text{cm}$) at constant feed flow rate ($Q = 9.65 \text{ L min}^{-1}$). The effect of residence time with the 3AH impeller on the extent of channeling and the fraction of fully mixed volume is exemplified in Figure (5.1-9a and b), respectively. Figure (5.1-9c) presents the channeling and fully mixed volume as a function of the residence time at constant power. As expected, it can be seen from the data that as the residence time of the fluid in the vessel increased, the extent of the channeling and dead volume decreased, while the fraction of fully mixed volume increased. As the residence time was increased, the fluid had more time to stay within the mixing vessel and had more chances to interact with the intense mixing zone around the impeller. As a result, a higher residence time would lead to more fully mixed volume in the mixing vessel [Figure (5.1-9b)]. As shown in Figure (5.1-9c), a higher residence time is able to reduce non-ideal flows in continuous-flow mixing vessels.



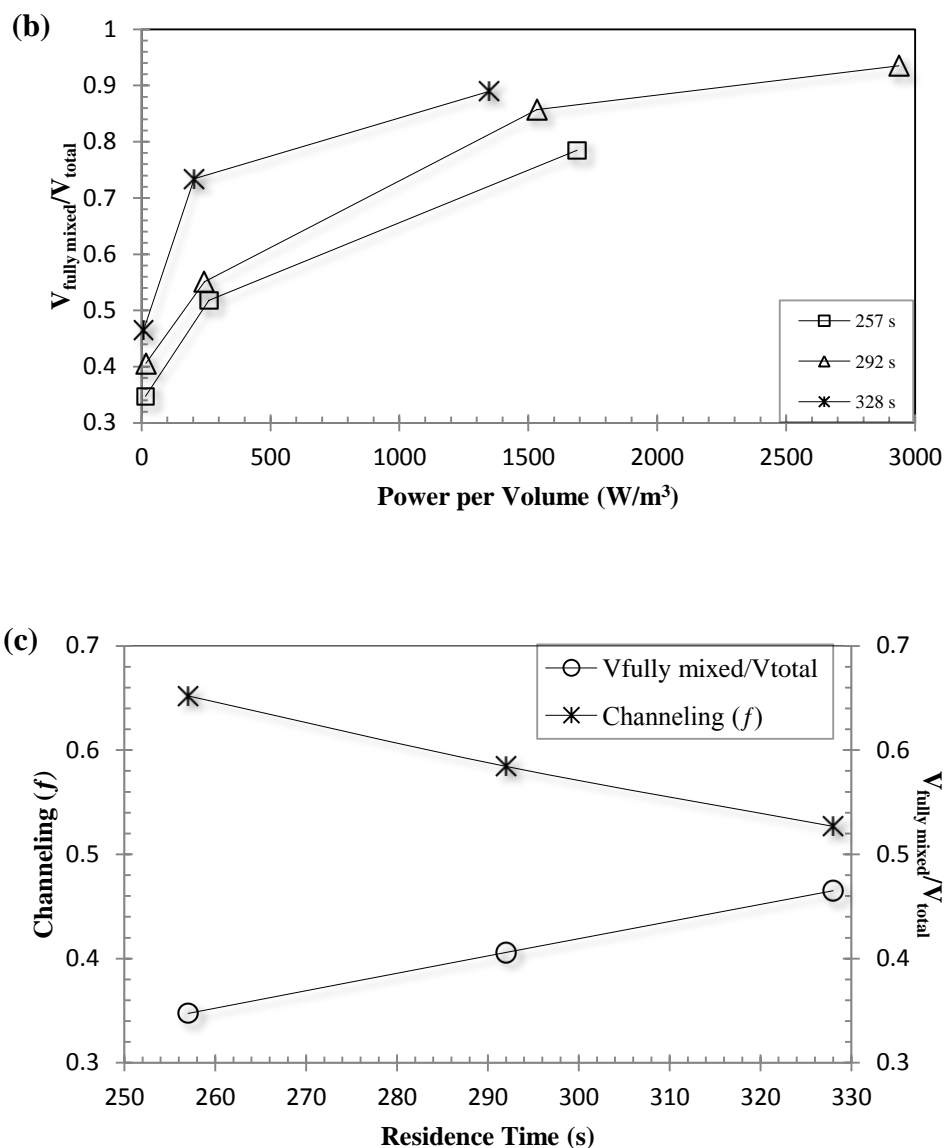


Figure (5.1-9). Effects of fluid residence time in the mixing vessel on the extents of (a) channeling and (b) fully mixed volume, and (c) channeling and fully mixed volume as a function of the residence time at power 16 W m^{-3} (at constant fluid flow rate (Q) = 9.65 L min^{-1} but different fluid height (H) = 36, 41, and 46cm, 3AH, 1.0% xanthan gum, $D = T/2.1$, $C = H/2.7$, $V_j = 0.317 \text{ m s}^{-1}$, input-output locations: TI-BO).

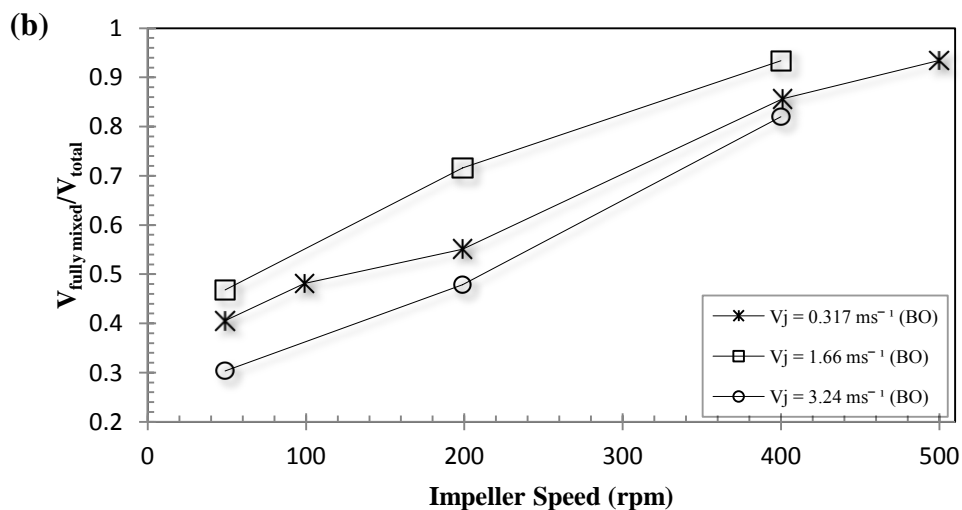
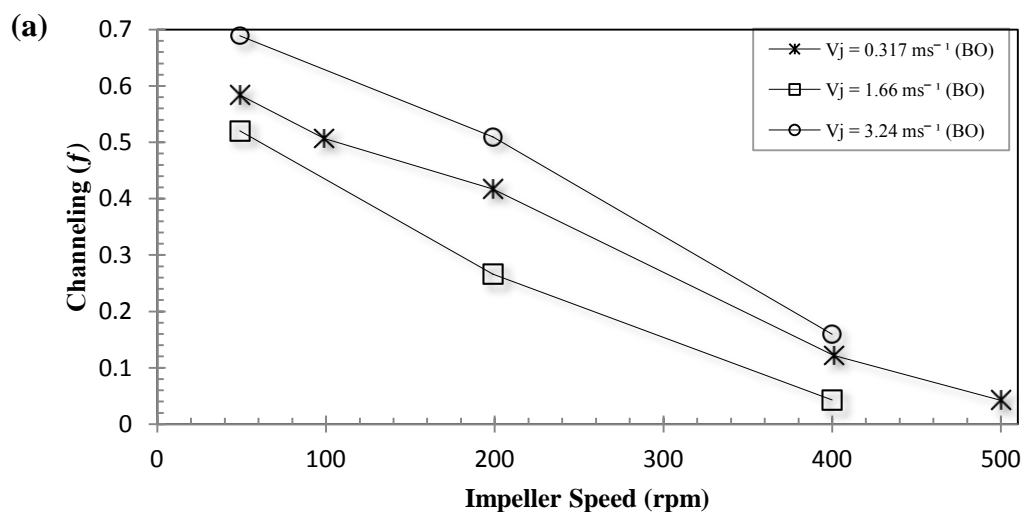
5.1.2.9 Effect of Jet Velocity

The mixing of fluids necessitates mechanical energy, which is applied through the impeller rotation to achieve a desired process result. An alternative method for getting mechanical energy into the fluid is to use a pump to generate a high velocity jet of fluid in the vessel at the

same flow rate by reducing the inlet diameter (Paul et al., 2004). The jet velocity (V_j), one of the effective parameters, can influence the efficiency of a continuous-flow mixing system. This study involves three different jet velocities ($V_j = 0.317, 1.66, \text{ and } 3.24 \text{ m s}^{-1}$) to see their effects on the dynamic performance of the continuous-flow mixing. The normal configuration TI-BO was used where the outlet was located at the bottom of the tank. The data in Figure (5.1-10a and b) represents the effects of the jet velocity on the extent of channeling and the fraction of fully mixed volume, respectively, while Figure (5.1-10c) shows the channeling and the fraction of fully mixed volume as a function of the jet velocity for the 3AH impeller at 400 rpm. The results show that, for the same operating conditions, as the jet velocity (V_j) was increased from 0.317 to 1.66 m s^{-1} , the channeling decreased and the fully mixed volume increased. When the inlet stream is fed into the tank at high velocity, it is expected that the surrounding bulk fluid is entrained into the feed zone, thus improving the mixing. Furthermore, the high jet velocity will transport the feed promptly to the impeller region where it is exposed to high turbulence and get better mixed. However, a further increase in the jet velocity from 1.66 to 3.24 m s^{-1} had an adverse effect on the mixing performance where the channeling increased and the fully mixed volume decreased. The potential problem related to a high jet velocity is that the jet can very easily pass through the impeller swept volume and reach to the outlet, which is located at the bottom of the tank whereby it bypasses the impeller turbulent zone. Thus, the channeling increases and the fully mixed volume decreases at very high jet velocity. There is a possibility of overcoming this potential problem involved with high jet velocity either by increasing the sufficient impeller speed to break the jet path or by relocating the outlet. However, higher impeller speed creates a deep vortex, which leads to surface aeration. Hence, further investigation was done by relocating the outlet using configuration TI-TO for the same operating conditions.

For the new configuration TI-TO, the results are depicted in Figure (5.1-11a and b), which represents the effects of the jet velocity on the extent of channeling and the fraction of fully mixed volume, respectively. Now, it is clear that as the jet velocity was increased from 0.317 to 3.24 m s^{-1} , the extent of channeling and dead volume decreased and the fraction of fully mixed volume increased. Still, the feed with a high jet velocity passed through the impeller swept volume and reached to the bottom of the tank where there was no outlet, which

reduced the extent of the channeling. Moreover, the feed that bypassed the impeller zone and directly reached the bottom of the tank had to face the intense discharge from the impeller before leaving the tank from the top side outlet and thus, the mixing in the tank was improved. For the purpose of comparison, Figure (5.1-12) represents the channeling as a function of the jet velocity for two different configurations (TI-BO and TI-TO) at 200 rpm impeller speed. It shows that even at a high jet velocity, the configuration TI-TO was able to reduce the channeling drastically compared to the configuration TI-BO.



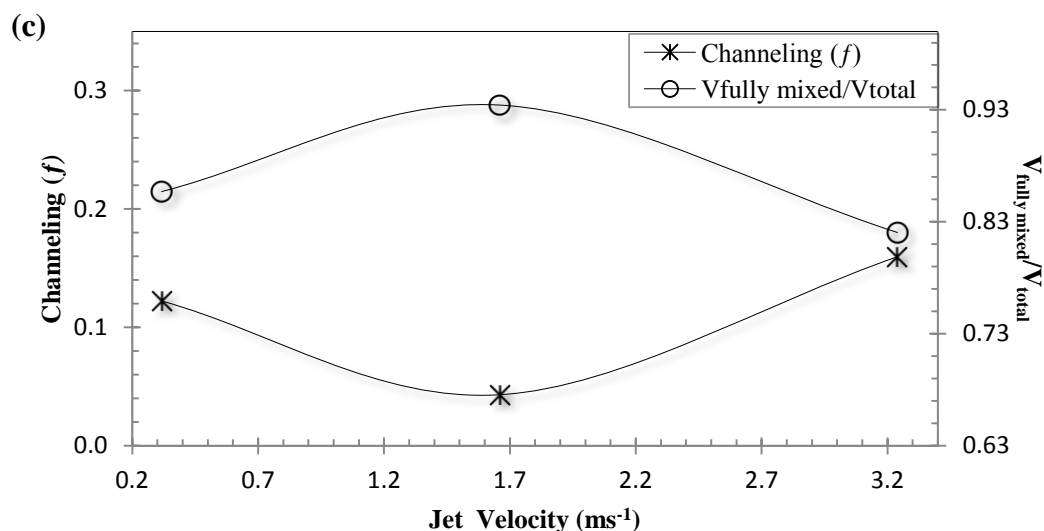
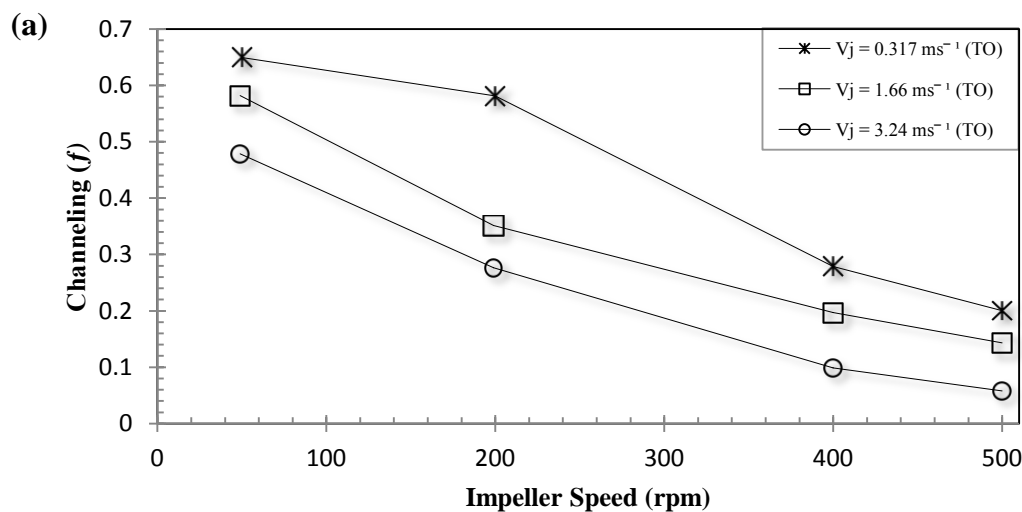


Figure (5.1-10). Effects of inlet jet velocity on the extents of (a) channeling and (b) fully mixed volume, and (c) channeling and fully mixed volume as a function of the jet velocity at 400rpm (3AH, $Q = 9.65 \text{ L min}^{-1}$, 1.0% xanthan gum, $D = T/2.1$, $C = H/2.7$, $H = T/0.93$, residence time = 292 s, input-output locations: TI-BO).



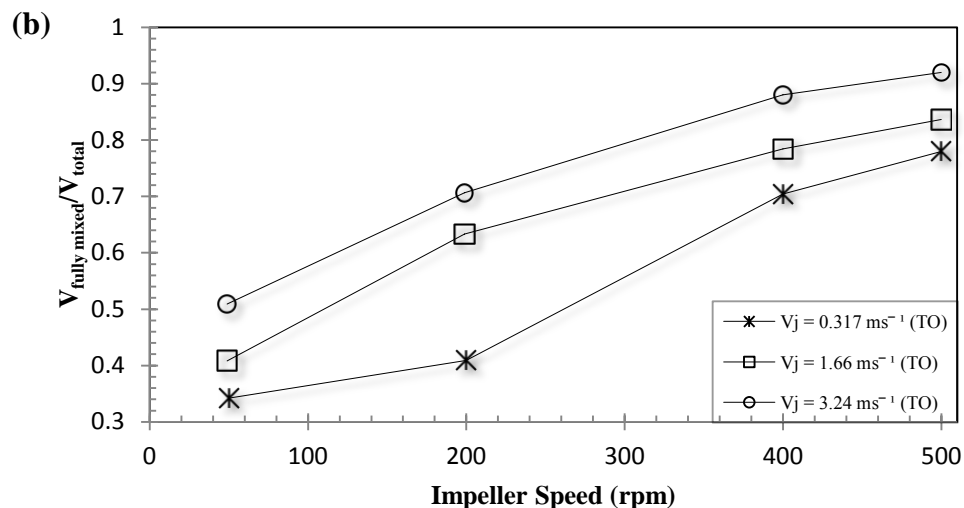


Figure (5.1-11). Effects of the inlet jet velocity on the extents of (a) channeling and (b) fully mixed volume (3AH, $Q = 9.65 \text{ L min}^{-1}$, 1.0% xanthan gum, $D = T/2.1$, $C = H/2.7$, $H = T/0.93$, residence time = 292 s, input-output locations: TI–TO).

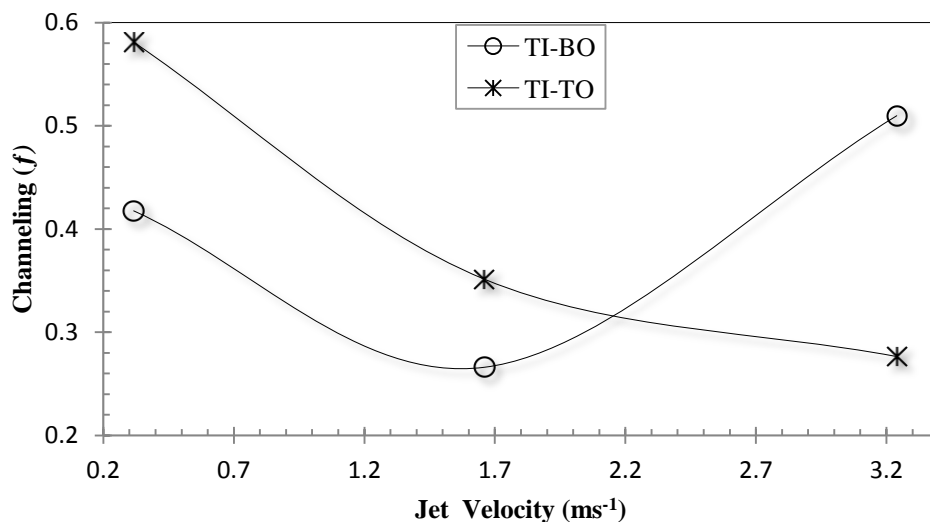


Figure (5.1-12). Effects of inlet jet velocity on the extents of channeling for different output locations (200 rpm, 3AH, $Q = 9.65 \text{ L min}^{-1}$, 1.0% xanthan gum, $D = T/2.1$, $C = H/2.7$, $H = T/0.93$, residence time = 292 s).

5.1.3 Conclusions

The efficiency of the continuous-flow mixing of non-Newtonian fluids with yield stress in reducing non-ideal flows and increasing the fully mixed volume was successfully measured through dynamic tests. The results and importance of each studied factor are concluded as below:

- **Impeller types:** The selection of the most effective impeller among the various choices is the most critical factor. This study showed that the A320 impeller was the most effective impeller among the seven axial-flow impellers and the Scaba impeller was the most effective among the four radial-flow impellers for reducing the non-ideal flows in the continuous-flow mixing system. Depending on the commercial price of impellers, the process requirements, and physical properties of fluids, either an impeller producing high pumping and low shear such as A320 impeller or a low pumping and high shear impeller such as the Scaba impeller should be chosen.
- **Impeller diameter:** The tests on the effect of the impeller diameters ($D = T/1.6, T/2.1, T/2.5$ and $T/3.2$) for A200 impellers revealed that the channeling decreased and the fully mixed volume increased with an increase in impeller diameter. Thus a larger diameter impeller makes the continuous-flow mixer more efficient.
- **Impeller off-bottom clearance:** The mixing quality was improved when the clearance of the impeller was increased from $H/3.4$ to $H/2.1$. Further increase in the clearance of the impeller ($H/1.7$) had an adverse effect on the mixing quality. Therefore, the optimum value of the impeller off-bottom clearance should be chosen to improve the mixing quality.
- **Direction of an axial-flow impeller:** Dynamic tests made with the A200 and 3AH impellers showed that the up-pumping impellers were more effective than the down-pumping impellers for reducing non-ideal flows. Hence the mixing quality in the continuous-flow mixer can be improved using the up-pumping impeller.
- **Fluid height in the vessel:** The three different fluid heights $H = T/0.83, T/0.93,$ and $T/1.06$ in the mixing vessel were tested with the 3AH impeller at constant residence time. It was observed that as the fluid height in the vessel was increased, the extent of non-ideal flows also increased. Consequently, increasing the fluid height in the vessel at constant residence time cannot improve the mixing quality.

- **Residence time:** Three different residence times (257, 292, and 328 s) by changing the fluid height ($H= 36, 41, \text{ and } 46\text{cm}$) at constant feed flow rate ($Q = 9.65 \text{ L min}^{-1}$) were also tested to see their effects on non-ideal flows. As the residence time of the fluid in the vessel was increased, the mixing quality was improved.
- **Jet velocity:** The effect of the jet velocity ($V_j = 0.317, 1.66, \text{ and } 3.24 \text{ m s}^{-1}$) on the dynamic performance of the continuous-flow mixing system was also investigated for two configurations TI–BO and TI–TO. The results showed that for the same operating conditions, as the jet velocity (V_j) was increased from 0.317 to 1.66 m s^{-1} , the mixing quality was improved for both configurations. Further increase in the jet velocity from 1.66 to 3.24 m s^{-1} had an adverse effect on the mixing quality for the TI–BO configuration, however, this potential problem was overcome by relocating the outlet using TI–TO configuration. Increasing the jet velocity does not always mean improving the mixing quality in the continuous-flow mixer; however, the location of the outlet also plays an important role.
- **Location of inlet and outlet:** The extensive study on the locations of inlet and outlet showed that the configuration BI–TO (**bottom inlet-top outlet**) was the most effective while the configurations TI–TO (**top inlet-top outlet**) and BI–BO(**bottom inlet- bottom outlet**) enabled a large percentage of feed to be conveyed directly to the outlet without being drawn into the mixing zone.
- **Impeller speed:** The results also showed that the channeling decreased and the fully mixed volume increased with an increase in impeller speed.

Applying the findings of this study will reduce the effects of non-ideal flows and improve the variability reduction in the continuous-flow mixing of non-Newtonian fluids.

5.2 Effect of Impeller Type on Continuous-Flow Mixing of Non-Newtonian Fluids in Stirred Vessels through Dynamic Tests (Patel et al., 2012b)

5.2.1 Introduction

Mixing of non-Newtonian fluids with axial and radial flow impellers is prone to a significant extent of non-ideal flows (e.g. dead zones and channeling) within the stirred reactors. To enhance the performance of the continuous-flow mixing of pseudoplastic fluids with yield stress, the close-clearance impellers such as helical ribbon and anchor impellers are utilized (Peters and Smith, 1969; Ohta et al., 1985; Prajapati and Ein-Mozaffari, 2009; Iranshahi et al., 2006; Shervin et al., 1991; Ihejirika and Ein-Mozaffari, 2007; Takahashi et al., 1988); however, these studies are confined to batch mixing.

No information is available regarding the efficiency of double helical ribbon impeller in reducing the extent of non-ideal flows in the continuous-flow mixing of yield-pseudoplastic fluids. Therefore, the objectives of this study were to explore the effects of various parameters such as the type of close-clearance impeller (i.e. the double helical ribbon (DHR) and anchor impellers), impeller speed (25–500 rpm), impeller pumping direction, fluid rheology (0.5–1.5% xanthan gum solution), fluid flow rate (3.20–14.17 L min⁻¹), and the locations of outlet (configurations: top inlet–top outlet, top inlet–bottom outlet) on the dynamic performance of the mixing vessel. The performance of the DHR impeller was then compared to the performance of various types of impellers such as axial-flow (Lightnin A320), and radial-flow (Scaba 6SRGT) impellers.

In this study, to perform the dynamic tests the continuous-flow mixing system shown in Figure (3.1-1) was used. The geometrical details of the DHR and anchor impellers are provided in Table (3.1-1). The dynamic model [Equation (2.4–7)] was used to quantify the extent of non-ideal flows such as channelling, recirculation, and dead volume in the mixing vessel. To estimate the dynamic model parameters, the system was excited using a frequency-modulated random binary input by injecting the saline solution. The extents of channelling (f) and the fully

mixed volume ($V_{fully\ mixed}$) were determined. To describe the rheological behaviour of the xanthan gum solutions the Herschel-Bulkley model [Equation (2.1–9)] was used.

5.2.2 Results and Discussion

The power number (P_o) for close-clearance impellers (the double helical ribbon and anchor impellers) was calculated using Equation (2.1–3). The Reynolds number (Re) was calculated using Equation (2.1–11). Figure (3.4-1) represents the power curve for the DHR and anchor impellers. The trend in the power number curve is similar to those general trends reported by several researchers (Paul et al., 2004; Kelly and Gigas, 2003; Holland and Chapman, 1966; Nagata, 1975).

5.2.2.1 Effect of Power Input

The power input significantly affects the dynamic performance of the continuous-flow mixing system. Characteristically, more power represents more intense mixing, which means that increasing the power input with an increase in the impeller speed reduces the degree of the non-ideal flows in the continuous-flow mixing systems. Figure (5.2-1a and b) shows the extent of channeling and the fraction of fully mixed volume as a function of power consumption per unit volume for all impellers utilized in this study, respectively. These results show that the channeling decreased and the fully mixed volume increased with an increase in the power input. At lower impeller speed the stagnant zones were observed visually on the surface of the vessel. The shear stress produced by the impeller was less than the yield stress of the fluid in the stagnant zones. However, at higher impeller speed the xanthan gum solution was swept away from the impeller, leading to improved mixing by overcoming the yield stress of the fluid in the stagnant zones. The optimum power input should be chosen in such a way that the channeling approaches zero and the fully mixed volume approaches the total volume of the fluid within the mixing tank, as further increases in impeller speed may lead to more power consumption for the same extent of the fully mixed volume.

5.2.2.2 Effect of Type of Impellers

The impeller type, one of the influencing geometrical parameters, affects the dynamic performance of the continuous-flow mixing systems. Literally, various impellers are presently available in the market for different mixing applications. The selection of the most effective impeller is one of the most crucial factors. Hence, this study involved various types of impeller (close-clearance impellers: double helical ribbon (DHR) and anchor; axial-flow impeller: Lightnin A320; and radial-flow impeller: Scaba 6SRGT) to investigate their performances on the continuous-flow mixing of the non-Newtonian fluids. Figure (5.2-1a and b) represents the efficiency of each impeller in terms of the extent of channeling and the fraction of fully mixed volume, respectively. Initially, when comparing the performances of only close clearance impellers, the results indicate that the DHR impeller is more effective than the anchor impeller in reducing the effect of non-ideal flows. The anchor impeller primarily generates tangential flow and induces a less vertical fluid motion and thus, it is generally ineffective unless it is used in combination with another impeller such as radial-flow impellers (Chhabra and Richardson, 2008). Iranshahi et al. (2006) studied the mixing characteristics of the Ekato Paravis, DHR, and anchor impellers in a batch vessel using CFD. The analysis of the flow pattern and mixing parameters showed that the DHR impeller was the most efficient impeller among the three impellers used in their study. This phenomenon supports the findings of our study. The ability of the DHR impeller to keep the entire vessel contents circulating and the strong uniform flow pattern generated by this impeller resulted in improving the efficiency of the continuous-flow mixing system. Further, to find the most effective impeller among all three types of impellers, we compared the efficiency of the most effective close clearance impeller (i.e. the DHR impeller) with the efficiencies of the axial-flow and radial-flow impellers. The results depicted in Figure (5.2-1) show that the DHR impeller was the most efficient impeller among the three types of impellers to eliminate the non-ideal flows with lower power consumption. Furthermore, when the channeling approached zero and the fully mixed volume approached the total volume of the fluid in the vessel, the power drawn by the A320 impellers and the Scaba impeller were approximately 2.8 and 4.2 times greater than that of the DHR impeller, respectively. Hence, the DHR impeller is recommended for the continuous-flow mixing of viscous fluids.

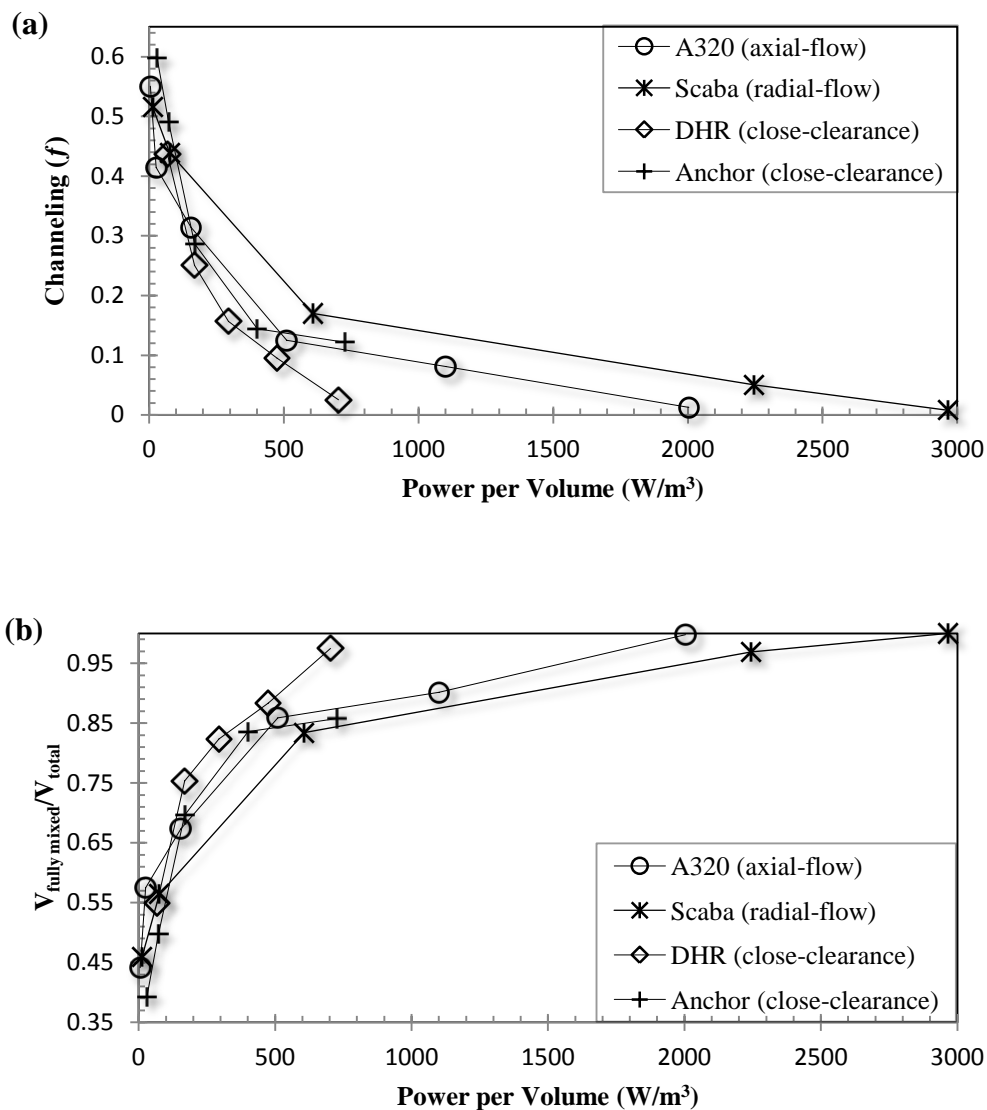


Figure (5.2-1). Effects of impeller speed and impeller types on the extents of (a) channeling and (b) fully mixed volume ($Q = 9.65 \text{ L min}^{-1}$, 1.0% xanthan gum, input-output locations: TI-BO)

5.2.2.3 Effect of Pumping Direction of the DHR Impeller

The impeller pumping direction (up-pumping and down-pumping) has an effect on the dynamic performance of the continuous-flow mixers. Figure (5.2-2) illustrates the effects of the pumping directions for the DHR impeller on the extent of channeling and the fraction of fully mixed volume.

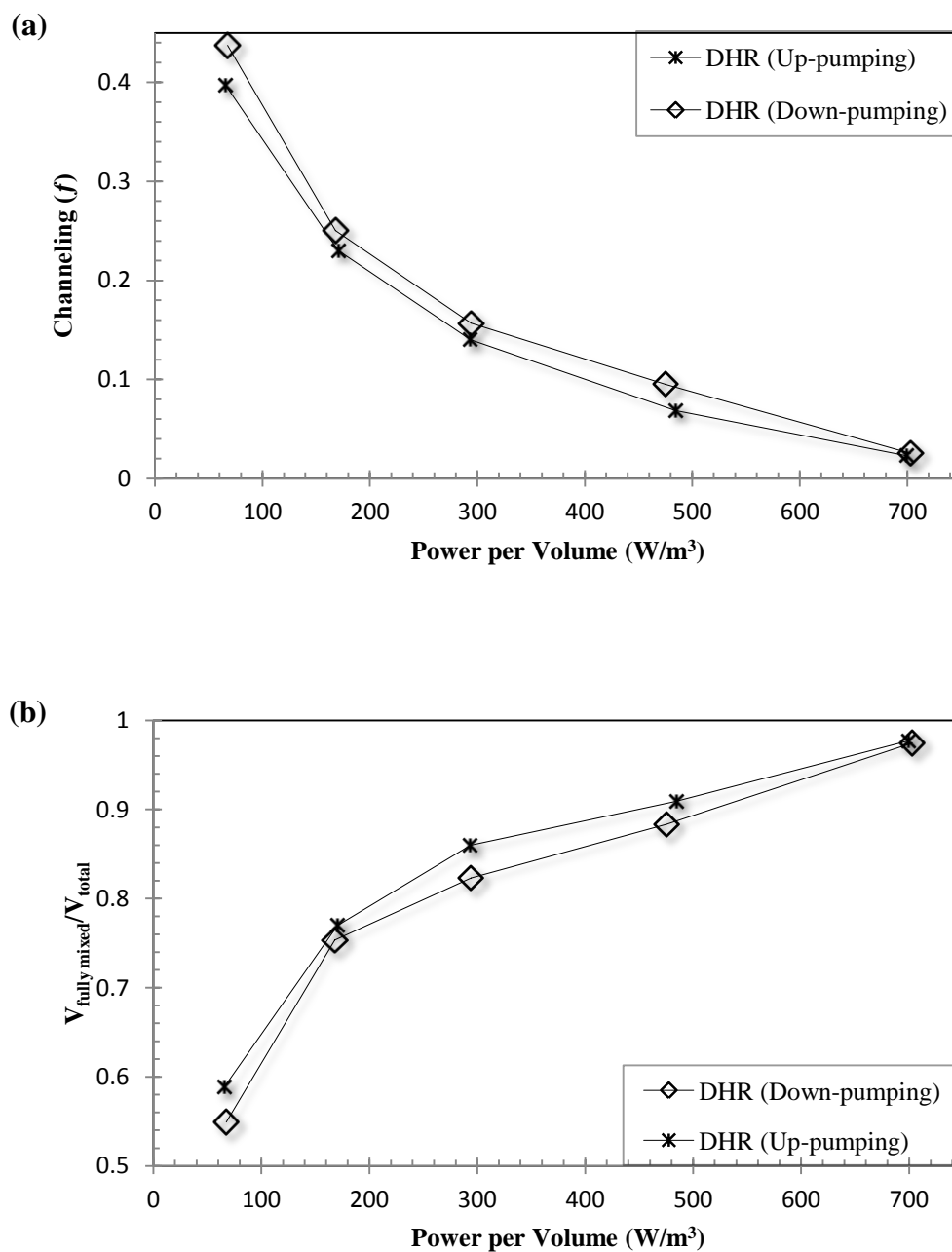


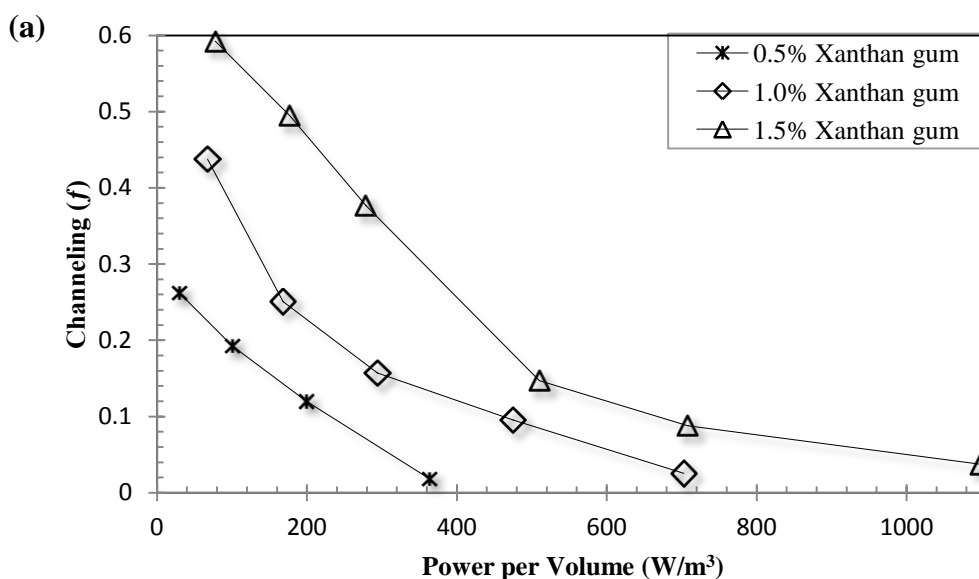
Figure (5.2-2). Effects of impeller pumping direction on the extents of (a) channeling and (b) fully mixed volume ($Q = 9.65 \text{ L min}^{-1}$, 1.0% xanthan gum, input-output locations: TI–BO).

The results show that the impeller with the up-pumping mode was more effective than the down-pumping mode in terms of reducing the non-ideal flows. The mixing performance in the case of the up-pumping mode impeller was improved because the feed stream was directly

facing the up-pumping stream from the impeller discharge and provided better mixing in the upper part of the tank. Moreover, the outlet was located at the bottom of the tank; therefore, the feed stream had to pass through the intense up-flow stream generated by the impeller before reaching the outlet. This feature is particularly useful for the surface feed applications. It must be mentioned that the effect of the pumping direction on the mixing quality achieved by the DHR impeller is not as sensitive as that of the axial-flow impeller. Similarly, Ihejirika and Ein-Mozaffari (2007) also found that the upward pumping mode was superior to the downward pumping mode for the mixing of pseudoplastic fluids with the helical ribbon impeller in a batch mixing vessel.

5.2.2.4 Effect of Fluid Rheology

The dynamic performance of the continuous-flow mixing is also affected by the fluid rheology. Therefore, this study explores the effect of xanthan gum concentration (0.5, 1.0, and 1.5%) on the extent of non-ideal flows. The effect of xanthan gum concentration on the extent of channeling and the fraction of fully mixed volume is exemplified in Figure (5.2-3). The results demonstrate that the extent of the channeling increased and the fraction of fully mixed volume decreased as xanthan gum concentration increased from 0.5 to 1.5% at a fixed power input.



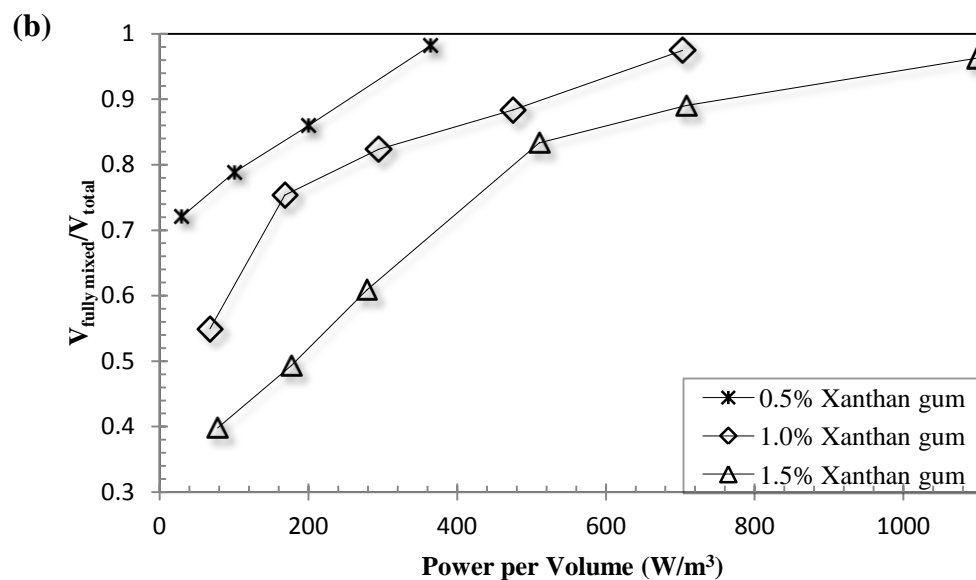


Figure (5.2-3). Effects of fluid rheology on the extents of (a) channeling and (b) fully mixed volume (DHR, $Q = 9.65 \text{ L min}^{-1}$, input-output locations: TI-BO).

These results also revealed that when the channeling approached zero and the fully mixed volume approached the total volume of the fluid in the vessel, the power consumed by an impeller at 1.5% concentration was about three times greater than that at 0.5% concentration. The solution yield stress increases with an increase in xanthan gum solution concentration. At higher yield stress the energy dissipation became faster, which resulted in an increase in the extent of non-ideal flows (Ein-Mozaffari et al., 2005). Moreover, the fluctuating velocities will weaken quickly in the area outside of the impeller zone due to a high fluid apparent viscosity, which is a function of the yield stress; although flows near the impeller might be turbulent. Such a phenomenon was also observed by Saeed et al. (2008).

5.2.2.5 Effect of Feed Flow Rate

The effects of three different feed flow rates (3.20, 9.65, and 14.17 L min^{-1}) on the extent of channeling and fully mixed volume are depicted in Figure (5.2-4a and b), respectively. These results show that the extent of the channeling increased and the fraction of fully mixed volume decreased as the fluid flow rate through the mixing vessel was increased. In fact, increasing the

feed flow rate through the mixing vessel decreases the mean residence time in the vessel, which induces the fluid to exit the vessel faster.

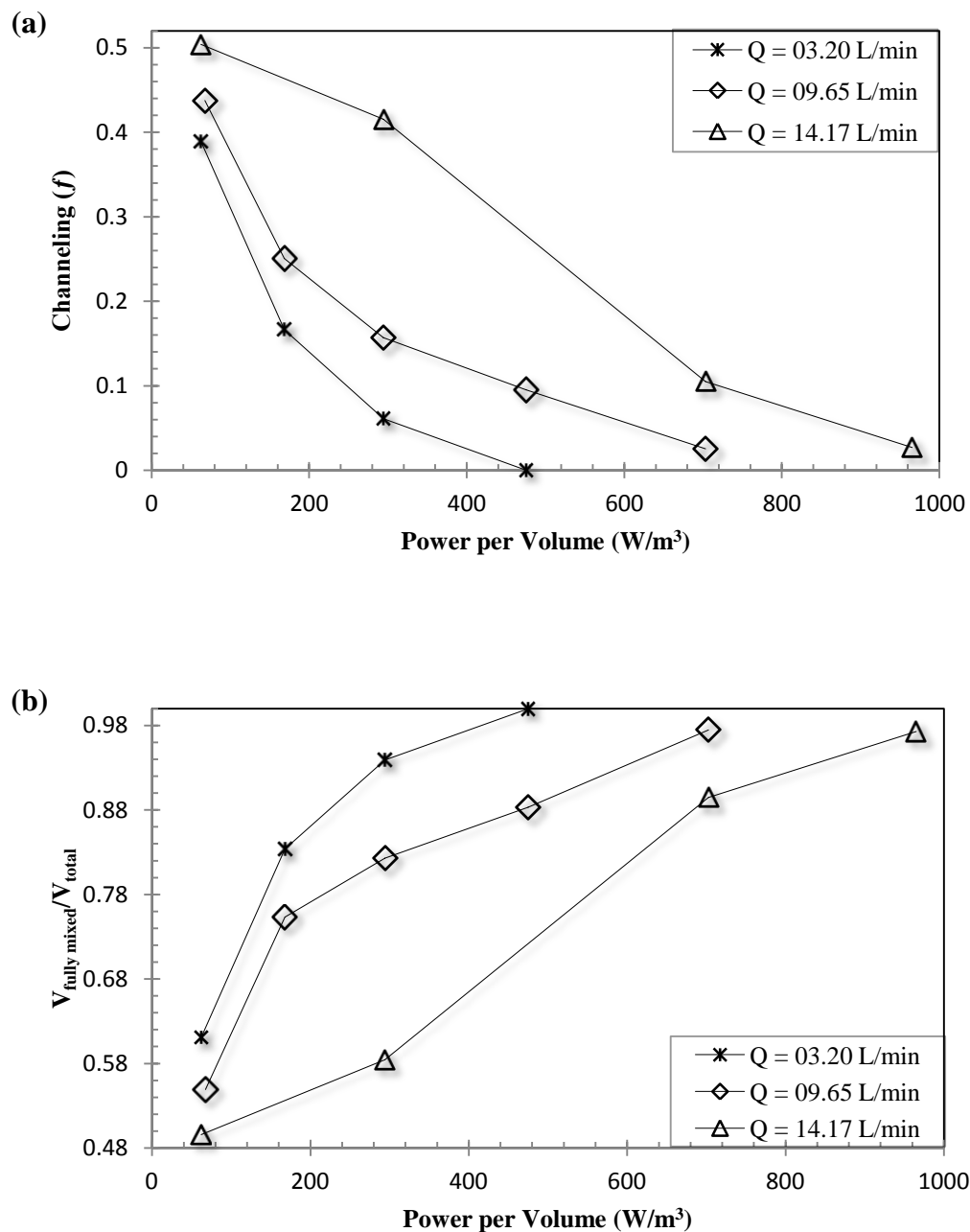
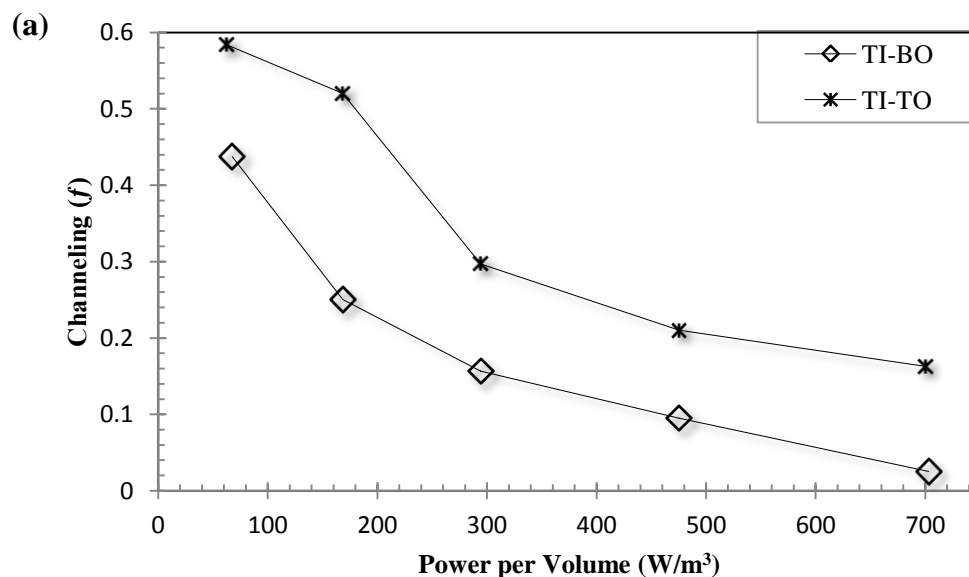


Figure (5.2-4). Effects of fluid flow rate through mixing vessel on the extents of (a) channeling and (b) fully mixed volume (DHR, 1.0% xanthan gum, input-output locations: TI-BO).

On other side, decreasing the fluid flow rate increases the mean residence time in the vessel, so the fluid gets more time with the intense motion created by the impeller within the tank; which ultimately improves the mixing quality in the vessel. Hence, for the similar operating conditions, the system was more susceptible to channeling at the lower mean residence time than the higher one. Similar results were also observed by other researchers (Saeed et al., 2008).

5.2.2.6 Effect of Input Locations

The mixing quality in the continuous-flow mixing system also largely depends on the inlet and outlet locations of the mixing vessel (Ein-Mozaffari et al., 2005). Hence, the effects of two different configurations; (1) TI-BO (top inlet-bottom outlet) and (2) TI-TO (top inlet-top outlet) on the extent of non-ideal flows were investigated in this study. The effects of the inlet and outlet locations on the extent of channeling and the fraction of fully mixed volume are depicted in Figure (5.2-5). The results demonstrate that for a given identical operating condition, the system was more liable to a high degree of channeling and dead volume for the TI-TO configuration than the TI-BO configuration. The identical phenomenon was also reported in the continuous-flow mixing of the non-Newtonian fluids with an axial-flow impeller (Saeed and Ein-Mozaffari, 2008).



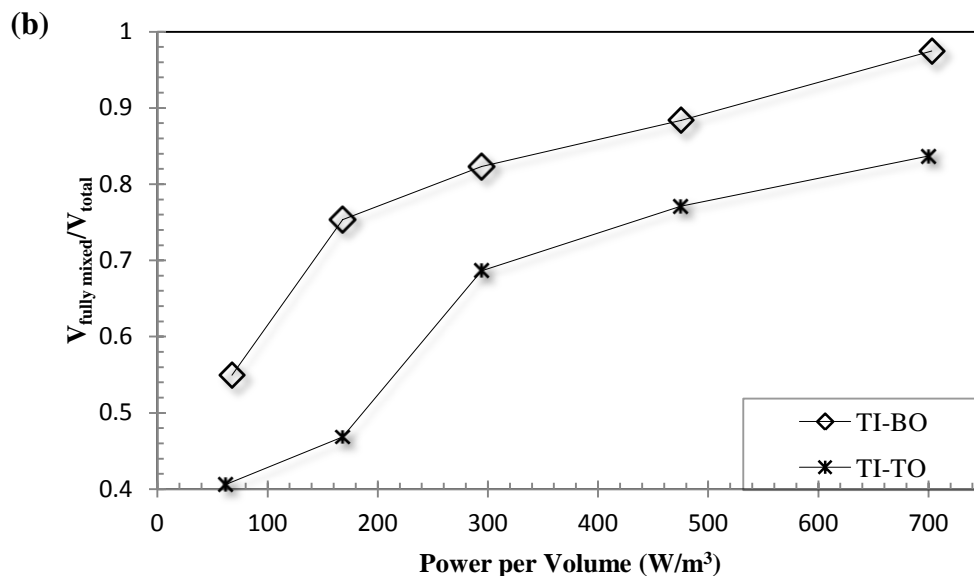


Figure (5.2-5). Effects of the locations of inlet and outlet on the extents of (a) channeling and (b) fully mixed volume (DHR, $Q = 9.65 \text{ L min}^{-1}$, 1.0% xanthan gum).

TI-TO configuration enabled a portion of the feed to be short-circuited directly to the outlet without passing through the intense mixing zone or impeller zone. However, in the case of the TI-BO configuration, the feed had to pass through the impeller zone before leaving the vessel, which eventually led to enhancement of the mixing quality. Thus, the locations of the inlet and outlet should be specified in such a way that a line sketched from the inlet to the outlet passes through the impeller or the intense mixing zone (Paul et al., 2004).

5.2.3 Conclusions

To determine the magnitude of non-ideal flows such as channeling and dead volume, dynamic tests were conducted on the continuous-flow mixing of non-Newtonian fluids possessing yield stress in a stirred vessel. To enhance the mixing quality, the channeling was minimized and the fraction of fully mixed volume was maximized in the mixing vessel. The importance of each studied factor and the results are listed as below:

- The DHR impeller was more effective than the anchor impeller in reducing the non-ideal flows within the mixing vessel. Furthermore, this study showed that the DHR impeller was

more efficient than the axial-flow impeller (Lightnin A320) and the radial-flow impeller (Scaba 6SRGT) for the mixing of pseudoplastic fluids with yield stress in the continuous stirred-tank reactors. It must be mentioned that the A320 and Scaba impellers are designed for transitional flow while the DBH and anchor impellers are designed for laminar flow.

- The dynamic tests showed that optimum impeller speed at which the channeling approaches zero and fully mixed volume approaches the total volume of fluid within the mixing vessel should be chosen, as further increases in impeller speed may lead to more power consumption for the same extent of the fully mixed volume.
- Dynamic tests made with the DHR impeller showed that the up-pumping mode was more effective than the down-pumping mode in reducing the non-ideal flows. However, the effect of the pumping direction on the mixing quality achieved with the DHR impeller was not as sensitive as that for an axial-flow impeller.
- The results showed that the extent of non-ideal flows in the mixing vessel was reduced by increasing the mean residence time.
- The performance of the continuous-flow mixing was considerably improved by decreasing the fluid yield stress.
- The extents of channeling and dead volume within the mixing vessel for the TI–TO configuration were significantly higher than those for the TI–BO one.
- Since ignoring non-ideal flows can lead to serious errors in the system design, the effect of non-ideal flows should be considered when a reactor is scaled-up.

Applying the findings of this study will enhance the efficiency of the continuous-flow mixers in terms of improving the mixing quality and reducing the power consumption.

5.3 Improving the Dynamic Performance of Continuous-Flow Mixing of Pseudoplastic Fluids Possessing Yield Stress Using Maxblend Impeller (Patel et al., 2012a)

5.3.1 Introduction

Apart from the traditional close-clearance impellers, the efficient, versatile, and very rapidly emerging close-clearance impeller, “the Maxblend impeller” was first introduced for mixing of highly viscous culture broths. The unified structure of the Maxblend impeller consists of a bottom paddle mounted by a top grid. The paddle assists in generating an overall flow circulation in a tank while the grid provides capacity for dispersing a second phase. Hence, it is suitable for a variety of applications in liquid-liquid, solid-liquid, and gas-liquid mixing. Few researchers have investigated the performance of the Maxblend impeller in batch mixing (Yao et al., 2001; Dohi et al., 2004; Takahashi et al., 2006a; Takahashi et al. 2006b; Iranshahi et al., 2007; Fradette et al., 2007; Devals et al., 2008; Guntzburger et al., 2009). A thorough literature review suggests that the rapidly emerging Maxblend impeller is more efficient, competent and economical than the conventional close-clearance impellers for mixing of Newtonian and non-Newtonian fluids; nevertheless, these studies are absolutely confined to batch mixing.

Based on the author’s knowledge, no information is available on the study of the continuous-flow mixing of non-Newtonian fluids with the Maxblend impeller. The strategic approach of this study is to characterize the continuous-flow mixing of pseudoplastic fluids possessing yield stress in a stirred reactor with the Maxblend impeller. The effects of important parameters such as impeller speed (25–500 rpm), absence of baffles, fluid rheology (0.5–1.5%), fluid flow rate (3.20–14.17 L min⁻¹), and the locations of inlet/outlet on the dynamic performance of the continuous-flow mixing vessel were explored. The performance of the Maxblend impeller was then compared to the performances of close-clearance impeller (an anchor), axial-flow (a Lightnin A320), and radial-flow (a Scaba 6SRGT) impellers.

Dynamic experiments were carried out through the frequency-modulated random binary input of a brine solution to determine the extent of non-ideal flows. Mixing quality was

determined on the basis of the extents of channelling (f) and the fully mixed volume ($V_{fully\ mixed}$). The extent of non-ideal flows was quantified using a dynamic model [Equation (2.4–7)]. The rheological behaviour of the xanthan gum solutions was described by the Herschel-Bulkley model [Equation (2.1–9)]. In this study, the continuous-flow mixing system shown in Figure (3.1-1) was used. The geometrical details of the Maxblend and anchor impellers are provided in Table (3.1-1).

5.3.2 Results and Discussion

In this study the performance of four impellers (Maxblend, anchor, Lightnin A320, and Scaba 6SRGT) was evaluated on the basis of power consumption and elimination of non-ideal flows in the continuous-flow mixing vessel. The power number (P_o) was calculated using Equation (2.1–3) and the Reynolds number (Re) was calculated using Equation (2.1–11). Figure (3.4-1) provides the power number curve for all impellers used in this study.

5.3.2.1 Effect of Power Input

The dynamic performance of a continuous-flow mixing system is significantly affected by the impeller power input. Typically increasing the power input reduces the non-ideal flows in the continuous-flow mixing vessel. Figure (5.3-1a and b) shows the extent of channeling and the fraction of fully mixed volume as a function of the impeller power consumption per unit volume, respectively. As expected, the channeling decreased and the fully mixed volume increased with an increase in the power input. This result confirmed the similar phenomenon observed by Ford et al. (2006). At lower impeller speed the stagnant zones were observed visually near the baffles at the top corner of the vessel. The shear stress produced by the impeller was less than the yield stress of the fluid in the stagnant zones. However, at higher impeller speed the xanthan gum solution was swept away from the impeller, leading to improved mixing by overcoming the yield stress of the fluid in the stagnant zones. The optimum power input should be chosen in such a way that the channeling approaches zero and the fully mixed volume approaches the total volume of the fluid within the mixing tank, as further increases in impeller speed may lead to more power consumption for the same extent of

the fully mixed volume, conversely a lower impeller speed than the optimum speed may cause dead volume in the mixing vessel.

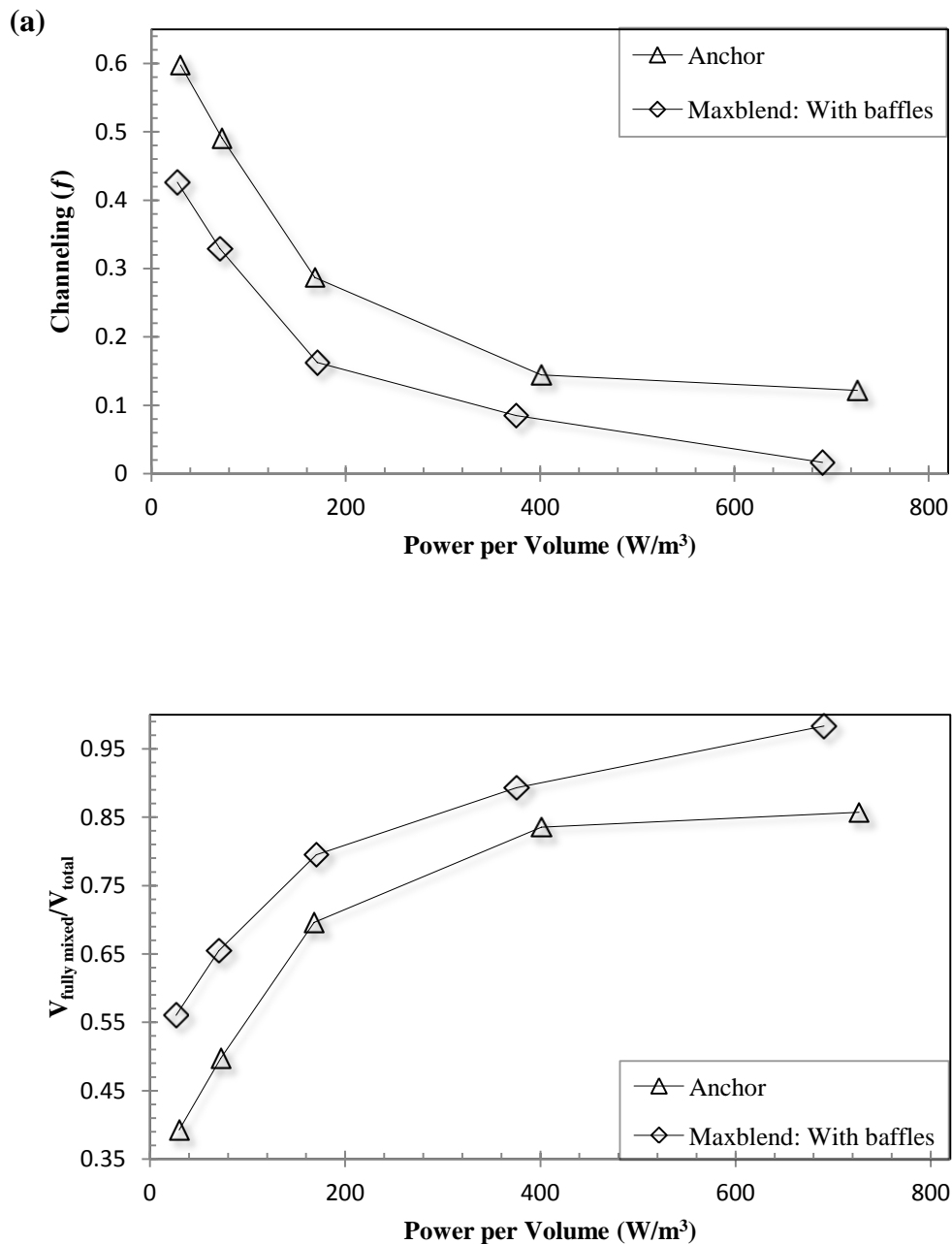


Figure (5.3-1). Effects of impeller power and the type of close-clearance impellers on the extents of (a) channeling and (b) fully mixed volume ($Q = 9.65 \text{ L min}^{-1}$, 1.0% xanthan gum, input-output locations: TI-BO).

5.3.2.2 Effect of Type of Impeller

The type of impeller significantly influences the dynamic performance of the continuous-flow mixing. As the viscosity of the fluid is increased, the preference moves from axial-flow to radial-flow impellers, and then, to close-clearance impellers such as anchor, helical ribbon, helical screw based on the fluid viscosity (Chhabra and Richardson, 2008). In the first step, we compared the performances of the most rapidly emerging Maxblend impeller and the conventional anchor impeller (the close-clearance impeller) in the continuous-flow mixing of the non-Newtonian fluid. The efficiency of both impellers in terms of the extent of channeling and the fraction of fully mixed volume is depicted in Figure (5.3-1a and b), respectively. The analysis of the data shows that the Maxblend impeller is more effective than the anchor impeller in reducing the effect of channeling and dead volume in the viscous system. The anchor impeller primarily generates tangential flow and induces a very little vertical fluid motion, and is thus generally ineffective unless it is used in combination with another impeller such as a radial-flow impeller (Chhabra and Richardson, 2008). Iranshahi et al. (2007) studied the flow pattern of the Maxblend impeller in a batch vessel and found that the bottom paddle of the Maxblend impeller generates a strong tangential flow and a weak axial flow at the vessel bottom, whilst the grid above the paddle produces an axial pumping with an upward motion at the vessel wall and a downward flow along the shaft. Moreover, they found that the Maxblend has a very uniform shear rate distribution through the vessel. Thus, the strong uniform flow pattern generated by the Maxblend impeller helped to improve the continuous-flow mixing of non-Newtonian fluid compared to the flow pattern generated by the anchor impeller.

The previous studies by Patel et al. (2011) showed that the Lightnin A320 impeller was the most effective among the seven axial-flow impellers (A100, A200, A310, A315, A320, 3AH, and 3AM) and the Scaba 6SRGT impeller was the most effective among the four radial-flow impellers (R500, RSB, RT, and Scaba 6SRGT) to reduce the non-ideal flows in the continuous-flow mixing of pseudoplastic fluids with yield stress. As mentioned earlier, the Maxblend impeller was more efficient than the anchor impeller.

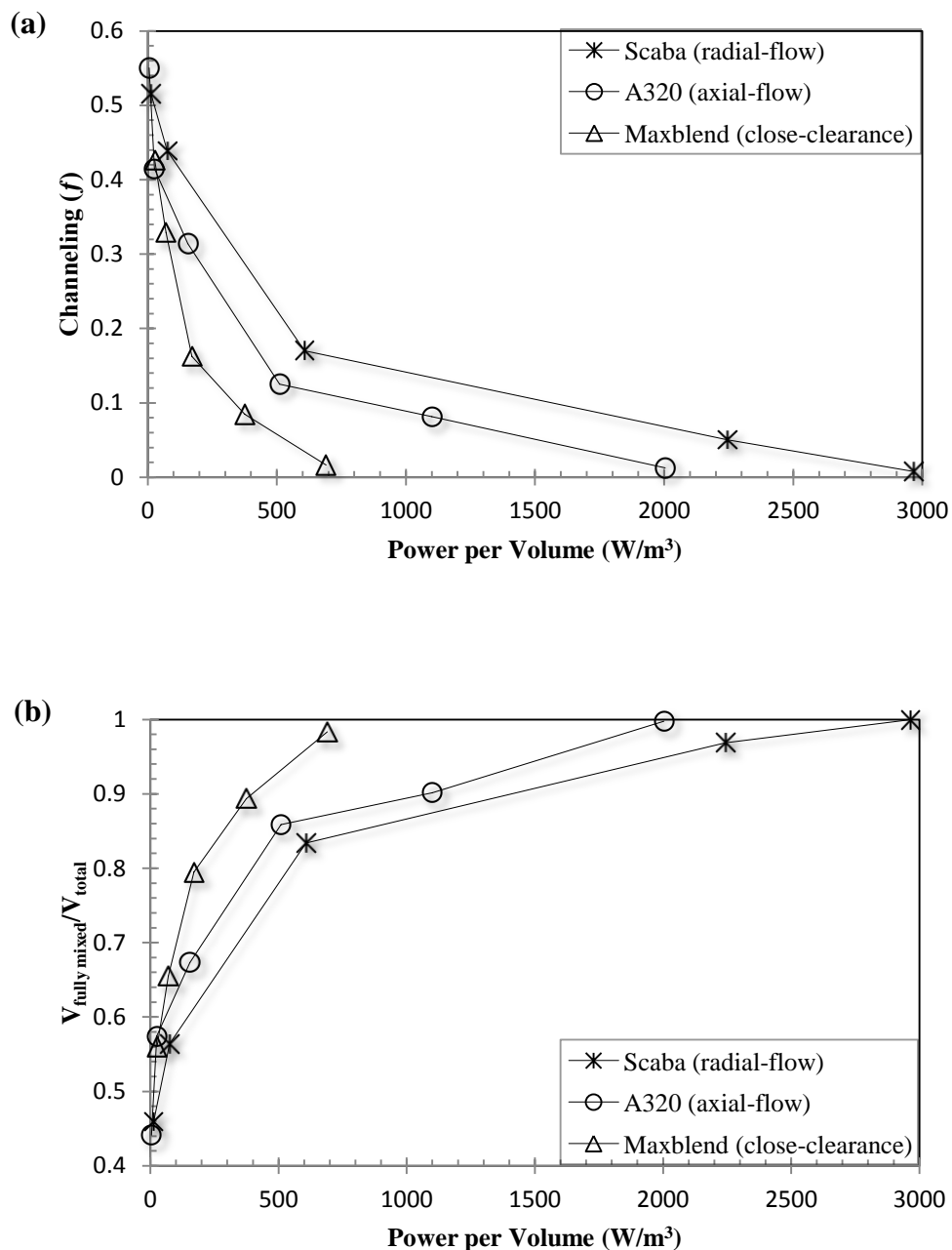


Figure (5.3-2). Effects of impeller type (axial-flow, radial-flow, and close-clearance) on the extents of (a) channeling and (b) fully mixed volume (Maxblend with baffles, $Q = 9.65 \text{ L min}^{-1}$, 1.0% xanthan gum, input-output locations: TI-BO).

Consequently, to demonstrate the most effective impeller among the axial-flow, radial-flow, and close-clearance impellers, Figure (5.3-2) represents the extent of channeling and the

fraction of fully mixed volume as a function of power consumption per unit volume for the A320 impeller (the most effective among the axial-flow impellers), the Scaba impeller (the most effective among the radial-flow impellers) and the Maxblend impeller (more effective than the anchor impeller). The trend of the graphs indicates that the Maxblend impeller was the most efficient impeller among the three types of impellers in terms of eliminating the channeling and dead volume with a lower power consumption. In addition, when the channeling approached zero and the fully mixed volume approached total mixed volume in the vessel, the power drawn by the A320 impeller and the Scaba impeller was about 2.9 and 4.3 times greater than that of the Maxblend impeller, respectively. Therefore, the Maxblend impeller could be recommended for the continuous-flow mixing of non-Newtonian fluids with yield stress.

5.3.2.3 Effect of Baffles

The presence and absence of the baffles have a major influence on the flow behavior and the resulting mixing quality. Generally, baffles are not employed with close-clearance impellers such as Anchor and helical ribbon impellers. The diameter of the Maxblend impellers is greater than that of the axial-flow and radial-flow impellers but less than that of the close-clearance impellers. It is feasible to install the baffles in the vessel while using the Maxblend impeller; hence, the effect of presence and absence of baffles on the performance of the Maxblend impellers was investigated. The efficiency of the Maxblend impeller in the presence and absence of the baffles in terms of the extent of channeling and fully mixed volume is depicted in Figure (5.3-3a and b), respectively. The results show that for the identical operating condition, the geometrical configuration with baffles provided better efficiency in reducing the extent of the non-ideal flows than that of the geometrical configuration without baffles. It was observed that an unbaffled (without baffles) configuration was susceptible to a strong vortex at higher impeller speed, which restricts the realistic operation by air entrainment. The presence of the baffles transforms tangential flows to vertical flows, provides top-to-bottom mixing without swirl, and minimizes air entrainment. Iranshahi et al. (2007) observed similar phenomena in the mixing of Newtonian fluid in the batch vessel. They found that the flow

number for the baffled configuration was higher than that for the unbaffled configuration and the presence of baffles increased the axial pumping.

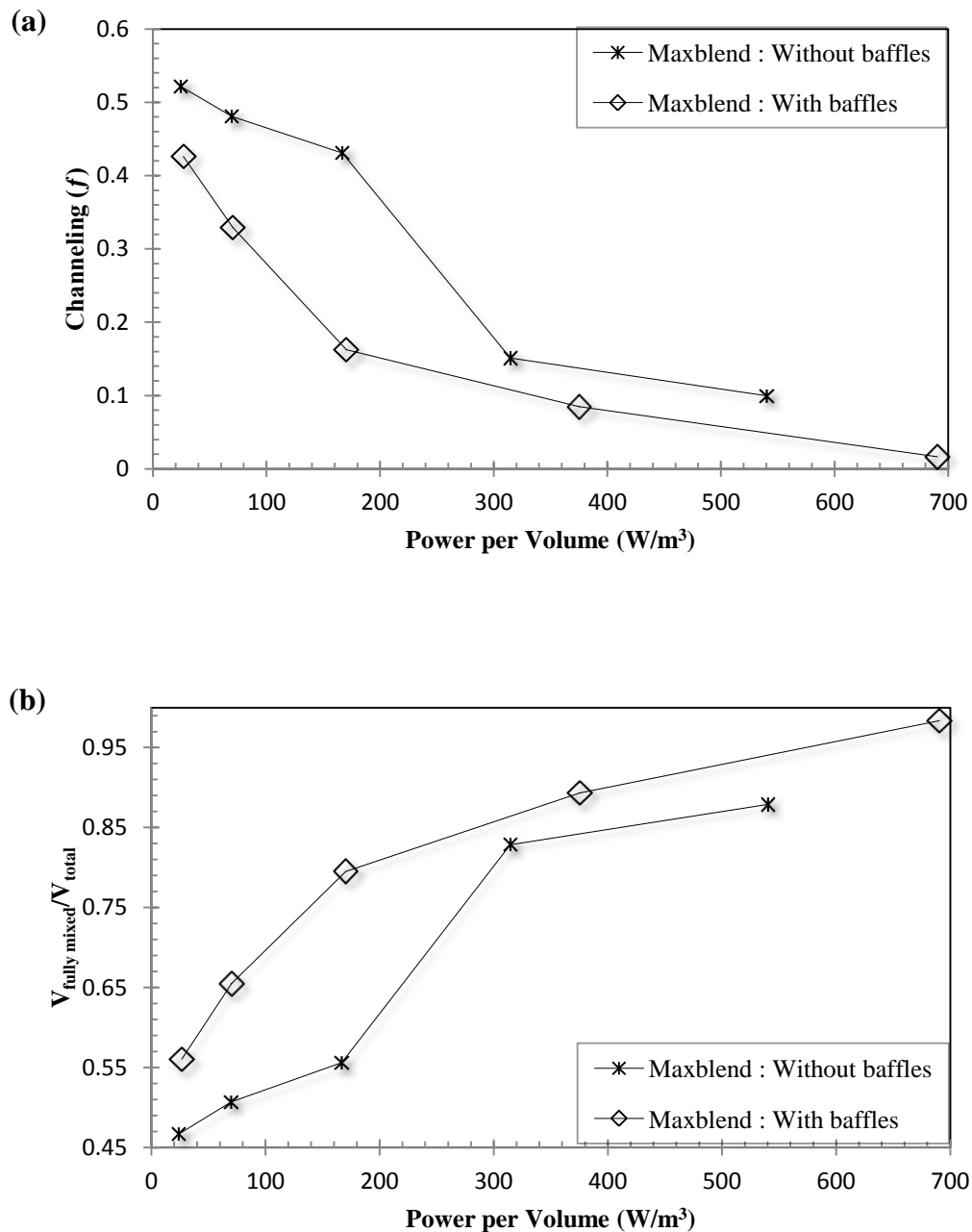
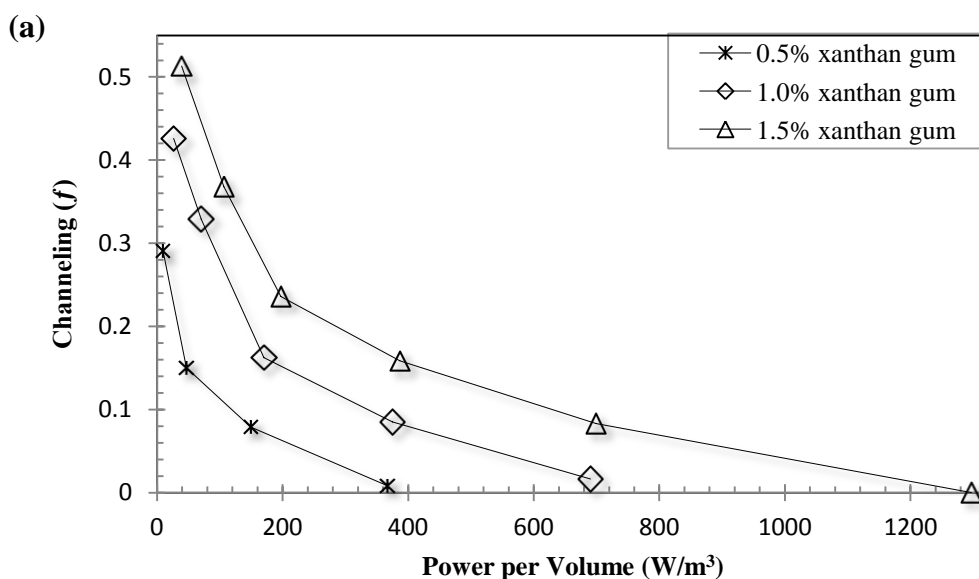


Figure (5.3-3). Effects of baffles on the extents of (a) channeling and (b) fully mixed volume ($Q = 9.65 \text{ L min}^{-1}$, 1.0% xanthan gum, input-output locations: TI-BO).

In addition, the dimensionless mixing time of the unbaffled configuration was 1.4 times greater than that of the baffled configuration. The Maxblend impeller with baffled configuration provided better mixing quality in the continuous-flow mixing of non-Newtonian fluid with yield stress.

5.3.2.4 Effect of Fluid Rheology

The fluid rheology has a momentous effect on the dynamic performance of continuous-flow mixing. In this study the effect of xanthan gum concentration (0.5, 1.0, and 1.5%) on the extent of non-ideal flows was examined. Figure (5.3-4) shows the effect of xanthan gum concentration on the extent of channeling and the fraction of fully mixed volume. It shows that the extent of channeling increased and the fraction of fully mixed volume decreased as xanthan gum concentration increased from 0.5 to 1.5% for a fixed power input. Further, it shows that when the channeling approached zero and the fully mixed volume approached total volume in the vessel, the power consumed by the impeller at 1.5% concentration was about 3.5 times greater than that at 0.5% concentration. Increasing the xanthan gum solution concentration increases the solution yield stress, resulting in an increase in the extent of non-ideal flows as the energy dissipation near the impeller becomes faster at higher yield stress (Ein-Mozaffari et al., 2005).



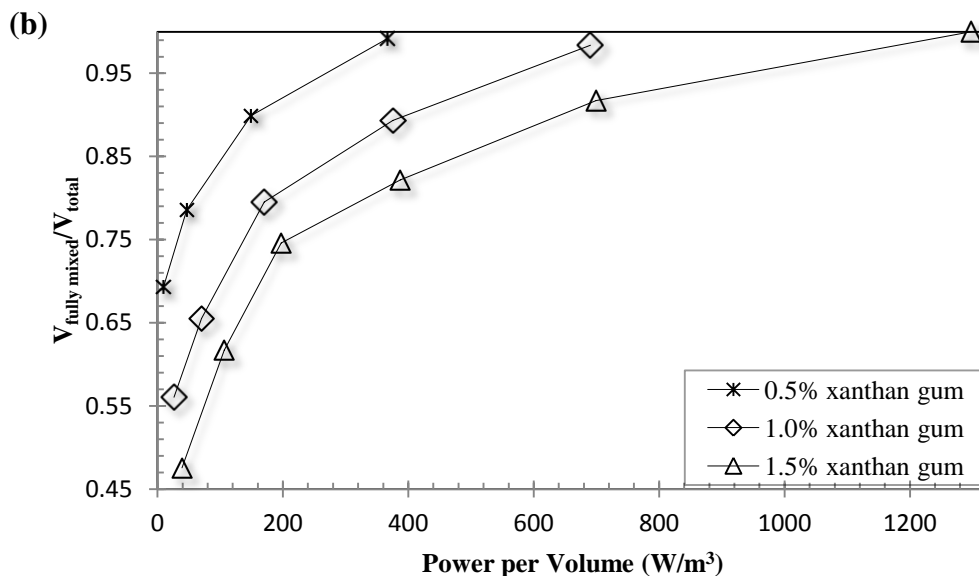


Figure (5.3-4). Effects of fluid rheology on the extents of (a) channeling and (b) fully mixed volume (Maxblend with baffles, $Q = 9.65 \text{ L min}^{-1}$, input-output locations: TI-BO).

Although flows near the impeller might be chaotic, the vibrant velocities will weaken quickly in the area outside the impeller zone owing to the apparent viscosity of the fluid, which is a function of the yield stress. A similar phenomenon was observed by Saeed et al. (2008) in the continuous-flow mixing of non-Newtonian fluid with yield stress using axial-flow impellers. They found that the system was more susceptible to a high percentage of the channeling and dead volume at higher xanthan gum concentration (higher fluid yield stress).

5.3.2.5 Effect of Feed Flow Rate

The research shows that the feed flow rate is also one of the crucial factors that impact on the performance of the continuous-flow mixing system (Ein-Mozaffari et al., 2003b). Therefore, this study involves the examination of the effect of fluid flow rate on the extent of non-ideal flows. The consequences of three different flow rates (3.20, 9.65, and 14.17 L min^{-1}) on the extent of channeling and fully mixed volume are demonstrated in Figure (5.3-5a and b), respectively, that represent how fluid flow rates affect non-ideal flows. It is clear that decreasing the fluid flow rate through the mixing vessel reduced the extent of the channeling and increased the fraction of fully mixed volume.

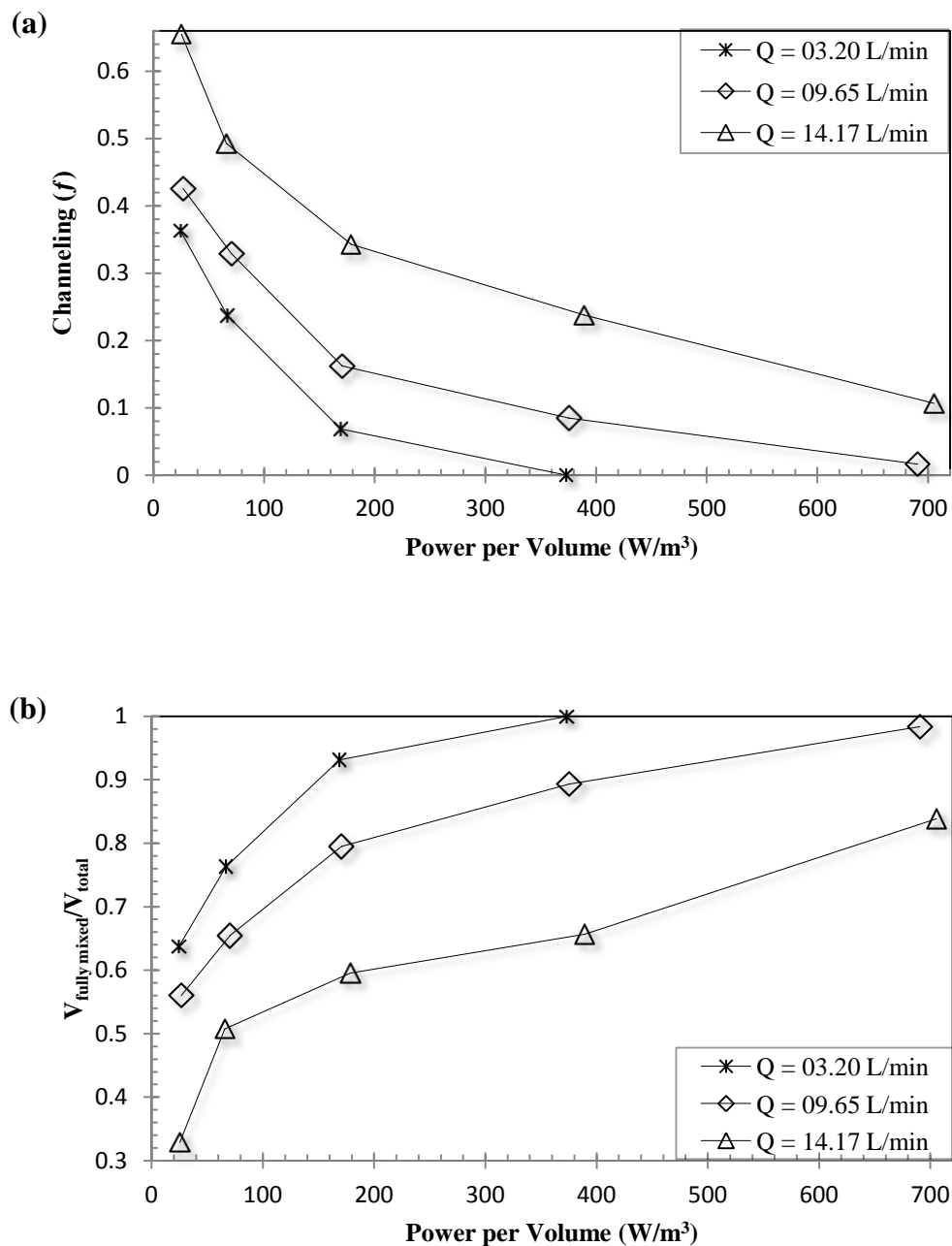


Figure (5.3-5). Effects of fluid flow rate through mixing vessel on the extents of (a) channeling and (b) fully mixed volume (Maxblend with baffles, 1.0% xanthan gum, input-output locations: TI-BO).

This phenomenon happened because of the fact that decreasing the fluid flow rate increases the mean residence time in the vessel, so the fluid gets more time with the intense motion of the

impeller. Increasing the fluid flow rate decreases the mean residence time in the vessel and this compels the fluid to exit the vessel sooner. On the other hand, for similar operating conditions, the system is more susceptible to channeling at a higher fluid flow rate than at a lower one. The research conducted by Ein-Mozaffari et al. (2004a) on the mixing of pulp suspension showed that the ratio of flow induced by the impeller (pumping action of the impeller) to the flow through the mixing tank (the flow that discharges the fluid from the vessel) affects the extent of the channeling. Similar results were reported by Saeed et al. (2008) in the continuous-flow mixing of non-Newtonian fluid with yield stress using a Lightnin A200 axial-flow impeller.

5.3.2.6 Effect of Inlet and Outlet Locations

The locations of inlet and outlet have a crucial effect on the extent of non-ideal flows in the continuous-flow mixing of non-Newtonian fluids (Ein-Mozaffari et al., 2005). This study investigated the effects of two different configurations; (1) TI-BO (**top inlet-bottom outlet**) and (2) BI-TO (**bottom inlet-top outlet**) on the extent of non-ideal flows. Figure (5.3-6a and b) represents the effect of the inlet and outlet locations on the extent of channeling and the fraction of fully mixed volume, respectively. It can be seen from the results that for the identical operating conditions the system was a little more susceptible to a high degree of channeling and dead volume for the TI-BO configuration than the BI-TO configuration. The identical phenomena were remarked in continuous-flow mixing of Newtonian fluid with an axial-flow impeller and it was reported that the mixing was improved by locating the inlet at the bottom and the overflow type outlet in lieu of an inlet at the top and an outlet at the bottom (Khopkar et al., 2004). The locations of the inlet and outlet should be chosen in such a way that a line drawn from the inlet to the outlet passes through the impeller or an intense mixing zone (Paul et al., 2004). In this study, the feed was forced to flow through the mixing zone before leaving the vessel in both configurations. However, in the case of BI-TO, the feed had to face the intense fluid discharge from the impeller and to pass through the mixing zone in the direction opposite to the gravitational force, which helped to improve the mixing quality. The effect of inlet and outlet locations on the continuous-flow mixing with axial-flow and radial-flow impellers was significant. However, in a similar condition, such an effect with the Maxblend impeller was rarely observed because the Maxblend produces more uniform mixing and reduces the non-

ideal flows in a mixing vessel for different configurations. In fact, it is to be highlighted that the effect of the inlet and outlet locations on continuous-flow mixing with the Maxblend impeller was not as sensitive as that of the axial-flow and radial-flow impellers.

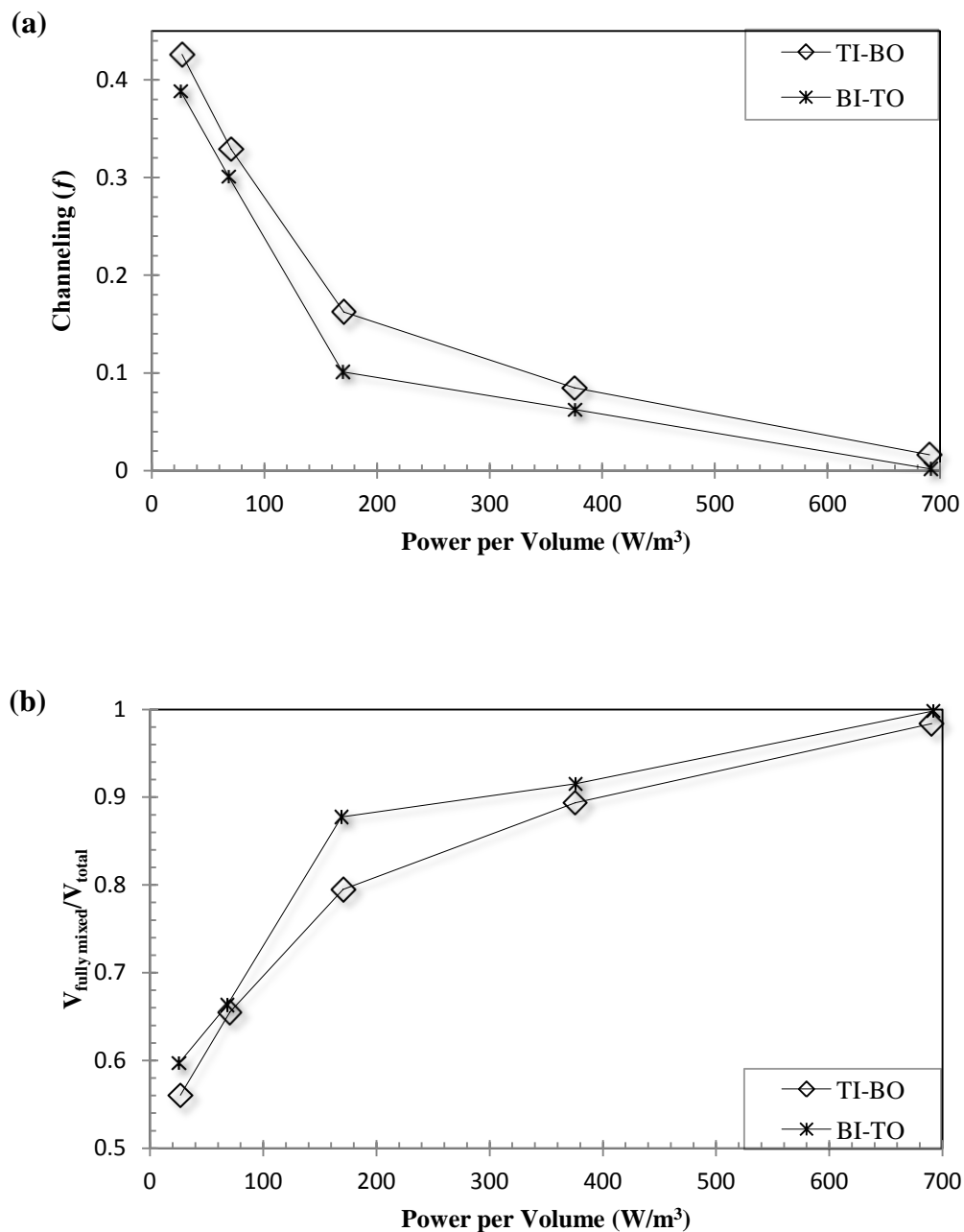


Figure (5.3-6). Effects of the inlet and outlet locations on the extents of (a) channeling and (b) fully mixed volume (Maxblend with baffles, $Q = 9.65 \text{ L min}^{-1}$, 1.0% xanthan gum).

5.3.3 Conclusions

Dynamic tests were carried out on the continuous-flow mixing of non-Newtonian fluids with yield stress in a stirred vessel to measure the degree of non-ideal flows such as channeling and dead volume. The mixing quality was improved by decreasing the channeling and increasing the fraction of fully mixed volume in the mixing vessel. The results and importance of each studied factor are concluded as below:

- The Maxblend impeller was more efficient than the axial-flow impeller (Lightnin A320), radial-flow impeller (Scaba 6SRGT), and close-clearance impeller (anchor) in terms of reducing the extent of channeling and dead zones within the mixing vessel with lower power consumption. Hence, the Maxblend impeller could be recommended for the continuous-flow mixing of non-Newtonian fluids possessing yield stress.
- The performance of the Maxblend impeller was poorer in the absence of the baffles while the presence of baffles improved mixing quality.
- The extent of channeling decreased and the fraction of fully mixed volume increased with an increase in power input by increasing the impeller speed. These results provide an interesting insight into energy savings of the operating costs. Along these lines, the optimum power input at which the extent of non-ideal flows approaches zero should be chosen, as further supply of power by increasing impeller speed may lead to more power consumption for the same extent of fully mixed volume.
- The mixing quality of the continuous-flow mixing was improved by decreasing the fluid flow rate and fluid yield stress (concentration of xanthan gum solution).
- The extent of non-ideal flows was further reduced by relocating the inlet-outlet locations from the TI-BO (top inlet-bottom outlet) to the BI-TO (bottom inlet-top outlet). Moreover, the effect of the input and output locations on continuous-flow mixing with the Maxblend impeller was not as sensitive as that for the axial-flow and radial-flow impellers.

Better mixing quality and more energy savings can be achieved by considering these concluding remarks in the design of continuous-flow mixing of pseudoplastic fluids possessing yield stress.

5.4 Characterization of the Continuous-Flow Mixing of Non-Newtonian Fluids Using the Ratio of Residence Time to Batch Mixing Time (Patel et al., 2013c)

5.4.1 Introduction

To identify the non-ideal flows in continuous-flow mixing systems, many researchers have employed the residence time distribution (RTD) technique (Danckwerts, 1953; Paul et al., 2004), while some others have related the mean residence time (τ) in a continuous-flow mixing vessel to the mixing time (θ) for the batch mode (Zannoud et al., 1991; Roussinova and Kresta, 2008). These studies showed that if the value of τ/θ is less than 10, the mixing system would be prone to the existence of non-ideal flows. A literature review shows that efforts have been made to find an optimum ratio of the residence time to the batch mixing time (τ/θ) for continuous-flow mixing systems. However, these studies are absolutely limited to the Newtonian fluids.

No study has been reported regarding the ratio of the residence time (τ) to the batch mixing time (θ) in open literature for the continuous-flow mixing of pseudoplastic fluids with yield stress. Therefore, the main objective of this study was to find the optimum values of τ/θ for the continuous-flow mixing of non-Newtonian fluids as a function of the different operating conditions and design parameters. To accomplish this goal, the effects of impeller types (four axial-flow impellers: A310, A315, 3AH, and 3AM; and three radial-flow impellers: RSB, RT, and Scaba), impeller speed (290–754 rpm), fluid rheology (0.5–1.5 w/v %), impeller off-bottom clearance ($H/2.7$ – $H/2.1$, where H is the fluid height in the vessel), locations of inlet and outlet (configurations: top inlet-bottom outlet and bottom inlet-top outlet), pumping directions of an axial-flow impeller (up-pumping and down-pumping), fluid height in the vessel ($T/1.06$ – $T/0.83$, where T is the tank diameter), residence time (257–328 s), and jet velocity (0.317–1.66 m s⁻¹) on the ratio of τ to θ were investigated.

Electrical resistance tomography (ERT), a non-intrusive technique, was employed to measure the mixing time in the batch mode while dynamic tests were performed to study the

mixing system in the continuous mode. In this study, the continuous-flow mixing system was considered as an ideal system when channeling (f) approached zero and the fully mixed volume ($V_{fully\ mixed}$) approached the total volume (V_{total}) of the fluid in the vessel. To achieve an ideal mixing for a given condition, impeller speed was gradually increased until the percentage of channeling approached approximately zero and the fully mixed volume approached approximately the total volume of the fluid in the vessel. Under these circumstances, the residence time (τ) was calculated from the ratio of the fluid volume (V_{total}) in the vessel to the feed flow rate (Q). This similar operating condition was then applied (impeller power per volume) to measure the mixing time in the batch mode, which was finally used to find the ratio of the residence time to the mixing time. In this study the mixing time (θ) was taken as a time at which the conductivity of the tracer at the detecting positions reached 98% of the steady-state conductivity.

To measure the mixing time in the batch mode, the experimental setup with ERT shown in Figure (3.2-1) and procedure explained in Section (3.4.3) were employed. Dynamic tests were performed using the experimental setup shown in Figure (3.1-1). The extent of non-ideal flows was quantified using a dynamic model [Equation (2.4-7)]. The rheological behaviour of the xanthan gum solutions was described by the Herschel-Bulkley model [Equation (2.1-9)].

5.4.2 Results and Discussion

5.4.2.1 Effect of Impeller Speed

The continuous-flow mixing systems must be designed at the optimum impeller speed/power when the extent of channeling approaches zero and the fully mixed volume approaches the total volume of the fluid within the vessel. Figure (5.4-1) shows the effect of the impeller speed (Reynolds numbers) on the ratio of the residence time to the mixing time for given operating conditions. These data were obtained when the dynamic tests were carried out using the Scaba impeller at $Q = 9.65\text{ L min}^{-1}$, 1.0% xanthan gum, $C = H/2.7$, $H = T/0.93$, $V_j = 0.317\text{ m s}^{-1}$, residence time = 292 s, and input-output locations: top inlet and bottom outlet (TI-BO). The similar operating conditions (the type of impeller, impeller speed, fluid rheology, impeller off-bottom clearance, and fluid height in the vessel) were applied in the batch mode to measure the

mixing time using ERT. The results show that as the impeller speed (Reynolds number) was increased, the ratio of τ to θ increased as well. Under these operating conditions, the extent of channeling (f) and dead volume approached zero (ideal mixing) at Re 597 (331 rpm). Figure (5.4-1) demonstrates that the ratio of τ to θ must be about 16.2 to achieve ideal mixing at Re 597 (331 rpm). Roussinova and Kresta (2008) studied continuous-flow mixing of the Newtonian fluid in a stirred vessel and recommended that to reach ideal mixing, the value of τ/θ should be at least 10. Other researchers (Aubin et al., 2006; Khopkar et al., 2004; Mavros et al., 1997, 2002a, 2002b; Samaras et al., 2006), who studied the continuous-flow mixing of Newtonian fluids, observed that when the ratio of τ to θ was less than 10, the system was susceptible to non-ideal flows.

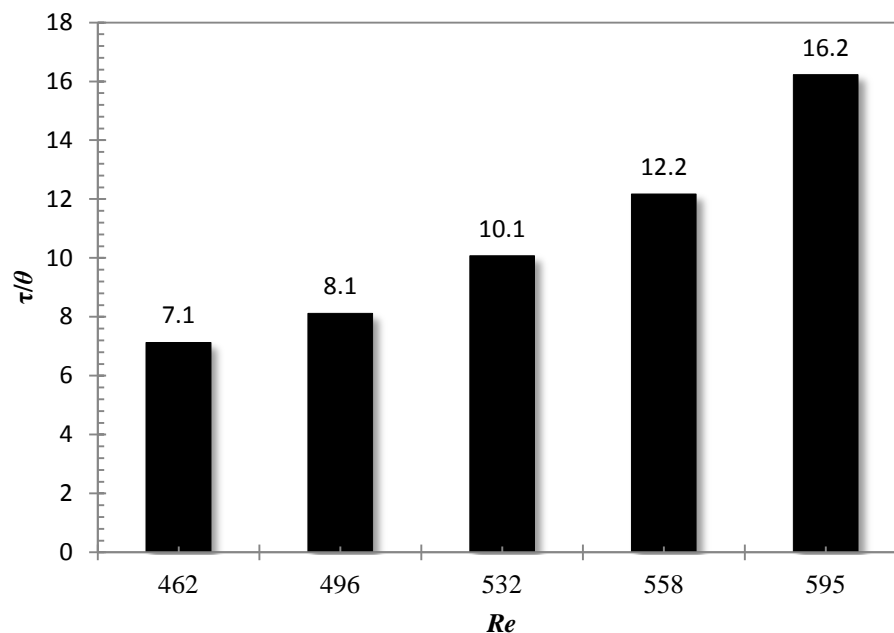


Figure (5.4-1). Effect of the impeller speed (Reynolds number) on the ratio of the residence time to the mixing time (Scaba 6 SRGT impeller, $Q = 9.65 \text{ L min}^{-1}$, 1.0% xanthan gum, $C = H/2.7$, $H = T/0.93$, $V_j = 0.317 \text{ m s}^{-1}$, residence time = 292 s, and input-output locations: TI-BO).

5.4.2.2 Effect of Fluid Rheology

In this study the effect of xanthan gum concentrations (0.5, 1.0, and 1.5%) on the ratio of τ to θ was also explored [Figure (5.4-2)]. In order to calculate the ratio of τ to θ at different xanthan

gum concentrations, the dynamic test data for the continuous-flow mixing system were taken from Saeed and Ein-Mozaffari (2008). The continuous-flow mixing experiments were carried out using the A200 impeller at $Q = 10.05 \text{ L min}^{-1}$, $C = H/2.7$, $H = T/0.93$, residence time = 280 s, and input-output locations: TI–BO. Similar operating conditions were applied to measure the mixing time using the ERT system. The results show that as the xanthan gum concentration was increased from 0.5 to 1.5%, the ratio of τ to θ also increased from 11.2 to 14.8. The solution yield stress increases with xanthan gum solution concentration. At a higher yield stress, the energy dissipation became faster, which resulted in an increase in the extent of non-ideal flows within the mixing vessel (Patel et al., 2012a, 2012b). As the xanthan gum concentration increases, higher impeller speed is required to eliminate non-ideal flow in the continuous-flow mixing system. When the impeller speed increases, mixing time in the batch mode decreases. As the mixing time decreases, the ratio of the residence time to the mixing time increases for a given residence time ($\tau = 280 \text{ s}$). Therefore, as the solution yield stress increases, a higher ratio of τ to θ must be considered to achieve ideal mixing.

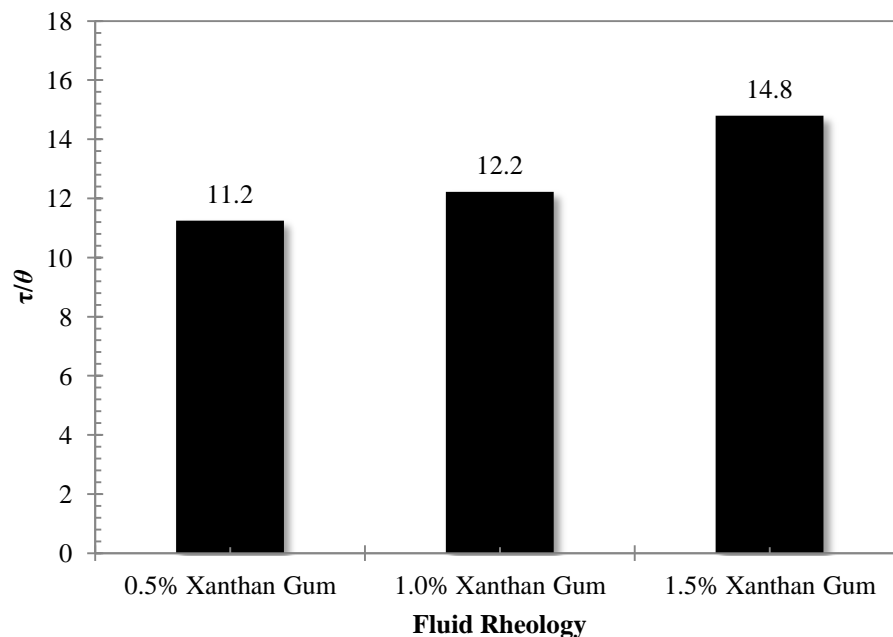


Figure (5.4-2). Effect of the fluid rheology on the ratio of the residence time to the mixing time (A200 impeller, $Q = 10.05 \text{ L min}^{-1}$, $C = H/2.7$, $H = T/0.93$, residence time = 281 s, and input-output locations: TI–BO).

5.4.2.3 Effect of Type of Impeller

In addition to the impeller speed and fluid rheology, the type of impeller also influences the performance of continuous-flow mixing operations. Depending on the process requirements, different types of impellers are used in the industry. Typically, the axial-flow and radial-flow impellers are used for mixing operations. Four axial-flow impellers (A310, A315, 3AH, and 3AM) were employed in this study. The hydrofoil impellers with a high solidity ratio have been recommended in the literature for mixing of viscous fluids (McFarlane and Nienow, 1995; Paul et al., 2004). The 3AH and A315 impellers have a higher solidity ratio than the A310 and 3AM impellers. Patel et al. (2011) reported that the A315 and 3AH impellers (with a high solidity ratio) were more effective than the A310 and 3AM impellers (with a low solidity ratio) in reducing the effect of non-ideal flows in the continuous-flow mixing of xanthan gum solutions. Figure (5.4-3) shows the effects of axial-flow impellers on the ratio of the residence time to the mixing time. The experiments were carried out at $Q = 9.65 \text{ L min}^{-1}$, 1.0% xanthan gum, $C = H/2.7$, $H = T/0.93$, $V_j = 0.317 \text{ m s}^{-1}$, residence time = 292 s, and input-output locations: TI–BO. These results show that the hydrofoil impellers with a high solidity ratio had a higher value of τ/θ than the hydrofoil impellers with a low solidity ratio. These data demonstrated that under the operating conditions required to achieve ideal mixing in the continuous mode, the mixing time in the batch mode obtained for the hydrofoil impellers with a high solidity ratio was lower than that for the hydrofoil impellers with a low solidity ratio. Therefore, for a given residence time ($\tau = 292 \text{ s}$) the ratio of τ to θ was higher for the high solidity ratio impellers than for the low solidity ratio impellers.

In addition to the axial flow impellers, three radial-flow impellers (RSB, RT, and Scaba) were also employed in this study. The disk-type radial-flow impellers such as the Scaba and RT provide a more uniform radial flow pattern than the radial-flow impellers without disk such as RSB. Figure (5.4-3) shows the effect of the type of the radial-flow impeller on the ratio of the residence time to the mixing time. The experiments were carried out at $Q = 9.65 \text{ L min}^{-1}$, 1.0% xanthan gum, $C = H/2.7$, $H = T/0.93$, $V_j = 0.317 \text{ m s}^{-1}$, residence time = 292 s, and input-output locations: TI–BO. The results show that the ratio of τ to θ obtained for the Scaba impeller was higher than those of RT and RSB impellers. In fact, under the circumstances required to attain

ideal mixing in the continuous mode, the mixing time in the batch mode recorded for the Scaba impeller was lower than those for RT and RSB impellers. The dynamic tests also showed that the RSB impeller was the least effective, while the Scaba impeller was the most effective in removing non-ideal flows among the radial-flow impellers utilized in this study. Therefore, the ratio of τ to θ was higher for the Scaba impeller than for the RT and RSB impellers.

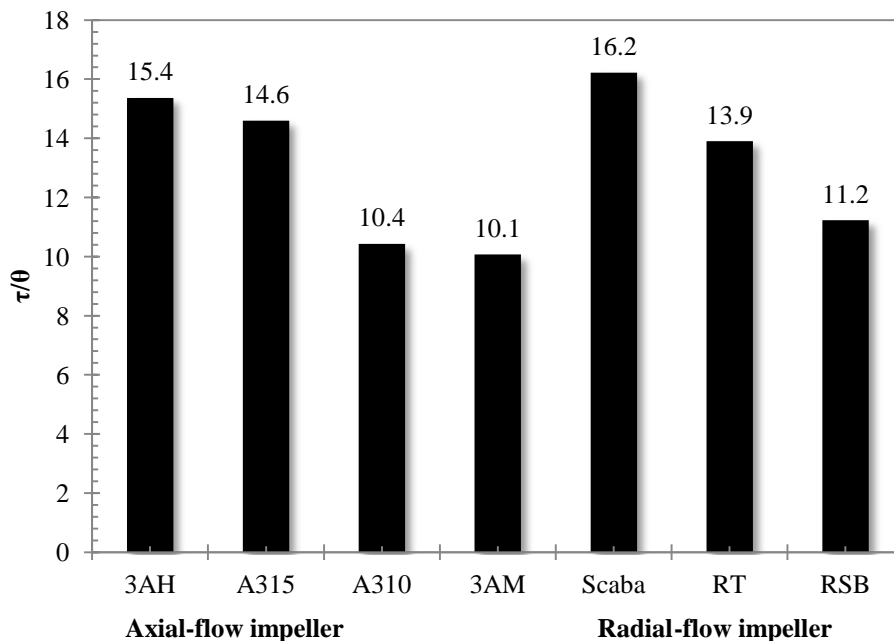


Figure (5.4-3). Effect of the type of (axial-flow and radial-flow) impellers on the ratio of the residence time to the mixing time ($Q = 9.65 \text{ L min}^{-1}$, 1.0% xanthan gum, $C = H/2.7$, $H = T/0.93$, $V_j = 0.317 \text{ m s}^{-1}$, residence time = 292 s, and input-output locations: TI–BO).

5.4.2.4 Effect of Pumping Direction of an Axial-flow Impeller

The pumping direction of an axial-flow impeller had an effect on the efficiency of a continuous-flow mixer especially when the outlet was located at the bottom of the tank. The down-pumping impeller creates a vortex, which can cause air entrainment while the up-pumping impeller avoids creating such a vortex problem. The effect of pumping direction of the 3AH impeller on the ratio of the residence time to the mixing time is represented in Figure (5.4-4). The experiments were carried out at $Q = 9.65 \text{ L min}^{-1}$, 1.0% xanthan gum, $C = H/2.7$, $H = T/0.93$, $V_j = 0.317 \text{ m s}^{-1}$, residence time = 292 s, and input-output locations: TI–BO. The results show that the ratio of τ to θ for the down pumping mode was higher than that for the up-

pumping mode. The dynamic tests showed that the up-pumping mode was more effective than the down-pumping mode in terms of reducing the non-ideal flows. In this case the feed stream had to pass through the intense up-flow stream generated by the impeller before reaching the outlet since the outlet was located at the bottom of the tank. Hence, the up-pumping mode was able to provide better mixing quality at a lower impeller speed than the down-pumping mode. Conversely, for the same operating conditions in the batch process, the mixing time was higher at a lower impeller speed for the up-pumping mode. Therefore, for a given residence time ($\tau = 292$ s) the up-pumping mode had a lower ratio of τ to θ than the down-pumping mode.

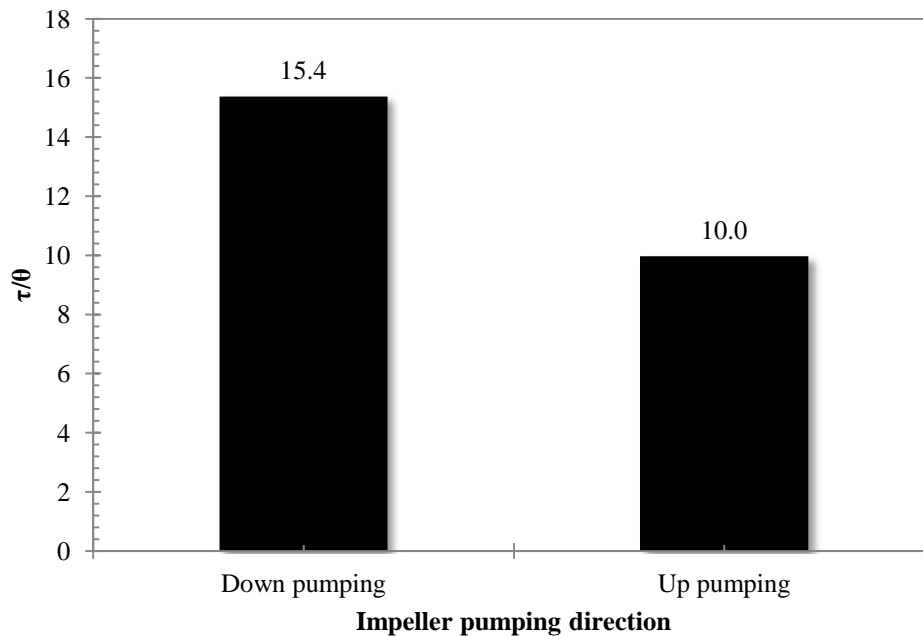


Figure (5.4-4). Effect of the pumping direction of an axial-flow impeller on the ratio of the residence time to the mixing time (3AH impeller, $Q = 9.65 \text{ L min}^{-1}$, 1.0% xanthan gum, $C = H/2.7$, $H = T/0.93$, $V_j = 0.317 \text{ m s}^{-1}$, residence time = 292 s, and input-output locations: TI–BO).

5.4.2.5 Effect Inlet and Outlet Locations

The locations of the inlet and outlet have a significant effect on the extent of non-ideal flows in the continuous-flow mixing of non-Newtonian fluids (Ein-Mozaffari et al., 2004a). Therefore, this study examined the effects of two different configurations: (1) TI–BO (top inlet-bottom outlet), and (2) BI–TO (bottom inlet-top outlet) on the ratio of the residence time to the mixing

time. Figure (5.4-5) illustrates the effect of the inlet and outlet locations on the ratio of τ to θ . The tests were carried out using the 3AH impeller at $Q = 9.65 \text{ L min}^{-1}$, 1.0% xanthan gum, $C = H/2.7$, $H = T/0.93$, $V_j = 0.317 \text{ m s}^{-1}$, and residence time = 292 s. The results revealed that the ratio of the residence time to the mixing time for TI-BO configuration was higher than that for the BI-TO configuration. The dynamic tests showed that for identical operating conditions, the BI-TO configuration was more effective than the TI-BO configuration in reducing the extent of the non-ideal flows. In the case of the BI-TO configuration, the feed had to face the intense fluid discharge from the impeller and pass through the mixing zone in the direction opposite to the impeller discharge flow, which resulted in improving the mixing quality. Thus, for identical operating conditions, the impeller speed required to remove non-ideal flows within the mixing tank for the BI-TO configuration was lower than that for the TI-BO configuration. However, at the lower impeller speed, the mixing time for the batch process was higher. Therefore, for a given residence time ($\tau = 292 \text{ s}$), the required ratio of τ to θ for the TI-BO configuration was higher than that for the BI-TO configuration.

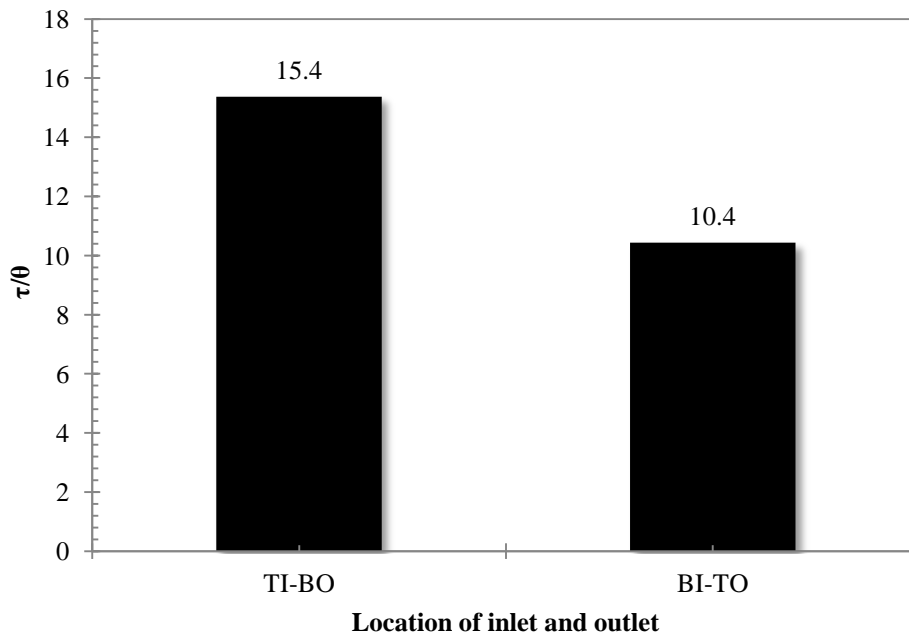


Figure (5.4-5). Effect of the inlet and outlet locations on the ratio of the residence time to the mixing time (3AH impeller, $Q = 9.65 \text{ L min}^{-1}$, 1.0% xanthan gum, $C = H/2.7$, $H = T/0.93$, $V_j = 0.317 \text{ m s}^{-1}$, and residence time = 292 s).

5.4.2.6 Effect of Impeller Off-bottom Clearance

The performance of the continuous-flow mixing system also depends on the impeller clearance (C) from the bottom of the tank. In the mixing of pseudoplastic fluids with yield stress, placing the impeller too low results in the majority of the fluid remaining unmixed at the upper part of the tank. Placing the impeller too high causes a deep vortex, which leads to surface aeration even at the lower impeller speed and also results in the creation of dead zones at the bottom of the tank. Hence, placing the impeller at an optimum clearance (C) can drastically reduce non-ideal flows in the continuous-flow mixing of viscous fluids. Two different impeller positions from the base of the tank ($C = H/2.1, H/2.7$) were tested. Figure (5.4-6) demonstrates the effect of the impeller off-bottom clearance on the ratio of the residence time to the mixing time.

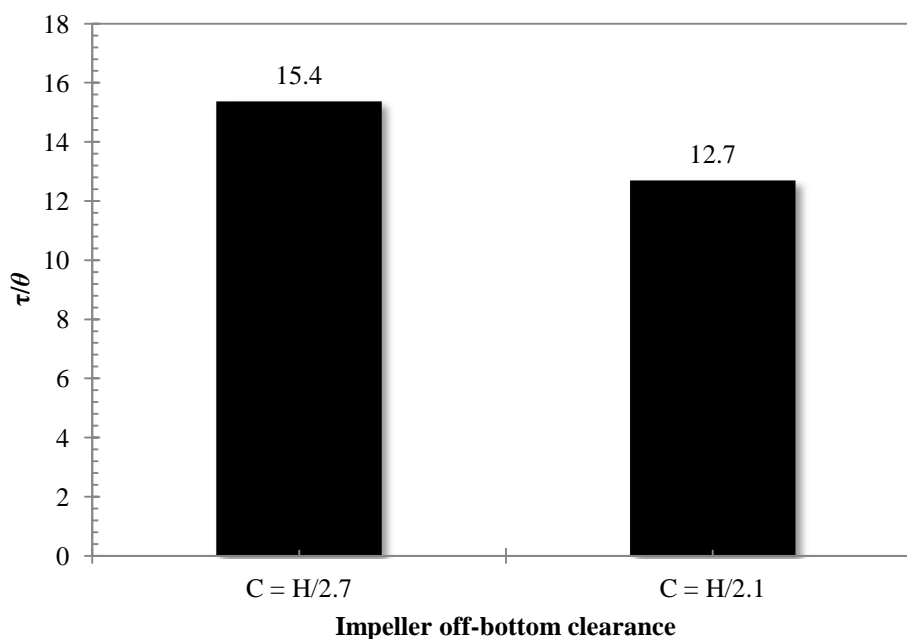


Figure (5.4-6). Effect of the impeller off-bottom clearance on the ratio of the residence time to the mixing time (3AH impeller, $Q = 9.65 \text{ L min}^{-1}$, 1.0% xanthan gum, $H = T/0.93$, $V_j = 0.317 \text{ m s}^{-1}$, residence time = 292 s, and input-output locations: TI–BO).

The experiments were carried out using the 3AH impeller at $Q = 9.65 \text{ L min}^{-1}$, 1.0% xanthan gum, $H = T/0.93$, $V_j = 0.317 \text{ m s}^{-1}$, residence time = 292 s, and input-output locations: TI–BO. The results show that as the impeller clearance was increased from $H/2.7$ to $H/2.1$, the ratio of τ to θ decreased. The dynamic test results showed that as the clearance of the impeller increased

from $H/2.7$ to $H/2.1$, the extent of non-ideal flows decreased. Thus, for identical operating conditions, the impeller speed required to eliminate non-ideal flows for the impeller clearance of $C = H/2.1$ was lower than that for the impeller clearance of $C = H/2.7$. However, the mixing time measured at the same operating conditions for the batch mode was higher at the lower impeller speed. Therefore, to achieve ideal mixing at a given residence time ($\tau = 292$ s), the ratio of τ to θ for the impeller clearance of $C = H/2.7$ was higher compared to that obtained for the impeller clearance $C = H/2.1$.

5.4.2.7 Effect of Jet Velocity

The jet velocity (V_j) can also influence the efficiency of a continuous-flow mixing system. By reducing the inlet pipe diameter, higher jet velocity is attained at the same flow rate. Two different jet velocities ($V_j = 0.317$ and 1.66 m s⁻¹) were employed in this study to explore the effect of this parameter on the ratio of the residence time to the mixing time [Figure (5.4-7)].

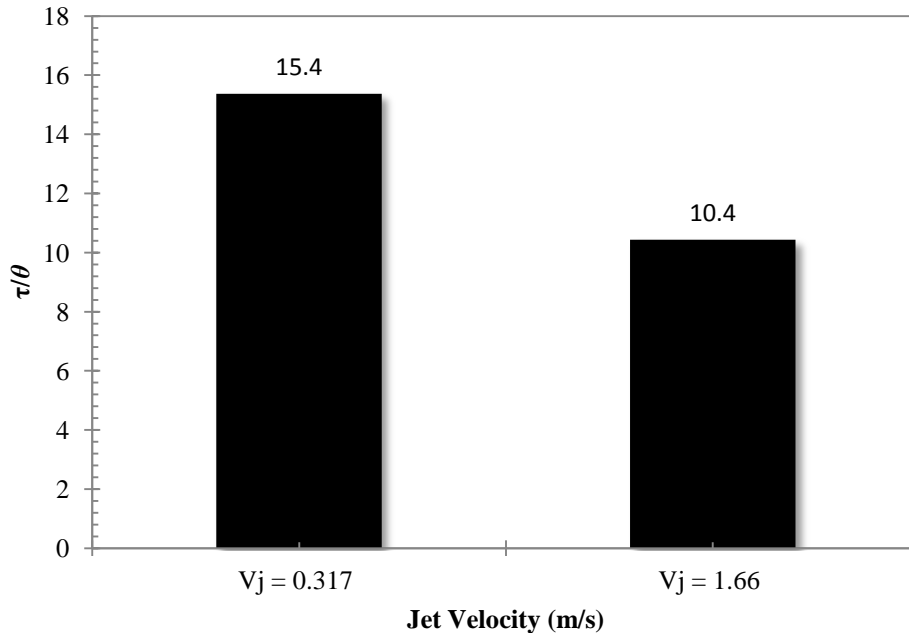


Figure (5.4-7). Effect of the jet velocity on the ratio of the residence time to the mixing time (3AH impeller, $Q = 9.65$ L min⁻¹, 1.0% xanthan gum, $C = H/2.7$, $H = T/0.93$, residence time = 292 s, and input-output locations: TI–BO).

The experiments were carried out using the 3AH impeller at $Q = 9.65 \text{ L min}^{-1}$, 1.0% xanthan gum, $C = H/2.7$, $H = T/0.93$, residence time = 292 s, and input-output locations: TI–BO. The results show that as the jet velocity was increased from 0.317 to 1.66 m s^{-1} , the ratio of τ to θ decreased. The dynamic test results showed that at the same operating conditions, as the jet velocity (V_j) was increased from 0.317 to 1.66 m s^{-1} , the extent of non-ideal flows decreased in the continuous-flow mixing vessel. When the inlet stream is fed into the tank at a high velocity, the surrounding bulk fluid is entrained into the feed zone, thus improving the mixing. Furthermore, the high jet velocity carries the feed promptly to the impeller region, where the feed is exposed to high turbulence and gets mixed better. At the same operating conditions the system with $V_j = 1.66 \text{ m s}^{-1}$ could remove non-ideal flows at a lower impeller speed than the system with $V_j = 0.317 \text{ m s}^{-1}$. However, at the lower impeller speed, the mixing time in the batch mode is higher. Therefore, for a given residence time ($\tau = 292 \text{ s}$), the ratio of τ to θ for the system with $V_j = 0.317 \text{ m s}^{-1}$ was higher than that for the system with $V_j = 1.66 \text{ m s}^{-1}$.

5.4.2.8 Effect of Fluid Height in the Vessel

Another parameter, which affects the efficiency of the continuous-flow mixing, is the fluid height within the mixing vessel. The volume of fluid in the mixing vessel relies on the vessel diameter (T) and fluid height (H) in the tank. Three different fluid heights ($H = T/0.83$, $T/0.93$, and $T/1.06$) in the mixing vessel were tested in this study. To maintain the constant residence time of the fluid in the continuous-flow mixing system, the inlet flow rates (Q) were manipulated accordingly ($Q = 8.47$, 9.65 and 10.8 L min^{-1}). Figure (5.4-8) shows the effect of the fluid height (H) in the vessel on the ratio of the residence time to the mixing time. The experiments were carried out using the 3AH impeller at 1.0% xanthan gum, $C = H/2.7$, $V_j = 0.317 \text{ m s}^{-1}$, residence time = 292 s, and input-output locations: TI–BO. The results show that when the fluid height in the vessel (at constant residence time) was increased, the ratio of τ to θ decreased. The dynamic test results showed that as the fluid height in the vessel was increased, the extent of non-ideal flows also increased. This was due to poor mixing at the upper part of the tank and below the fluid surface when the height of the fluid was increased at a fixed impeller clearance. Thus, for identical operating conditions, the system with a fluid height of $H = T/1.06$ was more effective in reducing non-ideal flows compared to those with fluid heights

of $H = T/0.83$, and $T/0.93$. However, in the batch mixing process, as the fluid volume in the vessel was increased (the other conditions were kept constant), the mixing time also increased. Therefore, for a given residence time ($\tau = 292$ s), the continuous-flow mixing system with a fluid height of $H = T/1.06$ required a higher value of τ/θ for the ideal mixing compared to those with $H = T/0.83$, and $T/0.93$.

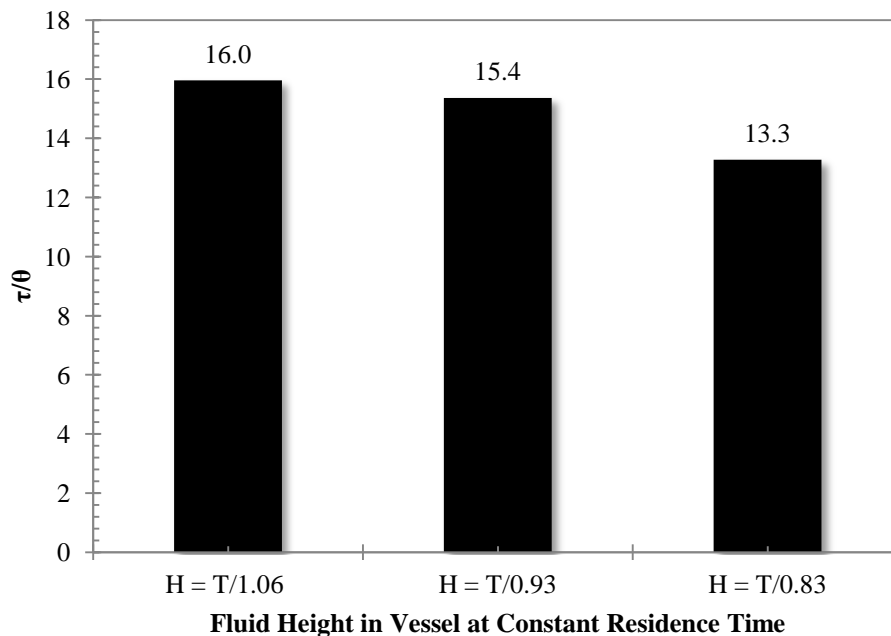


Figure (5.4-8). Effect of the fluid height (H) in the vessel on the ratio of the residence time to the mixing time (3AH impeller, 1.0% xanthan gum, $C = H/2.7$, $V_j = 0.317$ m s⁻¹, residence time = 292 s, and input-output locations: TI–BO).

5.4.2.9 Effect of Fluid Residence Time

The residence time of the fluid plays a significant role in continuous-flow mixing processes. Time taken by a fluid molecule to reach the outlet from the inlet is known as residence time and it is calculated from the ratio of the fluid volume (V_{total}) in the vessel to the feed flow rate (Q). In this study, three different residence times (257, 292, and 328 s) were tested by changing fluid heights ($H = 36, 41, \text{ and } 46$ cm) at a constant feed flow rate ($Q = 9.65$ L min⁻¹). Figure (5.4-9) shows the effect of the fluid residence time on the ratio of the residence time to the mixing time. The experiments were carried out using the 3AH impeller at $Q = 9.65$ L min⁻¹, 1.0% xanthan gum, $C = H/2.7$, $H = T/0.93$, $V_j = 0.317$ m s⁻¹, and input-output locations: TI–BO.

The results show that when the residence time was increased, the ratio of τ to θ decreased. The dynamic test results showed that the extent of non-ideal flows reduced with an increase in the fluid residence time. As the residence time was increased, the fluid had more time to stay within the mixing vessel and had more chances to interact with the intense mixing zone around the impeller. As a result, ideal mixing was achieved at lower impeller speed when the fluid residence time was higher. However, a lower impeller speed resulted in a longer mixing time in the batch process. Therefore, as the fluid residence time increased in the vessel, the ratio of τ to θ decreased.

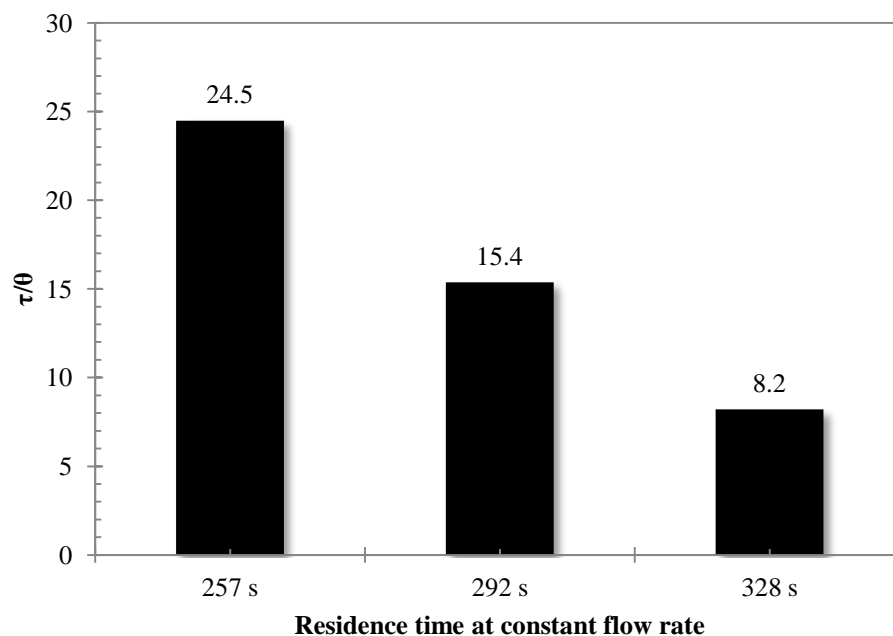


Figure (5.4-9). Effect of the fluid residence time in the mixing vessel on the ratio of the residence time to the mixing time (3AH impeller, $Q = 9.65 \text{ L min}^{-1}$, 1.0% xanthan gum, $C = H/2.7$, $H = T/0.93$, $V_j = 0.317 \text{ m s}^{-1}$, and input-output locations: TI-BO).

5.4.3 Conclusions

This study attempted to find the ratio of the residence time to the mixing time, which is required for ideal mixing as a function of different operating conditions and design parameters.

This ratio was calculated using the mixing time measured through ERT and the residence time obtained from the dynamic test. The importance of each factor and the results are listed below:

- As the fluid yield stress was increased by increasing the fluid concentration from 0.5 to 1.5%, the ratio of τ to θ increased from 11.2 to 14.8.
- The ratio of τ to θ for the axial-flow impellers with a high solidity ratio (3AH and A315) was higher than that for the low solidity ratio impellers (A310 and 3AM). The Scaba impeller provided the highest value of τ/θ among the radial-flow impellers utilized in this study.
- The value of τ/θ for the down pumping mode of an axial-flow impeller was higher than that for up-pumping of an axial-flow impeller.
- To achieve ideal mixing, the TI–BO configuration provided a higher value of τ/θ compared to the BI–TO configuration.
- The value of τ/θ required for ideal mixing decreased when the impeller was placed at half the fluid height ($C = H/2.1$) rather than lower ($C = H/2.7$).
- For the TI–BO configuration, as the jet velocity of the feed stream in the mixing system was increased the ratio of τ to θ decreased.
- The ratio of τ to θ decreased when the fluid height in the mixing vessel was increased.
- The ratio of τ to θ required to eliminate non-ideal flows within the continuous-flow mixing system decreased with an increase in the fluid resistance time.
- This study showed that for ideal mixing conditions the ratio of the residence time to the mixing time should be higher than 8.2 for the continuous-flow mixing of non-Newtonian fluids.

5.5 Tomography Images to Analyze the Deformation of the Cavern in the Continuous-Flow Mixing of Non-Newtonian Fluids (Patel et al., 2014a)

5.5.1 Introduction

Continuous-flow mixing of Newtonian-fluids in stirred vessels have been studied widely using CFD (Aubin et al., 2006; Khopkar et al., 2004), residence time distribution (Samaras et al., 2006), laser Doppler velocimetry (Mavros et al., 1997, 2000a, 2000b) and spectrophotometer (Roussinova and Kresta, 2008). While continuous-flow mixing of non-Newtonian fluids have been studies using Dynamic tests (Saeed and Ein-Mozaffari, 2008; Ein-Mozaffari et al., 2003a) and CFD (Ford et al., 2006). However, to study the fluid flows field in mixing system experimentally, electrical resistance tomography is more advantageous, efficient, and non-intrusive measurement technique.

Based on comprehensive literature review, no scientific work has been done regarding the application of ERT to quantify the deformation of the cavern in the continuous-flow mixing of non-Newtonian fluids. Furthermore, no study has been attempted to relate the volume of the cavern (V_c) in the batch mode to the fully-mixed volume ($V_{fully\ mixed}$) in the continuous-flow mode. Therefore, the objective of this study was to explore the effects of four inlet-outlet configurations, fluid rheology (0.5–1.5% xanthan gum concentration), high-velocity jet (0.317–1.660 m s⁻¹), and feed flow rate (3.20–14.17 L min⁻¹) on the deformation of the cavern using ERT. This study has demonstrated an efficient method for flow visualization in the continuous-flow mixing of opaque fluids using 2D and 3D tomograms.

To measure the cavern size in the batch mode, the experimental setup with ERT shown in Figure (3.2-1) and procedure explained in Section (3.4.4) were employed. To measure the fully mixed volume in the continuous mode, the experimental setup shown in Figure (3.1-1) were used. The extent of non-ideal flows was quantified using a dynamic model [Equation (2.4–7)]. The rheological behaviour of the xanthan gum solutions was described by the Herschel-Bulkley

model [Equation (2.1–9)]. To visualize the deformation of the cavern, the mixing tank with the ERT system was assembled with the continuous-flow mixing system used for dynamic tests.

5.5.2 Results and Discussion

5.5.2.1 Dimensionless Cavern Diameter

To measure the cavern size in the batch mode, 30 mL of 5% saline solution (tracer) was injected directly into the xanthan gum solution near the impeller hub (Plane P_4) using a plastic syringe and the tracer concentration was monitored using ERT. Measurements were collected from six planes of electrodes until the cavern size remained unchanged. The detail procure for cavern size measurement is provided in section (3.4.4) and an example is demonstrated in Figure (3.4-4). The measured cavern diameter was compared to those predicted using Elson's cylindrical model [Equation (2.3–1)]. This model can be used to estimate the cavern diameter before the cavern touches the vessel wall. Figure (5.5-1) shows the dimensionless diameter (D_c/D) versus dimensionless $P_o Re_y$ on a log-log scale for the RT impeller and two axial-flow impellers (A310 and 3AM). The diameter of the cavern was found to increase with an increase in the impeller speed and it continued to grow until the cavern reached the vessel wall. According to Elson's cylindrical model [Equation (2.3–1)], a log-log plot of the D_c/D versus $P_o Re_y$ should give a slope of 1/3. As shown in Figure (5.5-1), the slope of this line calculated using the least-square method was 0.34 for the RT impeller. However, the slope of the D_c/D versus $P_o Re_y$ for the axial-flow impellers was 0.25, which was lower than that expected from Elson's cylindrical model. Galindo and Nienow (1992) reported a value of 0.25 for the slope of the D_c/D versus $P_o Re_y$ for the A315 axial-flow impeller and Saeed et al. (2008) reported a value of 0.24 for the A200, A100, and A310 axial-flow impellers. Thus, the results found in this study agreed well with the value reported in the open literature. In this study, the slope of the D_c/D versus $P_o Re_y$ line was found to be lower for the axial-flow impeller than that of the RT impeller (a radial-flow impeller). It means that a radial-flow impeller can provide a larger cavern diameter compared to an axial-flow impeller. This is due to the nature of impellers, as radial-flow impellers discharge fluid radially outward to the vessel wall, while axial-flow

impellers discharge fluid axially along the shaft. Moreover, the radial-flow impellers provide a higher shear level with lower pumping compared to the hydrofoil impellers (A310 and 3AM).

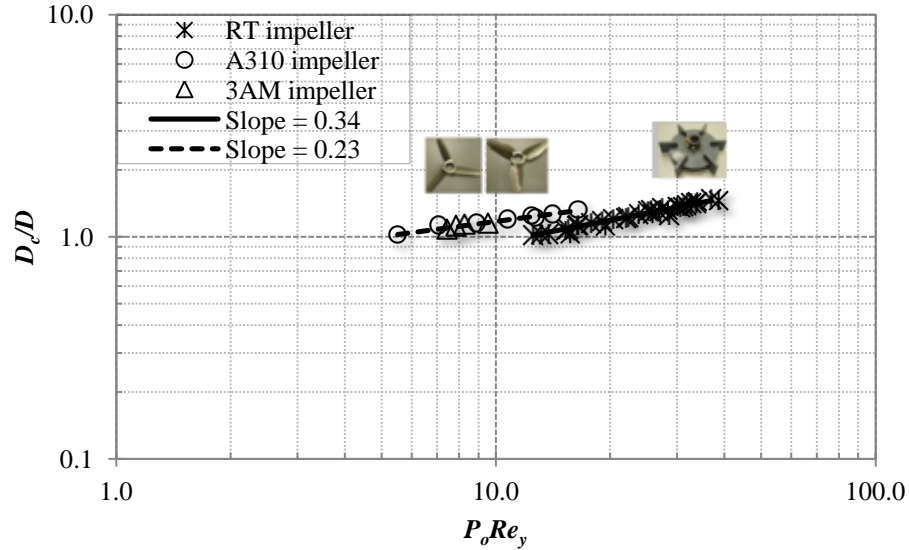


Figure (5.5-1). Dimensionless cavern diameter (D_c/D) vs. dimensionless $P_o Re_y$ for the radial-flow impeller (RT) and axial-flow impellers (A310 and 3AM).

5.5.2.2 Ratio of Cavern Height to Cavern Diameter

In addition to the cavern diameter, the cavern height (H_c) was measured on a vertical plane along the shaft and perpendicular to the horizontal plane of the impeller. Figure (5.5-2) demonstrates the dimensionless cavern height (H_c/D_c) versus the impeller speed (N) for the RT impeller and two axial-flow impellers (A310 and 3AM). It can be seen that before the cavern touched the wall, the ratio H_c/D_c was almost constant at 0.50 for the RT impeller. The value of this ratio is equal to the value reported by Hirata and Aoshima (1996). It can be also seen that the cavern height to cavern diameter ratio was constant at 0.78 for both axial-flow impellers. Saeed et al. (2008) reported that the H_c/D_c was constant at 0.80 for the A310 impeller (axial-flow impeller). The results were in good agreement with those reported in the literature. The results clearly demonstrate that the caverns generated by the axial-flow impellers are taller than those of the radial-flow impeller. This is due to the fact that the axial-flow impellers discharge fluid axially along the shaft while the radial-flow impellers discharge fluid radially outward to

the vessel wall. Elson (1988) also reported that the H_c/D_c ratio was higher for the axial-flow impellers (pitched blade turbine and paddle) than for the radial-flow impeller (disc turbine).

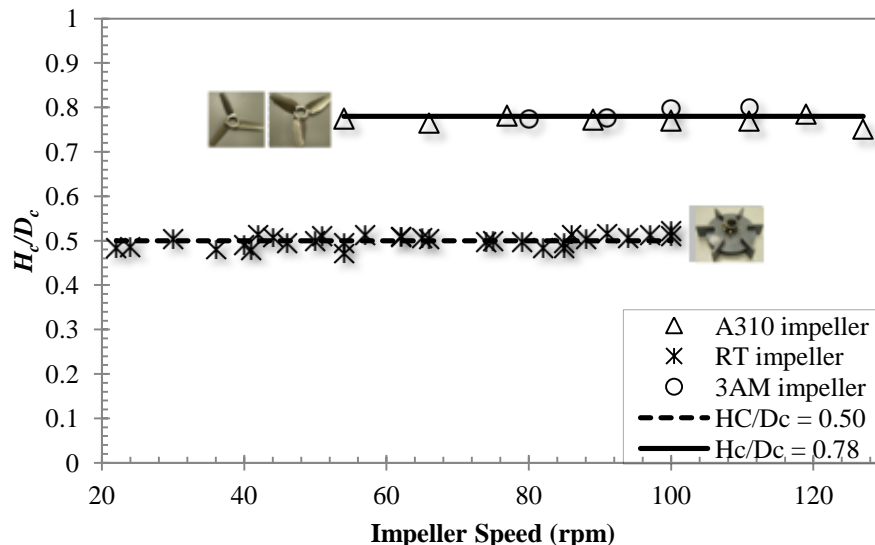


Figure (5.5-2). Dimensionless cavern height (H_c/D_c) vs. impeller speed (N) for the radial-flow impeller (RT) and axial-flow impellers (A310 and 3AM).

5.5.2.3 Effect of Fluid Rheology on Cavern Volume

The cavern volume (V_c) was calculated using the cavern diameter (D_c) and the cavern height (H_c) for a cylindrical shape. Figure (5.5-3) represents the effect of fluid rheology on the dimensionless cavern volume (V_c/V_{total}) versus the power per unit volume for the RT impeller at 0.5, 1.0, and 1.5% xanthan gum solutions in the batch mode. The results show that as the impeller speed/power was increased, the cavern diameter and height also increased for all concentrations and so did the cavern volume (V_c). However, with respect to the xanthan gum concentration, the dimensionless cavern volume (V_c/V_{total}) was observed as decreasing. This can be attributed to the effect of the yield stress, which increases with the xanthan gum concentrations. More stagnant regions are formed in the mixing vessel where shear stress fails to exceed yield stress, which reduces the cavern volume. Therefore, the dimensionless cavern volume decreased with an increase in the xanthan gum concentrations.

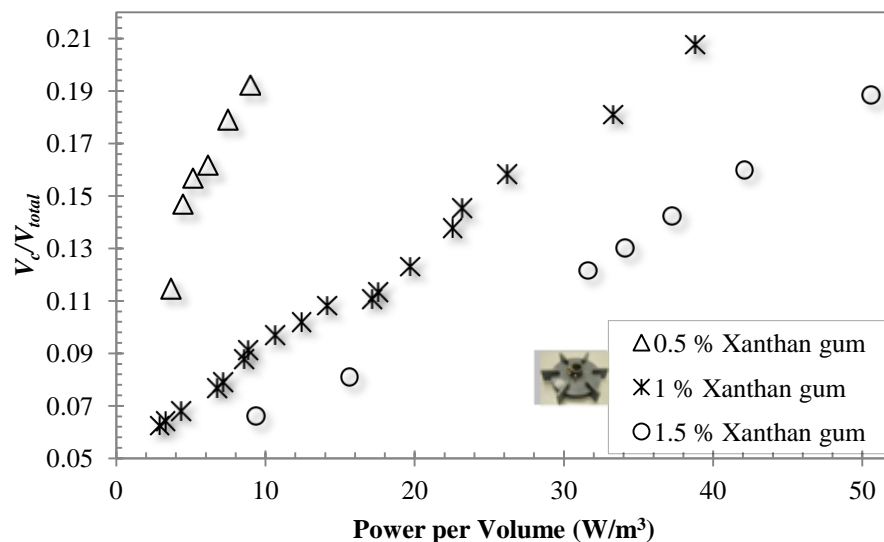


Figure (5.5-3). Effect of the fluid rheology on the dimensionless cavern volume for the RT impeller at 0.5, 1.0, and 1.5% xanthan gum solutions.

5.5.2.4 Effect of Impeller Type on Cavern Volume

The cavern volume was also calculated for the axial-flow impellers. Figure (5.5-4) demonstrates how impeller types (axial-flow and radial-flow) influenced the dimensionless cavern volumes at 1.0% xanthan gum solution in the batch mode. It can be seen that for given operating conditions, the hydrofoil impellers (A310 and 3AM) were more efficient than the radial-flow impeller (RT) in generating a larger cavern. Similar results were found by Amanullah et al. (1997) who showed that the axial-flow impeller produced larger cavern volumes for a given power input than the radial-flow impeller. It should be mentioned that although both axial-flow and radial-flow impellers are designed for the transitional and turbulent flow applications, the hydrofoil impellers (A310 and 3AM) can provide a high axial-flow at a reduced shear. They are also more efficient and are capable of more streamlined pumping. Compared to the axial-flow impellers, the radial-flow impellers provide a higher shear and turbulence level with lower pumping (Paul et al., 2004).

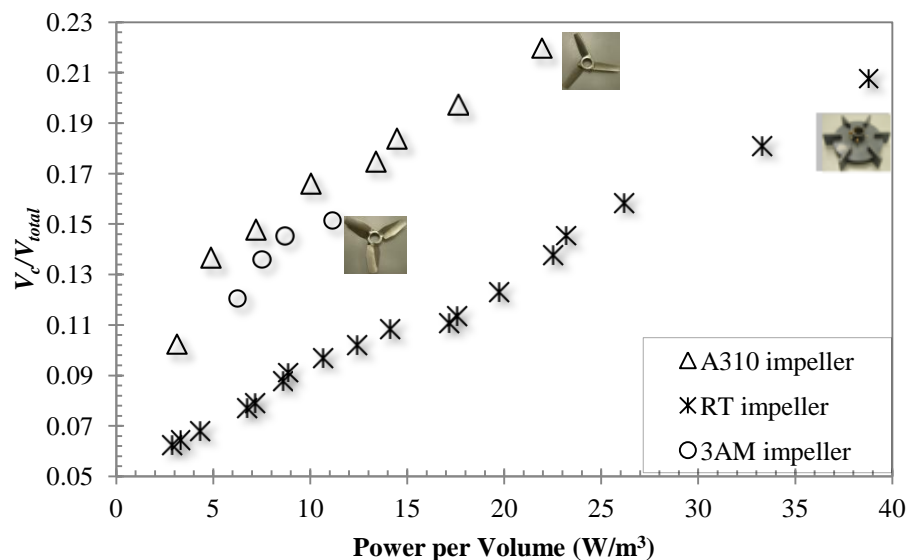


Figure (5.5-4). Effect of the impeller type on the dimensionless cavern volume (A310, RT, and 3AM impellers and 1.0% xanthan gum solution).

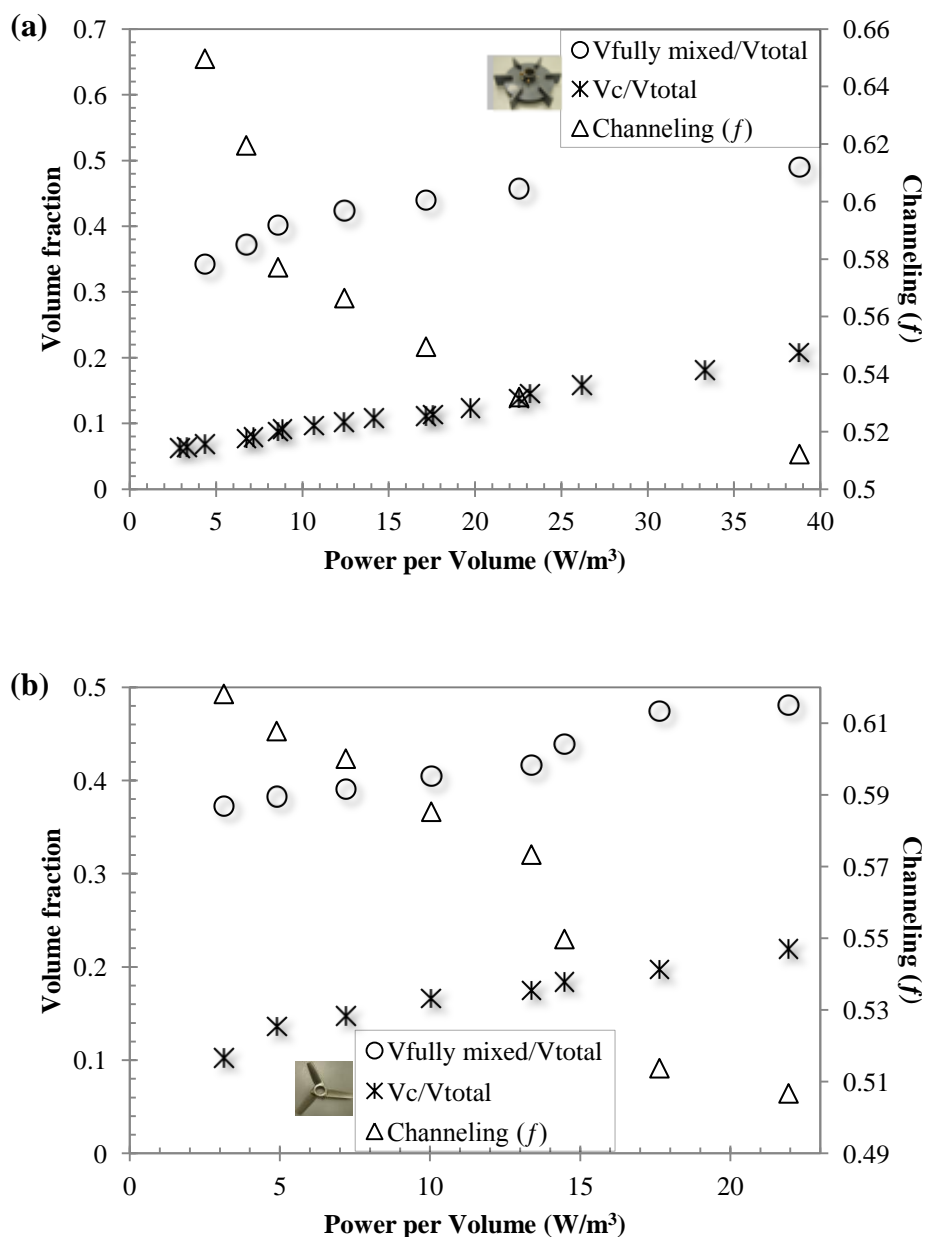
5.5.2.5 Comparison of Cavern Volume and Fully Mixed Volume

To compare the cavern volume (V_c) in the batch vessel with the fully mixed volume ($V_{fully\ mixed}$) in the continuous-flow mixing system, dynamic tests were also performed for the axial-flow impellers (A310 and 3AM) and the radial-flow impeller (RT) agitated in 1% xanthan gum solution. In these experiments, ERT tests in the batch mode and dynamic tests in the continuous-flow mode were conducted with the identical operating conditions except for the feed flow rate ($Q = 9.65\text{ L min}^{-1}$, residence time = 292 s) and the location of the inlet and outlet, which were additional to the continuous-flow mode. The comparisons between the dimensionless cavern volume (V_c/V_{total}) in the batch mode and the fraction of the fully mixed volume ($V_{fully\ mixed}/V_{total}$) in the continuous-flow mode for the RT, A310, and 3AM impellers are depicted in Figure (5.5-5a, b, and c), respectively. From the results, it can be clearly seen that the fully mixed volume generated in the continuous-flow mixing system was higher than the cavern volume generated in the batch mixing system for all three (RT, A310, and 3AM) impellers with the given operating conditions. This can be attributed to the momentum added to the fluid in the mixing vessel by the input and output flows passing through the vessel. Mixing of the fluid requires the input of mechanical energy to achieve the process results. In both the

batch and continuous-flow modes, this energy is generally provided through the impeller. An alternative method for getting energy into the fluid is to generate a jet stream of fluid in the vessel. This jet entrains and mixes the surrounding fluids, and the mechanical energy is supplied from a pump (Paul et al., 2004). This is achieved through the feed stream in the continuous-flow mode. In fact, in the continuous-flow mixing system the fluid passing from the inlet to the outlet generates extra flows and adds more momentum to the fluid flow in the stirred vessel. The extra momentum flux ($Q \rho v/A$, where v is the velocity of the fluid passing through the inlet, and A is the cross section area of the inlet pipe) added to the fluid in the mixing vessel at the inlet position was about $99.92 \text{ kg m}^{-1} \text{ s}^{-2}$. Due to this fact, the size of the mixed volume in the continuous mode was higher than that in the batch mode. It is very clear from the images shown in Figure (5.5-6a) that the size of the cavern increased as the flow passed through the mixing tank. These images are discussed in detail in the subsequent paragraph where the ERT flow visualization results are described. Furthermore, the momentum flux generated due to the inlet-outlet flow was compared with the momentum flux generated by the impeller. The impeller pumping rate ($Q_{impeller}$) is defined as $Q_{impeller} = N_Q N D^3$, where N_Q is the impeller flow number (Uhl and Gray, 1966). N_Q for the A310 impeller was obtained from the literature (Saeed, 2007). The momentum flux ($Q_{impeller} \rho v_{tip}/A_i$, where v_{tip} is the impeller tip velocity, and A_i is the swept area by the impeller) generated by the A310 impeller at $N = 30$ rpm was estimated at about $1.57 \text{ kg m}^{-1} \text{ s}^{-2}$, which was almost 63.5 times lower than the momentum flux generated by the inlet flow ($99.92 \text{ kg m}^{-1} \text{ s}^{-2}$). The momentum flux generated by the A310 impeller at $N = 100$ rpm was about $73.32 \text{ kg m}^{-1} \text{ s}^{-2}$, which was approximately 1.3 times lower than the momentum flux generated by the inlet flow ($99.92 \text{ kg m}^{-1} \text{ s}^{-2}$). Thus, these results demonstrate that at a lower impeller speed, the momentum flux added to the system due to the inlet flow had a tremendous effect on the mixing of the non-Newtonian fluids exhibiting yield stress.

In addition, the channeling (f) was identified through the dynamic tests with identical operating conditions for the RT, A310, and 3AM impellers and the results are depicted in Figure (5.5-5a, b, and c), respectively. The results show that as the power input was raised by increasing the impeller speed, the channeling (f) decreased for all three impellers. At a lower impeller speed, the shear stress produced by the impeller was less than the yield stress of the

fluid in the stagnant zone. At a higher impeller speed the xanthan gum solution was swept away from the impeller, leading to improved mixing by overcoming the fluid yield stress. Thus, it provided less channeling by entraining the feed into the mixing zones. In fact, the channeling (f) should be minimized to enhance the efficiency of the continuous-flow mixing system.



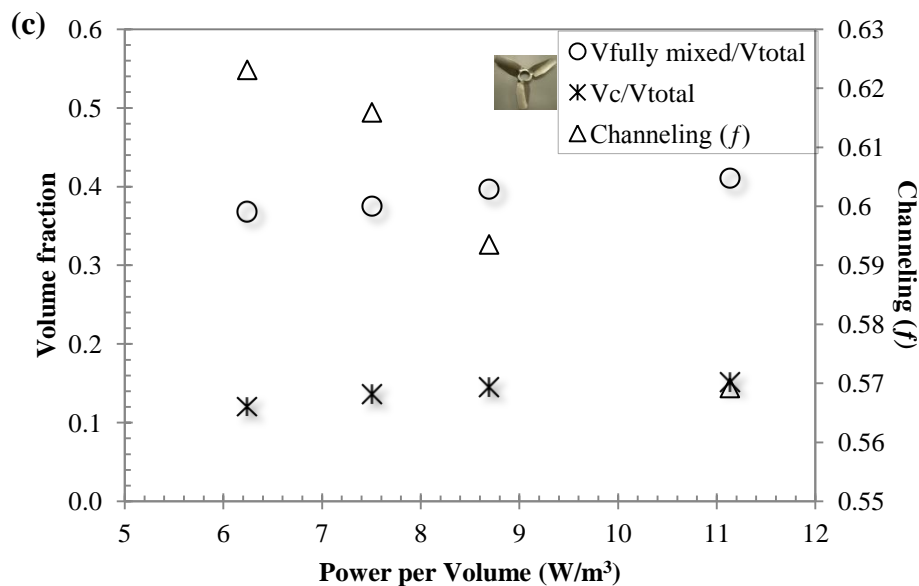


Figure (5.5-5). Dimensionless cavern volume (V_c/V_{total}), the fraction of fully mixed volume ($V_{\text{fully mixed}}/V_{\text{total}}$), and the extent of channeling (f) as a function of the specific power at 1% xanthan gum solution for the (a) RT impeller, (b) A310 impeller, and (c) 3AM impeller.

5.5.2.6 Deformation of the Cavern Using Tomography Images

The subsequent discussions explain how the input-output flow in continuous-flow mixing affected the cavern formation. As described in the procedure [section (3.4.4)], once the cavern remained unchanged in the batch mode, the feed and discharge pumps were turned on simultaneously. ERT data were collected and 2D tomography images were generated. As shown in Figure (3.4-4), 2D tomograms were converted into 3D images and were sliced using the Slicer Dicer software to get insight into what was happening within the mixing vessel. As mentioned earlier, the cavern volume (V_c) was calculated using the cavern diameter (D_c) and the cavern height (H_c) for a cylindrical shape. However, the shape of the deformed cavern was not exactly cylindrical. Therefore, to measure the total volume of the deformed cavern, the cavern was divided into the small cylindrical segments to approximate the volume of the deformed cavern. The cavern volume measured in batch mixing, when the feed and discharge pumps were off, was used as a reference to estimate the increase in cavern volume due to deformation in continuous mode. Error involved in estimating the cavern volume assuming the cylindrical shape was approximately 4%. The images in Figure (5.5-6) to Figure (5.5-9) are

presented in four columns in a time series (1st column from the left: Slicer Dicer X-axis image; 2nd column: Slicer Dicer Y-axis image; 3rd column: Slicer Dicer block for the inverted position of the tank; and 4th column: 2D tomograms from planes $P1$ to $P6$). In the 3rd column, the Slicer Dicer images of the tank are presented in an inverted position as it is difficult to view the bottom of the tank from the top. In this 3D image, the upper surface shows the bottom of the tank and the lower surface shows the top of the tank. The locations of the inlet and outlet are also shown in the Slicer Dicer images. The ERT images depicted in the first row in Figure (5.5-6) to Figure (5.5-9) were obtained at zero second (i.e. when the cavern size remained unchanged after the injection of the tracer in the batch mode and before the pumps were turned on). The images in the first row at zero second show that there was almost no tracer at the bottom plane $P6$ in the 2D tomogram and the top surface of the inverted position of the tank. In Figure (5.5-6) to Figure (5.5-9), the images in the 2nd, 3rd, 4th, and 5th rows were taken at 15, 25, 50, and 125 s, respectively after the pumps were turned on in the continuous mode.

5.5.2.7 Effect of Inlet and Outlet Locations on Cavern Deformation

To explore the effects of inlet and outlet locations on the deformation of the cavern, four different configurations, namely, (i) TI–BO (top inlet–bottom outlet), (ii) BI–BO (bottom inlet–bottom outlet), (iii) TI–TO (top inlet–top outlet), and (iv) BI–TO (bottom inlet–top outlet) were tested in the continuous mode for the RT impeller at $N = 30$ rpm, $Q = 9.65$ L min⁻¹, 1.0% xanthan gum, $V_j = 0.317$ m s⁻¹, and the ERT results are depicted in Figure (5.5-6a, b, c, and d), respectively. In the case of the TI–BO configuration [Figure (5.5-6a)], as the feed and discharge pumps were started simultaneously, images in the second row clearly show that the cavern shape was slightly deformed at the bottom. This was due to the flow of fluid sucked from the bottom outlet (BO) by the discharge pump. At that moment, the tracer appeared at plane $P6$ in the 2D tomogram and the top surface of the inverted position of the tank. As time passed, the fresh xanthan gum solution was continuously fed to the tank through the top inlet (TI) and the mixed solution was drawn from the vessel through the bottom outlet (BO). Due to this input-output flow, the cavern shape recorded in the batch mode was deformed in the continuous mode. The concentration of the tracer at the bottom plane $P6$ in the 2D tomogram and the top surface of the inverted position of the tank increased as shown in subsequent

images. It is very clear from the images that the size of the cavern increased as the flow passed through the mixing tank. Finally, the size of the cavern was increased by 11.2% due to the deformation caused by the inlet-outlet flow. This was due to the momentum added to the fluid in the mixing vessel by the input-output flow passing through it. The extra momentum flux added to the fluid in the mixing vessel at the inlet position was about $99.92 \text{ kg m}^{-1} \text{ s}^{-2}$.

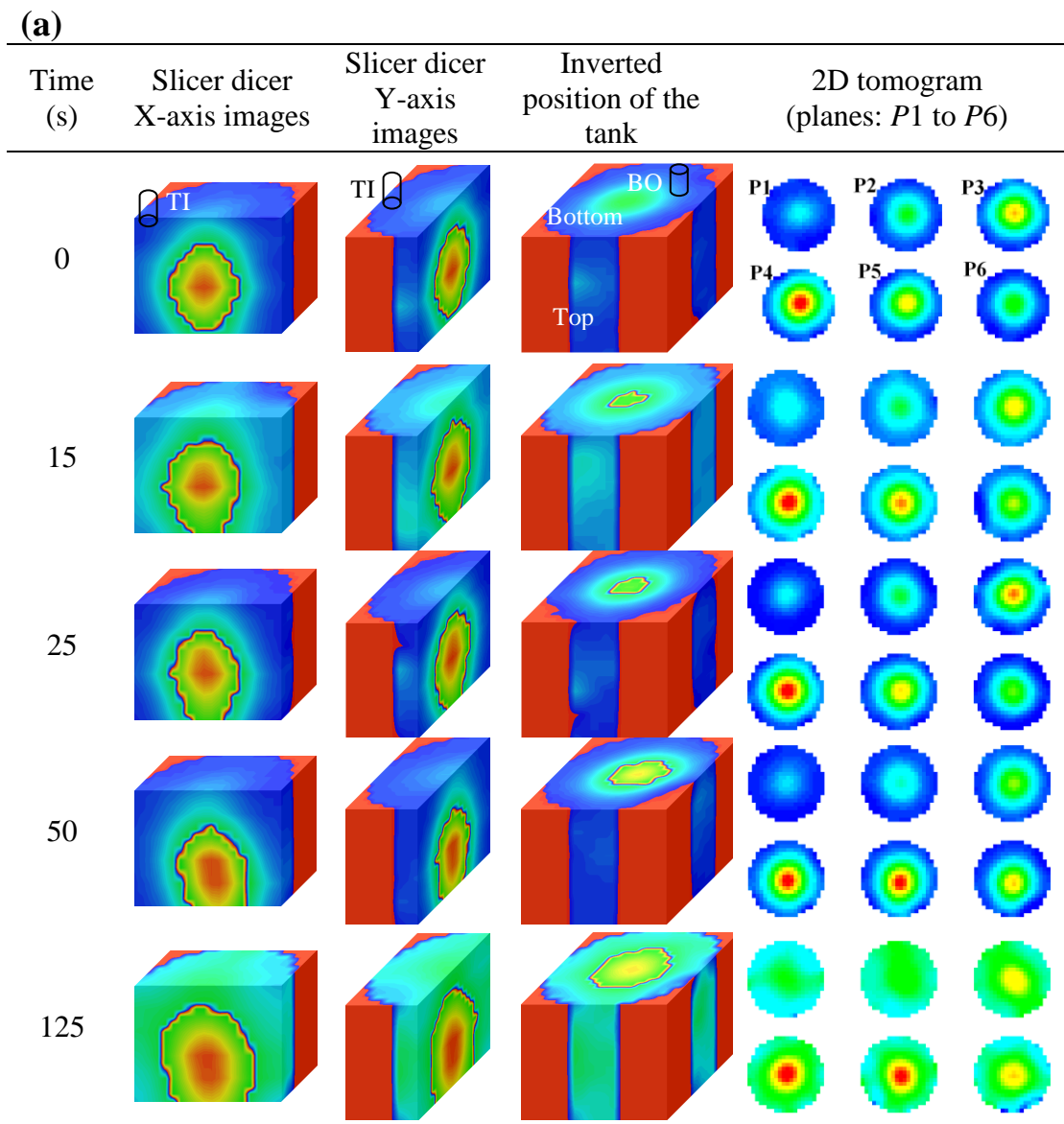


Figure (5.5-6). Effect of inlet and outlet locations on the deformation of the cavern for four different configurations: (a) TI–BO, (b) BI–BO, (c) TI–TO, and (d) BI–TO (RT impeller, $N = 30 \text{ rpm}$, $Q = 9.65 \text{ L min}^{-1}$, 1.0% xanthan gum, and $V_j = 0.317 \text{ m s}^{-1}$).

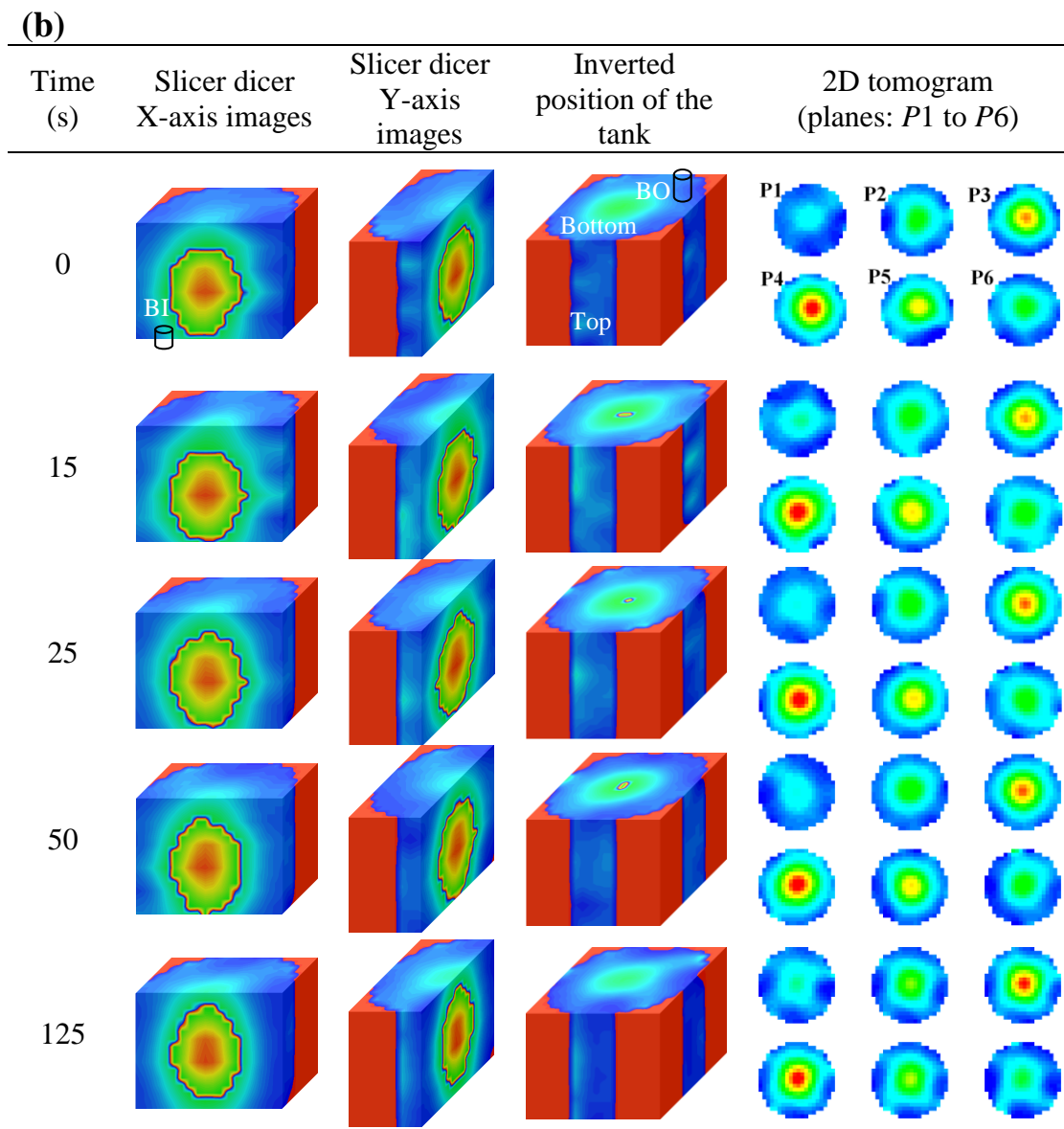


Figure (5.5-6). (Continued).

In the study of the BI–BO configuration as shown in Figure (5.5-6b), a small amount of tracer appeared on the bottom plane $P6$ in the 2D tomogram and on the top surface of the inverted position of the tank in the time series rows 2–4 after the feed and discharge pumps were turned on. In the last row the tracer disappeared at the bottom of the tank and there was no significant change in the shape of the cavern. The BI–BO configuration was more susceptible to a high degree of channeling and dead volume than the TI–BO configuration. For the BI–BO configuration, the cavern volume increased only by 2.6%.

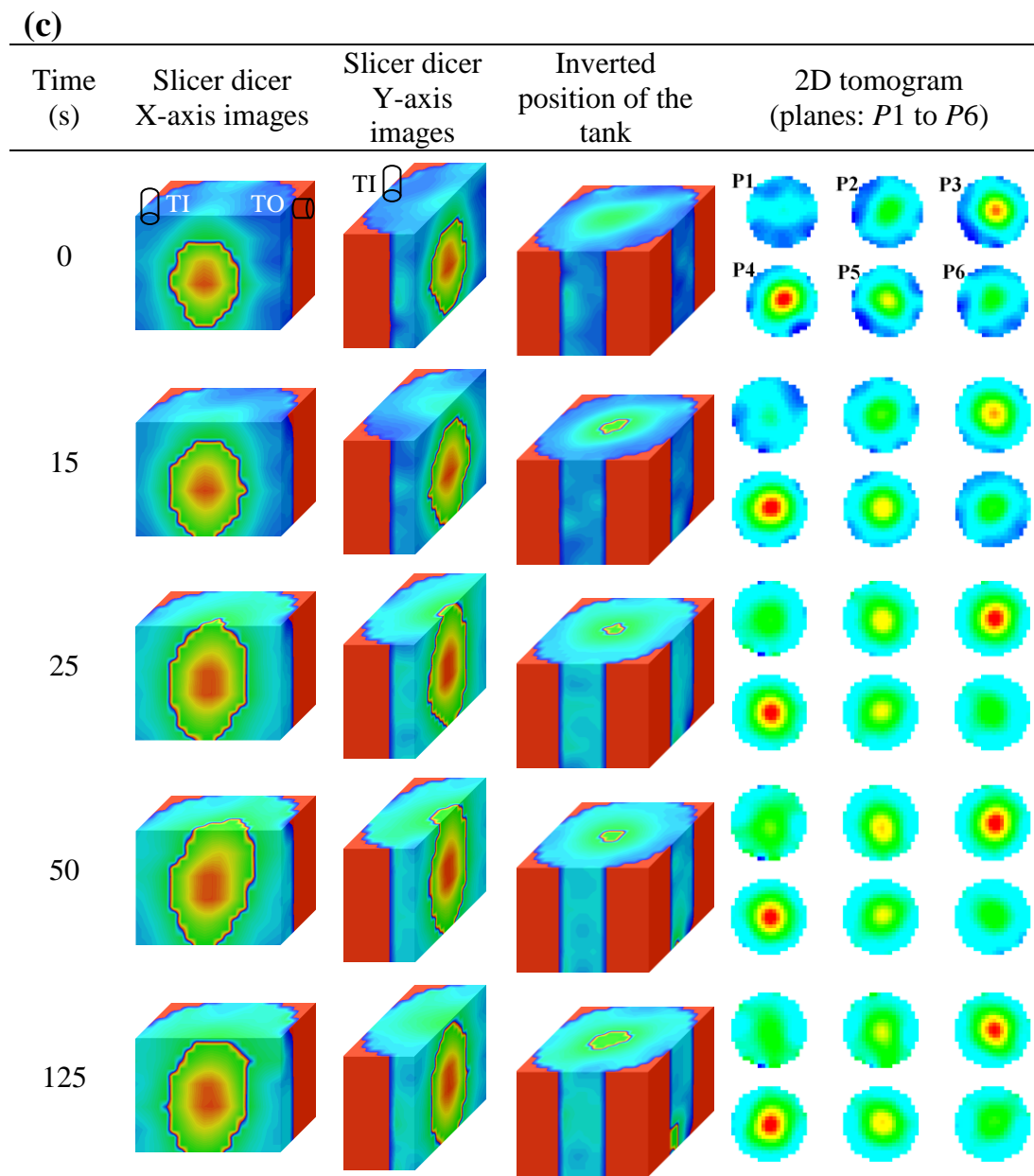


Figure (5.5-6). (Continued).

These results show that the extent of the cavern deformation was higher for the TI-BO configuration compared to that for the BI-BO configuration. Patel et al. (2011) studied the dynamic performance of the continuous-flow mixing of non-Newtonian fluids in the stirred vessel. They found that the channeling and dead volume were increased by about 5.27% and 5.15%, respectively, when the inlet location was changed from the TI-BO configuration to the BI-BO configuration for the 3AH impeller at 50 rpm. The BI-BO configuration, where both

inlet and outlet were located at the bottom of the tank, enabled a large percentage of the feed to be conveyed to the outlet without being drawn into the impeller mixing zone. Therefore, according to the cavern deformation depicted in the last row of Figure (5.5-6a and b), the input-output flow had the least effect on the deformation of the cavern in the BI-BO configuration.

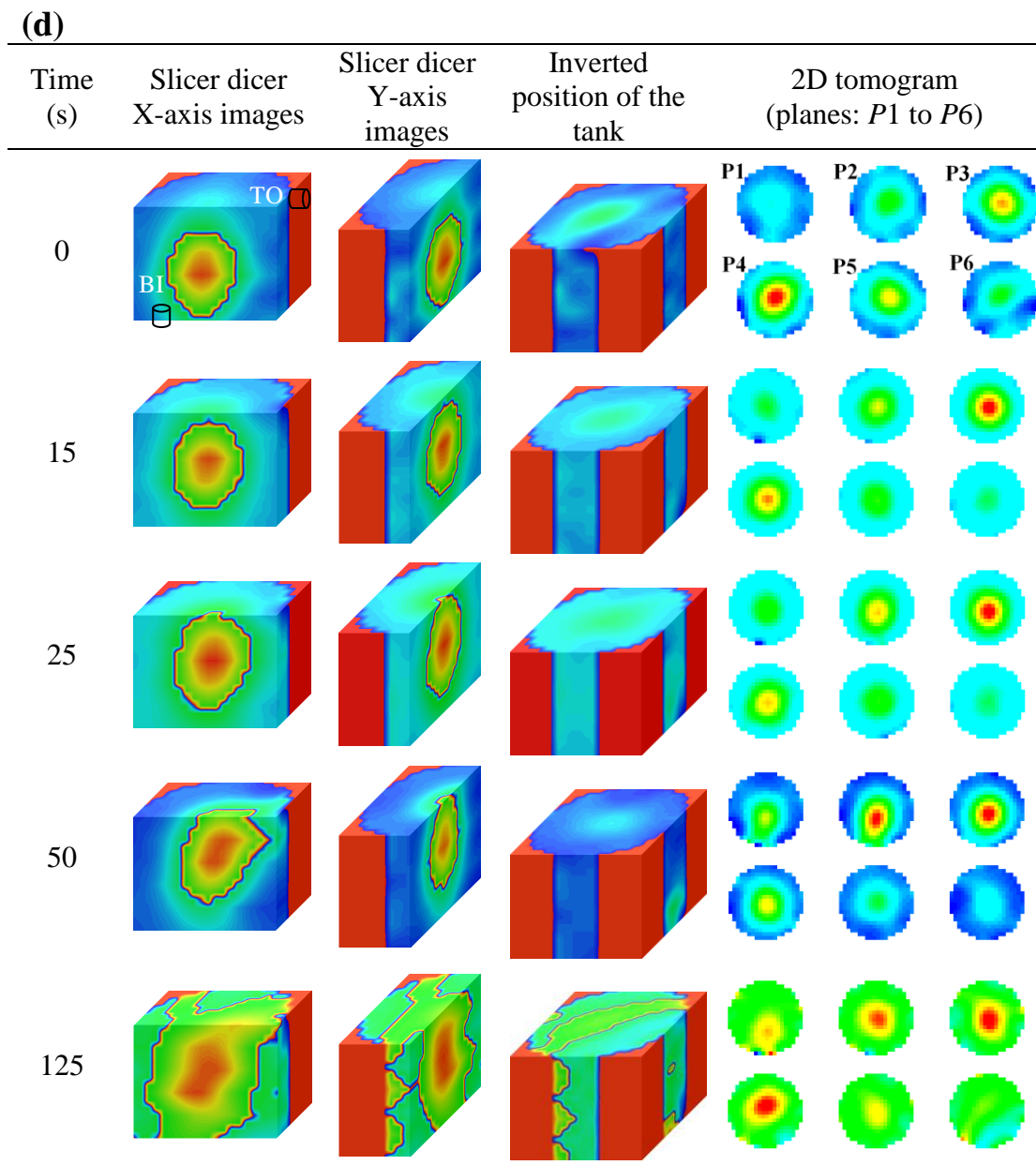


Figure (5.5-6). (Continued).

In the TI-TO configuration [Figure (5.5-6c)], once the feed and discharge pumps were turned on, the cavern shape deformed in such a way that it inclined towards the top outlet (TO).

This was due to the flow of fluid sucked from the top outlet (TO) by the discharge pump. In this configuration, the size of the cavern was increased by about 8% due to the deformation, which was less than that of the TI-BO configuration. According to the deformation of the cavern demonstrated in the last row of Figure (5.5-6a and c), it can be seen that the extent of cavern deformation was slightly more in the TI-BO configuration compared to that in the TI-TO configuration. This was due to the fact that the TI-TO configuration enabled a portion of the feed to be channeled directly to the outlet without passing through the impeller mixing zone.

In the BI-TO configuration [Figure (5.5-6d)], once the feed and discharge pumps were turned on, as shown in the 2nd to 4th rows, initially the whole cavern was slightly pushed from the lower part and shifted towards the upper part of the tank. This was due to the fact that the fresh feed was pumped to the bottom of the tank and this pushed the whole cavern from the lower part of the tank to the upper part of the tank. Simultaneously, the discharge fluid from the mixing tank was drawn from the top outlet by the discharge pump, which helped the cavern move upwards. Moving towards the last row, the amount of the tracer increased gradually on the top plane *PI* in the 2D tomogram and at the top surface of the Slicer Dicer images. The images presented in the last row show that the cavern was completely deformed by the input-output flow and spread over the entire mixing tank in the BI-TO configuration. Eventually, the enlargement of the cavern due to the deformation was about 26.7%. Based on the cavern deformation presented in the last row of Figure (5.5-6a, b, c and d), the BI-TO configuration was the most effective configuration in deforming the cavern shape rigorously in comparison to the other configurations (TI-BO, BI-BO, and TI-TO). In the case of the BI-TO and TI-BO configurations, the feed was forced to pass through the mixing zone before leaving the vessel. Nevertheless, in the BI-TO configuration, the feed had to face fluid discharge from the impeller and pass through the mixing zone in the direction opposite to the bulk flow within the vessel. Similar results were observed in the study of the dynamic performance of the continuous-flow mixing system in a stirred vessel (Patel et al., 2011).

5.5.2.8 Effect of Fluid Rheology on Cavern Deformation

The fluid rheology significantly affects the performance of the continuous-flow mixing of non-Newtonian fluids. To explore the effect of this parameter, the ERT tests were performed at the same operating conditions as those mentioned in Figure (5.5-6a) except the xanthan gum concentration. Figure (5.5-7) demonstrates the cavern deformation at 0.5% xanthan gum concentration.

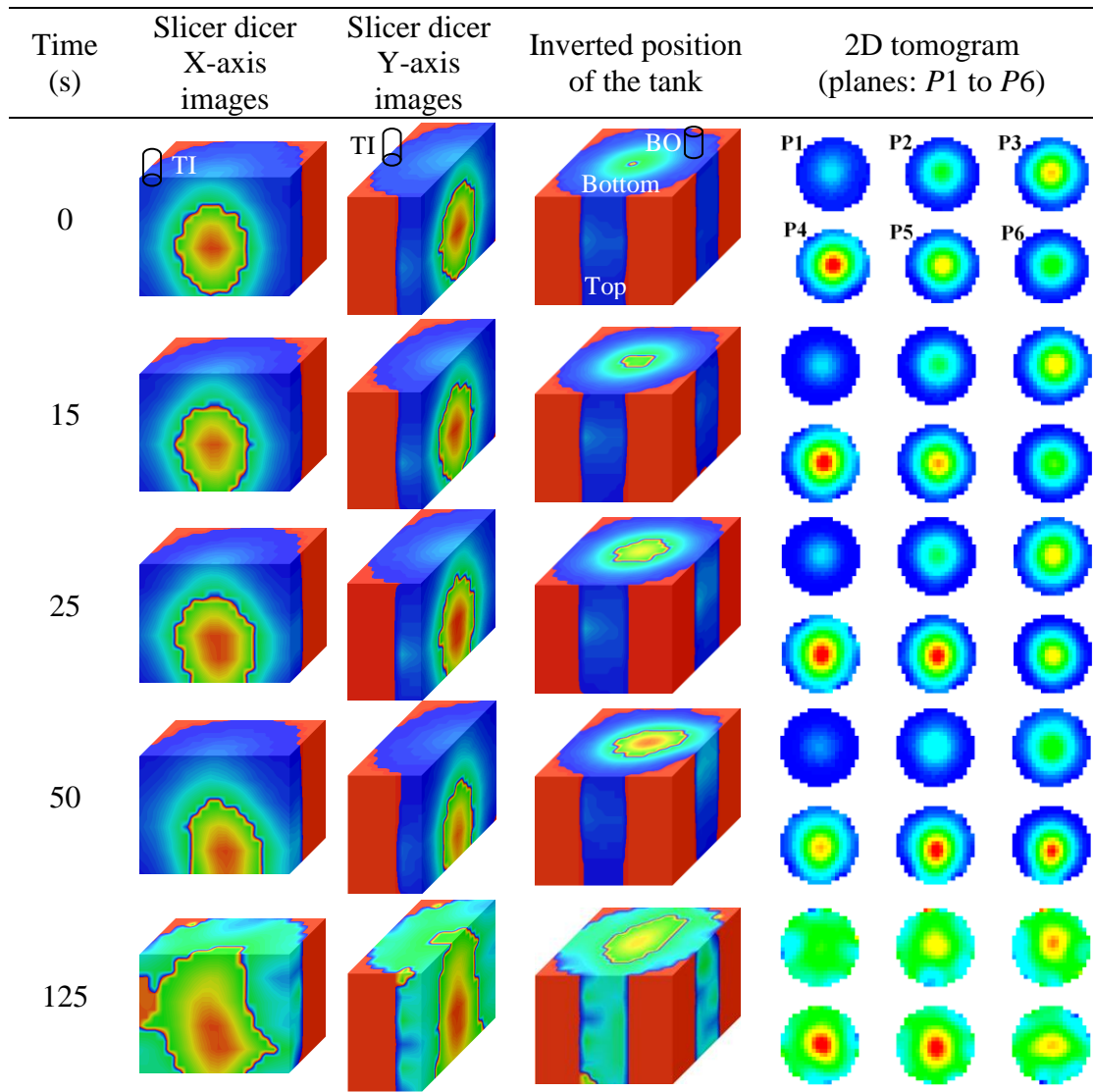


Figure (5.5-7). Tomography images obtained for the RT impeller at $N = 30 \text{ rpm}$, $Q = 9.65 \text{ L min}^{-1}$, 0.5% xanthan gum, $V_j = 0.317 \text{ m s}^{-1}$, and inlet-outlet locations: TI-BO.

Once the feed and discharge pumps were turned on, the images in the second row show that the cavern shape was slightly deformed at the bottom due to the discharge of the fluid from the bottom outlet. In the subsequent images presented in the time series, the cavern shape got more deformed and higher tracer concentration was detected at the bottom plane $P6$ in the 2D tomogram and at the top surface of the inverted position of the tank. The ERT images in the last row show that the cavern was completely deformed by the input-output flow and reached the fluid surface and the vessel wall. The size of the cavern was increased by about 21.1% due to the deformation. The images in the last row of Figure (5.5-6a) and Figure (5.5-7) show that the cavern shape was more deformed at the 0.5% xanthan gum solution than at the 1.0% xanthan gum solution. This was due to the fluid yield stress which decreased when the xanthan gum concentration was decreased from 1.0% to 0.5%. The energy dissipation at the lower yield stress is slower than that at the higher yield stress. The fluctuating velocities penetrate quickly in the area outside of the impeller zone at the lower yield stress because of the lesser apparent viscosity of the fluid, which is a function of the fluid yield stress.

5.5.2.9 Effect of Jet Velocity on Cavern Deformation

The inlet jet velocity (V_j) can also improve the efficiency of the continuous-flow mixing system. To generate a high-velocity jet of the feed in the vessel at the same flow rate, the inlet diameter was reduced. Figure (5.5-8) represents the ERT results at the same operating conditions as those mentioned in Figure (5.5-6a) except the jet velocity, which was $V_j = 1.66 \text{ m s}^{-1}$. After the feed and discharge pumps were turned on, the images in the second row show that the cavern shape was slightly deformed at the bottom due to the discharge fluid flow from the bottom outlet. The successive Slicer Dicer images presented in the 2nd to 4th rows show that the cavern shape at the left hand side was squeezed more compared to the right hand side due to the inlet jet flow. The ERT images in the last row demonstrate that cavern shape was rigorously deformed by the high-velocity jet of the fluid and the cavern volume was increased by about 14.8% due to this deformation. From the images depicted in Figure (5.5-6a) and Figure (5.5-8), it can be seen that as the jet velocity (V_j) was increased from 0.317 to 1.66 m s^{-1} , the deformation of the cavern shape was more noticeable. When an inlet stream is fed into a tank at high velocity, it is expected that the surrounding bulk fluid will be entrained into the feed zone,

thus improving the mixing quality. Moreover, the high-velocity jet of fluid transports the feed promptly to the impeller zone, where it is exposed to high turbulence and is mixed better (Patel et al., 2011).

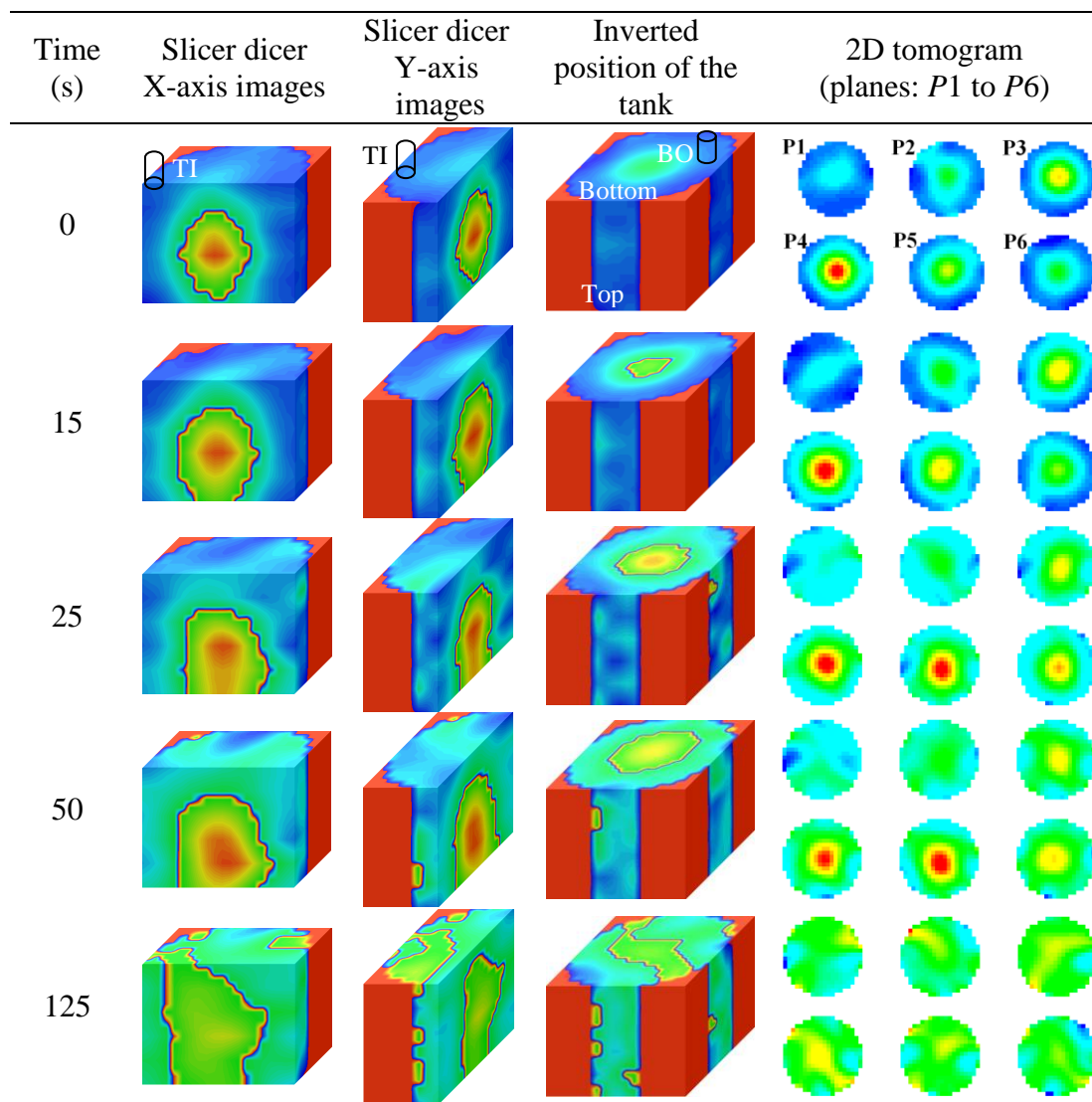


Figure (5.5-8). Tomography images obtained for the RT impeller at $N = 30$ rpm, $Q = 9.65$ L min^{-1} , 1.0% xanthan gum, $V_j = 1.66$ m s^{-1} , and inlet-outlet locations: TI–BO.

5.5.2.10 Effect of Fluid Flow Rate on Cavern Deformation

The mixing quality in the continuous-flow mixing system also largely depends on the feed flow rate through the mixing vessel. To study the effects of the feed flow rates on the deformations of the cavern, the ERT tests were conducted at the same operating conditions as those

mentioned in Figure (5.5-6a) except the feed flow rate (Q). Figure (5.5-9a and b) depicts the tomography images for $Q = 3.2 \text{ L min}^{-1}$ and $Q = 14.17 \text{ L min}^{-1}$, respectively.

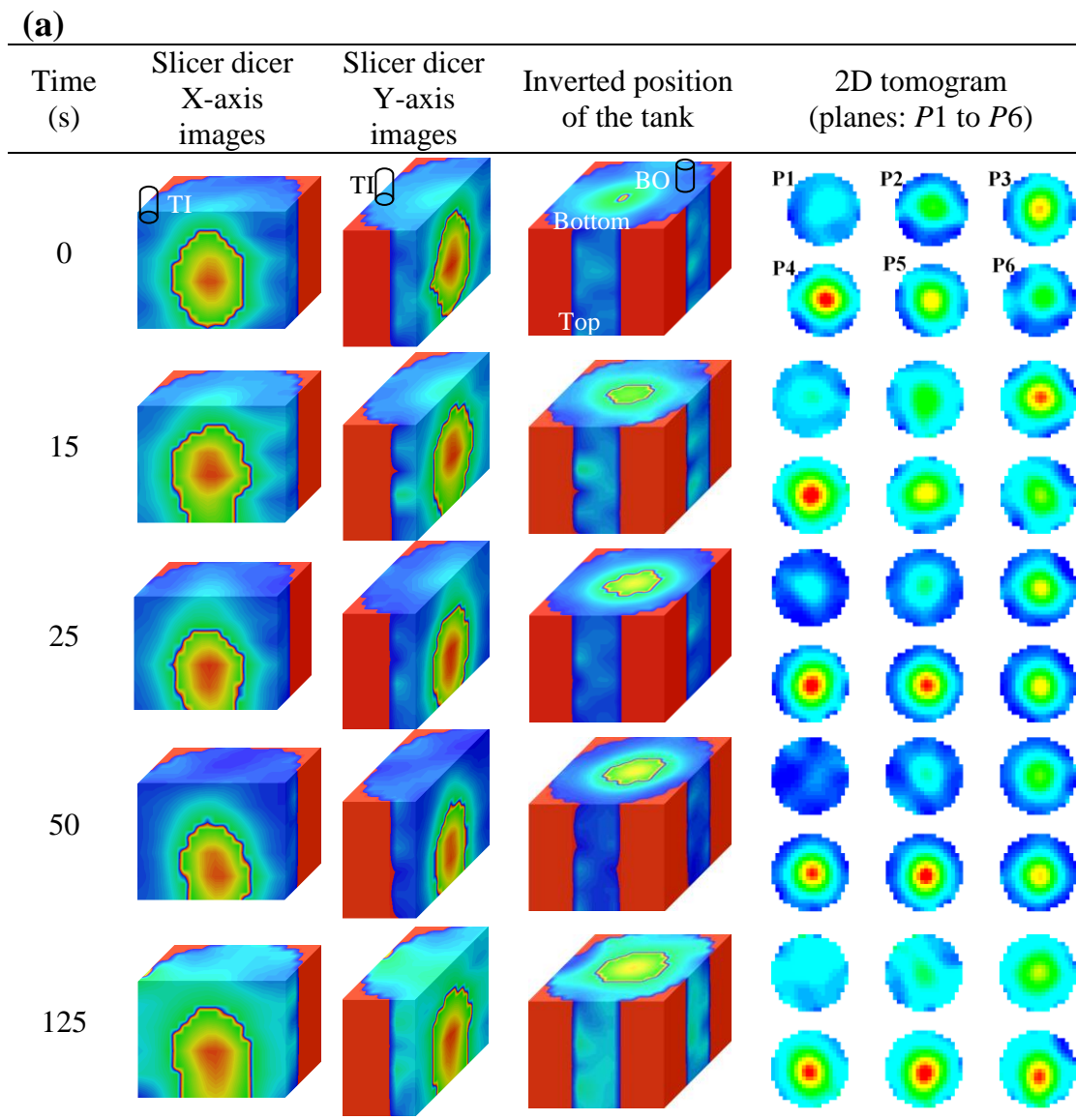


Figure (5.5-9). Effect of the feed flow rate on the deformation of the cavern (a) $Q = 3.2 \text{ L min}^{-1}$ and (b) $Q = 14.17 \text{ L min}^{-1}$ (RT impeller, $N = 30 \text{ rpm}$, 1.0% xanthan gum, and inlet-outlet locations: TI–BO).

Due to the deformation, the cavern volumes increased by nearly 5.6% and 17.7% for $Q = 3.2 \text{ L min}^{-1}$ and $Q = 14.17 \text{ L min}^{-1}$, respectively. From the images demonstrated in the last row of Figure (5.5-6a) and Figure (5.5-9a), it can be observed that the cavern deformation achieved at $Q = 9.65 \text{ L min}^{-1}$ was more pronounced than that at $Q = 3.2 \text{ L min}^{-1}$. Figure (5.5-9b) shows that

the shape of the cavern was deformed severely and the tracer dispersed all around the tank when the feed flow rate was increased to $Q = 14.17 \text{ L min}^{-1}$. In fact, the ratio of the $Q/Q_{impeller}$ was employed to study the effect of the feed flow rate on the deformation of the cavern. In order to calculate $Q_{impellers}$, an N_Q of 0.72 (Paul et al., 2004; Nienow, 1998; Weetman and Oldshue, 1988) was chosen for the RT impeller.

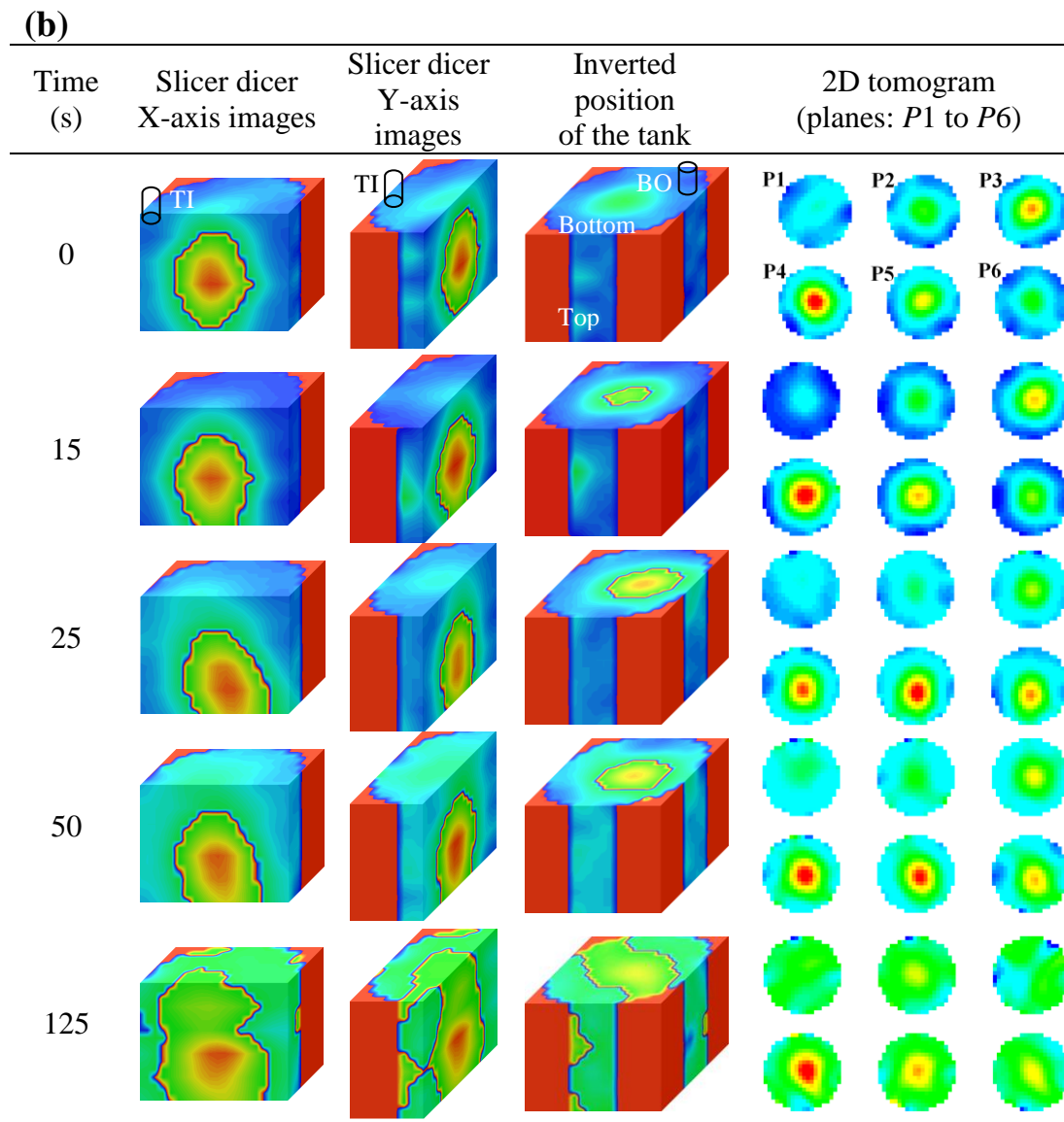


Figure (5.5-9). (Continued).

When the ratio of $Q/Q_{impeller}$ was increased by a factor of three (i.e. Q was increased from 3.2 to 9.65 L min^{-1}), the enlargement of the cavern due to the deformation increased from 5.6 to

11.2%. When the ratio of $Q/Q_{impeller}$ was further increased by a factor of 1.5 (i.e. Q was increased from 9.65 to 14.17 L min⁻¹), the enlargement of the cavern due to the deformation also increased from 11.2 to 17.7%. In addition to this, the quantitative results also show that when the feed flow rate (Q) was increased from 3.2 to 9.65 L min⁻¹, the momentum flux created by the inlet flow increased from 10.99 to 99.92 kg m⁻¹ s⁻². When the feed flow rate (Q) was further increased from 9.65 to 14.17 L min⁻¹, the momentum flux generated by the inlet flow also increased from 99.92 to 215.42 kg m⁻¹ s⁻². In fact, the extra momentum induced by the input-output flow increased with an increase in the feed flow rate through the mixing tank. Therefore, the deformation of the cavern was more pronounced at the higher flow rate.

5.5.3 Conclusions

Electrical resistance tomography (ERT) was used to measure the cavern volume (V_c) in the mixing of non-Newtonian fluids with yield stress in a batch vessel for the RT, A310, and 3AM impellers. Analysis using the 3D Slicer Dicer images showed that the axial-flow impellers (A310 and 3AM) created taller caverns and higher cavern volumes than those of the radial-flow impeller (RT). Moreover, tests for the cavern volume were carried out for the RT impeller at 0.5, 1.0, and 1.5% xanthan gum concentrations. As the fluid yield stress was decreased by decreasing the fluid concentration, the cavern volume increased. In addition to ERT tests, dynamic tests were performed to estimate the fully mixed volume ($V_{fully\ mixed}$) in the continuous-flow mixing system. The cavern volume (V_c) was compared with the fully mixed volume ($V_{fully\ mixed}$) for the RT, A310, and 3AM impellers. The results showed that, for the identical operating conditions, the fully mixed volume ($V_{fully\ mixed}$) in a continuous-flow mixing vessel was higher than the cavern volume (V_c) in a batch vessel for each impeller used in this study. This was due to the extra momentum induced by the inlet-outlet flow. The extra momentum flux generated by the inlet-outlet flow was estimated and compared with the momentum flux generated by the impeller. These results demonstrated that at a lower impeller speed, the momentum flux added to the system due to the inlet flow had a tremendous effect on the mixing of the non-Newtonian fluids exhibiting yield stress. Moreover, the ratio of the $Q/Q_{impeller}$ was employed to study the effect of the feed flow rate on the deformation of the cavern. When the ratio of $Q/Q_{impeller}$ was increased by a factor of three, the enlargement of the cavern due to the deformation increased

from 5.6 to 11.2%. When the ratio of $Q/Q_{impeller}$ was further increased by a factor of 1.5, the enlargement of the cavern due to the deformation also increased from 11.2 to 17.7%.

The ERT system was also employed to visualize the flow of non-Newtonian fluids with yield stress in the continuous-flow mixing system. The effect of the input-output flow on the deformation of the cavern was analyzed using the 2D tomographic images and the 3D Slicer Dicer images at different operating conditions and design parameters. The extent of the cavern enlargement due to the extra momentum induced by the input-output flow was estimated for each case. The effect of each factor on the deformation of the cavern is described below:

- **Fluid rheology:** The enlargement of the cavern due to the deformation increased from 11.2 to 21.1%, when the fluid yield stress was decreased by reducing the fluid concentration from 1.0 to 0.5%.
- **Jet effect:** When the jet velocity (V_j) was increased from 0.317 to 1.66 m s⁻¹, the enlargement of the cavern due to the deformation increased from 11.2 to 14.8%, and the tracer was dispersed throughout the tank widely.
- **Feed flow rate:** When the feed flow rate (Q) was increased from 3.2 to 14.17 L min⁻¹, the enlargement of the cavern due to the deformation also noticeably increased from 5.6 to 17.7%. The deformation of the cavern was more pronounced at the higher flow rate because of the more momentum flux induced by the input-output flow. In fact, when the feed flow rate (Q) was increased from 3.2 to 14.17 L min⁻¹, the momentum flux added to the system by the inlet flow increased from 10.99 to 215.42 kg m⁻¹ s⁻².
- **Inlet and outlet locations:** The cavern volume increased by about 2.6, 8.0, 11.2, and 26.7% for BI–BO, TI–TO, TI–BO, and BI–TO, respectively due to the deformation. The TI–TO and BI–BO configurations enabled the fluid to pass from inlet to outlet without being pushed into the impeller mixing zone, while in the BI–TO and TI–BO configurations, the feed was forced to pass through the mixing zone before leaving the vessel.

5.6 Using Tomography to Visualize the Continuous-Flow Mixing of Biopolymer Solutions inside a Stirred Tank Reactor (Patel et al., 2014b)

5.6.1 Introduction

The vast majority of non-Newtonian fluids are naturally opaque; therefore, visualizing the flow field of such fluids inside a reactor is a challenging task. To envisage the flow of fluids in the stirred vessels, numerous conventional techniques (ultrasound Doppler velocimetry, laser-Doppler velocimetry, particle image velocimetry, hot-wire anemometry, simple imaging, laser-induced fluorescence, color change, thermography, pitot tube, flow-followers, and positron emission particle tracking) have been used (Distelhoff et al., 1997; Lee and Yianneskis, 1997; Ascanio et al., 2003; Bouaifi and Roustan, 2001; Rewatkar and Joshi, 1991; Pant et al., 2001). However, these techniques have their own limitations as they are not suitable for opaque fluids or they might interfere in the local flow pattern. To overcome these shortcomings, the non-intrusive ERT technique can be an alternative solution. Literature review shows that study on continuous-flow mixing of Newtonian and non-Newtonian fluids in stirred tank reactors have been done mostly using dynamic tests, CFD, RTD, and LDV in which the data were generally fitted with the dynamic model.

As per the author's knowledge, no study has employed the tomography technique to visualize the flow in the continuous-flow mixing of pseudoplastic fluids exhibiting yield stress in a stirred tank reactor. Therefore, the key objective of this study was to employ the ERT technique in order to explore the effects of the inlet and outlet locations (four configurations: top inlet-bottom outlet, bottom inlet-top outlet, bottom inlet-bottom outlet, and top inlet-top outlet), fluid rheology (0.5–1.5% xanthan gum concentration), jet velocity (0.317–1.660 m s⁻¹), feed flow rate (3.20–14.17 L min⁻¹), impeller type (the Rushton turbine and Maxblend impellers), and impeller speed (54–250 rpm) on the flow patterns generated in the continuous-flow mixing of the xanthan gum solution, which is a pseudoplastic fluid exhibiting yield stress. Using 2D and 3D tomography images, this article effectively presents a competent method to visualize the flow of opaque fluids in laminar and transitional regions inside a reactor. In this

study, the existence of non-ideal flows in a stirred tank reactor for opaque fluids was identified using ERT.

To visualize the flow in the continuous mode, the mixing tank with ERT system [Figure (3.2-1)] was assembled to the experimental setup shown in Figure (3.1-1). Procedure for the visualization of the tracer distribution in a continuous-flow mixing system is described in Section (3.4.4). The rheological behaviour of the xanthan gum solutions was described by the Herschel-Bulkley model [Equation (2.1-9)].

5.6.2 Results and Discussion

The visualization of the tracer distribution in a continuous-flow mixing system is described below. As described procedure in the Section (3.4.4), the feed and discharge pumps were turned on simultaneously and the tracer was injected into the feed stream. ERT data was collected and 2D tomography images were reconstructed. Figure (3.4-4a) demonstrates how the flow of xanthan gum solution inside the mixing vessel can be visualized using two dimensional (2D) tomograms. As shown in this figure, the impeller was located on plane *P4*. Colors in the tomograms show the dispersion of the tracer in the vessel. The red color in the tomograms demonstrates the high-conductivity regions, and indicates the higher tracer concentration in those zones. The blue color in these tomograms shows the low-conductivity zones, and represents the lower tracer concentrations. To facilitate the flow visualization, 2D images were converted into three dimensional (3D) images. The ERT raw data were exported for visualization using a tab 'stack images of the same frame' and were saved to a file in a format readable by Slicer Dicer. Figure (3.4-4b) shows the 3D images generated from the 2D images using Slicer-Dicer software (PIXOTEC, LLC, WA, USA). The Slicer Dicer uses the interpolation scheme to convert the 2D tomograms into 3D images. To visualize thoroughly how the tracer was dispersed in the opaque fluid (xanthan gum solutions), 3D images were generated by cutting the block in the *x*, *y* and *z* directions to provide enough information about the cavern formation. Various 3D images shown in Figure (3.4-4b) were generated by cutting the vertical plane at the center of the tank and / or the horizontal plane on the impeller surface. In this study, a similar approach was adopted to analyze the flow pattern generated in the continuous-flow mixing of the xanthan gum solutions. The ideal mixing in the continuous-flow

mode is achieved when the channeling approaches zero and the fully-mixed volume approaches to the total volume of the fluid inside the vessel.

5.6.2.1 Effect of Inlet and Outlet Locations on Flow Pattern

The locations of the inlet and outlet, one of the vital geometric parameters of the mixing vessel, have a significant impact on the performance of the continuous-flow mixing system. To explore the effects of the inlet and the outlet locations on the fluid flow in the continuous-flow mixing, four different configurations, namely, (i) TI–BO (top inlet-bottom outlet), (ii) BI–TO (bottom inlet-top outlet), (iii) BI–BO (bottom inlet-bottom outlet), and (iv) TI–TO (top inlet-top outlet) were tested in the continuous mode for the RT impeller at $N = 54$ rpm, $Re = 19$ (transitional flow), $Q = 9.65$ L min⁻¹, 1.0% xanthan gum, residence time = 292 s, and $V_j = 0.317$ m s⁻¹, and the ERT results are depicted in Figure (5.6-1a, b, c, and d), respectively. These images are presented in four columns in a time series (1st column from the left: Slicer Dicer x -axis image; 2nd column: Slicer Dicer y -axis image; 3rd column: Slicer Dicer block for the inverted position of the tank; and 4th column: 2D tomograms from planes $P1$ to $P6$). In the 3rd column, the Slicer Dicer images of the tank are presented in an inverted position since it is difficult to view the bottom of the tank from the top. In this 3D image, the upper surface shows the bottom of the tank and the lower surface shows the top of the tank. The locations of the inlet and outlet are also shown in the Slicer Dicer images. The blue color in the tomograms in the first row of Figure (5.6-1) to Figure (5.6-5) and Figure (5.6-7) shows that only the xanthan gum solution was present and there was no tracer in the tank at that moment (i.e. after the pumps were turned on and before the injection of the tracer). In Figure (5.6-1) to Figure (5.6-5) and Figure (5.6-7), the images in the 2nd, 3rd, 4th, and 5th rows were taken at 5, 10, 20, and 100 s, respectively, after the injection of the tracer into the feed stream.

In the case of the TI–BO configuration, the ERT images in the first row of Figure (5.6-1a) show that there was no tracer in the tank at that moment. In the second row, the color change in the ERT images shows that the tracer was injected into the feed at the top of the vessel. As the time passed, the fresh xanthan gum solution was added through the top inlet (*TI*) and the mixed solution was withdrawn from the vessel through the bottom outlet (*BO*). The continuous flow of the fresh feed at the top of the tank pushed the tracer downwards while the mixed solution

was sucked through the bottom outlet; therefore, in the 3rd row the tracer disappeared at plane *P1* in the 2D tomogram and the top surface of the tank in the Slicer Dicer images.

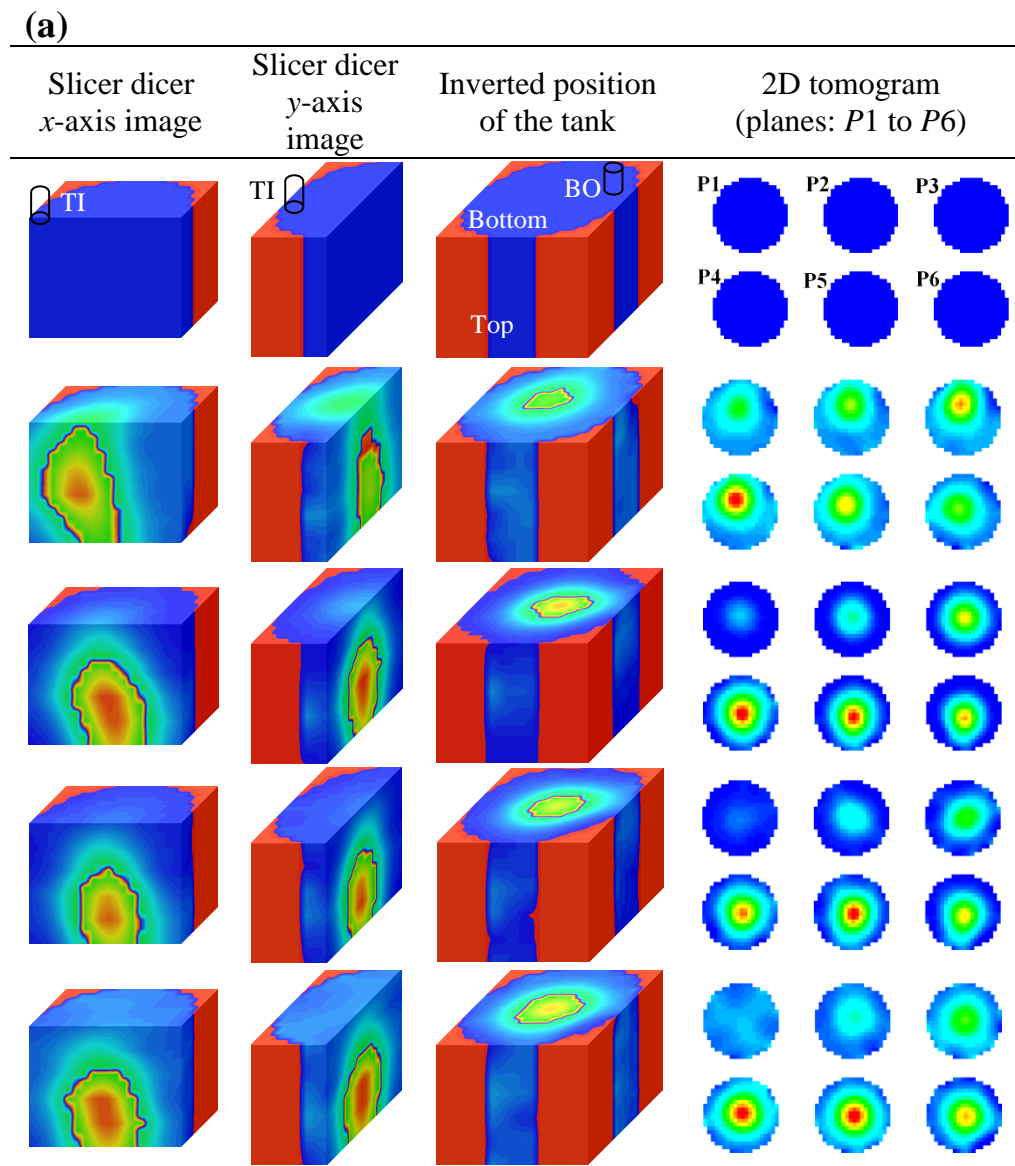


Figure (5.6-1). Effect of the inlet and outlet locations on the fluid flow inside a vessel for the four configurations: (a) TI–BO, (b) BI–TO, (c) BI–BO, and (d) TI–TO (RT impeller, $N = 54$ rpm, $Q = 9.65 \text{ L min}^{-1}$, 1.0% xanthan gum, and $V_j = 0.317 \text{ m s}^{-1}$).

Due to the nature of the yield pseudoplastic fluid, the tracer was not observed in the dead zones, where the impeller imparted stresses were below the fluid yield stress. In fact, the formation of the cavern around the impeller can be seen in the subsequent images. Other than the impeller, the extra momentum generated by the inlet-outlet flow also facilitated the

dispersion of the tracer inside the reactor and consequently the tracer channeled through the bottom outlet. The extra momentum flux ($Q \rho v/A$, where v is the velocity of the fluid passing through the inlet, and A is the cross section area of the inlet pipe) added to the fluid in the mixing vessel at the inlet position was about $99.92 \text{ kg m}^{-1} \text{ s}^{-2}$. In addition, the momentum flux generated due to the inlet-outlet flow was compared with the momentum flux generated by the impeller. The impeller pumping rate ($Q_{impeller}$) is defined as $Q_{impeller} = N_Q N D^3$, where N_Q is the impeller flow number (Uhl and Gray, 1966). In order to calculate $Q_{impeller}$, an N_Q of 0.72 was chosen for the RT impeller (Paul et al., 2004; Nienow, 1998; Weetman and Oldshue, 1988). The momentum flux ($Q_{impeller} \rho v_{tip}/A_i$, where v_{tip} is the impeller tip velocity, and A_i is the swept area by the impeller) generated by the RT impeller at $N = 54 \text{ rpm}$ was estimated at about $73.31 \text{ kg m}^{-1} \text{ s}^{-2}$, which was approximately 1.3 times lower than the momentum flux generated by the inlet flow ($99.92 \text{ kg m}^{-1} \text{ s}^{-2}$). Thus, these results demonstrate that at a lower impeller speed, the momentum flux added to the system due to the inlet flow had a tremendous effect on the mixing of the non-Newtonian fluids exhibiting yield stress. Besides, the cavern volume (V_c) was calculated using the cavern diameter (D_c) and the cavern height (H_c) for a cylindrical shape. However, the shape of the deformed cavern was not exactly cylindrical. Therefore, to measure the total volume of the deformed cavern, the cavern was divided into the small cylindrical segments to approximate the volume of the deformed cavern. According to the images depicted in the last row of Figure (5.6-1a), the volume in which the tracer distributed was nearly 28% of the total volume of the fluid in the vessel.

In the BI–TO configuration, contrarily, the inlet was located at the bottom of the tank and the outlet was located at the top side of the tank. In the second row of Figure (5.6-1b), the red color in the tomograms (planes $P5$ – $P6$) indicates that the tracer entered with the feed through the bottom inlet. In the 3rd row, initially the tracer was pushed slightly from the lower section by the fresh feed and shifted towards the upper part of the tank. As the fresh feed was pumped at the bottom of the tank, this pushed the tracer from the lower part of the tank to the upper part of the tank. Moreover, the solution from the mixing tank was drawn from the top outlet by the discharge pump, which also helped the tracer move upwards. The images in the 4th rows excellently demonstrate that, even in the BI–TO configuration, the tracer was channeled by simply following the fluid path from the inlet to the outlet.

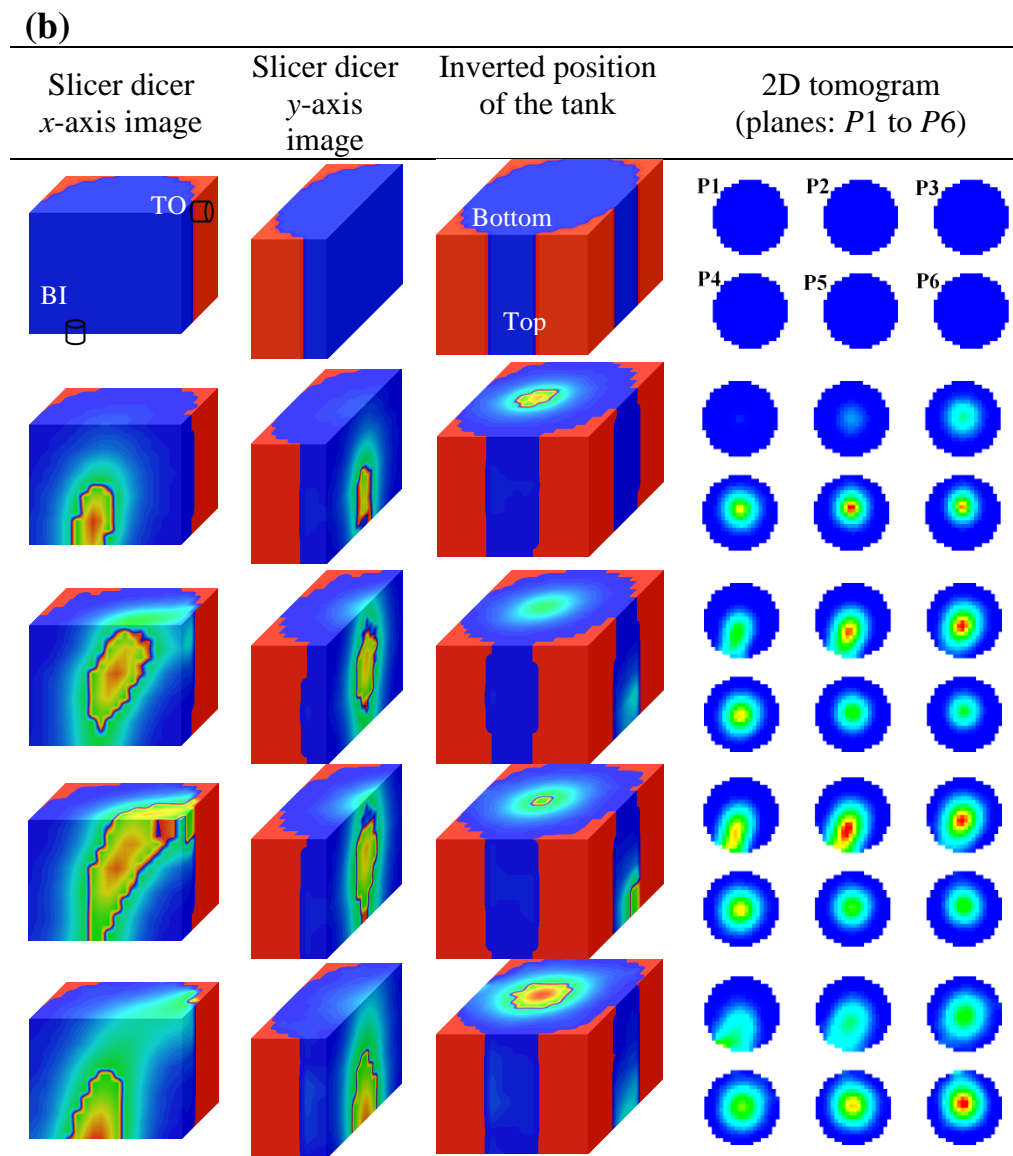


Figure (5.6-1). (Continued).

This was due to the fact that the momentum induced by the input-output flow also forced the tracer to move from the bottom inlet to the top outlet. It can be also observed that a pseudoplastic fluid with yield stress constrained the tracer distribution in a certain path, where the impeller imparted stress and extra momentum by the inlet-outlet flow prevailed. This means that the tracer could not move into the stagnant regions, where the stresses were below the fluid yield stress. The images displayed in the last row show that no tracer appeared at the upper part of the tank since it exited from the top outlet; however, the tracer was still present below the

impeller in the lower part of the tank and the volume in which the tracer distributed was approximately 20% of the total volume of the fluid in the vessel.

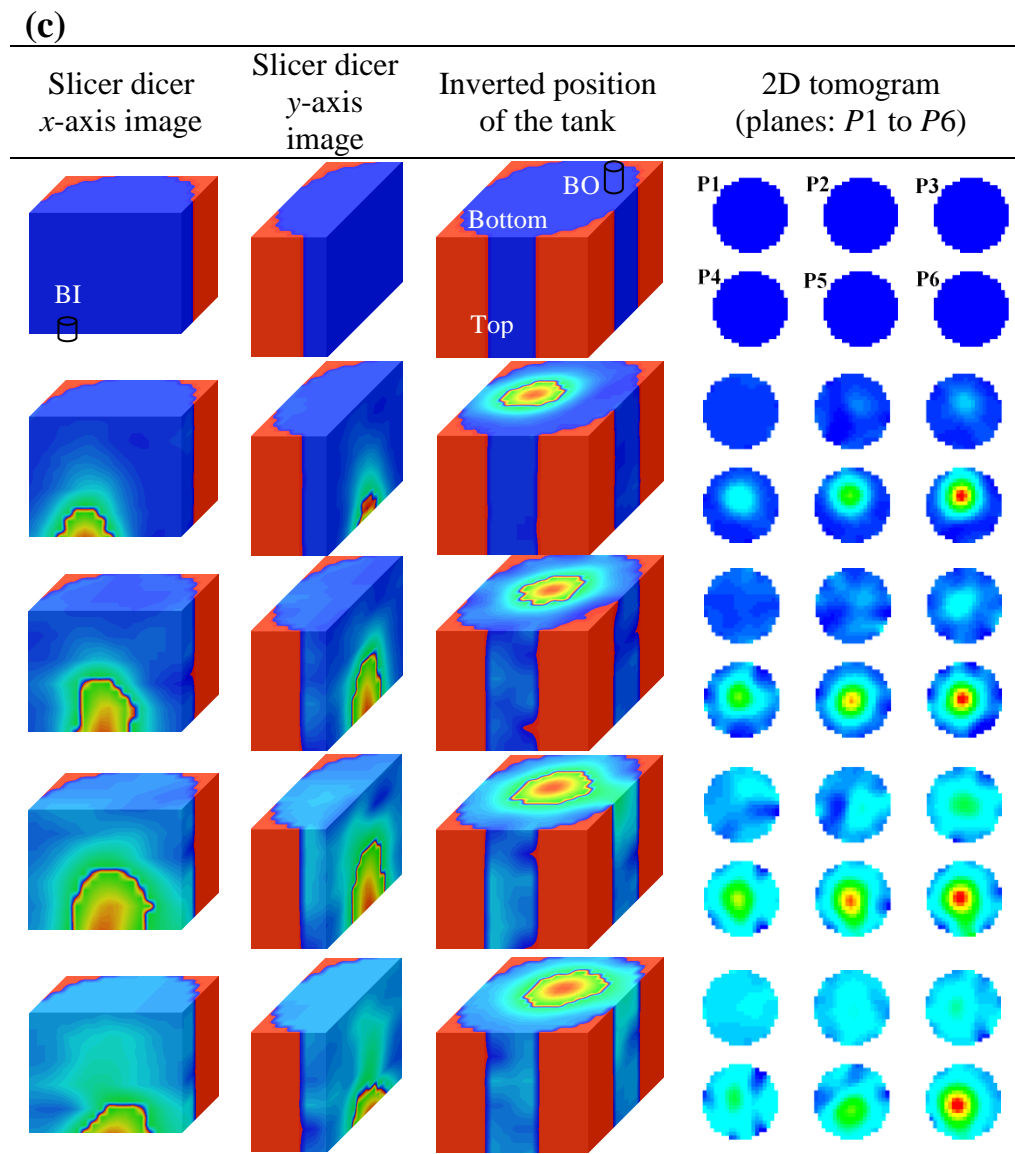


Figure (5.6-1). (Continued).

In the study of the BI–BO configuration, both the inlet and outlet were located at the bottom of the tank. Once the tracer was injected into the feed at the bottom inlet, as shown in the 2nd row of Figure (5.6-1c), the tracer appeared on the bottom planes (P5–P6) in the 2D tomograms and the left hand side of the top surface of the tank’s inverted position. As time passed (3rd–5th rows), the tracer was slowly dispersed around the impeller region but could not enter the upper

part of the tank. This is due to the fact that both the inlet and outlet were located at the bottom of the tank; therefore, the amount of fresh xanthan gum fed through the bottom inlet was drawn by the bottom outlet without passing through the impeller zone. It can also be observed through the Slicer Dicer images of the inverted position of the tank (3rd column) that the tracer initially appeared on the left hand side of the tank; however, in a time series, the tracer slowly moved towards the right hand side of the tank near the outlet. The results obtained in the study of the BI–BO configuration revealed that the channeling was most likely to occur if both the inlet and outlet were located nearby. In the last row of Figure (5.6-1c), the volume in which the tracer distributed was about 8% of the total volume of the fluid in the vessel.

In the study of the TI–TO configuration, the inlet and outlet were located at the upper side of the tank. As shown in the 2nd row of Figure (5.6-1d), when the tracer was injected into the feed, it appeared at the upper side of the tank. The images in the 3rd and 4th rows indicate that the tracer moved towards the impeller zone because the fresh xanthan gum solution fed from the top inlet pushed the tracer downward. The discharge pump continuously withdrew the solution from the top outlet. Therefore in the last row, the cavern shape was deformed in such a way that it inclined towards the top outlet (TO) and the volume in which the tracer distributed was estimated about 10% of the total volume of the fluid in the vessel.

It should be mentioned that the channeling and dead volume were identified in all four (TI–BO, BI–TO, BI–BO, and TI–TO) configurations, in which the impeller-imparted stresses were not sufficient to overcome the yield stress of the xanthan gum (biopolymer) solution. The tracer distribution achieved in the TI–BO and BI–TO configurations was more than that of in the BI–BO and TI–TO configurations. Overall, the BI–BO and TI–TO configurations were more susceptible to a higher channeling and dead volume compared to the TI–BO and BI–TO configurations. The BI–BO and TI–TO configurations, where both the inlet and outlet were located at the one side of the impeller horizontal plane (either the bottom-side or the top-side of the tank), enabled a high percentage of the feed to be conveyed to the outlet without being drawn into the impeller mixing zone. On the other hand, in the case of the BI–TO and TI–BO configurations, the feed was forced to pass through the mixing zone before leaving the vessel. Even in the BI–TO configuration, the feed had to face the fluid discharge from the impeller and

passed through the mixing zone in the direction opposite to the bulk flow within the vessel. Similar results were observed in the study of the dynamic performance of the continuous-flow mixing system in a stirred vessel (Patel et al., 2011). The locations of the inlet and outlet should be chosen in such a way that a line drawn from the inlet to the outlet passes through the impeller zone (Paul et al., 2004).

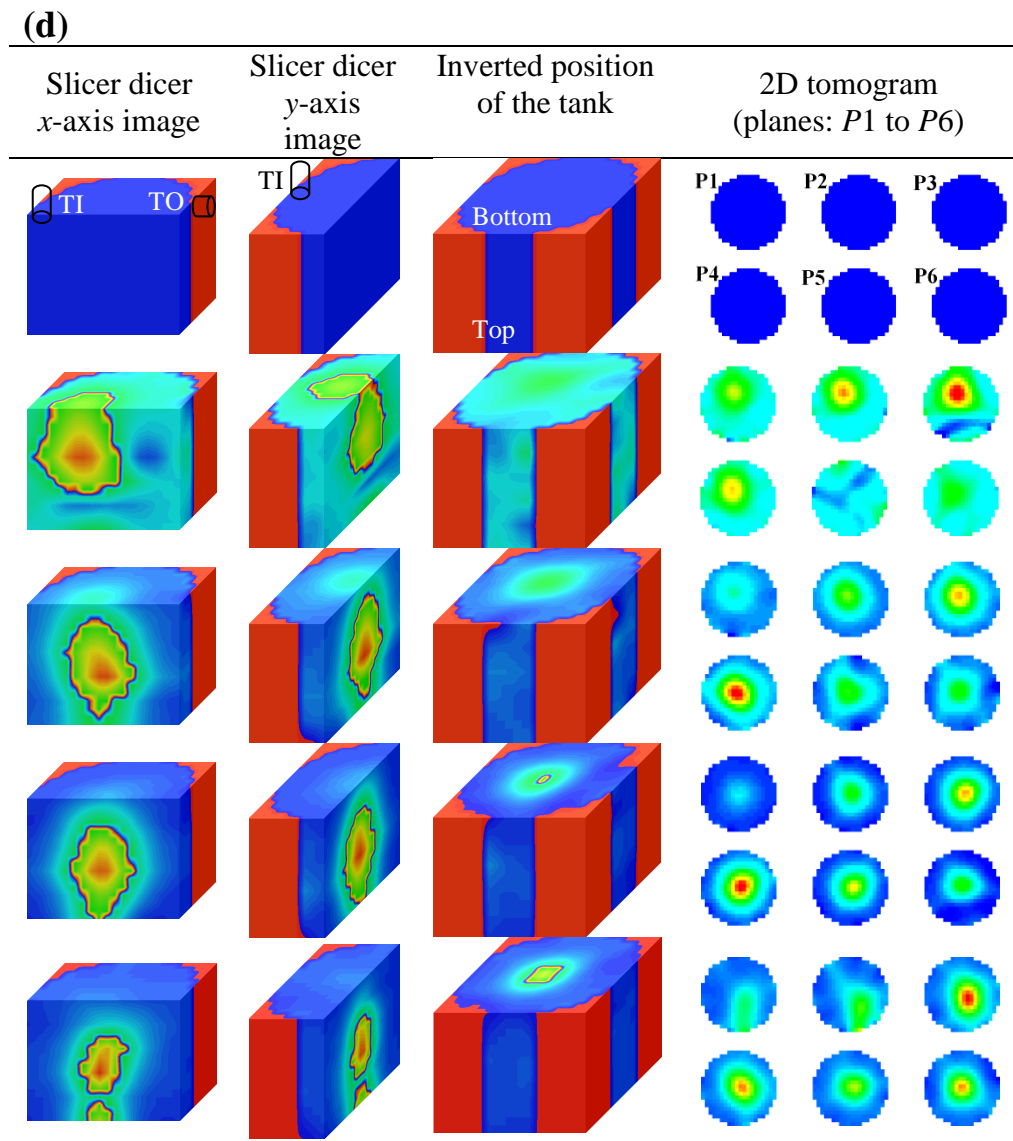


Figure (5.6-1). (Continued).

5.6.2.2 Effect of Jet Velocity on Flow Pattern

The efficiency of the continuous-flow mixing system can be affected by the inlet jet velocity (V_j). The inlet diameter can be reduced to generate a high-velocity jet of the feed in the vessel. Figure (5.6-2) represents the ERT results at the same operating conditions as those mentioned in Figure (5.6-1a) except the jet velocity, which was $V_j = 1.66 \text{ m s}^{-1}$.

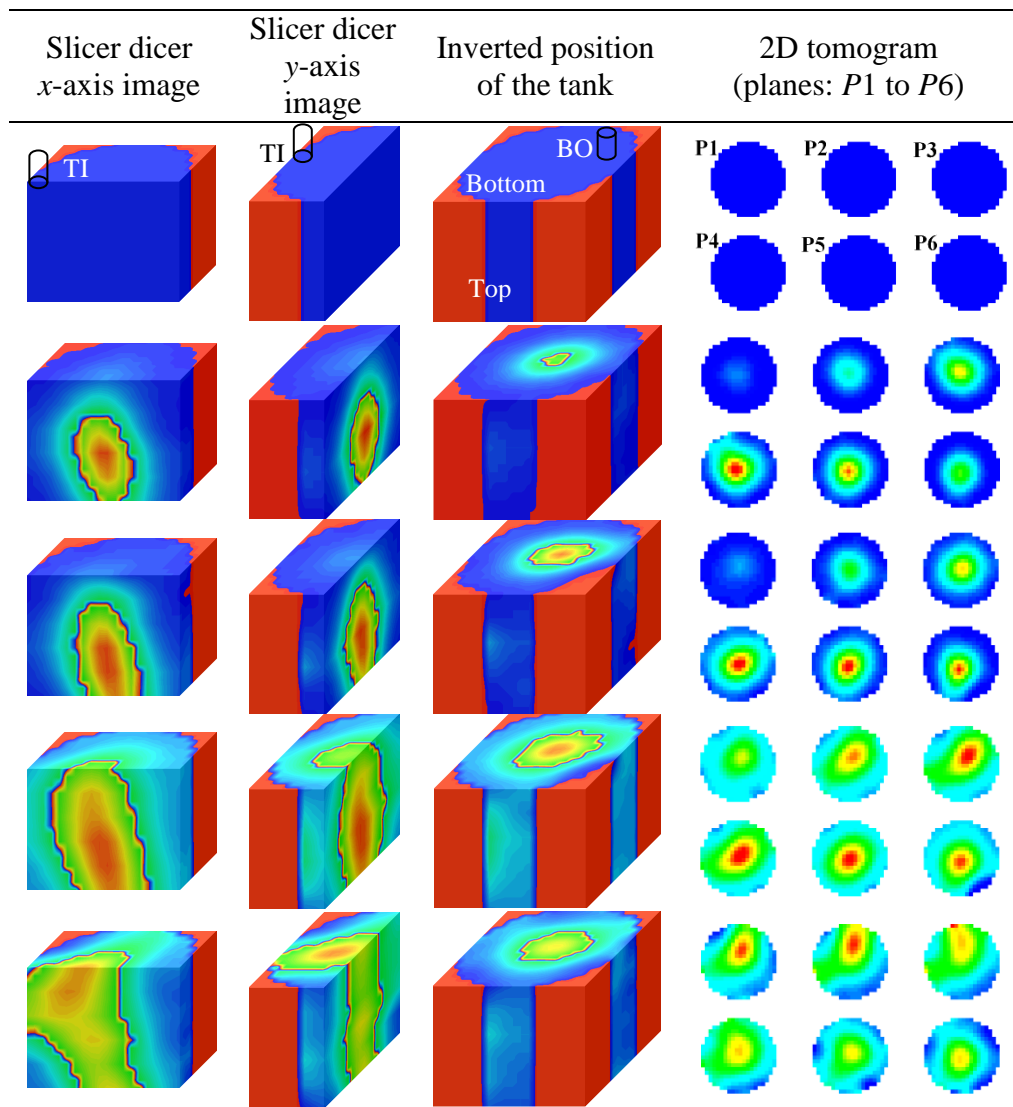


Figure (5.6-2). Effect of the inlet jet velocity on the fluid flow (RT impeller, $N = 54 \text{ rpm}$, $Q = 9.65 \text{ L min}^{-1}$, 1.0% xanthan gum, $V_j = 1.66 \text{ m s}^{-1}$, and input-output locations: TI–BO).

Once the tracer was injected into the feed, the images in the second row show that the tracer appeared in the tank from planes P2–P6 because the high-velocity jet of the fluid pushed the

feed rapidly to the impeller zone. The consecutive Slicer Dicer images presented in the 3rd and 4th rows show that the tracer was dispersed more vertically in the direction of the feed jet flow. Moreover, the tracer distribution was more dominant on the left hand side compared to that on the right hand side due to the inlet jet flow. The ERT images in the last row display that the tracer distribution was rigorously affected by the high-velocity jet of the fluid and was dispersed almost throughout the tank. In the last row of Figure (5.6-2), the volume in which the tracer distributed was estimated about 44% of the total volume of the fluid in the vessel. The ERT results in Figure (5.6-1a) and Figure (5.6-2) show that as the jet velocity (V_j) was increased from 0.317 to 1.66 m s⁻¹, the volume in which the tracer was distributed increased from 28 to 44% of the total volume of the fluid in the vessel. It means the dispersion of the tracer was more noticeable. When an inlet stream is fed into a tank at a high velocity, it is expected that the surrounding bulk fluid will be entrained into the feed zone, thus improving the mixing quality. Moreover, the high-velocity jet of fluid transports the feed promptly to the impeller zone, where it is exposed to high turbulence and gets mixed better (Patel et al., 2011).

5.6.2.3 Effect of Feed Flow Rate on Flow Pattern

The mixing quality in the continuous-flow mixing system also mostly relies on the fluid flow rate through the mixing vessel. To study the effect of the fluid flow rate on the tracer distribution in a vessel, the ERT tests were conducted with the identical operating conditions as those mentioned in Figure (5.6-1a) except the feed flow rate (Q). Figure (5.6-3a and b) depicts the tomography images obtained for $Q = 3.2 \text{ L min}^{-1}$ and $Q = 14.17 \text{ L min}^{-1}$, respectively. The results depicted in the 2nd row show that once the tracer was injected into the feed, it appeared in the upper part of the tank in Figure (5.6-3a) and was not detected at the bottom planes ($P5$ and $P6$) in the 2D tomogram and at the bottom surfaces in the 3D Slicer Dicer images. Adversely, looking at the 2nd row in Figure (5.6-3b) the tracer appeared mainly in the lower part of the tank and no tracer was detected in the top plane ($P1$) in the 2D tomogram and on the top surfaces in the 3D Slicer Dicer images. This is attributed to the effect of the fluid flow rate passing through the reactor. The tracer distribution achieved in the last row of Figure (5.6-3a and b) was quantified about 17% and 33% of the total volume of the fluid in the vessel, respectively.

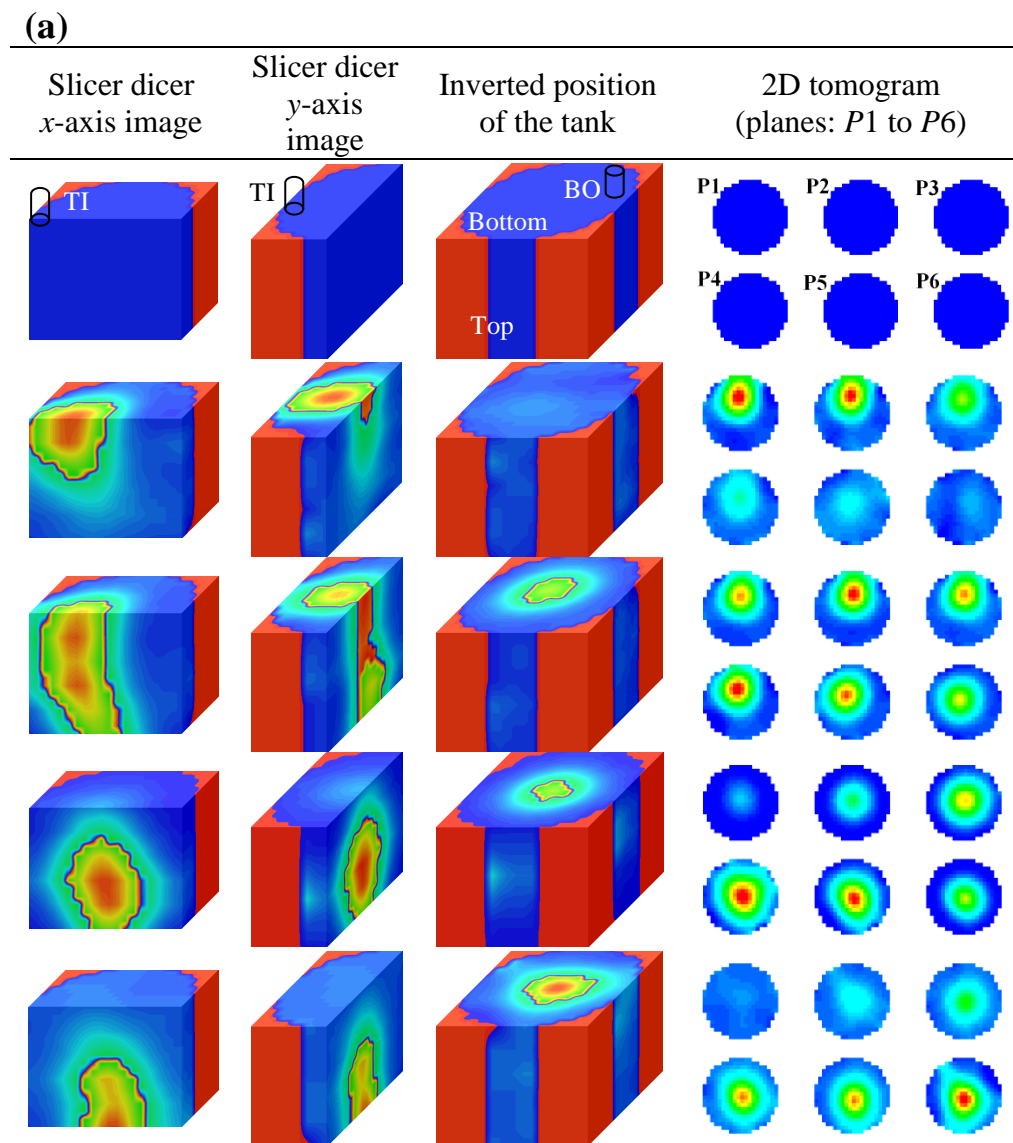


Figure (5.6-3). Effect of the feed flow rate on the fluid flow (a) $Q = 3.2 \text{ L min}^{-1}$ and (b) $Q = 14.17 \text{ L min}^{-1}$ (RT impeller, $N = 54 \text{ rpm}$, 1.0% xanthan gum, and input-output locations: TI–BO).

The results demonstrate that the tracer distribution achieved at $Q = 14.17 \text{ L min}^{-1}$ was more pronounced (about double) than that at $Q = 3.2 \text{ L min}^{-1}$. Figure (5.6-3b) shows that the tracer was dispersed throughout the tank when the flow rate was increased to $Q = 14.17 \text{ L min}^{-1}$. The ratio of the $Q/Q_{impeller}$ was also employed to study the effect of the feed flow rate on the tracer distribution. When the ratio of $Q/Q_{impeller}$ was increased by a factor of three (i.e. Q was increased from 3.2 to 9.65 L min^{-1}), the tracer distribution due to higher feed flow rate increased. When the ratio of $Q/Q_{impeller}$ was further increased by a factor of 1.5 (i.e. Q was

increased from 9.65 to 14.17 L min⁻¹), the tracer distribution at the higher feed flow rate even increased more. In addition to this, the quantitative results also show that when the feed flow rate (Q) was increased from 3.2 to 9.65 L min⁻¹, the momentum flux created by the inlet flow increased from 10.99 to 99.92 kg m⁻¹ s⁻². When the feed flow rate (Q) was further increased from 9.65 to 14.17 L min⁻¹, the momentum flux generated by the inlet flow also increased from 99.92 to 215.42 kg m⁻¹ s⁻². In fact, the extra momentum induced by the input-output flow increased with an increase in the feed flow rate through the mixing tank. Therefore, the tracer distribution was more pronounced at the higher flow rate.

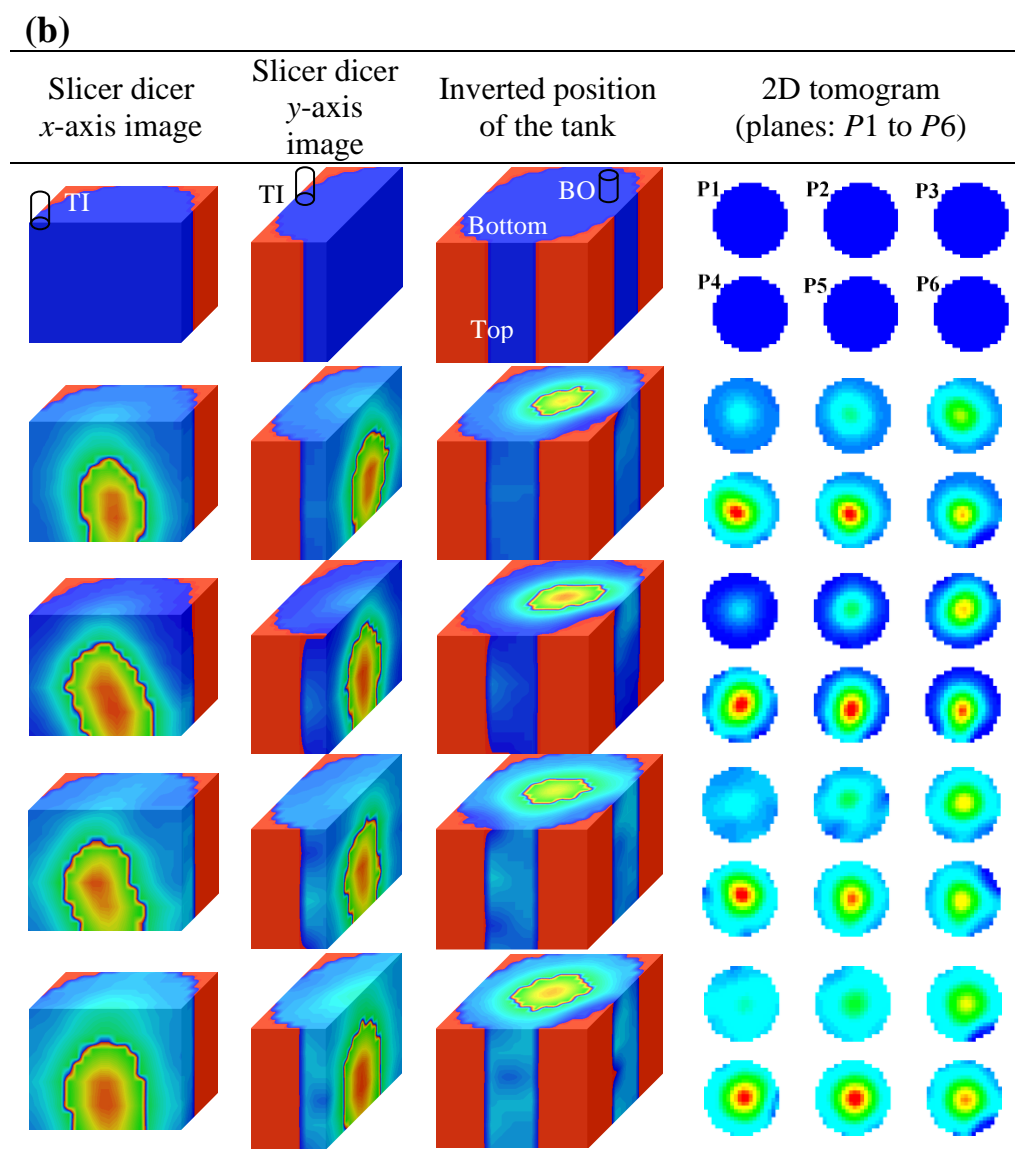


Figure (5.6-3). (Continued).

5.6.2.4 Effect of Fluid Rheology on Flow Pattern

The fluid rheology also considerably influences the efficiency of the continuous-flow mixing of non-Newtonian fluids. To explore the effect of this parameter, the ERT tests were performed with the same operating conditions as those mentioned in Figure (5.6-1a) except the xanthan gum concentration. Figure (5.6-4a and b) displays the tomography images generated in the mixing of 0.5 and 1.5% xanthan gum solutions, respectively.

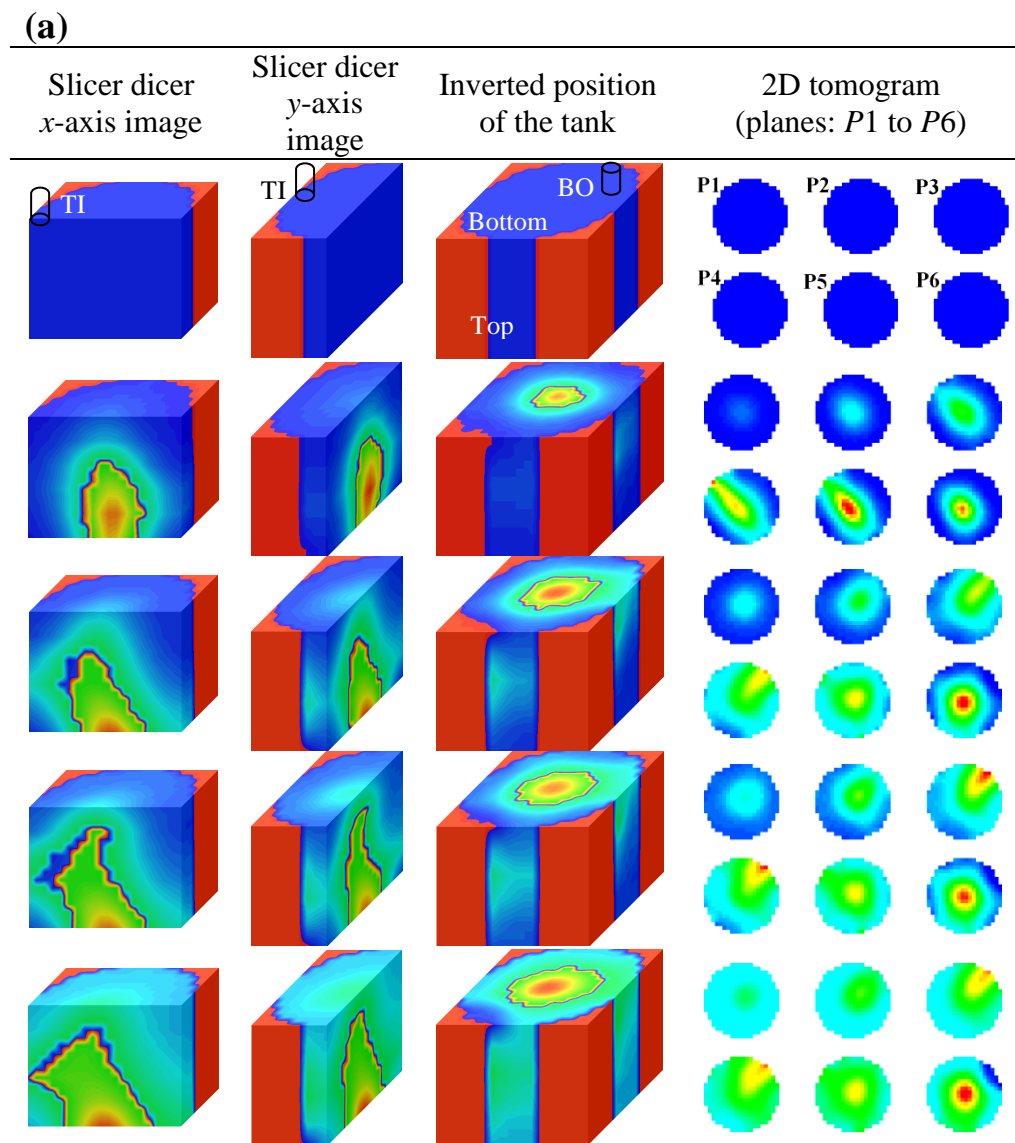


Figure (5.6-4). Effect of the fluid rheology on the fluid flow (a) 0.5% xanthan gum and (b) 1.5% xanthan gum (RT impeller, $N = 54$ rpm, $Q = 9.65$ L min⁻¹, $V_j = 0.317$ m s⁻¹, and input-output locations: TI-BO).

When the tracer was injected into the feed, as shown in the 2nd row of Figure (5.6-4a), the tracer appeared largely in the lower part of the tank and no tracer was detected at the top planes (*P1* and *P2*) in the 2D tomogram and at the top surfaces in the 3D Slicer Dicer images. However, in the 2nd row of Figure (5.6-4b), the tracer appeared in the upper part of the tank (planes *P1–P3*) but was not detected at the bottom planes (*P5* and *P6*) in the 2D tomogram and at the bottom surfaces in the 3D Slicer Dicer images.

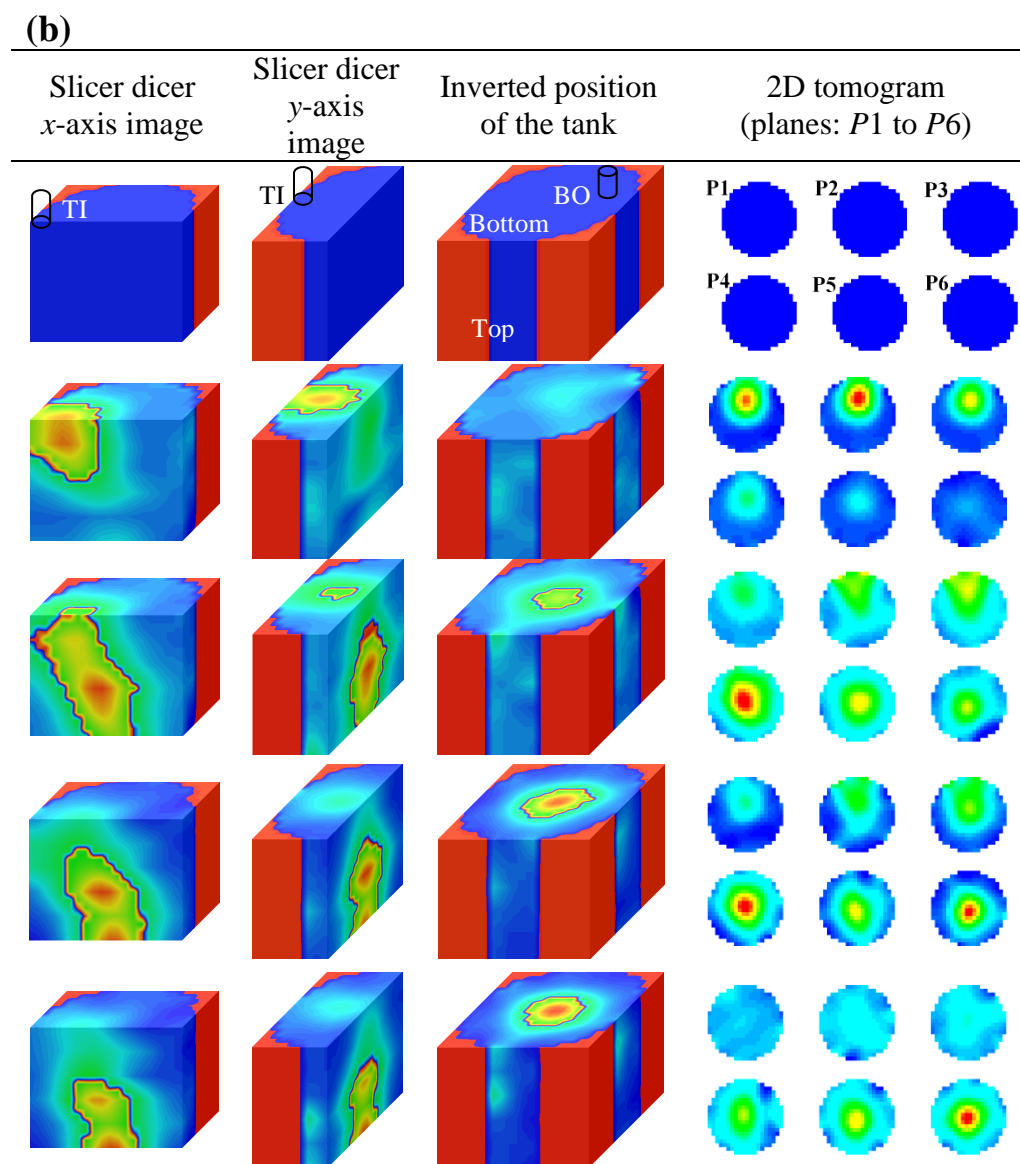


Figure (5.6-4). (Continued).

This means that the tracer was trapped and held at the upper part of the tank at the higher concentration of the xanthan gum solution. In the subsequent images presented in a time series (3rd–4th rows), the tracer was distributed more and a higher tracer concentration was detected at the bottom plane *P6* in the 2D tomogram and at the top surface of the inverted position of the tank. The ERT images in the last row for the 0.5% xanthan gum concentration show that the tracer was distributed and almost reached the fluid surface and the left hand side of the vessel wall. The volume in which the tracer distributed in the last row of Figure (5.6-4a and b) was noticed about 39% and 20% of the total volume of the fluid in the vessel, respectively. The quantitative analysis shows that the tracer distribution was more significant (almost double) at the 0.5% xanthan gum solution than that at the 1.5% xanthan gum solution. This was due to the fluid yield stress which decreased when the xanthan gum concentration was decreased from 1.5 to 0.5%. The energy dissipation at the lower yield stress is slower than that at the higher yield stress. The fluctuating velocities penetrate quickly in the area outside of the impeller zone at the lower yield stress because of the lesser apparent viscosity of the fluid, which is a function of the fluid yield stress.

5.6.2.5 Effect of Type of Impeller on Flow Pattern

The impeller type plays a crucial role in performance of the continuous-flow mixing system. To examine the effects of the impeller type on the distribution of the tracer in a reactor at a similar power consumption per unit volume (58.9 W m^{-3}), the ERT tests were performed with the same operating conditions as those given in Figure (5.6-7b) except impeller type, which was the close clearance impeller (the Maxblend impeller). The results of the ERT tests are depicted in Figure (5.6-5). When the tracer was injected into the feed stream, as shown in the 2nd row, the tracer was detected in the 2D tomogram and 3D Slicer Dicer images. Comparing the images depicted in Figure (5.6-7b) and Figure (5.6-5), overall the Maxblend impeller was capable of dispersing the tracer more effectively than the RT impeller. The Maxblend impeller consisted of a bottom paddle mounted by a top grid. The paddle was designed to generate flow circulation and the grid to provide capacity for dispersing a second phase. These grids slowly assisted the tracer in dispersing to the upper region of the tank. Moreover, the size of the Maxblend impeller was larger compared to the RT impeller.

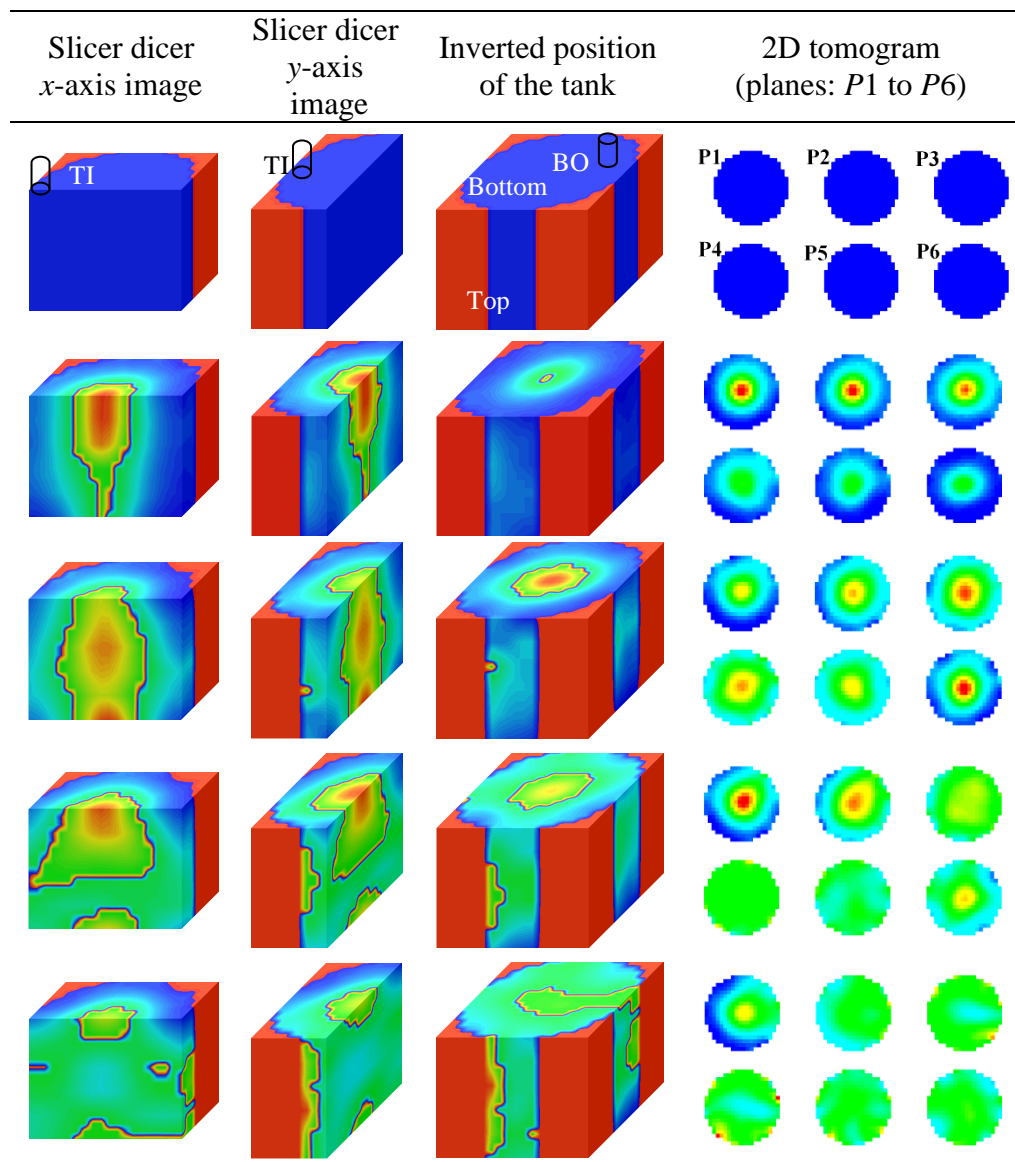


Figure (5.6-5). Effect of the impeller type on the fluid flow (Maxblend impeller, $N = 54$ rpm, $Q = 9.65$ L min⁻¹, 1.0% xanthan gum, $V_j = 0.317$ m s⁻¹, and input-output locations: TI–BO).

Thus, it swept higher volumes of fluids within the tank and provided a better mixing quality. Therefore, the dispersion of the tracer in the 3rd row was more noticeable for the Maxblend impeller than that for the RT impeller. The images in the 4th–5th rows show that the presence of the Maxblend impeller’s paddle effectively mixed the tracer at the bottom of the tank. Therefore, the tracer was dispersed throughout the tank and reached the surface, walls, and bottom of the tank as shown in the last row of Figure (5.6-5).

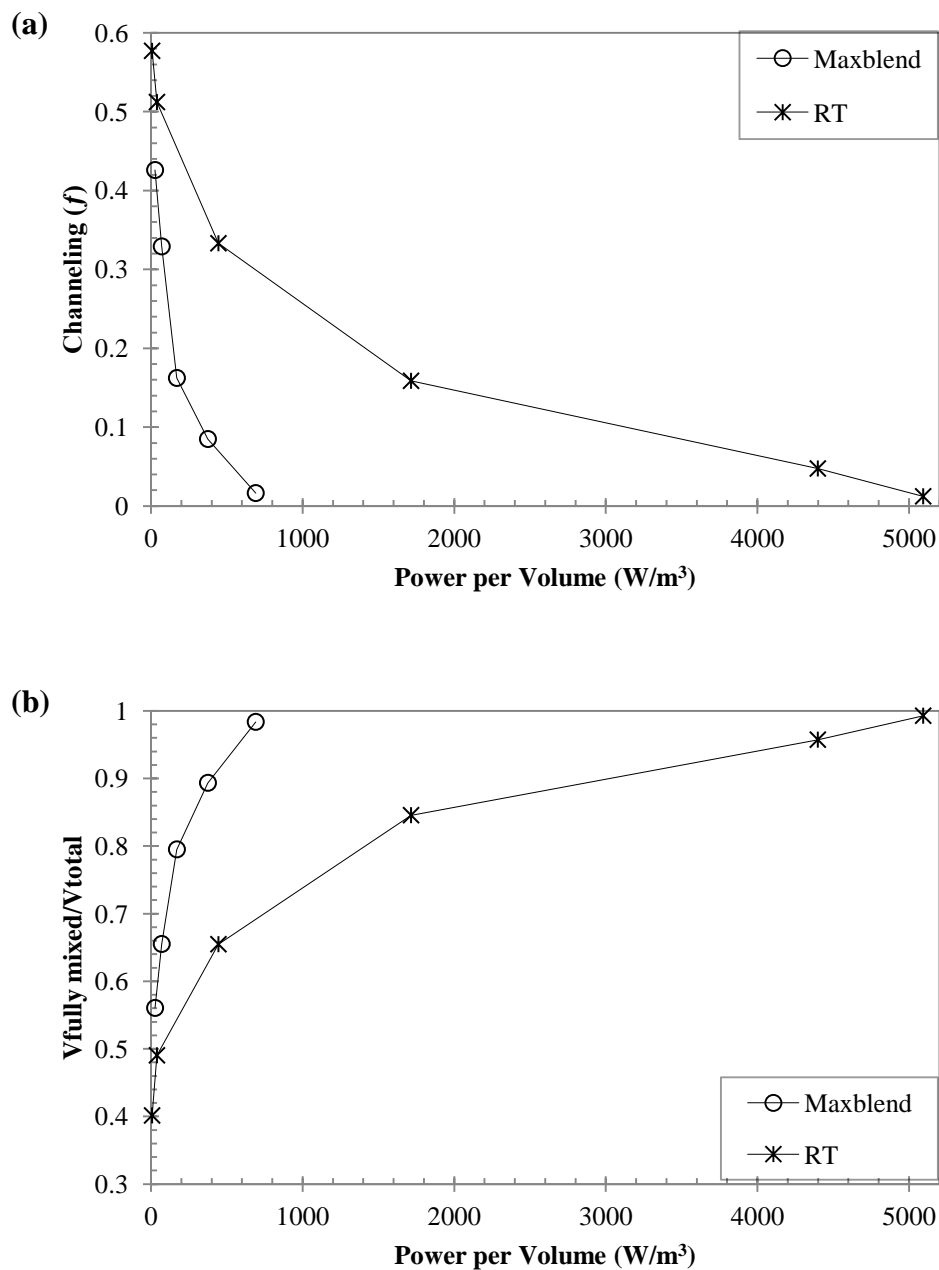


Figure (5.6-6). Effect of the impeller speed and the impeller type on the extent of (a) channeling and (b) fully mixed volume ($Q = 9.65 \text{ L min}^{-1}$, 1.0% xanthan gum, $V_j = 0.317 \text{ m s}^{-1}$, and input-output locations: TI-BO).

The volume in which the tracer distributed in the last row of Figure (5.6-5) and Figure (5.6-7b) was evaluated about 63% and 33% of the total volume of the fluid in the vessel, respectively.

The quantitative analysis shows that the tracer distribution achieved using the Maxblend impeller was more significant than using the RT impeller. Previously, Patel et al. (2011, 2012a) studied the dynamic performance of continuous-flow mixing for the RT (Patel et al., 2011) and Maxblend impellers (Patel et al., 2012a), respectively, at $Q = 9.65 \text{ L min}^{-1}$, 1.0% xanthan gum, and $V_j = 0.317 \text{ m s}^{-1}$ and those results are depicted in Figure (5.6-6). These data show the extent of channeling (f) and the fraction of fully mixed volume ($V_{fully\ mixed}/V_{total}$), respectively, as a function of power per unit volume. The outcome of the studies shows that the Maxblend impeller was more effective than the RT impellers for reducing channeling and increasing the fully mixed volume in the continuous flow mixing of the non-Newtonian fluid.

5.6.2.6 Effect of Impeller Speed on Flow Pattern

The impeller speed has a significant effect on the performance of the continuous-flow mixing system. To investigate the effects of the impeller speed on the tracer distribution in the mixing vessel, the ERT tests were performed with the same operating conditions as those given in Figure (5.6-1a) except impeller speed (N). The ERT tests were carried out at 77, 100, and 250 rpm and their results are given in Figure (5.6-7a, b, and c), respectively. When the tracer was injected into the feed stream, as shown in the 2nd row of Figure (5.6-1a) and Figure (5.6-7), the tracer was detected in the tank (in the 2D tomogram and 3D Slicer Dicer images). As the impeller speed was increased from 54 to 250 rpm, the tracer appeared more towards the bottom of the tank in the 2nd row of Figure (5.6-1a) and Figure (5.6-7). This is credited to the effect of a higher impeller speed, which helped the tracer to move from the inlet to the impeller region. As the impeller speed was increased from 54 to 250 rpm, the images in the 3rd–4th rows of Figure (5.6-1a) and Figure (5.6-7) show that the tracer distribution in the tank also improved. When the impeller speed was increased from 54 to 100 rpm, the volume in which the tracer distributed in the last row of Figure (5.6-1a) and Figure (5.6-7a and b) was calculated approximately 28, 31, and 33% of the total volume of the fluid in the vessel, respectively. As the impeller speed was increased from 54 to 250 rpm, the 3D Slicer Dicer images, depicted in the last row of Figure (5.6-7c), show that the tracer completely dispersed throughout the tank and reached the surface, bottom and wall of the tank. At higher impeller speeds the xanthan

gum solution was swept away from the impeller, leading to improved mixing by overcoming the yield stress of the fluid in the stagnant zones.

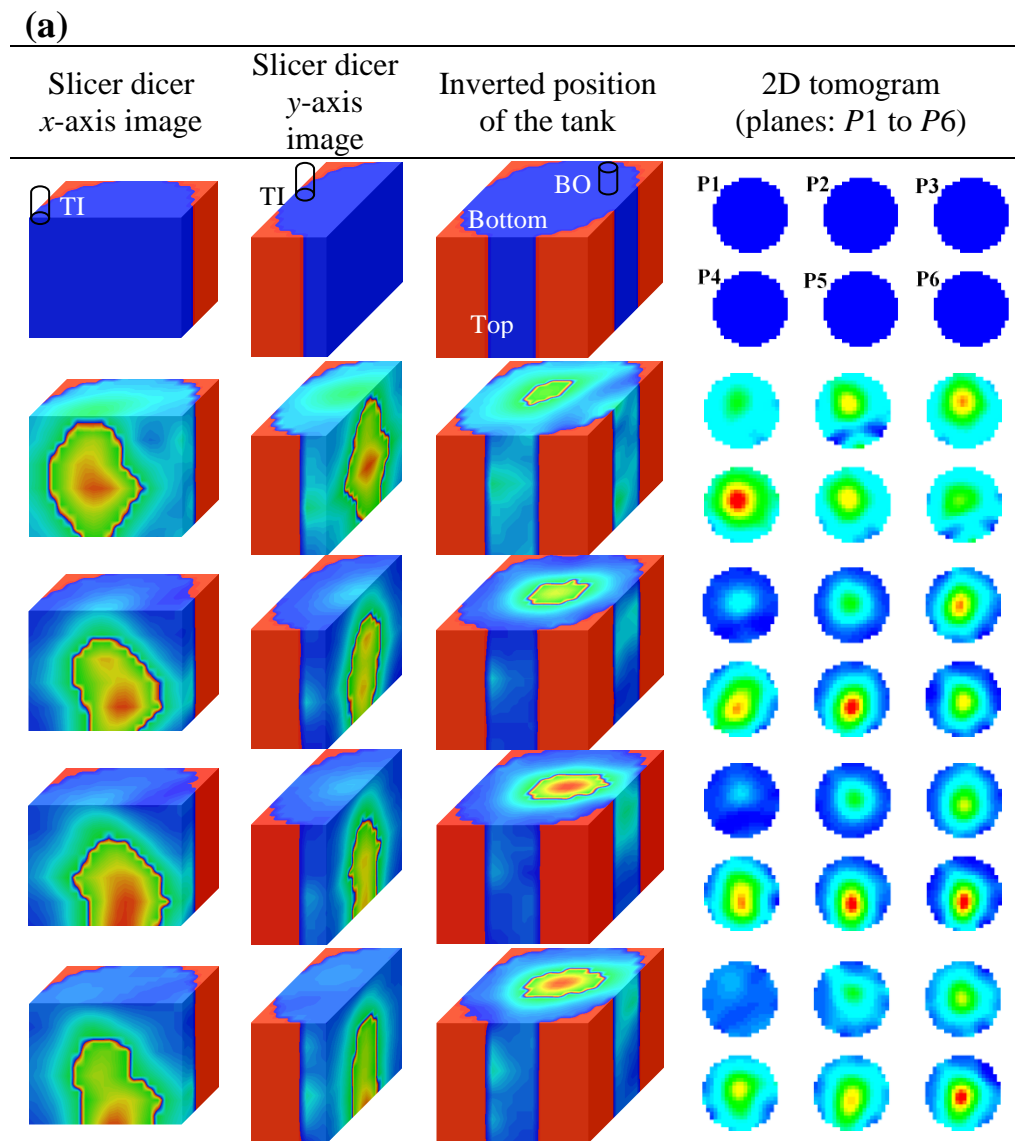


Figure (5.6-7). Effect of the impeller speed on the fluid flow (a) $N = 77$ rpm, (b) $N = 100$ rpm, and (c) $N = 250$ rpm (RT impeller, $Q = 9.65 \text{ L min}^{-1}$, 1.0% xanthan gum, $V_j = 0.317 \text{ m s}^{-1}$, and input-output locations: TI–BO).

At lower impeller speeds, the stagnant zones were present at the surfaces and corners of the vessel because the shear stress produced by the impeller was less than the yield stress of the fluid in the stagnant zones. This is attributed to the momentum flux generated by the impellers. As mentioned earlier, the momentum flux generated by the RT impeller at $N = 54$ rpm was

estimated at about $73.31 \text{ kg m}^{-1} \text{ s}^{-2}$, which was approximately 1.3 times lower than the momentum flux generated by the inlet flow ($99.92 \text{ kg m}^{-1} \text{ s}^{-2}$).

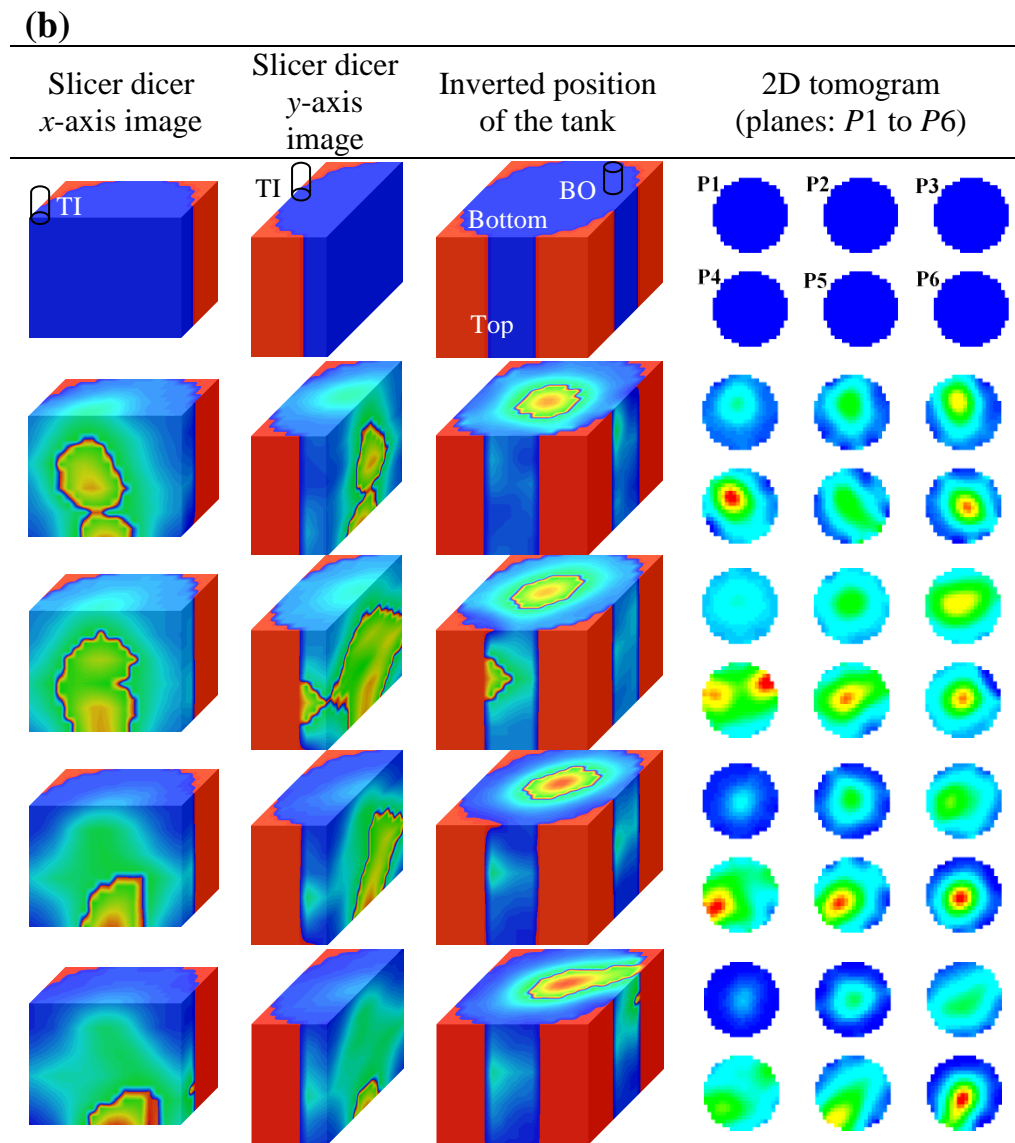


Figure (5.6-7). (Continued).

The momentum flux generated by the RT impeller at $N = 250 \text{ rpm}$ was estimated at about $1571.21 \text{ kg m}^{-1} \text{ s}^{-2}$, which was approximately 16 times higher than the momentum flux generated by the inlet flow ($99.92 \text{ kg m}^{-1} \text{ s}^{-2}$) and about 21 times higher than that generated by the RT impeller at $N = 54 \text{ rpm}$ ($73.31 \text{ kg m}^{-1} \text{ s}^{-2}$). Figure (5.6-6) shows that as the power input was raised by increasing the impeller speed, the extent of channeling (f) decreased and the fraction of fully mixed volume increased for both impellers. In fact, the degree of channeling

(f) should be minimized and the fraction of the fully mixed volume should be maximized to enhance the efficiency of the continuous-flow mixing system.

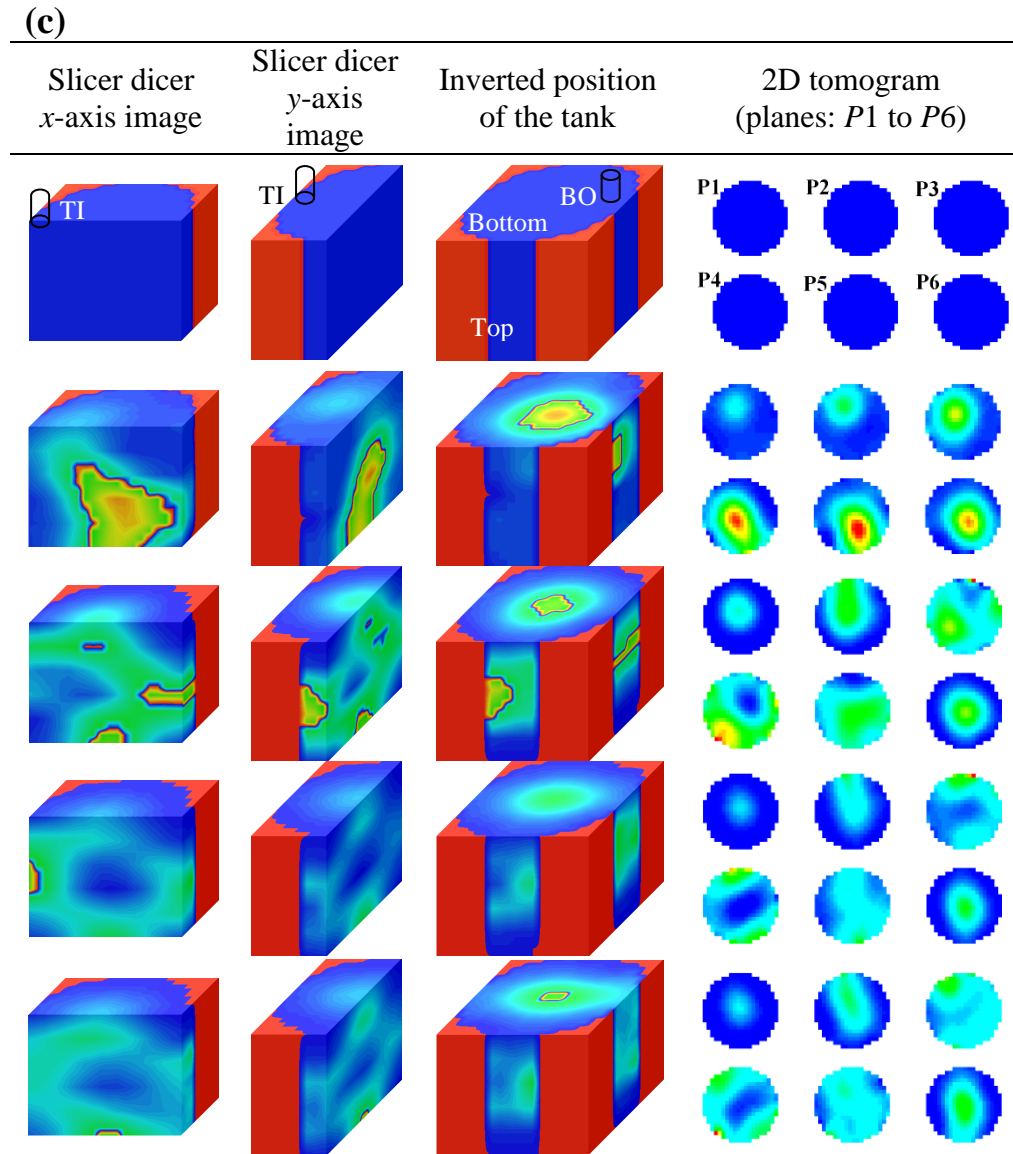


Figure (5.6-7). (Continued).

5.6.3 Conclusions

In this study, electrical resistance tomography (ERT) was used to visualize the flow of opaque fluid (biopolymer solutions) in the continuous-flow mixing system. The 2D and 3D

tomography images were utilized to analyze the flow field inside the reactor at different operating conditions and design parameters. The volume in which the tracer distributed inside the mixing vessel was quantified for each operating conditions and design parameters. The extra momentum flux generated by the inlet-outlet flow was estimated and compared with the momentum flux generated by the impeller. At a lower impeller speed, the momentum flux added to the system due to the inlet flow had a tremendous effect on the mixing of the non-Newtonian fluids exhibiting yield stress. Moreover, the ratio of the $Q/Q_{impeller}$ was employed to study the effect of the feed flow rate on the tracer distribution. The effect of each factor on the flow field is described below:

- **Impeller type:** The quantitative analysis shows that the tracer distribution achieved using the Maxblend impeller was more significant than using the RT impeller. The Maxblend impeller was able to distribute the tracer more evenly than the RT impeller with the same operating conditions. It should be mentioned that the RT impellers are designed for the transitional flow while the Maxblend impeller are designed for both laminar and transitional flows.
- **Impeller speed:** When the impeller speed was increased from 54 rpm to 250 rpm with identical operating conditions, the non-ideal flows, such as dead zones and channeling, decreased inside the vessel. This was due to the momentum flux generated by the RT impeller at $N = 250$ rpm, which was approximately 16 times higher than the momentum flux created by the inlet flow and about 21 times higher than that generated by the RT impeller at $N = 54$ rpm.
- **Jet effect and feed flow rate:** When the jet velocity (V_j) was increased from 0.317 to 1.66 m s^{-1} , with identical operating conditions, the volume of the tracer distribution also increased from 28 to 44% of the total volume of the fluid in the vessel. Moreover, when fluid flow rate (Q) was increased from 3.2 to 14.17 L min^{-1} , the tracer distribution was higher at the higher flow rate.
- **Inlet and outlet locations:** The channeling and dead zones were observed in all four configurations (BI–TO, TI–BO, BI–BO, and TI–TO) with identical operating conditions. However, in the BI–TO and TI–BO configurations, the feed was forced to pass through the mixing zone before leaving the vessel, therefore, the tracer distribution achieved in the TI–

BO and BI-TO configurations was more than those in the BI-BO and TI-TO configurations. The TI-TO and BI-BO configurations enabled the fluid to pass from the inlet to the outlet without being pushed into the impeller mixing zone. Thus, the degree of channeling within the mixing tank increased.

- **Fluid rheology:** The quantitative analysis also shows that as the fluid yield stress was decreased by decreasing the fluid concentration from 1.5 to 0.5%, the volume in which the tracer distribution achieved increased from 20 to 39% of the total volume of the fluid in the vessel.

5.7 Effect of Rheological Parameters on the Continuous-Flow Mixing of Biopolymer Solutions

5.7.1 Introduction

A novel study on exploring the effect of the rheological parameters of the pseudoplastic fluids with yield stress on the non ideal flows in a continuous-flow mixing system was performed. The xanthan gum solution (a biopolymer solution) is a yield-pseudoplastic fluid whose rheology can be described by the Herschel-Bulkley model. In fact, varying the xanthan gum concentration changes the values of all rheological parameters (i.e., consistency index (K), power law index (n) and fluid yield stress (τ_y)) simultaneously. Thus, merely studying the effect of the xanthan gum concentration on the flow nonideality represents the combined effect of all Herschel-Bulkley model parameters. No study has attempted to investigate the effect of the rheological parameters of the Herschel-Bulkley model on the performance of the continuous-flow mixing of shear thinning fluids possessing yield stress in the stirred vessels. Therefore, the core objective of this research was to investigate the effects of K (3–33 Pa s ^{n}), n (0.11–0.99), τ_y (1.7–20.6 Pa), xanthan gum concentration (0.5–1.5%), and feed flow rate (Q) (03.20–14.17 L min⁻¹) on the extent of channeling (f) and fully mixed volume ($V_{fully\ mixed}$) in the continuous stirred-tank reactor using computational fluid dynamics (CFD).

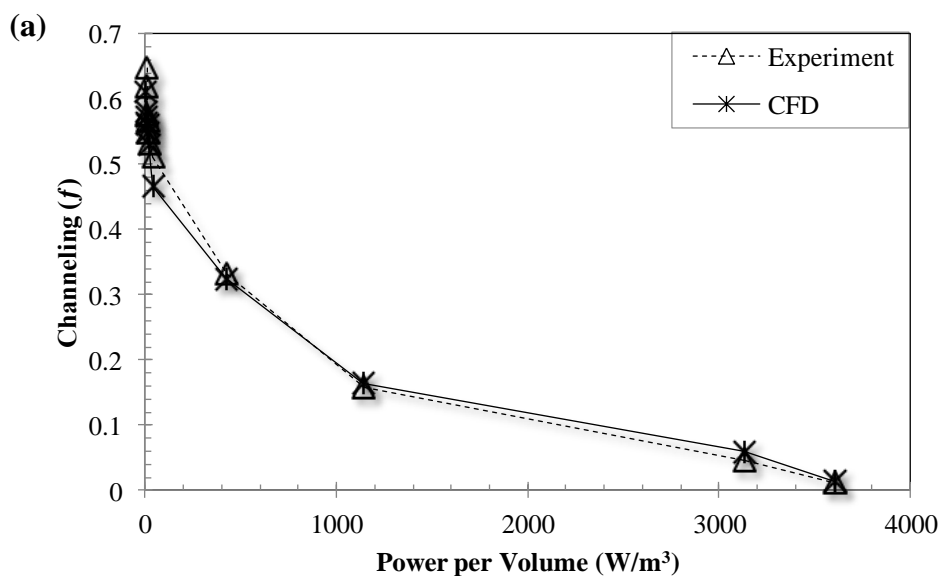
A mixing tank with identical geometry to the one used in the experiments Figure (3.1-1) was modeled using ANSYS DesignModeler [Section (4.2.1)]. The Radial-flow impeller (the RT impeller) was used in this study. Grid independence was verified by demonstrating that additional cells did not change the calculated velocity magnitude measured in the regions of high velocity gradients around the impeller blades by more than 6% [Figure (4.2-2)]. The optimal mesh of the model, which consisted of 817,077 cells, was used in all simulations [Figure (4.2-1)]. Fluid rheological parameters applied in CFD modeling are provided in Table (4.2-1). As demonstrated in Figure (4.2-6) and Figure (4.2-7), the CFD model was validated with the experimental data for continuous-flow mixing system. A user-defined function (UDF) written in C programming language was linked to the ANSYS Fluent 14.5 solver for simulating the dynamic tests. CFD model development is fully described in Section (4.2).

5.7.2 Results and Discussion

The power number (P_o) for RT impellers was calculated using Equation (2.1–3). The Reynolds number (Re) was calculated using Equation (2.1–11). Figure (3.4-1) represents the power curve for the DHR and anchor impellers. The power number curve for the RT impeller depicted in Figure (4.2-7) showed good agreement between the calculated power numbers through CFD and the experimentally determined values.

5.7.2.1 Effect of Power Input

The dynamic performance of a continuous-flow mixing system is extensively affected by the impeller speed or power input. Normally, more power produces more intense mixing, which means that increasing the power input with an increase in the impeller speed reduces the extent of the non-ideal flows in the continuous-flow mixing systems. The CFD predicted results in Figure (5.7-1a and b) shows the extent of channeling and the fraction of fully mixed volume as a function of power consumption per unit volume for the RT impellers, respectively. These results indicated that the channeling decreased and the fully mixed volume increased with an increase in the power input.



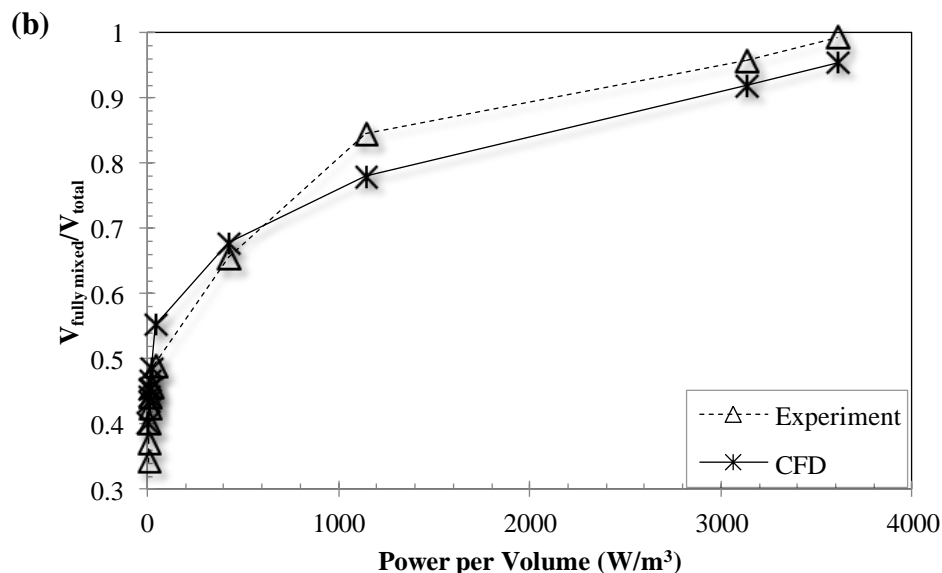


Figure (5.7-1). Effect of impeller power on the extent of (a) channeling and (b) fully mixed volume ($Q = 9.65 \text{ L min}^{-1}$ and 1.0% xanthan gum).

This result confirmed the similar phenomenon observed by Ford et al. (2006) and Saeed et al. (2008) in the mixing of yield-pseudoplastic fluids. At lower impeller speed, the shear stress produced by the impeller was less than the yield stress of the fluid in the stagnant zones. While at higher impeller speed the xanthan gum solution was swept away from the impeller, leading to improved mixing by overcoming the yield stress of the fluid. The optimum power input should be chosen in such a way that the channeling approaches zero and the fully mixed volume approaches the total volume of the fluid within the mixing tank, as further increases in impeller speed may lead to more power consumption for the same extent of the fully mixed volume.

5.7.2.2 Effect of Fluid Rheology

The fluid mass concentration is one of the crucial factors that have a significant effect on the dynamic performance of the continuous-flow mixing. Therefore, this study explores the effect of 0.5, 1.0, and 1.5% xanthan gum concentrations on the extent of non-ideal flows. The effect of xanthan gum concentration on the extent of channeling and the fraction of fully mixed volume is represented in Figure (5.7-2).

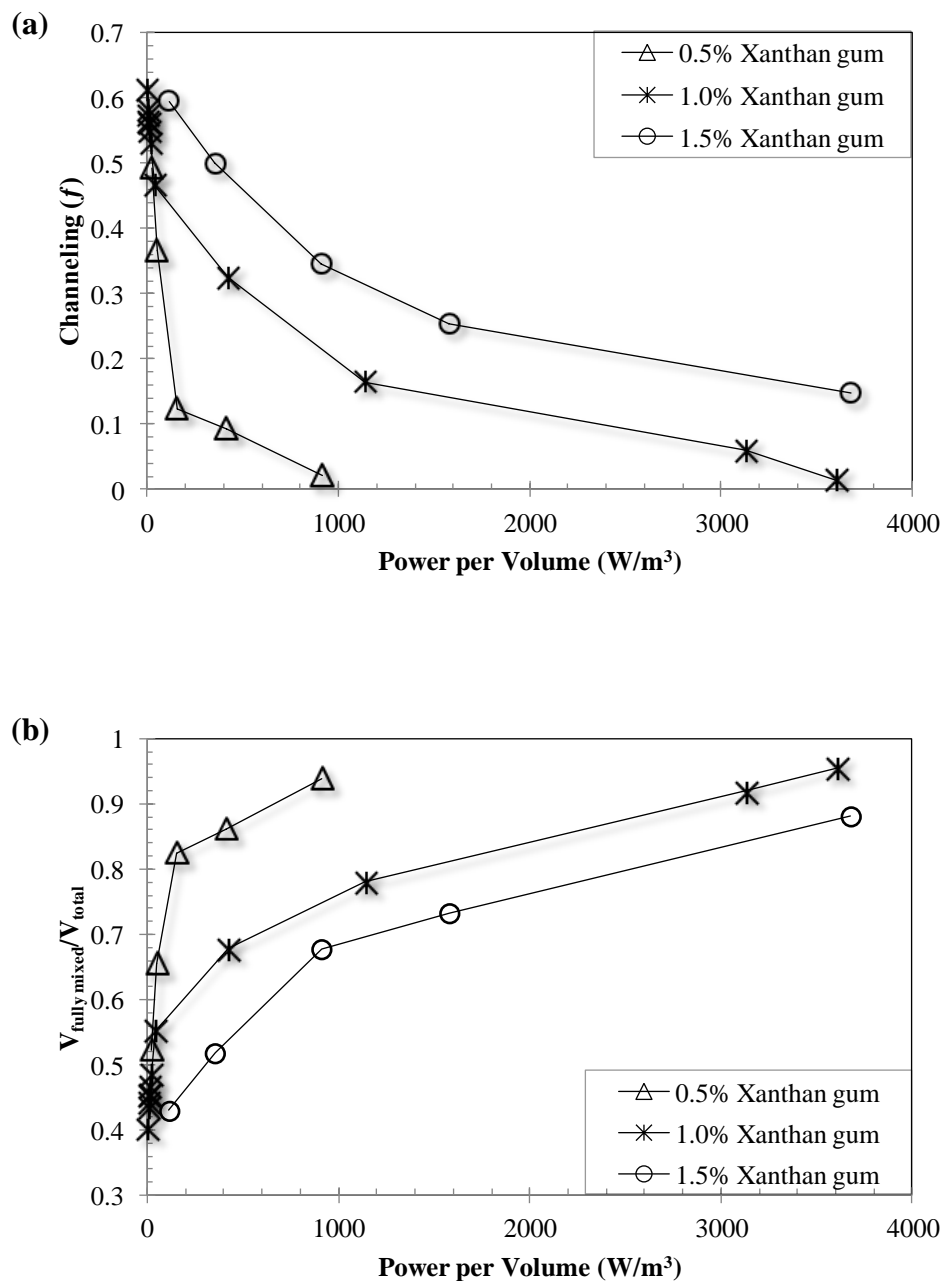


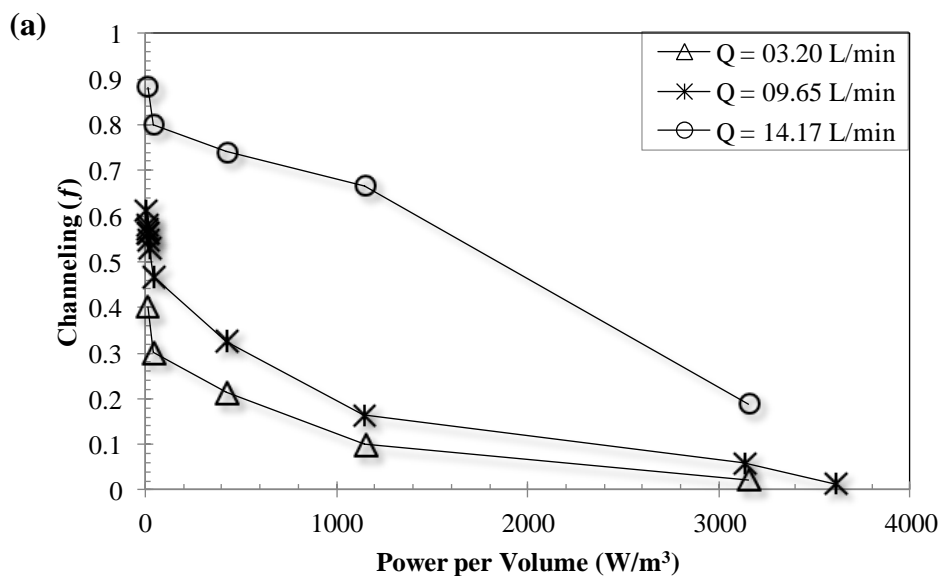
Figure (5.7-2). Effect of fluid rheology on the extent of (a) channeling and (b) fully mixed volume ($Q = 9.65 \text{ L min}^{-1}$).

The CFD prediction showed that the extent of the channeling increased and the fraction of fully mixed volume decreased as xanthan gum concentration increased from 0.5 to 1.5% at a fixed power input. The solution yield stress increases with an increase in xanthan gum solution

concentration. At higher yield stress the energy dissipation became faster, which resulted in an increase in the extent of non-ideal flows (Ein-Mozaffari et al., 2005). In addition, the fluctuating velocities will weaken quickly in the area outside of the impeller zone due to a high fluid apparent viscosity, which is a function of the yield stress; although the flow near the impeller might be turbulent. Such a phenomenon was also observed by Saeed et al. (2008).

5.7.2.3 Effect of Feed Flow Rate

Fluid flow rate is also one of the important parameters that affect the efficiency of the continuous-flow mixers. CFD results in Figure (5.7-3a and b) show the effects of three different feed flow rates (3.20, 9.65, and 14.17 L min⁻¹) on the extent of channeling and fully mixed volume, respectively. These graph shows that the extent of the channeling increased and the fraction of fully mixed volume decreased as the fluid flow rate through the mixing vessel was increased. In fact, increasing the feed flow rate through the mixing vessel decreases the mean residence time in the vessel, which forces the fluid to exit the vessel faster. In contrast, decreasing the fluid flow rate increases the mean residence time in the vessel, so the fluid gets more time with the intense motion created by the impeller within the tank; this ultimately improves the mixing quality in the vessel.



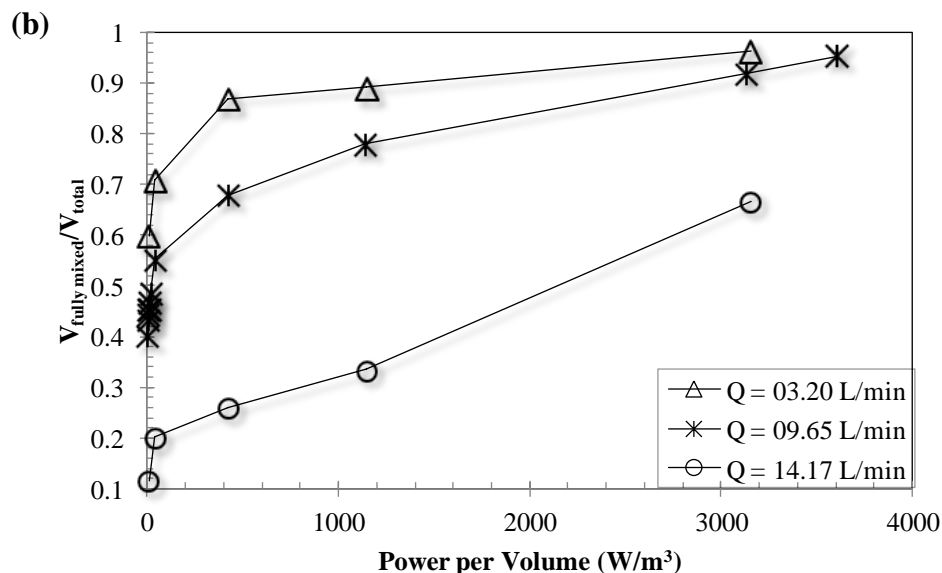


Figure (5.7-3). Effect of fluid flow rate through mixing vessel on the extent of (a) channeling and (b) fully mixed volume (1.0% xanthan gum).

Hence, for the similar operating conditions, the system was more susceptible to channeling at the lower mean residence time than the higher mean residence time. Similar results were also observed by other researchers (Ford et al., 2006).

5.7.2.4 Effect of Power Law Index

The fluid rheology has a considerable effect on the dynamic performance of the continuous-flow mixing. Therefore, the effect of the shear-thinning (power law index, n) on the non-ideal flows was explored in the continuous-flow mixer. In the CFD simulations, it is possible to hold the values of K , τ_y and μ_0 constant and vary the values of power law index (n). In this CFD study, the power law index was varied from 0.11 to 0.99 while holding the other parameters at $K = 8 \text{ Pa S}^n$, $\tau_y = 5.254 \text{ Pa}$, and $\mu_0 = 22.613 \text{ Pa S}$. The effect of power law index (n) on the extent of the channeling (f) and fully mixed volume ($V_{\text{fully mixed}}$) are illustrated in Figure (5.7-4). The results show that the extent of the channeling increased and the fraction of fully mixed volume decreased as the power law index was increased. The power law index for a Newtonian fluid is $n = 1$. When the power law index (n) approaches zero, the fluid exhibits a highly shear-thinning behavior.

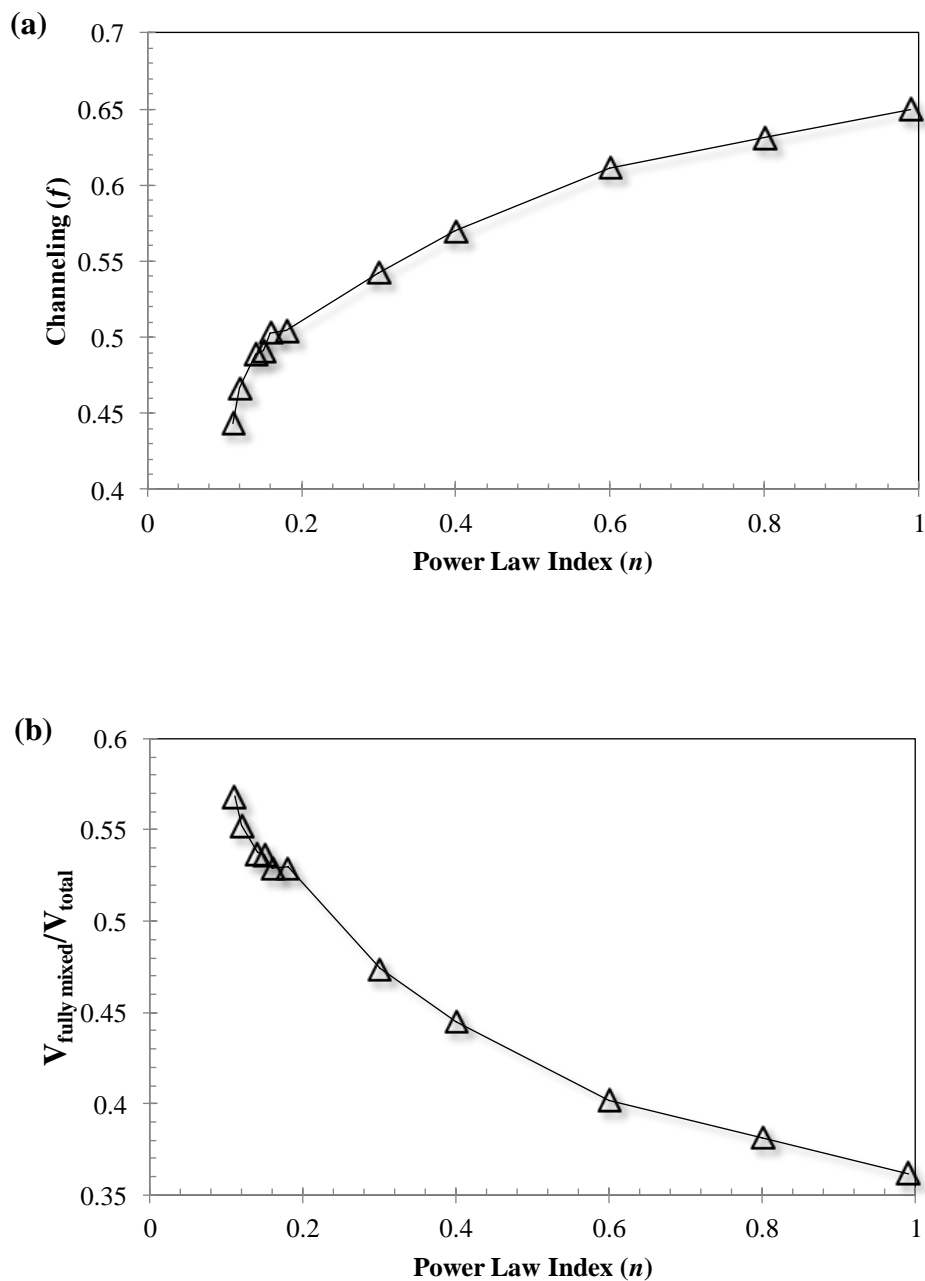


Figure (5.7-4). Effect of power law index (n) on the extent of (a) channeling and (b) fully mixed volume ($Q = 9.65 \text{ L min}^{-1}$, $N = 100 \text{ rpm}$, $K = 8 \text{ Pa s}^n$, $\tau_y = 5.25 \text{ Pa}$, and $\mu_o = 22.61 \text{ Pa s}$).

Due to instinctive nature of a shear-thinning fluid, the apparent viscosity of the fluid decreases with an increase in the shear rate; consequently the fluid flows easily within the mixing vessel and thus the mixing quality is enhanced (Wichterle and Wein, 1975). Therefore, the extent of

the channeling decreased and the fraction of fully mixed volume increased at the lower values of the power law index. However, when the power law index of the fluid increases, the apparent viscosity increases as well. Hence, the extent of the channeling increased and the fraction of fully mixed volume decreased as the value of n was increased from 0.11 to 0.99. Similar results were observed by Liu et al. (2006), who studied the laminar mixing of shear thinning fluids in a static mixer using CFD. They used power-law model to capture shear-thinning behavior of the fluid. Using the particle tracking technique, they found that shear-thinning behavior of the fluid resulted in better mixing quality and lower pressure drop in comparison with the Newtonian fluids.

5.7.2.5 Effect of Fluid Yield Stress

This CFD study also explored the effect of fluid yield stress (τ_y) on the non-ideal flows. In this case, the value of τ_y was varied from 1.79 to 20.6 Pa while holding other parameters at $K = 8 \text{ Pa S}^n$ and $n = 0.12$. Figure (5.7-5) represents the effect of fluid yield stress (τ_y) on the extent of the channeling (f) and fully mixed volume ($V_{fully\ mixed}$). These results showed that the extent of the channeling increased and the fraction of fully mixed volume decreased as the fluid yield stress (τ_y) was increased from 1.79 to 20.6 Pa. To some extent the shear stress imparted by the impeller failed to exceed the fluid yield stress in the regions away from the impeller as τ_y increased. This resulted in the formation of the poor mixing regions within the vessel at the higher fluid yield stress.

5.7.2.6 Effect of Fluid Consistency Index

Further, the effect of consistency index (K) on the performance of the continuous-flow mixing system was studied using CFD. To achieve this goal, the value of K was varied from 3.0 to 33.1 Pa S^n while holding the other parameters at $n = 0.12$, $\tau_y = 5.254 \text{ Pa}$, and $\mu_0 = 22.613 \text{ Pa S}$. Figure (5.7-6) displays the effect of the consistency index (K) on the extent of channeling (f) and fully mixed volume ($V_{fully\ mixed}$). These data showed that the extent of the channeling increased and the fraction of fully mixed volume decreased as K was increased from 3.0 to 33.1 Pa S^n . According to Equation (2.1–9), the fluid apparent viscosity increases with an increase in

the consistency index. Thus, the mixing system is susceptible to poor mixing and existence of non-ideal flows due to the higher apparent viscosity of the fluid.

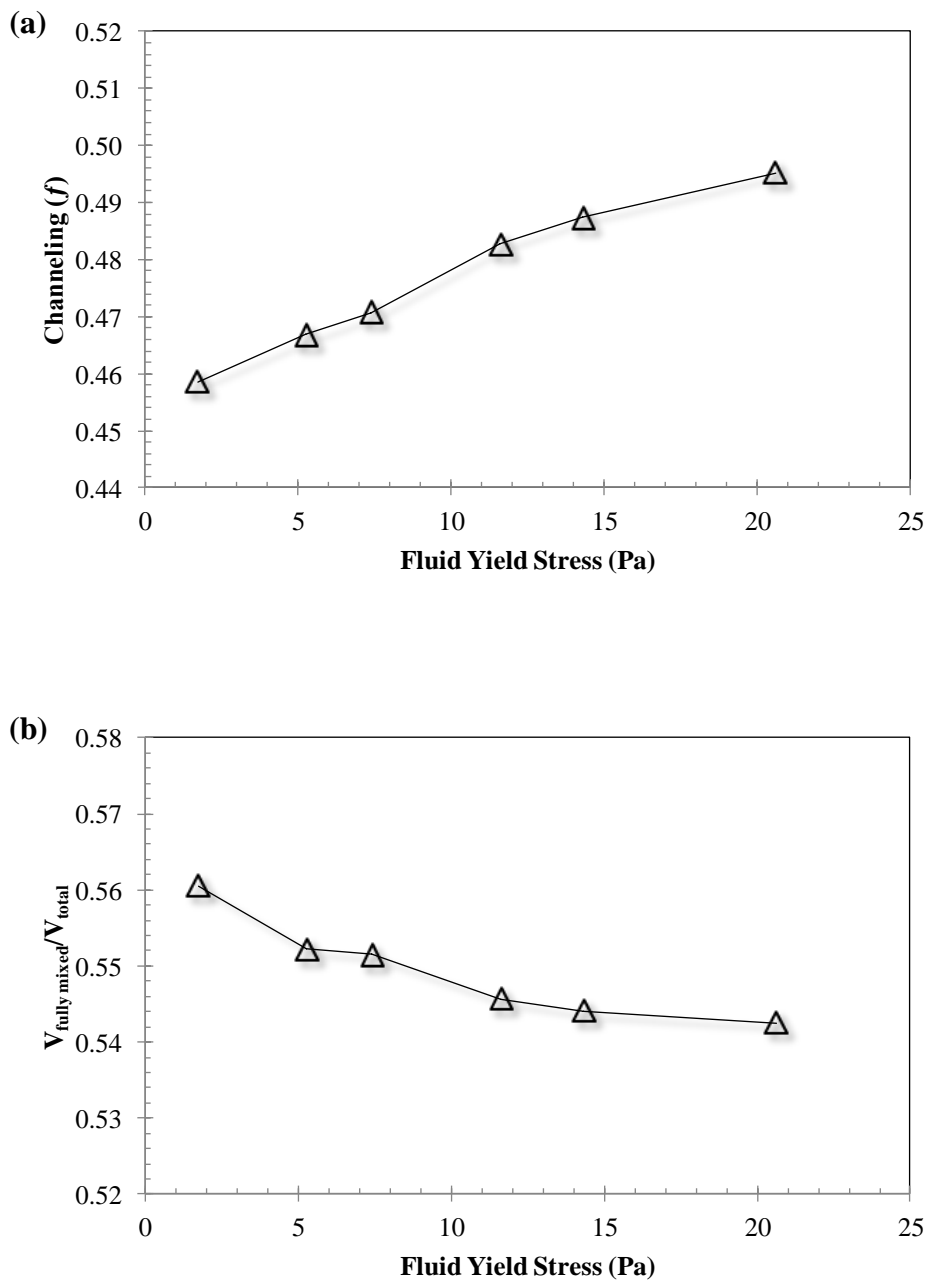


Figure (5.7-5). Effect of fluid yield stress (τ_y) on the extent of (a) channeling and (b) fully mixed volume ($Q = 9.65 \text{ L min}^{-1}$, $N = 100 \text{ rpm}$, $K = 8 \text{ Pa s}^n$, and $n = 0.12$).

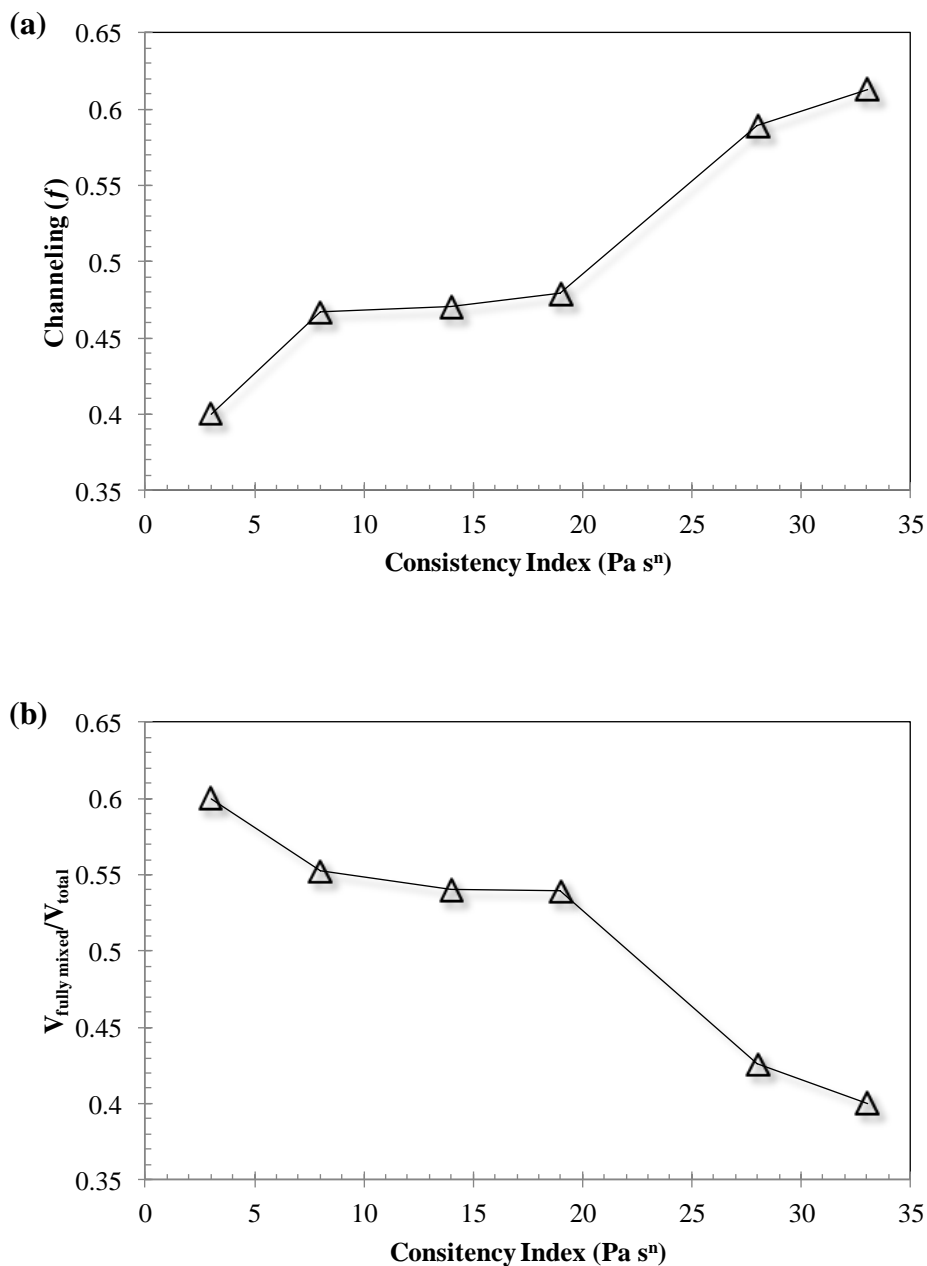


Figure (5.7-6). Effect of consistency index (K) on the extent of (a) channeling and (b) fully mixed volume ($Q = 9.65 \text{ L min}^{-1}$, $N = 100 \text{ rpm}$, $n = 0.12$, $\tau_y = 5.25 \text{ Pa}$, and $\mu_o = 22.61 \text{ Pa s}$).

5.7.3 Conclusions

The computational fluid dynamics (CFD) modeling was successfully employed to study the continuous-flow mixing of xanthan gum solution, which is a shear thinning fluid possessing

yield stress, in a stirred reactor. The MRF technique was used to model the rotation of the impeller. Grid independence was confirmed by showing that additional cells did not change the calculated velocity magnitude measured in the regions of high velocity gradients by more than 5%. The optimal mesh of the model (817,077 cells) was used in all simulations. The power number calculated by the CFD model was in good agreement with the experimentally measured values. The calculated CFD flow field was used to obtain the dynamic response of the continuous mixing system to a frequency-modulated random binary input signal. The calculated dynamic responses matched reasonably well with the measured responses. The dynamic model was used to quantify the extent of channeling and fully mixed volume in the continuous-flow mixing vessel. The validated CFD model was then employed to explore the effect of fluid rheology, especially the Herschel-Bulkley model parameters, on the mixing quality. The CFD results showed that the extent of non-ideal flows increased and the fraction of fully mixed volume decreased as the power law index (n) was increased from 0.11 to 0.99. When the power law index (n) approaches zero, the fluid exhibits a highly shear-thinning behavior. Due to instinctive nature of a shear-thinning fluid, the apparent viscosity of the fluid decreases with an increase in the shear rate, consequently the fluid flows easily within the mixing vessel and thus the mixing quality is enhanced. It was also found that when the Herschel-Bulkley model parameters K (consistency index) and τ_y (fluid yield stress) were decreased, the performance of the continuous-flow mixer was improved. In fact, the fluid apparent viscosity increases with an increase in the consistency index and yield stress. Thus, the mixing system is susceptible to poor mixing and existence of non-ideal flows due to the higher apparent viscosity of the fluid. In addition, the CFD results also showed that the efficiency of the continuous-flow mixing system can be improved by increasing the fluid residence time in the mixing vessel and reducing the solution mass concentration.

5.8 Using CFD to Study the Effect of Rheological Parameters on Mixing Time for the Shear Thinning Fluids with Yield Stress

5.8.1 Introduction

The xanthan gum solution (a biopolymer solution) is a yield-pseudoplastic fluid whose rheology is described by the Herschel-Bulkley model. In reality, changing the xanthan gum concentration varies the values of all rheological parameters (i.e. consistency index (K), power law index (n) and fluid yield stress (τ_y)) simultaneously. Therefore, simply studying the effect of the xanthan gum concentration on the mixing performance represents the combined effect of all Herschel-Bulkley model parameters.

To the best of the author's knowledge, no attempt has been made to study the effect of the rheological parameters of the Herschel-Bulkley model on the performance of the batch mixing of shear thinning fluids possessing yield stress in the stirred vessels. The main objective of this research was to investigate the effects of K (3–33 Pa sⁿ), n (0.11–0.99), τ_y (1.7–20.6 Pa), xanthan gum mass concentration (0.5–1.5 wt/v %), and impeller speed (N) (500–1000 rpm) on the mixing time (θ) in the stirred-tank reactor using computational fluid dynamics (CFD). CFD was also used to measure the cavern volume (V_c) in the batch mode. CFD dynamic tests were also performed to estimate the fully mixed volume ($V_{fully\ mixed}$) in a continuous-flow mixing system.

A mixing tank with identical geometry to the one used in the experiments [Figure (3.2-1)] was modeled using ANSYS DesignModeler [Section (4.2.1)]. The Radial-flow impeller (the RT impeller) was used in this study. Grid independence was verified by demonstrating that additional cells did not change the calculated velocity magnitude measured in the regions of high velocity gradients around the impeller blades by more than 6% [Figure (4.2-2)]. The optimal mesh of the model, which consisted of 817,077 cells, was used in all simulations. Fluid rheological parameters applied in CFD modeling are provided in Table (4.2-1). As demonstrated in Figure (4.2-7), the CFD model was validated with the experimental power number for batch mixing. CFD model development is fully described in Section (4.2).

To measure the mixing time (θ) using CFD, procedure described in Section (4.2.5) was used. The tracer having the same physical properties as xantahn gum solution was added below the liquid surface at point ($x = 0.07, y = 0.11, z = 0.34$). In this study, the mixing time (θ) was defined as the time required for the mass concentration of the fluid to reach 98% of the steady-state value after the injection of the tracer. The tracer was monitored at point-1 ($x = -0.09, y = -0.09, z = 0.34$); point-2 ($x = 0.03, y = -0.13, z = 0.28$); point-3 ($x = 0.09, y = 0.09, z = 0.22$); point-4 ($x = 0.11, y = 0.03, z = 0.16$); point-5 ($x = -0.12, y = 0.04, z = 0.10$); and point-6 ($x = 0.09, y = -0.07, z = 0.04$). The vertical position of each monitoring point in CFD model was set identical to that of the ERT planes shown in Figure (3.2-1). Figure (4.2-8) shows a practical approach to measure the mixing time after the injection of the tracer for six monitoring points. The cavern size was also measure suing CFD modeling. The procedure to measure the cavern size in batch mixing using CFD is described in Section (4.2.6).

5.8.2 Results and Discussion

5.8.2.1 CFD and Experimental Cavern Diameter

To measure the cavern size using CFD results, the shape of the cavern was approximated by a right circular cylinder; therefore, the characteristics of the cavern can be described by the diameter and height of this region. The cavern diameter was measured on a horizontal plane passing through the impeller on plane *P4* (point-4). The cavern height was measured on a vertical plane along the shaft and perpendicular to the horizontal plane of the impeller. As shown in Figure (4.2-9), the cavern boundary was determined as a position at which the velocity magnitude of xanthan gum solution was zero. Section (4.2.6) describes the procedure to measure the cavern size in batch mixing using CFD. The measured cavern diameter was compared to those predicted using Elson's cylindrical model [Equation (2.3-1)]. This model can be used to estimate the cavern diameter before the cavern touches the vessel wall. Figure (5.8-1) shows comparison between CFD and experimental data for dimensionless cavern diameter (D_c/D) versus dimensionless P_oRe_y on a log-log scale for the RT impeller at 0.5, 1.0, and 1.5% xanthan gum solutions. The CFD results found in this study agreed well with the value measured in the ERT experiments. The diameter of the cavern was found to increase with

an increase in the impeller speed and it continued to grow until the cavern reached the vessel wall. As per Elson's cylindrical model [Equation(2.3-1)], a log-log plot of the D_c/D versus P_oRe_y should give a slope of 1/3. As shown in Figure (5.8-1), the slope of this line calculated using the least-square method was 0.34 for the RT impeller. Pakzad et al. (2008) reported a value of 0.35 for the slope of the D_c/D versus P_oRe_y for the Scaba radial-flow impeller. The results found in this study agreed well with the value reported in the open literature.

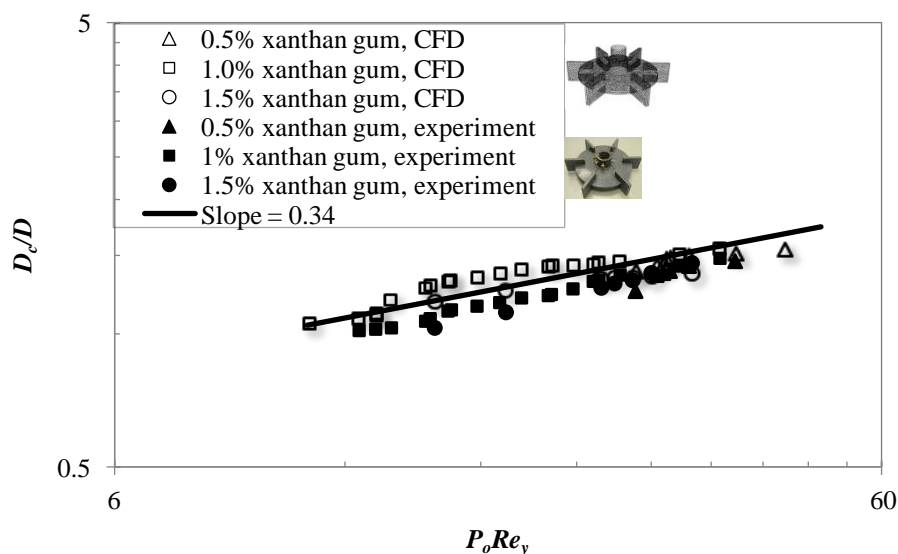


Figure (5.8-1). Comparison between CFD and experimental data for dimensionless cavern diameter (D_c/D) versus dimensionless P_oRe_y at 0.5, 1.0, and 1.5% xanthan gum solutions.

5.8.2.2 Effect of Fluid Rheology on Cavern Volume

The cavern volume (V_c) was calculated using the cavern diameter (D_c) and the cavern height (H_c) for a cylindrical shape. Figure (5.8-2) represents the effect of fluid rheology on the dimensionless cavern volume (V_c/V_{total}) versus the power per unit volume for the RT impeller at 0.5, 1.0, and 1.5% xanthan gum solutions in the batch mode. This figure also represents the comparison between the cavern volume calculated using CFD and cavern volume measured using ERT experiments. The CFD and ERT experimental results show good agreement with each other. These results show that as the impeller speed/power was increased, the cavern diameter and height also increased for all concentrations and so did the cavern volume (V_c). Though, with respect to the xanthan gum concentration, the dimensionless cavern volume

(V_c/V_{total}) was observed as decreasing. This can be attributed to the effect of the yield stress, which increases with the xanthan gum concentrations. More stagnant regions are formed in the mixing vessel where shear stress fails to exceed yield stress, which reduces the cavern volume. Hence, the dimensionless cavern volume decreased with an increase in the xanthan gum concentrations.

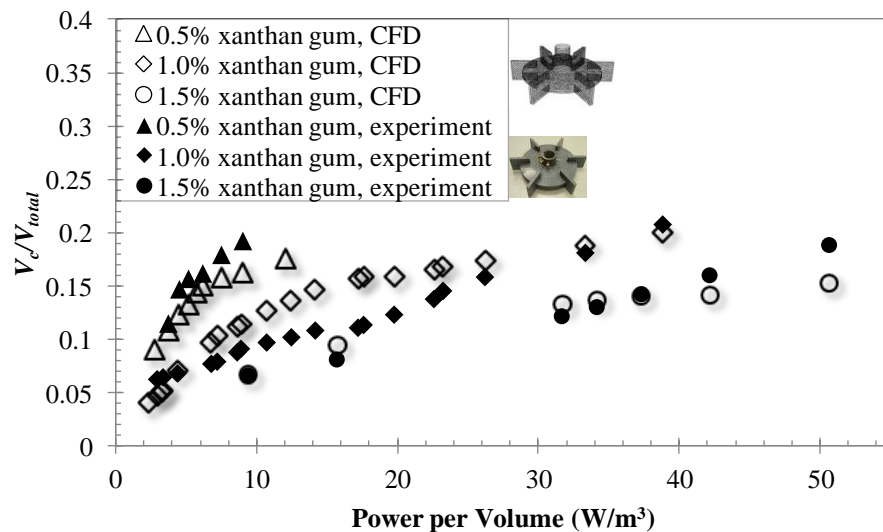


Figure (5.8-2). Effect of the fluid rheology on the dimensionless cavern volume (V_c/V_{total}) at 0.5, 1.0, and 1.5% xanthan gum solutions using CFD and experimental data.

5.8.2.3 Comparison between Cavern and Fully Mixed Volume

To relate the cavern volume (V_c) in the batch vessel to the fully mixed volume ($V_{fully\ mixed}$) in the continuous-flow mixing system, CFD dynamic simulations were performed at 1% xanthan gum solution for the RT impeller. In these CFD simulations, the cavern size in the batch mode and the fully-mixed volume in the continuous mode were conducted at the identical operating conditions except for the feed flow rate ($Q = 9.65\ L\ min^{-1}$; residence time = 292 s) and the location of the inlet and outlet, which were additional to the continuous-flow mode. The comparisons between the dimensionless cavern volume (V_c/V_{total}) in the batch mode and the fraction of the fully mixed volume ($V_{fully\ mixed}/V_{total}$) in the continuous-flow mode for the RT impeller is shown in Figure (5.8-3). From the results, it can be seen that the fully mixed volume generated in the continuous-flow mixing system was higher than the cavern volume generated

in the batch mixing system for RT impeller at the given operating conditions. This can be attributed to the momentum added to the fluid in the mixing vessel by the input and output flows passing through the vessel. Mixing of the fluid requires the input of mechanical energy to achieve the process results. In both the batch and continuous-flow modes, this energy is generally provided through the impeller. An alternative method for getting energy into the fluid is to generate a jet stream of fluid in the vessel. This jet entrains and mixes the surrounding fluids through the mechanical energy supplied by the pump (Paul et al, 2004). This is achieved through the feed stream in the continuous-flow mode. In fact, in the continuous-flow mixing system the fluid passing from the inlet to the outlet generates extra flows and adds more momentum to the fluid flow in the stirred vessel. The extra momentum flux ($Q \rho v/A$, where v is the velocity of the fluid passing through the inlet, and A is the cross section area of the inlet pipe) added to the fluid in the mixing vessel at the inlet position was about $99.92 \text{ kg m}^{-1} \text{ s}^{-2}$. Due to this fact, the size of the mixed volume in the continuous mode was higher than that in the batch mode. Patel et al. (2014a) demonstrated that at a lower impeller speed, the momentum flux added to the system due to the inlet flow had a tremendous effect on the mixing of the non-Newtonian fluids exhibiting yield stress.

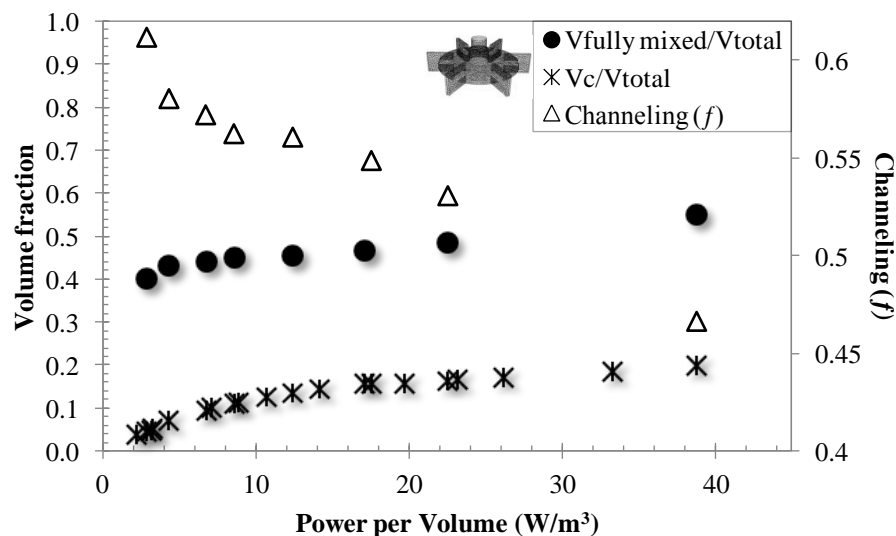


Figure (5.8-3). Dimensionless cavern volume (V_c/V_{total}), the fraction of fully mixed volume ($V_{\text{fully mixed}}/V_{\text{total}}$), and the extent of channeling (f) as a function of the specific power at 1% xanthan gum solution.

Figure (5.8-3) also represents the extent of channeling (f) identified through the CFD dynamic tests for the RT impellers. The results show that as the power input was raised by increasing the impeller speed, the channeling (f) decreased. At a lower impeller speed, the shear stress produced by the impeller was less than the yield stress of the fluid in the stagnant zone. At a higher impeller speed the xanthan gum solution was swept away from the impeller, leading to improved mixing by overcoming the fluid yield stress. Thus, it provided less channeling by entraining the feed into the mixing zones. In fact, the extent of channeling (f) should be minimized to enhance the efficiency of the continuous-flow mixing system.

5.8.2.4 Effect of Impeller Speed on Mixing Time

The effect of the impeller speed on the mixing time (θ) as a function of the xanthan gum concentration is depicted in Figure (5.8-4). The results demonstrate that as the impeller rotational speed was increased, the mixing time decreased. It can be observed that the variation in the mixing time was much faster at the lower impeller speeds compared to that at the higher impeller speeds. The slow moving fluid was observed visually near the baffles at the top corner of the vessel at the lower impeller speeds. At a higher impeller speed the xanthan gum solution was agitated vigorously and disrupted farther from the impeller, leading to an improved mixing quality. The optimum power input should be chosen in such a way that further increases in the impeller speed leads to slight variations in the mixing time. In fact, under these circumstances, considerable power consumption is required to achieve a slight improvement in the mixing quality. Conversely, a lower impeller speed than the optimum speed may cause dead volume in the mixing vessel. This result confirmed the similar phenomenon observed by Patel et al. (2013b) for the mixing of pseudoplastic fluids possessing yield stress.

5.8.2.5 Effect of Fluid Rheology on Mixing Time

The fluid rheology has a significant effect on the mixing performance of the impellers. We explored the effect of xanthan gum concentration (0.5, 1.0, and 1.5 w/v %) on the mixing time (θ). Figure (5.8-4) represents the effect of the xanthan gum concentrations on the mixing time as a function of the impeller speed as well. The results show that as the xanthan gum concentration was increased from 0.5 to 1.5%, the mixing time also rapidly increased for a

fixed power input. Increasing the xanthan gum solution concentration increases the solution yield stress and the apparent viscosity resulting in an increase in the mixing time as the energy dissipation near the impeller becomes faster at the higher yield stress and at higher apparent viscosity (Ein-Mozaffari et al., 2005). Although flow near the impeller might be chaotic, the fluctuant velocities will weaken quickly in the area outside the impeller zone due to the higher apparent viscosity of the fluid, which is a function of the yield stress.

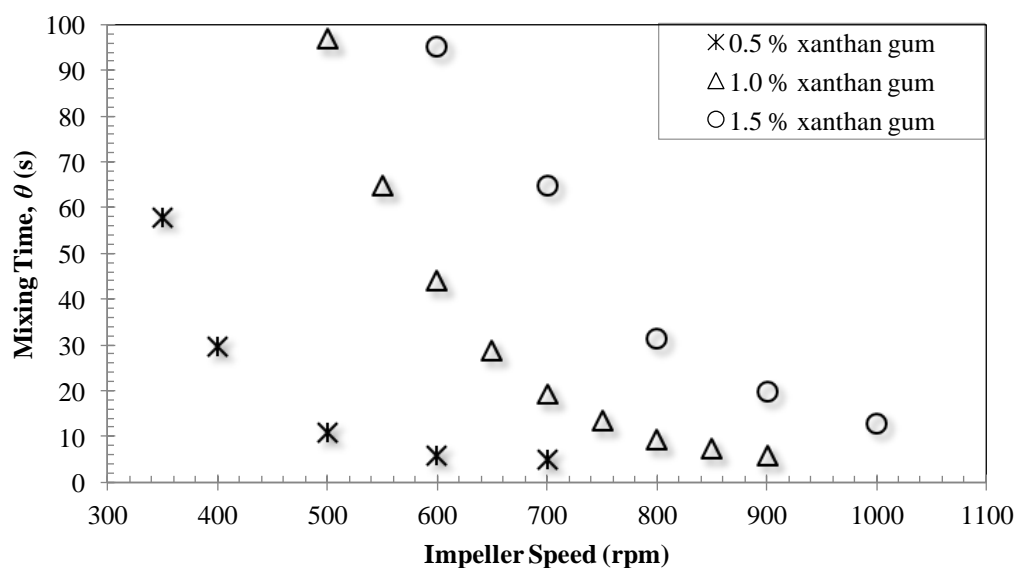


Figure (5.8-4). Effect of impeller speed on the mixing time at 0.5, 1.0, and 1.5% xanthan gum solutions using CFD.

5.8.2.6 Dimensionless Mixing Time

Using different mathematical models, mixing time is frequently correlated with the different design parameters. Many mathematical models have been proposed for the prediction of mixing time. Moo-Young et al. (1972) studied the mixing time of miscible liquids having the same viscosity and density using various types of impellers such as the turbine, helical ribbon, and tubular agitators. They used a decolorization method to measure the mixing time and correlated the results using Equation (2.2-1) (Tatterson, 1991). Figure (5.8-5) represents the

dimensionless mixing time ($N\theta$) as a function of the Reynolds number for the RT impeller. The results show that as the Reynolds number was increased, the dimensionless mixing time decreased in the transition region. The data shown in Figure (5.8-5) were fitted to Equation (2.2-2) using the regression analysis. The values of coefficients a and b were found to be about 1.03×10^9 and -1.95 , respectively.

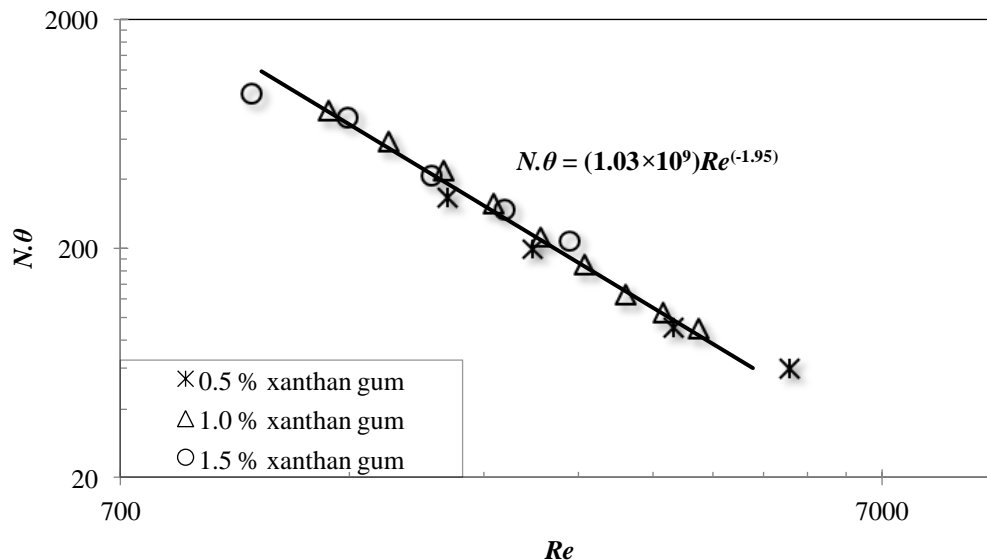


Figure (5.8-5). Dimensionless mixing time as a function of Reynolds number using CFD.

Power consumption is one of the most influential factors when estimating the operating cost in the design of mixing vessels in industry. Therefore, many researchers attempted to study the efficiency of mixing systems by correlating the mixing time with the power consumption per unit volume (P/V) using Equation (2.2-2) (Moo-Young et al., 1972; Nienow, 1997). Figure (5.8-6) shows the effect of xanthan gum concentration on the mixing time as a function of power consumption per volume. The mixing time and power consumption data shown in Figure (5.8-6) were fitted to Equation (2.2-2) using the regression analysis for each concentration. The values of c and d are listed in Table (5.8-1). It shows that mixing time measured for all three concentrations is well correlated with this model. The results also show that the coefficients c and d are functions of the fluid rheology.

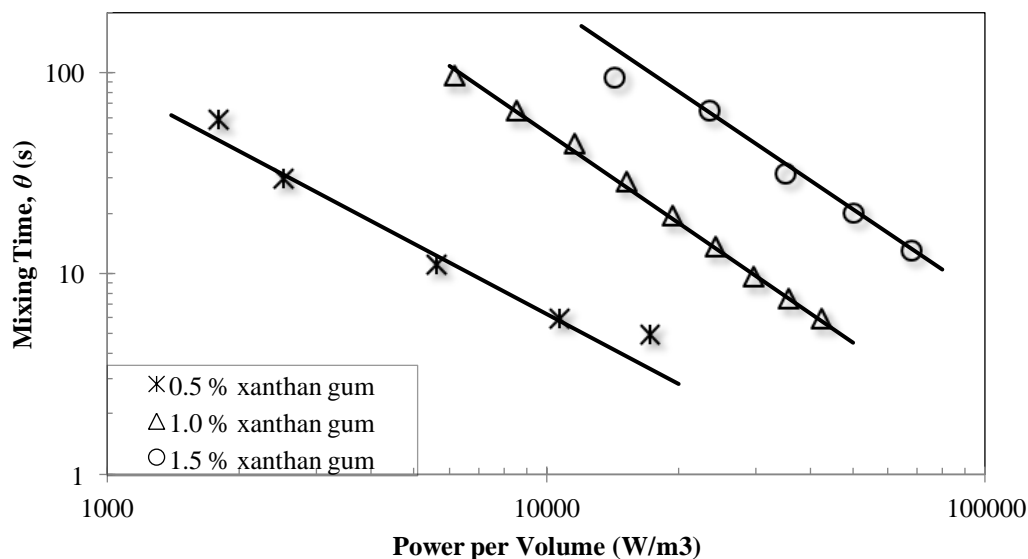


Figure (5.8-6). Effect of the fluid rheology on the mixing time as a function of power per volume.

Table (5.8-1). Coefficients of the mixing time correlation using Equation (2.2–2).

Solutions	Re	c	d	R^2
0.5% xanthan gum	1882–5297	1.64×10^5	-1.089	0.964
1.0% xanthan gum	1311–4036	4.52×10^7	-1.487	0.997
1.5% xanthan gum	1038–2725	2.29×10^8	-1.502	0.993

5.8.2.7 Effect of Power Law Index on Mixing Time

The fluid rheology is one of the crucial factors that have a significant effect on the performance of stirred-tank reactors. Therefore, the effect of the shear-thinning (power law index, n) on the mixing time (θ) was explored in the stirred-tank reactors. In the CFD simulations, it is possible to hold the values of K , τ_y , and μ_0 constant and vary the values of power law index (n). In this CFD study, the power law index was varied from 0.11 to 0.99 while holding the other parameters at $K = 8 \text{ Pa s}^n$, $\tau_y = 5.254 \text{ Pa}$, and $\mu_0 = 22.613 \text{ Pa s}$. The effect of power law index

(n) on the mixing time (θ) is presented in Figure (5.8-7). The results show that the mixing time (θ) increased as the power law index was increased. The power law index for a Newtonian fluid is $n = 1$. When the power law index (n) approaches zero, the fluid exhibits a highly shear-thinning behavior. Due to unique nature of a shear-thinning fluid, the apparent viscosity of the fluid decreases with an increase in the shear rate; consequently the fluid flows easily within the mixing vessel and thus the mixing quality is enhanced (Wichterle and Wein, 1975). Therefore, the mixing time (θ) decreased at the lower values of the power law index. However, when the power law index of the fluid increases, the apparent viscosity also increases. Therefore, the mixing time (θ) increased as the value of n was increased from 0.11 to 0.99. Similar phenomena were observed by Liu et al. (2006) who studied the laminar mixing of shear thinning fluids in a static mixer using CFD. They used power-law model to capture shear-thinning behavior of the fluid. Using the particle tracking technique, they found that shear-thinning behavior of the fluid resulted in better mixing quality and lower pressure drop in comparison with the Newtonian fluids.

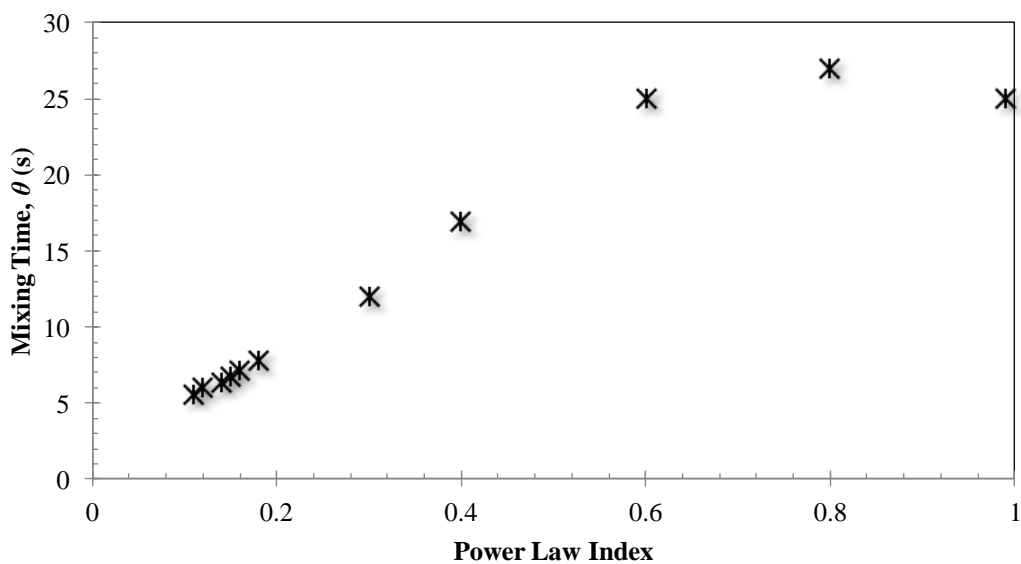


Figure (5.8-7). Effect of power law index (n) on the mixing time ($N = 900$ rpm, $K = 8$ Pa s ^{n} , $\tau_y = 5.25$ Pa, and $\mu_o = 22.61$ Pa s).

5.8.2.8 Effect of Fluid Yield stress on Mixing Time

The effect of fluid yield stress (τ_y) on the mixing time (θ) was also explored. In this situation, the value of τ_y was varied from 1.79 to 20.6 Pa while holding other parameters at $K = 8 \text{ Pa s}^n$ and $n = 0.12$. Figure (5.8-8) shows the effect of fluid yield stress (τ_y) on the mixing time (θ). These results showed that the mixing time (θ) increased as the fluid yield stress (τ_y) was increased from 1.79 to 20.6 Pa. To some extent the shear stress imparted by the impeller failed to exceed the fluid yield stress in the regions away from the impeller as τ_y increased. This resulted in the formation of the poor mixing regions within the vessel at the higher fluid yield stress.

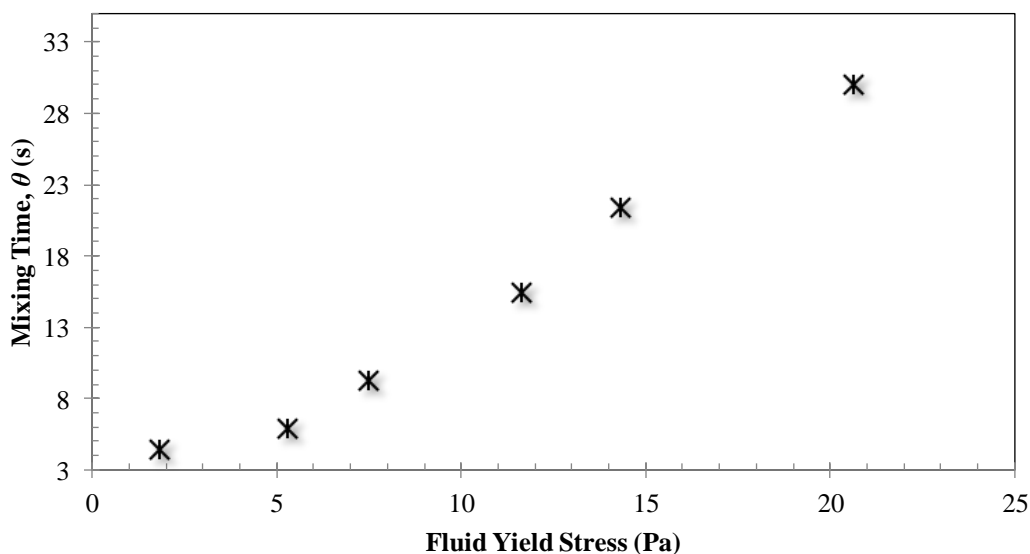


Figure (5.8-8). Effect of fluid yield stress (τ_y) on the mixing time ($N = 900 \text{ rpm}$, $K = 8 \text{ Pa s}^n$, and $n = 0.12$).

5.8.2.9 Effect of Consistency Index on Mixing Time

In addition, the effect of consistency index (K) on the performance of the stirred-tank reactors was studied using CFD. To attain this objective, the value of K was varied from 3.0 to 33.1 Pa s^n while holding the other parameters at $n = 0.12$, $\tau_y = 5.254 \text{ Pa}$, and $\mu_0 = 22.613 \text{ Pa s}$. Figure (5.8-9) presents the effect of the consistency index (K) on the mixing time (θ). These data

showed that the mixing time (θ) increased as K was increased from 3.0 to 33.1 Pa Sⁿ. According to Equation (2.1–9), the fluid apparent viscosity increases with an increase in the consistency index. Thus, the mixing system is susceptible to poor mixing and existence of non-ideal flows due to the higher apparent viscosity of the fluid.

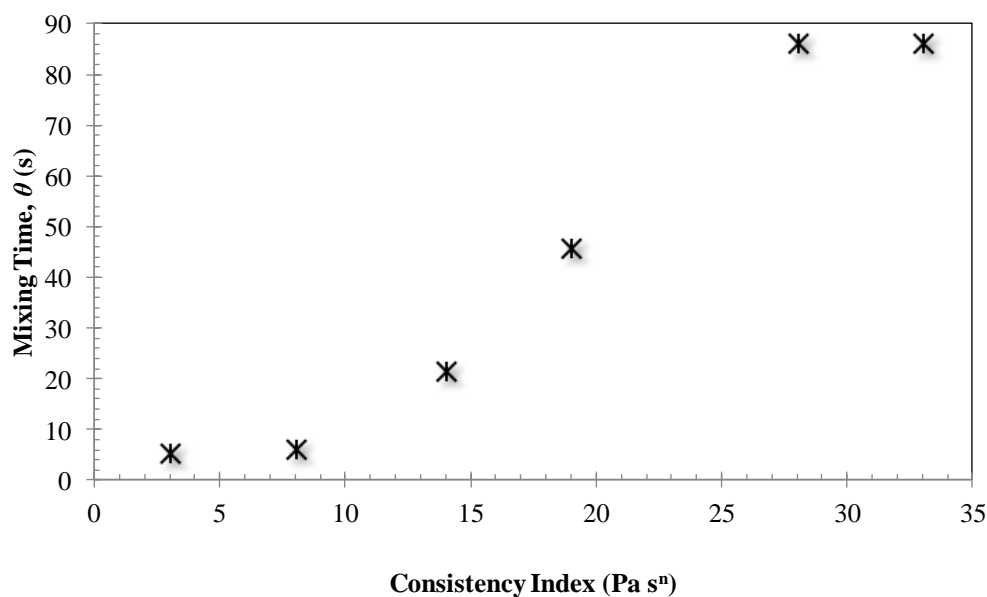


Figure (5.8-9). Effect of consistency index (K) on the mixing time ($N = 900$ rpm, $n = 0.12$, $\tau_y = 5.25$ Pa, and $\mu_o = 22.61$ Pa s).

5.8.3 Conclusions

To study the mixing of xanthan gum solution, which is a shear thinning fluid possessing yield stress, in a stirred reactor, the computational fluid dynamics (CFD) was used. To model the rotation of the impeller, the MRF technique was used. Grid independence was confirmed by presenting that additional cells did not change the calculated velocity magnitude measured in the regions of high velocity gradients by more than 6%. The optimal mesh of the model (817,077 cells) was used in all simulations. The power number calculated by the CFD model was in good agreement with the experimentally measured values. The calculated CFD flow field was used to obtain the dynamic response of the continuous mixing system to a frequency-modulated random binary input signal. The calculated dynamic responses matched reasonably well with the measured responses. The dynamic model was used to quantify the extent of channeling and

fully mixed volume in the continuous-flow mixing vessel. Comparison between CFD and experimental data for the dimensionless cavern diameter (D_c/D) was made. The dimensionless cavern versus dimensionless $P_o Re_y$ on the log-log scale was linear with a slope of 0.34 for the RT impeller. The CFD results for the cavern size agreed well with those measured through ERT. Moreover, the cavern volume (V_c) was compared with the fully mixed volume ($V_{fully\ mixed}$) for the RT impeller. The results showed that for the identical operating conditions the fully mixed volume ($V_{fully\ mixed}$) in a continuous-flow mixing vessel was higher than the cavern volume (V_c) in a batch vessel. This was due to the extra momentum induced by the inlet-outlet flow.

Using CFD, the effect of the xanthan gum concentration on the mixing time (θ) was also explored. The results showed that when the xanthan gum concentration was increased from 0.5 to 1.5%, the value of θ also rapidly increased for a fixed power input. The mixing time (θ) measured for the RT impeller was well correlated with the specific power consumption and the Reynolds number. We also explored the effect of the rheological parameters of the Herschel-Bulkley model on the mixing quality. The CFD results showed that mixing time (θ) increased as the power law index (n) was increased from 0.11 to 0.99. When the power law index (n) approaches zero, the fluid exhibits a highly shear-thinning behavior. Due to inherent nature of a shear-thinning fluid, the apparent viscosity of the fluid decreases with an increase in the shear rate, consequently the fluid flows easily within the mixing vessel and thus the mixing quality is enhanced. It was also found that when K (consistency index) and τ_y (fluid yield stress) were decreased, the mixing time (θ) was decreased. In fact, the fluid apparent viscosity decreases with a decrease in the consistency index and yield stress. Therefore, the mixing was improved at lower K and τ_y due to the lower apparent viscosity of the fluid.

5.9 Using Tomography to Characterize the Mixing of Non-Newtonian Fluids with a Maxblend Impeller (Patel et al., 2013b)

5.9.1 Introduction

To study the effect of various parameters on the performance of batch mixing, the mixing time provides a potent way for the evaluation of mixing effectiveness. To measure the mixing time, different techniques have been employed, including laser-induced fluorescence (Distelhoff et al., 1997), liquid-crystal thermography (Lee and Yianneskis, 1997), dye addition (Ascanio et al., 2003), conductivity probe (Bouaifi and Roustan, 2001), thermocouple-based techniques (Rewatkar and Joshi, 1991) and radioactive liquid tracer (Pant et al., 2001). In fact, each of these techniques has its own drawbacks. Some of these techniques require transparent vessels, are not applicable to opaque fluids, are limited to a few monitoring points in the vessel for measuring the mixing time, have the disadvantage of affecting the flow pattern. To overcome all these limitations, electrical resistance tomography (ERT), which is a non-intrusive, non-hazardous, and robust measurement technique, can be used to study the mixing of opaque fluids in a non-transparent vessel.

A comprehensive literature review [see Section (2.4.1.2)] suggests that the Maxblend impeller is more competent and economical than the conventional close-clearance impellers for the mixing of Newtonian and non-Newtonian fluids except in the laminar region. However, most of these studies have been carried out using decolorization methods, which are not completely reliable for studying the mixing of opaque liquids. Based on the author's knowledge, no study has utilized the ERT technique on the mixing of non-Newtonian fluids in a stirred vessel equipped with the Maxblend impeller. Little information is available regarding the mixing of yield-pseudoplastic fluids with the Maxblend impeller. Consequently, in this study the effects of various parameters such as impeller types (Maxblend, anchor, Lightnin A320, and Scaba 6SRGT), impeller speed ($N = 75\text{--}613$ rpm), fluid rheology (0.5–1.5% xanthan gum solutions), power consumption (P/V , where P is the power and V is the fluid volume), Reynolds number (Re), and absence of baffles on the mixing time (θ) were investigated.

In this study the mixing time (θ) was taken as a time at which the conductivity of the tracer at the detecting positions reached 98% of the steady-state conductivity. To measure the mixing time in the batch mode, the experimental setup with ERT shown in Figure (3.2-1) and procedure explained in Section (3.4.3) were employed. The rheological behaviour of the xanthan gum solutions was described by the Herschel-Bulkley model [Equation (2.1–9)].

5.9.2 Results and Discussion

5.9.2.1 Effect of Impeller Speed

To minimize the operating cost of the mixer, the power consumption should be considered as a vital issue. In fact, the batch mixing reactors must be designed at the optimum impeller speed/power required to achieve the desired degree of homogeneity. Generally, increasing the impeller rotation speed reduces dead zones in the mixing vessel. The effect of the impeller speed on the mixing time (θ) as a function of the xanthan gum concentration is represented in Figure (5.9-1). The results show that as the impeller rotational speed was increased, the mixing time decreased. It can be observed that the variation in the mixing time was much faster at a lower impeller speed compared to that at a higher impeller speed. The slow moving fluid was observed visually near the baffles at the top corner of the vessel at a lower impeller speed. The shear stress produced by the impeller was less than the yield stress of the fluid in the dead zones. However, at a higher impeller speed the xanthan gum solution was swept away from the impeller, leading to an improved mixing quality by overcoming the yield stress of the fluid in the dead zones. The optimum power input should be chosen in such a way that further increases in impeller speed leads to slight variations in the mixing time. In fact, under these circumstances, considerable power consumption is required to achieve a slight improvement in the mixing quality. Conversely, a lower impeller speed than the optimum speed may cause dead volume in the mixing vessel. This result confirmed the similar phenomenon observed by Ihejirika and Ein-Mozaffari (2007) for the mixing of pseudoplastic fluids possessing yield stress.

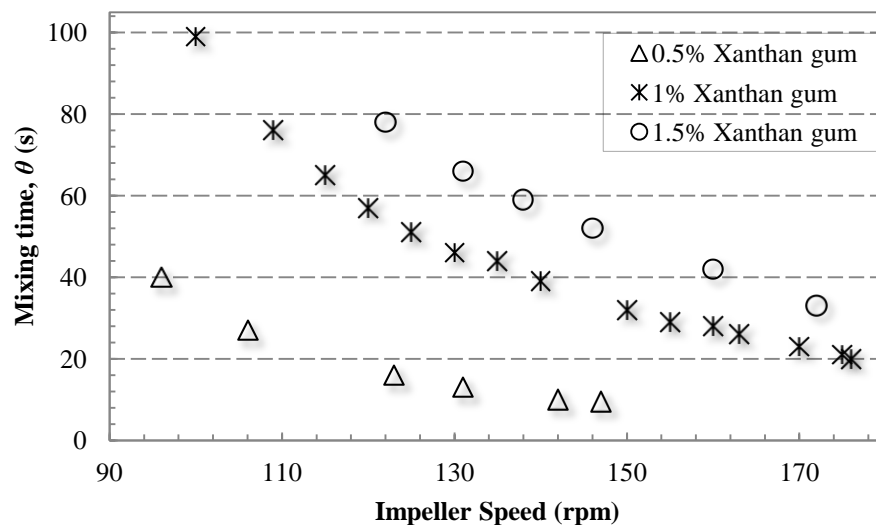


Figure (5.9-1). Effect of impeller speed on the mixing time as a function of the xanthan gum concentration for the Maxblend impeller (with baffles).

5.9.2.2 Effect of Fluid Rheology

The fluid rheology has a significant effect on the mixing performance of the impellers. Ein-Mozaffari et al. (2003a) studied the mixing of pulp suspension (a yield stress fluid) and showed that the fluid yield stress has a momentous effect on the mixing time. In this study, we explored the effect of xanthan gum concentration (0.5, 1.0, and 1.5 w/v %) on the mixing time. Figure (5.9-1) shows the effect of the xanthan gum concentrations on the mixing time as a function of the impeller speed. The results show that as the xanthan gum concentration was increased from 0.5 to 1.5%, the mixing time also rapidly increased for a fixed power input. Increasing the xanthan gum solution concentration increases the solution yield stress and the apparent viscosity resulting in an increase in the mixing time as the energy dissipation near the impeller becomes faster at a higher yield stress and at higher apparent viscosity (Ein-Mozaffari et al., 2005). Although flow near the impeller might be chaotic, the fluctuant velocities will weaken quickly in the area outside the impeller zone due to the higher apparent viscosity of the fluid, which is a function of the yield stress.

5.9.2.3 Dimensionless Mixing Time

Mixing time is often correlated with the various design parameters using different mathematical models. Many mathematical models have been proposed for the prediction of mixing time. Moo-Young et al. (1972) studied the mixing time of miscible liquids having the same viscosity and density using various types of impellers such as the turbine, helical ribbon, and tubular agitators. They used a decolorization method to measure the mixing time and correlated the results using Equation (2.2-1) (Tatterson, 1991). Figure (5.9-2) shows dimensionless mixing time ($N\theta$) as a function of the Reynolds number for the Maxblend impeller. The results show that as the Reynolds number was increased, the dimensionless mixing time decreased in the transition region. The data shown in Figure (5.9-2) were fitted to Equation (2.2-1) using the regression analysis. The values of coefficients a and b were found to be about 1.05×10^4 and -0.81 , respectively. This correlation is valid up to $Re = 569$.

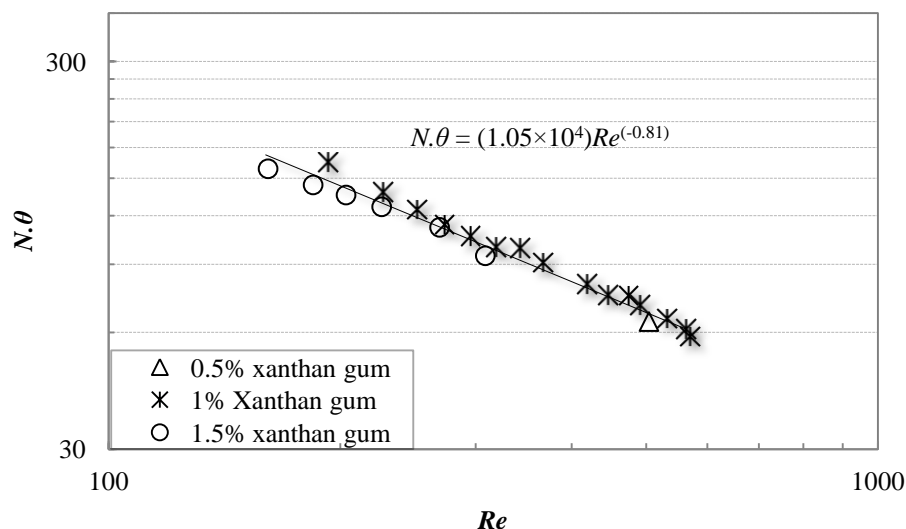


Figure (5.9-2). Dimensionless mixing time as a function of Reynolds number for the Maxblend impeller (with baffles).

As mentioned earlier, power consumption is one of the most influential factors when estimating the operating cost in the design of mixing vessels in any industry. Therefore, many researchers attempted to study the efficiency of mixing systems by correlating the mixing time with the power consumption per unit volume (P/V) using Equation (2.2-2) (Moo-Young et al.,

1972; Nienow, 1997). Figure (5.9-3) shows the effect of xanthan gum concentration on the mixing time as a function of power consumption per volume for the Maxblend impeller. The mixing time and power consumption data shown in Figure (5.9-3) were fitted to Equation (2.2–2) using the regression analysis for each concentration. The values of c and d are listed in Table (5.9-1). It shows that mixing time measured for all three concentrations is well correlated with this model. The results also show that the coefficients c and d are functions of the fluid rheology.

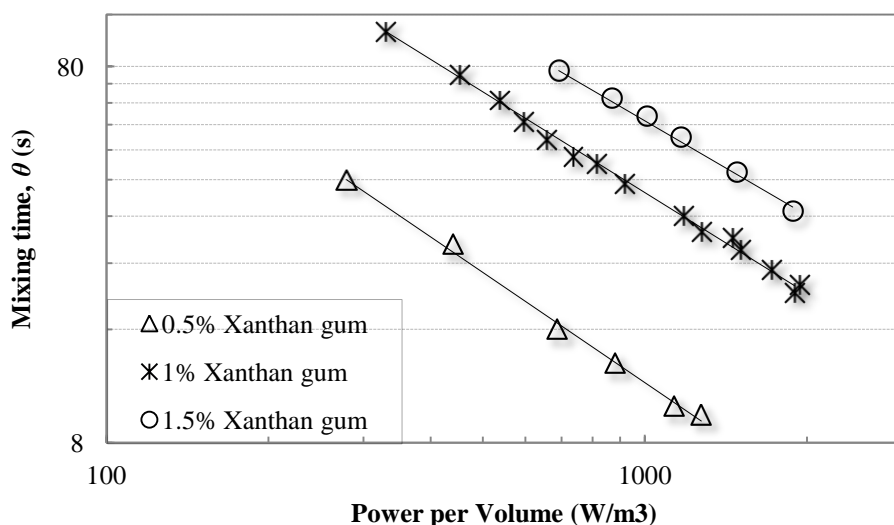


Figure (5.9-3). Effect of the fluid rheology on the mixing time as a function of power per volume for the Maxblend impeller (with baffles).

Table (5.9-1). Coefficients of the mixing time correlation [Equation (2.2–2)] for the Maxblend impeller as a function of the xanthan gum concentration.

Solutions	Re	c	d	R^2
0.5% xanthan gum	500-1150	1.00×10^4	-0.979	0.996
1.0% xanthan gum	190-570	1.60×10^4	-0.880	0.996
1.5% xanthan gum	150-310	2.23×10^4	-0.860	0.995

5.9.2.4 Effect of Type of Impeller

The rigorous study, focused on the design and selection of impellers which utilize power more efficiently, is also critical, in addition to the exhaustive study of the correlation of power consumption by inefficient mixing devices (Moo-Young et al., 1972; Uhl and Gray, 1966). It means that the geometry of the impeller significantly influences the mixing performance of the stirred tank reactors. As the viscosity of the fluid is increased, the preference moves from axial-flow to radial-flow impellers, and then, to close-clearance impellers (Chhabra and Richardson, 2008). In this study, the Maxblend, anchor, Lightnin A320 and Scaba 6SRGT impellers were utilized to agitate the 1% xanthan gum solution and the efficiency of each impeller was measured in terms of the mixing time and power consumption. Figure (5.9-4) shows the effect of impeller types on the mixing time as a function of power consumption per unit volume.

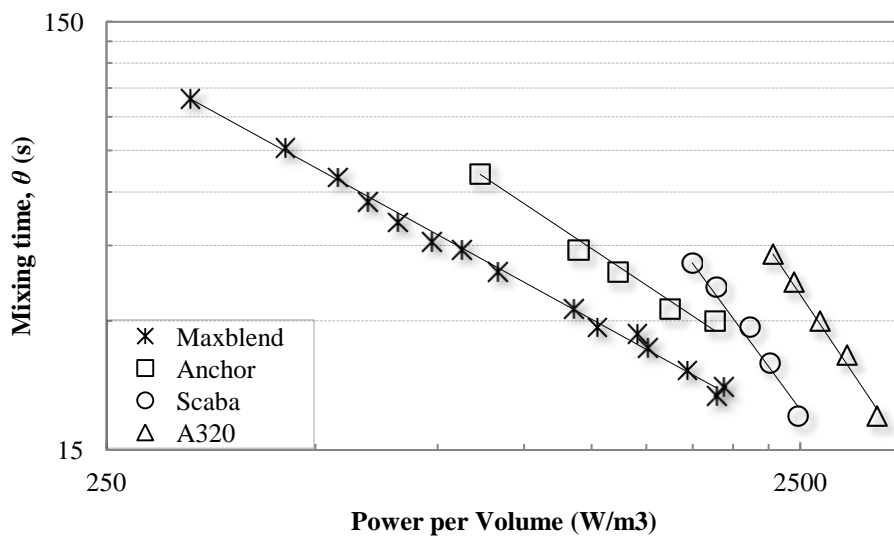


Figure (5.9-4). Effect of the types of impellers on the mixing time at 1% xanthan gum concentration (with baffles).

The analysis of the data shows that the mixing time measured at a fixed power consumption for the Maxblend impeller was lower than those obtained for the other impellers employed in this study. Therefore, the Maxblend impeller is the most effective impeller among given impellers in achieving the homogeneous solution in the viscous system. Especially with non-Newtonian fluids, the pumping capacity of the anchor impeller declines and the impeller slips in the liquid,

and is thus generally ineffective unless mixing with an anchor can be complemented by adding another impeller such as a radial-flow impeller (Paul et al., 2004; Chhabra and Richardson, 2008). Iranshahi et al. (2007) studied the flow pattern of the Maxblend impeller in a batch vessel and found that the Maxblend has a uniform shear rate distribution throughout the vessel. Hidalgo-Millan et al. (2012) studied the hydrodynamics generated by the Maxblend impeller with Newtonian fluid in a baffled stirred tank. They observed that the Maxblend impeller generated a more regular circulation pattern, with an efficient top-bottom pumping. This uniform flow pattern generated by the Maxblend impeller led to a more efficient mixing of non-Newtonian fluids compared to that achieved by the anchor.

Table (5.9-2). Coefficients of the mixing time correlation using Equation (2.2–2).

Solutions	Re	c	d	R^2
A320	1612-1937	8.26×10^9	-2.46	0.992
Scaba	462-595	1.46×10^9	-2.32	0.982
Anchor	217-699	7.14×10^4	-1.03	0.982

The previous studies by Patel et al., (2011) showed that the Lightnin A320 impeller was the most effective among the seven axial-flow impellers (A100, A200, A310, A315, A320, 3AH, and 3AM), and the Scaba 6SRGT impeller was the most effective among the four radial-flow impellers (R500, RSB, RT, and Scaba 6SRGT) in reducing the nonideal flows in the continuous-flow mixing of pseudoplastic fluids with yield stress. Therefore, to select the most effective impeller for batch mixing, we attempted to compare the performance of the most effective axial and radial flow impellers (Lightnin A320, Scaba 6SRGT) with the close clearance impellers (the Maxblend and anchor) in the batch mode. The results depicted in Figure (5.9-4) indicate that the Maxblend impeller was the most efficient impeller among the three types of impellers in terms of achieving uniform mixing in a shorter time and with a lower power input. However, it must be mentioned that the A320 and Scaba impellers are designed for the transitional flow while the anchor impellers are designed for the laminar flow. Similar results were also observed for the continuous-flow mixing of non-Newtonian fluid in

stirred tanks (Patel et al., 2011). The mixing time and power consumption data shown in Figure (5.9-4) were fitted to Equation (2.2-2) via regression analysis for each impeller. The values of c and d are listed in Table (5.9-2).

5.9.2.5 Effect of Baffles

Away from the deep laminar region as we move toward the transitional region, the presence and absence of the baffles play a major role in batch mixing. Baffles cannot be employed with close-clearance impellers such as anchor and helical ribbon impellers due to the lack of space between the wall and the impeller tip. On the other hand, the size of the Maxblend impeller is generally less than that of the close-clearance impellers for a fixed tank diameter. Therefore, baffles can be installed in the vessel while using the Maxblend impeller. Hence, the effect of the presence and absence of baffles on the performance of the Maxblend impellers was investigated. The mixing time of the Maxblend impeller in the presence and absence of the baffles as a function of power per unit volume is presented in Figure (5.9-5).

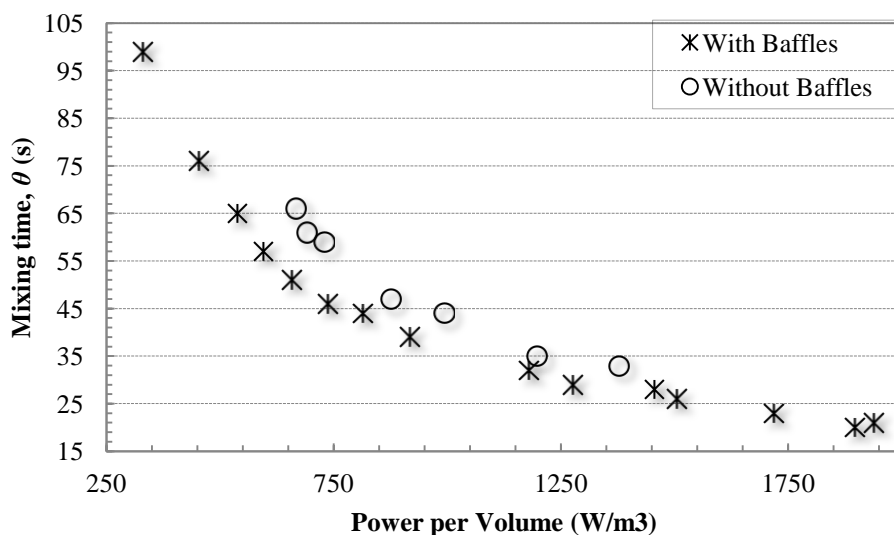


Figure (5.9-5). Effect of the baffles on the mixing time (Maxblend, 1% xanthan gum).

The results show that for the identical operating condition, the geometrical configuration with baffles provided better efficiency than the geometrical configuration without baffles. It was observed that at a higher impeller speed the configuration without baffles was subject to a

strong vortex, which restricted the realistic operation by the air entrainment. In fact, the presence of the baffles transforms tangential flows to vertical flows, provides the top-to-bottom mixing without swirl, and minimizes the air entrainment. A similar phenomenon was observed by Iranshahi et al. (2007) in the mixing of Newtonian fluids in the batch vessel. They found that the presence of baffles increased the axial pumping and the flow number for the baffled configuration compared to the unbaffled configuration. Moreover, the dimensionless mixing time of the unbaffled configuration was 1.4 times greater than that of the baffled configuration. Our results demonstrated that the Maxblend impeller with baffled configuration had better efficiency in the batch mixing of non-Newtonian fluids with yield stress.

5.9.3 Conclusions

Electrical resistance tomography (ERT) was employed to study the mixing of non-Newtonian fluids with yield stress in a stirred vessel equipped with the Maxblend impeller. The mixing performance of the impeller was evaluated using the mixing time and the specific power consumption. The results showed that the Maxblend impeller was more efficient compared to the A320 (axial-flow), the Scaba (radial-flow), and the anchor (close-clearance) impellers in terms of achieving uniform mixing in a shorter time and with a lower power input. The data demonstrated that the fluid yield stress had a significant effect on the mixing quality. For instance, when the xanthan gum concentration was increased from 0.5 to 1.5%, the mixing time rapidly increased for a fixed power input. The Maxblend impeller installed in a baffled tank had better mixing efficiency since the presence of the baffles transformed the tangential flows to vertical flows, provided top-to-bottom mixing without swirl, and minimized the air entrainment. The mixing time measured for the Maxblend impeller was well correlated with the specific power consumption and the Reynolds number. Better mixing quality and more energy savings can be achieved by applying the findings of this study in the design of mixing vessels for pseudoplastic fluids possessing yield stress.

Chapter 6

6. OVERALL CONCLUSIONS

Using electrical resistance tomography (ERT), computational fluid dynamics (CFD), and dynamic tests, this study reports various important features of mixing performance of the continuous-flow mixers in the mixing of the yield-pseudoplastic fluids. The following main conclusions were drawn:

1. The performance of the Double Helical Ribbon (DHR) impeller was evaluated in the continuous-flow mixing of yield-pseudoplastic fluids in stirred vessel through dynamic tests.
 - The dynamic tests showed that the DHR impeller was the most efficient impeller for reducing the extent of non-ideal flows in the continuous-flow mixer among axial-flow, radial-flow, and conventional close-clearance impellers used in this study.
 - In addition, the mixing quality was further improved by optimizing the power input, increasing the mean residence time, decreasing the fluid yield stress, using the up-pumping impeller mode, and using the top inlet-bottom outlet (TI-BO) configuration
2. The dynamic performance of the continuous-flow mixing of yield-pseudoplastic fluids was improved by employing a new emerging Maxblend impeller.
 - It was found when the channeling approached zero and the fully mixed volume approached the total fluid volume in the vessel, the power drawn by the A320 impeller and the Scaba impeller were about 2.9 and 4.3 times greater than that of the Maxblend impeller. Thus, the Maxblend impeller was able to drastically improve the performance of continuous-flow mixing with huge power savings.

- The mixing quality was further improved by optimizing the impeller speed, decreasing the fluid flow rate, decreasing the fluid concentration, and using bottom inlet-top outlet (BI–TO) configuration. The flow non-ideality of the mixing system increased in the absence of the baffles.
3. The dynamic performance of the continuous-flow mixing of yield-pseudoplastic fluids for the axial-flow impeller (the 3AH impeller) was assessed for various important operating conditions and design parameters.
 - The mixing quality in the continuous-flow mixer was substantially improved by increasing impeller diameter, increasing residence time, optimizing impeller off-bottom clearance, decreasing fluid height, optimizing jet velocity, and using the up-pumping axial-flow impeller.
 4. The ratio of the residence time (τ) to the batch mixing time (θ) was evaluated to achieve ideal mixing for the continuous-flow mixing of yield-pseudoplastic fluids using dynamic tests and ERT. Effects of impeller types, fluid rheology, impeller off-bottom clearance, locations of inlet and outlet, pumping directions of an axial-flow impeller, fluid height in the vessel, residence time, and jet velocity on the ratio of τ to θ were investigated.
 - The results showed that the extent of the non-ideal flows (channeling and dead volume) in the continuous-flow mixing approached zero when the value of τ/θ varied from 8.2 to 24.5 depending on the operating conditions and design parameters. Thus, to design an efficient continuous-flow mixing system for non-Newtonian fluids, the ratio of the residence time to the mixing time should be at least 8.2 or higher.
 5. The deformation of the cavern was analyzed in the continuous-flow mixing system for yield-pseudoplastic fluids using ERT. This study has demonstrated an efficient method for flow visualization in the continuous-flow mixing of opaque fluids using 2D and 3D tomograms.
 - Moreover, the cavern volume (V_c) was compared with the fully mixed volume ($V_{fully\ mixed}$) for the RT, A310, and 3AM impellers. The results showed that, for the identical operating conditions, the fully mixed volume ($V_{fully\ mixed}$) in a continuous-flow mixing vessel was higher than the cavern volume (V_c) in a batch vessel for

- each impeller used in this study. This was due to the extra momentum induced by the inlet-outlet flow.
- The enlargement of the cavern due to the deformation increased from 11.2 to 21.1%, when the fluid yield stress was decreased by reducing the fluid concentration from 1.0 to 0.5%.
 - The cavern volume increased by about 2.6, 8.0, 11.2, and 26.7% for BI–BO, TI–TO, TI–BO, and BI–TO, respectively due to the deformation.
6. ERT was employed successfully to visualize the flow of opaque fluid (biopolymer solutions) in the continuous-flow mixing in the stirred vessel. Using 2D and 3D tomography images, this study effectively presents a competent method to visualize the flow of opaque fluids in laminar and transitional regions inside a reactor.
- When the jet velocity (V_j) was increased from 0.317 to 1.66 m s⁻¹, with identical operating conditions, the volume of the tracer distribution also increased from 28 to 44% of the total volume of the fluid in the vessel.
 - The quantitative analysis also shows that as the fluid yield stress was decreased by decreasing the fluid concentration from 1.5 to 0.5%, the volume in which the tracer distribution achieved also increased from 20 to 39% of the total volume of the fluid in the vessel.
 - The quantitative results also shows that the tracer distribution achieved using the Maxblend impeller was more significant than using the RT impeller. The results also revealed that the location of the inlet and outlet streams has a significant effect on the mixing quality.
7. A novel study on exploring the effect of the rheological parameters of the pseudoplastic fluids with yield stress on the non ideal flows in a continuous-flow mixing system was performed using computational fluid dynamics (CFD).
- The validated CFD model predicted that the extent of channeling increased and the fraction of fully mixed volume decreased as the power law index (n) was increased from 0.11 to 0.99. This result revealed that the mixing quality was improved when the degree of the shear thinning was increased.
 - Moreover, the mixing efficiency of the continuous-flow mixing system was enhanced by decreasing the consistency index, decreasing the fluid yield stress,

increasing the fluid residence time in the mixing vessel, and the reducing the solution mass concentration.

8. A novel study on exploring the effect of the rheological parameters of the yield-pseudoplastic fluids on the mixing time (θ) in a batch mode was performed using computational fluid dynamics (CFD).
 - The validated CFD model predicted that the mixing time (θ) increased as the power law index (n) was increased from 0.11 to 0.99.
 - Moreover, the mixing efficiency of the stirred-tank reactor was enhanced by decreasing the consistency index, decreasing the fluid yield stress, increasing the impeller speed, and the reducing the solution mass concentration.
9. The ability of the ERT system to evaluate the hydrodynamic performance of the Maxblend impeller was demonstrated in a batch mode.
 - The effects of various parameters such as impeller types (Maxblend, anchor, Lightnin A320, and Scaba 6SRGT), impeller speed, fluid rheology, power consumption, Reynolds number, and absence of baffles on the mixing time were investigated.
 - The results showed that the Maxblend impeller was able to improve the mixing performance of non-Newtonian fluids in a batch reactor. The mixing quality was further improved by decreasing the xanthan gum concentration and using baffles in the mixing vessel.
 - The mixing time measured for the Maxblend impeller was well correlated with the specific power consumption and the Reynolds number.

6.1 Recommendations for Future Work

The experimental and numerical results of this study drew attention to the following areas for future considerations:

- The performance of the continuous-flow mixers for the multiphase mixing operations (e.g. gas-liquid and solid-liquid) should be assessed.
- The efficiency of the continuous-flow mixers should be analyzed for the other types of the non-Newtonian fluids.
- The scale-up criteria for the continuous-flow mixer for yield-pseudoplastic fluids should be developed.
- The performances of the co-axial impellers in the continuous-flow mixing of the non-Newtonian fluids should be assessed.

Publications

(a) Articles Published in Refereed Journals

- 1) Patel, D., Ein-Mozaffari, F., and Mehrvar, M. (2014) Tomography images to analyze the deformation of the cavern in the continuous-flow mixing of non-Newtonian fluids. *AIChE Journal*. 60 (1): 315-331.
- 2) Patel, D., Ein-Mozaffari, F., and Mehrvar, M. (2014) Using tomography to visualize the continuous-flow mixing of biopolymer solutions inside a stirred tank reactor. *Chemical Engineering Journal*. 239: 257-273.
- 3) Patel, D., Ein-Mozaffari, F., and Mehrvar, M. (2013) Characterization of the continuous-flow mixing of non-Newtonian fluids using the ratio of residence time to batch mixing time. *Chemical Engineering Research and Design*. 91 (7): 1223-1234.
- 4) Patel, D., Ein-Mozaffari, F., and Mehrvar, M. (2013) Using tomography to characterize the mixing of non-Newtonian fluids with a Maxblend impeller. *Chemical Engineering & Technology*. 36 (4): 687-695.
- 5) Patel, D., Ein-Mozaffari, F., and Mehrvar, M. (2013) Using tomography technique to characterize the continuous-flow mixing of non-Newtonian fluids in stirred vessels. *Chemical Engineering Transactions*. 32: 1465-1470.
- 6) Patel, D., Ein-Mozaffari, F., and Mehrvar, M. (2012) Improving the dynamic performance of continuous-flow mixing of pseudoplastic fluids possessing yield stress using Maxblend impeller. *Chemical Engineering Research and Design*. 90 (4): 514-523.
- 7) Patel, D., Ein-Mozaffari, F., and Mehrvar, M. (2012) Effect of impeller type on continuous-flow mixing of non-Newtonian fluids in stirred vessels through dynamic tests. *Canadian Journal of Chemical Engineering*. 90 (2): 290-298.

- 8) Patel, D., Ein-Mozaffari, F., and Mehrvar, M. (2011) Dynamic performance of continuous-flow mixing of pseudoplastic fluids exhibiting yield stress in stirred reactors. *Industrial & Engineering Chemistry Research*. 50 (15): 9377-9389.
- 9) Hosseini, S., Patel, D., Ein-Mozaffari, F., and Mehrvar, M. (2010) Study of solid-liquid mixing in agitated tanks through electrical resistance tomography. *Chemical Engineering Science*. 65 (4): 1374-1384.
- 10) Hosseini, S., Patel, D., Ein-Mozaffari, F., and Mehrvar, M. (2010) Study of solid-liquid mixing in agitated tanks through computational fluid dynamics modeling. *Industrial & Engineering Chemistry Research*. 49 (9): 4426-4435.

(b) Articles Submitted to Refereed Journal

- 11) Patel, D., Ein-Mozaffari, F., and Mehrvar, M. (2014) Effect of rheological parameters on non-ideal flows in the continuous-flow mixing of biopolymer solutions. *Journal of Non-Newtonian Fluid Mechanics*. Manuscript ID: JNNFM-D-14-00190. Submitted on July 26, 2014.
- 12) Patel, D., Ein-Mozaffari, F., and Mehrvar, M. (2014) Using CFD to study the effect of rheological parameters on the mixing quality of the shear thinning fluids with yield stress. *Industrial & Engineering Chemistry Research*. Manuscript ID: ie-2014-02995q. Submitted on July 30, 2014.
- 13) Patel, D., Ein-Mozaffari, F., and Mehrvar, M. (2014) Using electrical resistance tomography images to analyze the batch and continuous-flow mixing of pseudoplastic fluids possessing yield stress in the agitated tanks. *International Journal of Chemical Engineering*. Manuscript ID: 147523. Submitted on August 5, 2014.

(c) Conference Proceedings/Online Journal Papers

- 14) Patel, D., Ein-Mozaffari, F., and Mehrvar, M. (2013) Using a tracer technique to identify the extent of non-ideal flows in the continuous mixing of non-Newtonian fluids. *European*

- Physical Journal. EPJ Web of Conferences. 50, 01006: 1-7, doi:10.1051/epjconf/20135001006. Proceedings of the 6th International Conference on Tracers and Tracing Methods, Oslo, Norway (June 6-8, 2011).
- 15) Patel, D., Ein-Mozaffari, F., and Mehrvar, M. (2012) Using ultrasonic Doppler velocimetry to investigate the mixing of non-Newtonian fluids. IOP Conf. Series: Material Science and Engineering. 42 (1), 012048: 1-4, doi:10.1088/1757-899X/42/1/012048. International Symposium of Ultrasound in the Control of Industrial Processes (UCIP), Madrid, Spain (April 18-20, 2012).
- 16) Patel, D., Saeed, S., Ein-Mozaffari, F., and Mehrvar, M. (2010) Study of continuous-flow mixing of pseudoplastic fluids possessing yield stress in stirred vessels through dynamic tests and computational fluid dynamics modeling. Proceedings of the 19th International Congress of Chemical and Process Engineering (CHISA-2010) and 7th European Congress of Chemical Engineering (ECCE-7), Prague, Czech Republic. Paper # H.4.6 (433): 1-12 (August 28-September 01, 2010).
- (d) **Conference Oral Presentation**
- 17) Patel, D., Ein-Mozaffari, F., and Mehrvar, M. (June 22-27, 2014) Tomography images to analyze the deformation of the cavern in the continuous-flow mixing of non-Newtonian fluids. North American Mixing Forum (NAMF XXIV), Lake George, NY, USA (*one of the three finalists in the 2014 NAMF (North American Mixing Forum) students award competition for the best research paper*).
- 18) Patel, D., Ein-Mozaffari, F., and Mehrvar, M. (October 19–22, 2014) Using computational fluid dynamics to study the effect of rheological parameters on the continuous-flow mixing of biopolymer solutions. 64th Canadian Chemical Engineering Conference, Niagara Falls, ON.
- 19) Patel, D., Ein-Mozaffari, F., and Mehrvar, M. (October 19–22, 2014) Effect of rheological parameters on the mixing time in the agitation of shear thinning fluids with yield stress in

- a stirred-tank reactor. 64th Canadian Chemical Engineering Conference, Niagara Falls, ON.
- 20) Patel, D., Ein-Mozaffari, F., and Mehrvar, M. (October 19–22, 2014) Tomography images to analyze the batch and continuous-flow mixing of yield-pseudoplastic fluids in an agitated tank. 64th Canadian Chemical Engineering Conference, Niagara Falls, ON.
- 21) Patel, D., Ein-Mozaffari, F., and Mehrvar, M. (October 20–23, 2013) To visualize the flow field of continuous-flow mixing of biopolymer solutions inside an agitated tank using electrical resistance tomography. 63rd Canadian Chemical Engineering Conference, Fredericton, NB.
- 22) Patel, D., Ein-Mozaffari, F., and Mehrvar, M. (October 20–23, 2013) Investigation of the cavern deformation in the continuous-flow mixing of non-Newtonian fluids possessing yield stress. 63rd Canadian Chemical Engineering Conference, Fredericton, NB.
- 23) Patel, D., Ein-Mozaffari, F., and Mehrvar, M. (October 20–23, 2013) Using dynamic tests and tomography images to analyze the fully mixed volume in a continuous mode and cavern volume in a batch mode for the mixing of non-Newtonian fluids. 63rd Canadian Chemical Engineering Conference, Fredericton, NB.
- 24) Patel, D., Ein-Mozaffari, F., and Mehrvar, M. (October 20–23, 2013) Using computational fluid dynamics to study the effect of fluid yield stress, consistency index, and flow behavior index on the dynamic behavior of the continuous-flow mixing of Herschel-Bulkley fluids. 63rd Canadian Chemical Engineering Conference, Fredericton, NB.
- 25) Patel, D., Ein-Mozaffari, F., and Mehrvar, M. (October 20–23, 2013) Effect of various operating conditions and design parameters on the ratio of residence time to batch mixing time in the mixing of non-Newtonian fluids. 63rd Canadian Chemical Engineering Conference, Fredericton, NB.

- 26) Patel, D., Ein-Mozaffari, F. , and Mehrvar, M. (June 2-5, 2013) Using a tomography technique to characterize the continuous-flow mixing of non-Newtonian fluids in stirred vessels. 11th international conference on Chemical and Process Engineering, Milan, Italy.
- 27) Patel, D., Ein-Mozaffari, F., and Mehrvar, M. (October 14–17, 2012) Continuous-flow mixing of non-Newtonian fluids in the stirred reactor equipped with a Maxblend impeller. 62nd Canadian Chemical Engineering Conference, Vancouver, BC.
- 28) Patel, D., Ein-Mozaffari, F., and Mehrvar, M. (October 14–17, 2012) Using electrical resistance tomography to measure mixing time in the agitation of non-Newtonian fluids in a batch reactor. 62nd Canadian Chemical Engineering Conference, Vancouver, BC.
- 29) Hosseini, S., Patel, D., Ein-Mozaffari, F., and Mehrvar, M. (June 17–23, 2012) Using tomography and CFD to measure the degree of homogeneity in solid-liquid mixing operations. North American Mixing Forum (NAMF XXIII), Mayan Riviera, Mexico.
- 30) Patel, D., Ein-Mozaffari, F., and Mehrvar, M. (October 23–26, 2011) Characterization and optimization of the continuous-flow mixing of pseudoplastic fluids possessing yield stress in stirred reactors. 61st Canadian Chemical Engineering Conference, London, ON.
- 31) Patel, D., Ein-Mozaffari, F., and Mehrvar, M. (October 23–26, 2011) Dynamic performance of continuous-flow mixing of non-Newtonian fluids in stirred reactors using close-clearance impellers. 61st Canadian Chemical Engineering Conference, London, ON.
- 32) Patel, D., Ein-Mozaffari, F., and Mehrvar, M. (October 24–27, 2010) Effect of impeller type on continuous-flow mixing of non-Newtonian fluid in stirred vessels through dynamic tests. 60th Canadian Chemical Engineering Conference, Saskatoon, SK.
- 33) Hosseini, S., Patel, D., Ein-Mozaffari, F., and Mehrvar, M. (October 24–27, 2010) Using tomography and computational fluid dynamics to investigate the solid-liquid mixing in agitated vessels. 60th Canadian Chemical Engineering Conference, Saskatoon, SK.

(e) **Conference Poster (posters size: 36" × 48") Presentation**

- 34) Patel, D., Ein-Mozaffari, F., and Mehrvar, M. (October 14–17, 2012) Using ratios of residence time to batch mixing time to characterize the continuous-flow mixing of non-Newtonian fluids. 62nd Canadian Chemical Engineering Conference, Vancouver, BC.
- 35) Patel, D., Ein-Mozaffari, F., and Mehrvar, M. (October 14–17, 2012) Effects of operating conditions and design parameters on the dynamic performance of the continuous-flow mixing of Herschel-Bulkley Fluids in stirred reactors. 62nd Canadian Chemical Engineering Conference, Vancouver, BC.

Bibliography

Adams, L.W., Barigou, M., 2006. CFD Analysis of caverns and pseudo-caverns developed during mixing of non-Newtonian fluids. *Chem. Eng. Res. Des.* 85, 598-604.

Agricola, G., 1950. *De Re Metallica* (originally published in 1556), translated by H.C. Hoover and L.H. Hoover, Dover Publications, New York.

Ahmad, J., Ramaswamy, H.S., Ngadi, M.O., 2005. Rheological characteristics of Arabic gum in combination with guar and xanthan gum using response surface methodology: effect of temperature and concentration. *Int. J. Food Prop.* 8, 179-192.

Amanullah, A., Hjorth, S.A., Nienow, A.W. 1997. Cavern sizes generated in highly shear thinning viscous fluids by scaba 3SHP1 impellers. *Food and Bioproducts Processing.* 75(4), 232-238.

Amanullah, A., Hjorth, S.A., Nienow, A.W. 1998. A new mathematical model to predict cavern diameters in highly shear thinning, power law liquids using axial flow impellers. *Chem. Eng. Sci.* 53, 455-469.

Arratia, P.E., Kukura, J., Lacombe, J., Muzzio, F.J., 2006. Mixing of shear-thinning fluids with yield stress in stirred tanks. *AIChE J.* 52, 2310-2322.

Ascanio, G., Foucault, S., Tanguy, P.A., 2003. Performance of a new mixed down pumping impeller. *Chem. Eng. Technol.* 26, 908-911.

Aubin, J., Fletcher, D.F., Xuereb, C., 2004. Modeling turbulent flow in stirred tanks with CFD: the influence of the modeling approach, turbulence model, and numerical scheme. *Exp. Thermal and Fluid Sci.* 28, 431-445.

Aubin, J., Kresta, S.M., Bertrand, J., Xuereb, C., Fletcher, D.F., 2006. Alternate operating methods for improving the performance of continuous stirred tank reactors. *Chem. Eng. Res. Des.* 84(A7), 569-582.

Aubin, J., Xuereb, C., 2006. Design of multiple impeller stirred tanks for the mixing of highly viscous fluids using CFD. *Chem. Eng. Sci.* 61, 2913-2920.

Bakker, A., Gates, L.E., 1995. Properly choose mechanical agitators for viscous liquids. *Chem. Eng. Prog.* 91, 25-34.

Barber, C.D., Brown, B.H., 1984. Applied potential tomography. *J. of Phys. E: Sci. Instrum.* 17, 723-733.

Barber, C.D., Brown, B.H., Freeston, I.L., 1983. Imaging spatial distributions of resistivity using applied potential tomography. *Electron. Lett.* 19, 933-935.

Batchelor, G.K., 1967. *An Introduction to Fluid Dynamics*. Cambridge Univ. Press, Cambridge, England.

Bertrand, F., Tanguy, P.A., Brito De La Fuente, E., Carreau, P., 1999. Numerical modeling of the mixing flow of second-order fluids with helical ribbon impellers. *Computer Methods in Applied Mechanics and Eng.* 180, 267-80.

Bird, R.B., Stewart, W.E., Lightfoot, E.N., 2007. *Transport Phenomena*. 3rd ed., John Wiley & Sons. Inc., New York.

Blazek, J., 2005. *Computational Fluid Dynamics: Principles and Applications*. 2nd ed., Elsevier Inc., Amsterdam.

Bolton, G.T., Hooper, C.W., Mann, R., Stit, E.H., 2004. Flow distribution velocity measurement in a radial flow fixed bed reactor using electrical resistance tomography. *Chem. Eng. Sci.* 59, 1989-1997.

Bouaifi, M., Roustan, M., 2001. Power consumption, mixing time and homogenization energy in dual-impeller agitated gas-liquid reactors. *Chem. Eng. Proc.* 40, 87-95.

Bujalski, W., Jaworski, Z., Nienow, A.W., 2002. CFD study of homogenization with dual rushton turbines-comparison with experimental results part II: the multiple reference frame. *Chem. Eng. Res. Des.* 80, 97-104.

Calderbank, P.H., Moo-Young, M.B., 1959. The prediction of power consumption in the agitation of non-Newtonian fluids. *Trans IChem E.* 37, 26-33.

Chapman, C.M., Nienow, A.W., Cooke, M., Middleton, J.C., 1983. Particle–gas–liquid mixing in stirred vessels. Part III. Three phase mixing. *Chem. Eng. Res. Des.* 60, 167–181.

Chhabra, R.P., Richardson, J.F., 1999. *Non-Newtonian Flow in the Process Industries.* 1st ed. Butterworth Heinemann, Oxford.

Chhabra, R.P., Richardson, J.F., 2008. *Non-Newtonian Flow and Applied Rheology, Engineering Application;* Elsevier, Butterworth-Heinemann, Amsterdam.

Cullen, P.J., 2009. *Food Mixing: Principles and Applications.* John Wiley & Sons, West Sussex.

Danckwerts, P.V., 1953. Continuous flow systems. Distribution of residence times. *Chem. Eng. Sci.* 2, 1-13.

Delaplace, G., Leuliet, J.C., Relandeau, V., 2000. Circulation and mixing times for helical ribbon impellers. Review and experiments. *Exp Fluids.* 28, 170-182.

Devals, C., Heniche, M., Takenaka, K., Fradette, L., Tanguy, P.A., 2008. CFD analysis of several design parameters affecting the performance of the Maxblend impeller. *Comp. Chem. Eng.* 32, 1831-1841.

Dickin, F., Wang, M., 1996. Electrical resistance tomography for process applications. *Meas. Sci. Technol.* 7, 247-260.

Distelhoff, M.F.W., Marquis, A.J., Nouri, J.M., Whitelaw, J.H., 1997. Scalar mixing measurements in batch operated stirred tanks. *Can. J. Chem. Eng.* 75, 641-652.

Dohi, N., Takahashi, T., Minekawa, K., Kawase, Y., 2004. Power consumption and solid suspension performance of large-scale impellers in gas-liquid-solid three-phase stirred tank reactors. *Chem. Eng. J.* 97, 103-114.

Edgar, T.F., Himmelblau, D.M., Lasdon, L.S., 2001. Optimization of Chemical Processes. 2nd ed., McGraw-Hill, New York.

Ein-Mozaffari, F., 2002. Macorscale Mixing and Dynamic Behavior of Agitated Pulp Stock Chests. PhD Thesis; University of British Columbia, BC.

Ein-Mozaffari, F., Bennington, C.P.J., Dumont, G.A., 2004b. Dynamic mixing in agitated industrial pulp chests. *J. Pulp Paper Can.* 105(5), 41-45.

Ein-Mozaffari, F., Bennington, C.P.J., Dumont, G.A., 2005. Suspension yield stress and the dynamic response of agitated pulp chests. *Chem. Eng. Sci.* 60, 2399-2408.

Ein-Mozaffari, F., Bennington, C.P.J., Dumont, G.A., 2007. Optimization of rectangular pulp stock mixing chest dimensions using dynamic tests. *TAPPI J.* 6(2), 24-30.

Ein-Mozaffari, F., Dumont, G.A., Bennington, C.P.J., 2003a. Performance and design of agitated pulp stock chests. *Appita J.* 56 (2), 127-133.

Ein-Mozaffari, F., Kammer, L.C., Dumont, G.A., Bennington, C.P.J., 2003b. Dynamic modeling of agitated stock chests. *TAPPI J.* 2, 13-17.

Ein-Mozaffari, F., Kammer, L.C., Dumont, G.A., Bennington, C.P.J., 2004a. The effect of operating conditions and design parameters on the dynamic behaviour of agitated pulp stock chests. *Can. J. Chem. Eng.* 82, 154-161.

Ein-Mozaffari, F., Upreti S.R., 2009. Using ultrasonic Doppler velocimetry and CFD modeling to investigate the mixing of non-Newtonian fluids possessing yield stress. *Chem. Eng. Res. Des.* 87, 515-523.

Ekambara, K., Joshi, J.B., 2003. CFD simulation of mixing and dispersion in bubble columns. *Chem. Eng. Res. Des.* 81, 987–1002.

Elson, T.P., 1988. Mixing of fluids possessing a yield stress. *Proc. 6th Euro. Conf. Mixing.*, Pavia. Italy, 485–492.

Elson, T.P., Cheesman, D.J., 1986. X-Ray studies of cavern sizes and mixing performance with fluids possessing a yield stress. *Chem. Eng. Sci.* 41, 2555-2562.

Elson, T.P., Cheesman, D.J., Nienow, A.W., 1986. X-Ray studies of cavern sizes and mixing performance with fluids possessing a yield stress. *Chem. Eng. Sci.* 41(10), 2555-2562.

Etchells, A.W., Ford, W.N., Short, D.G.R., 1987. Mixing of Bingham plastics on an industrial scale. *Fluid Mixing III, IChE Symp. Ser.* 108, 271-285.

Fletcher, R., 1987. *Practical Methods of Optimization*. 2nd ed. John Wiley Sons, Chichester, UK.

Ford, C., Ein-Mozaffari, F., Bennington, C.P.J., Taghipour, F., 2006. Simulation of mixing dynamics in agitated pulp stock chests using CFD. *AIChE J.* 52, 3562-3569.

Fradette, L., Thome, G., Tanguy, P.A., Takenaka, K., 2007. Power and mixing time study involving a Maxblend impeller with viscous Newtonian and non-Newtonian fluids. *Chem. Eng. Res. Des.* 85 (A11), 1514-1523.

Galindo, E., Arguello, M.A., Velasco, D., Albiter, V., Martinez, A., 1996. A comparison of cavern development in mixing a yield stress fluid by Rushton and intermig impellers. *Chem. Eng. Technol.* 19, 315-323.

Galindo, E., Nienow, A.W., 1992. Mixing of highly viscous simulated xanthan fermentation broths with the Lightnin A-315 impeller. *Biotechnol. Prog.* 8, 223-239.

Galindo, E., Nienow, A.W., 1993. The performance of the Scaba 6SRGT agitator in the mixing of simulated xanthan gum broths. *Chem. Eng. Technol.* 16, 102-108.

Garcia-Ochoa, F., Casas, J.A., 1994. Apparent yield stress in xanthan gum solution at low concentration. *Chem. Eng. J.* 53, 41-46.

Garcia-Ochoa, F., Santos, V.E., Casas, J.A., Gomes, E., 2000. Xanthan gum: production, recovery, and properties. *Biotechnol. Adv.* 18, 549-579.

Gumery, F., Ein-Mozaffari, F., Dahman, Y., 2011. Mixing characteristics of draft tube airlift bioreactor using electrical resistance tomography. *Bioprocess Biosyst. Eng.* 34, 135-144.

Guntzburger, Y., Fradette, L., Farhat, M., Heniche, M., Tanguy, P.A., Takenaka, K., 2009. Effect of the geometry on the performance of the Maxblend impeller with viscous Newtonian fluids. *Asia-Pac. J. Chem. Eng.* 4, 528-536.

Hamood-ur-Rehman, M., Dahman, Y., Ein-Mozaffari, F., 2012. Investigation of mixing characteristics in a packed-bed external loop airlift bioreactor using tomography images. *Chem. Eng. J.* 213, 50-61.

Herschel, W.E., Bulkley, R., 1926. Measurements of consistency as applied to rubber-benzene solutions. *Proc. Am. Soc. Test. Mater.* 26, 621-633.

Hidalgo-Millan, A., Zenit, R., Palacios, C., Yatomi, R., Horiguchi, H., Tanguy, P. A., 2012. On the hydrodynamics characterization of the straight Maxblend® impeller with Newtonian fluids. *Chem. Eng. Res. Des.* 90 (9), 1117-1128.

Hirata, Y., Aoshima, Y., 1996. Formation and growth of cavern in yield stress fluids agitated under baffled and non-Newtonian conditions. *Chem. Eng. Res. Des.* 74, 438-444.

Holden, P.J., Wang, M., Mann, R., Dickin, F.J., Edwards, R.B., 1998. Imaging stirred-vessel macromixing using electrical resistance tomography. *AIChE J.* 44, 780-790.

Holland, F.A., Chapman, F.S., 1966. *Liquid mixing and processing in stirred tank*; Reinhold Publishing Corporation, New York.

Hosseini, S., Patel, D., Ein-Mozaffari, F., Mehrvar, M., 2010a. Study of solid-liquid in agitated tanks through electrical resistance tomography. *Chem. Eng. Sci.* 65, 1374-1384.

Hosseini, S., Patel, D., Ein-Mozaffari, F., Mehrvar, M., 2010b. Study of solid-liquid mixing in agitated tanks through computational fluid dynamics modeling. *Ind. Eng. Chem. Res.* 49, 4426-4435.

Houcine, I., Plasari, E., David, R., 2000. Effects of the stirred tank's design on power consumption and mixing time in liquid phase. *Chem. Eng. Technol.* 23, 605.

Hui, L.K., Bennington, C.P.J., Dumont, G.A., 2009. Cavern formation in pulp suspensions using side-entering axial-flow impellers. *Chem. Eng. Sci.* 64, 509-519.

Ihejirika, I., Ein-Mozaffari, F., 2007. Using CFD and ultrasonic velocimetry to study the mixing of pseudoplastic fluids with a helical ribbon impeller. *Chem. Eng. Technol.* 30, 606-614.

Iranshahi, A., Devals, C., Heniche, M., Fradette, L., Tanguy, P.A., Takenaka, K., 2007. Hydrodynamics characterization of the maxblend impeller. *Chem. Eng. Sci.* 62, 3641-3653.

Iranshahi, A., Heniche, M., Bertrand, F., Tanguy, P.A., 2006. Numerical investigation of the mixing efficiency of the ekato paravisc impeller. *Chem. Eng. Sci.* 61, 2609-2617.

Jahoda, M., Tomášková, L., Mořtěk, M., 2009. CFD prediction of liquid homogenisation in a gas-liquid stirred tank. *Chem. Eng. Res. Des.* 87, 460-467.

Jaworski, Z., Bujalski, W., Otomo, N., Nienow, A.W., 2000. CFD study of homogenization with dual Rushton turbines-comparison with experimental results. Part I: Initial studies. *Chem. Eng. Res. Des.* 78, 327-333.

Jaworski, Z., Nienow, A.W., 1994. On flow close to cavern boundaries in yield stress fluids. *Chem. Eng. Sci.* 49, 3321-3324.

Johnson, D.N., Hubbard, D.W., 1974. Mixing by impeller agitation in continuous flow systems containing polysaccharide solutions. *Biotech. Bioeng.* 16(9), 1283-1297.

Jones, P.N., Ozcan-Taskin, N.G., Yianneskis, M., 2009. The use of momentum ratio to evaluate the performance of CSTRs. *Chem. Eng. Res. Des.* 87 (4A), 485-491.

Kaminoyama, M., Taguchi, S., Misumi, R., Nishi, K., 2005. Monitoring stability of reaction and dispersion states in a suspension polymerization reactor using electrical resistance tomography measurements. *Chem. Eng. Sci.* 60, 5513-5518.

Kammer, L.C., Ein-Mozaffari, F., Dumont, G.A., Bennington, C.P.J., 2005. Identification of channeling and recirculation parameters of agitated pulp stock chests. *J. Process Control.* 15, 31-38.

Kelly, W., Gigas, B., 2003. Using CFD to predict the behavior of power law fluids near axial-flow impellers operating in the transitional flow regime. *Chem. Eng. Sci.* 58, 2141-2152.

Kelly, W., Humphrey, A.E., 1998. Computational fluid dynamics model for predicting flow of viscous fluids in a large fermentor with hydrofoil flow impellers and internal cooling coils. *Biotechnol. Prog.* 14, 248-258.

Khopkar, A.R., Kasat, G.R., Pandit, A.B., Ranade, V.V., 2006. CFD simulation of mixing in tall gas-liquid stirred vessel: role of local flow patterns. *Chem. Eng. Sci.* 61, 2921-2929.

Khopkar, A.R., Mavros, P., Ranade, V.V., Bertrand, J., 2004. Simulation of flow generated by an axial flow impeller - batch and continuous operation. *Chem. Eng. Res. Des.* 82(A6), 737-751.

Kim, S., Nkaya, A.N., Dyakowski, T., 2006. Measurement of mixing of two miscible liquids in a stirred vessel with electrical resistance tomography. *Int. Commun. in Heat and Mass Transfer* 33, 1088-1095.

Kukukova, A., Mostek, M., Jahoda, M., Machon, V., 2005. CFD prediction of flow and homogenization in a stirred vessel: Part I vessel with one and two impeller. *Chem. Eng. Technol.* 28, 1125-1133.

Lee, K.C., Yianneskis, M., 1997. Measurement of temperature and mixing time in stirred vessels with liquid crystal thermography. *Proc. 9th Europ. Conf. Mixing, Paris*, 121-128.

Liu, S., Hrymak, A., Wood, P., 2006. Laminar mixing of shear thinning fluids in a SMX static mixer. *Chem. Eng. Sci.* 61, 1753.

Ljung, L., 1999. *System Identification: Theory for the User*, 3rd ed., PTR Prentice Hall, USA.

Lucas, G.P., Cory, J., Mann, R., Dickin, F.J., Edwards, R.B., 1999. Measurement of the solids volume fraction and velocity distributions in solids-liquid flows using dual-plane electrical resistance tomography. *Flow Meas. Instrum.* 10, 249-258.

Luo, J.Y., Gosman, A.D., Issa, R.I., 1994. Prediction of impeller induced flows in mixing vessels using multiple frames of reference. *Inst. Chem. Eng. Symp.* 136, 549-556.

Luo, J.Y., Gosman, A.D., Issa, R.I., Middleton, J.C., Fitzgerald, M.K., 1993. Full flow field computation of mixing in baffled stirred vessels. *Trans IChem E.*, 71, 342-344.

Magelli, F., Pasquali, G., Foraboschi, F.P., Lelli, U., 1978. A note on the validity of perfect mixing as a model for continuous stirred tanks. *Int. Symp. on mixing, Faculté polytechnique de mons*, **A2**, 1-11.

Mann, R., Dickin, F.J., Wang, M., Dyakowski, T., Williams, R.A., Edwards, R.B., Forrest, A.E., Holden, P.J., 1997. Application of electrical resistance tomography to interrogate mixing process at plant scale. *Chem. Eng. Sci.* 52, 2087-2097.

Mann, R., Wang, M., Dickin, F.J., Dyakowski, T., Holden, P.J., Forrest, A.E., Edwards, R.B., 1996. Resistance tomography imaging of stirred vessel mixing at plant scale. *IChem. Eng. Symp.* 140, 155-162.

Mavros, P., Naude, I., Xuereb, C., Bertrand, J., 1997. Laser Doppler velocimetry in agitated vessels: Effect of continuous liquid stream on flow patterns. *Chem. Eng. Res. Des.*, 75(A), 763-776.

Mavros, P., Xuereb, C., Fort, I., Bertrand, J., 2002a. Investigation by laser Doppler velocimetry of the effects of liquid flow rates and feed positions on the flow patterns induced in a stirred tank by an axial-flow impeller. *Chem. Eng. Sci.* 57, 3939-3952.

Mavros, P., Xuereb, C., Fort, I., Bertrand, J., 2002b. Investigation of flow patterns in continuous-flow stirred vessels by laser Doppler velocimetry. *Can. J. Chem. Eng.* 80, 591-600.

McFarlane, C.M., Nienow, A.W., 1995. Studies of high solidity ratio hydrofoil impellers for aerated bioreactors. 1. Review. *Biotechnol. Prog.* 11, 601-607.

Metzner, A.B., Feehs, R.H., Ramos, H.L., Otto, R.E., Tuthill, J.D., 1961. Agitation of viscous Newtonian and non-Newtonian fluids. *AIChE J.* 7, 3-9.

Metzner, A.B., Otto, R.E., 1957. Agitation of non-Newtonian fluids. *AIChE J.* 3, 3-11.

Mishima, M., 1992. New trend of mixing vessel. *Chem. Eng. Jpn.* 56, 131-137.

Montante, G., Magelli, F., 2005. Modeling of solids distribution in stirred tanks: analysis of simulation strategies and comparison with experimental data. *Int. J. Comput. Fluid. Dynamics.* 19, 253–262.

Montante, G., Moštěk, M., Jahoda, M., Magelli, F., 2005. CFD simulation and experimental validation of homogenization curves and mixing time in stirred Newtonian and pseudoplastic liquids. *Chem. Eng. Sci.* 60, 2427-2437.

Moo-Young, M., Tichar, K., Dullib, A.L. 1972. The blending efficiencies of some impellers in batch mixing. *AIChE J.* 18, 178-182.

Morrison, F.A., 2001. *Understanding Rheology*. Oxford University Press.

Murthy, B.N., Ghadge, R.S., Joshi, J.B., 2007. CFD simulations of gas–liquid–solid stirred reactor: prediction of critical impeller speed for solid suspension. *Chem. Eng. Sci.* 62, 7184–7195.

Murthy, S.S., Jayanti, S., 2003a. Mixing of power-law fluids using anchors: Metzner-Otto concept revisited. *AIChE J.* 49, 30-40.

Murthy, S.S., Jayanti, S., 2003b. Mixing of pseudoplastic fluids using helical ribbon impellers. *AIChE J.* 49, 2768-2772.

Nagata, S., 1975. *Mixing: Principles and Applications*. John Wiley & Sons, New York.

Nauman, E.B. 2002. Chemical Reactor Design, Optimization and Scale-up. McGraw-Hill, New York.

Nienow A.W., Elson, T.P. 1988. Aspects of mixing in rheologically complex fluids. Chem. Eng. Res. Des. 66, 5-15.

Nienow, A.W., 1997. On impeller circulation and mixing effectiveness in the turbulent flow regime. Chem. Eng. Sci. 52, 2557-2565.

Nienow, A.W., 1998. Hydrodynamics of stirred bioreactors. App. Mech. Rev. 51(1), 3-32.

Ohta, M., Kuriyama, M., Arai K., Saito S. 1985. A two-dimensional model for the secondary flow in an agitated vessel with anchor impeller. J. Chem. Eng. Jpn. 18(1), 81-84.

Oldshue, J.Y., 1983. Fluid Mixing Technology. McGrawHill, New York.

Pakzad, L., Ein-Mozaffari, F., Chan, P., 2008a. Using electrical resistance tomography and computational fluid dynamics modeling to study the formation of cavern in the mixing of pseudoplastic fluids possessing yield stress. Chem. Eng. Sci. 63, 2508-2522.

Pakzad, L., Ein-Mozaffari, F., Chan, P., 2008b. Measuring mixing time in the agitation of non-Newtonian fluids through electrical resistance tomography. Chem. Eng. Technol. 12, 1838-1845.

Pant, H.J., Kundu, A., Nigam, K.D.P., 2001. Radiotracer applications in chemical process industry. Rev. Chem. Eng. 17, 165-252.

Patankar, S.V., 1980. Numerical Heat Transfer and Fluid Flow. Taylor & Francis Group, New York.

Patel, D., Ein-Mozaffari, F., Mehrvar, M., 2011. Dynamic performance of continuous-flow mixing of pseudoplastic fluids exhibiting yield stress in stirred reactors. Ind. Eng. Chem. Res. 50(15), 9377.

Patel, D., Ein-Mozaffari, F., Mehrvar, M., 2012a. Improving the dynamic performance of continuous-flow mixing of pseudoplastic fluids possessing yield stress using Maxblend impeller. *Chem. Eng. Res. Des.* 90 (4), 514-523.

Patel, D., Ein-Mozaffari, F., Mehrvar, M., 2012b. Effect of impeller type on continuous-flow mixing of non-Newtonian fluids in stirred vessels through dynamic tests. *Can. J. Chem. Eng.* 90 (2), 290-298.

Patel, D., Ein-Mozaffari, F., Mehrvar, M., 2013a. Using tomography technique to characterize the continuous-flow mixing of non-Newtonian fluids in stirred vessels. *Chem. Eng. Trans.* 32, 1465.

Patel, D., Ein-Mozaffari, F., Mehrvar, M., 2013b. Using tomography to characterize the mixing of non-Newtonian fluids with a Maxblend impeller. *Chem. Eng. Technol.* 36 (4), 687.

Patel, D., Ein-Mozaffari, F., Mehrvar, M., 2013c. Characterization of the continuous-flow mixing of non-Newtonian fluids using the ratio of residence time to batch mixing time. *Chem. Eng. Res. Des.* 91 (7), 1223-1234.

Patel, D., Ein-Mozaffari, F., Mehrvar, M., 2014a. Tomography images to analyze the deformation of the cavern in the continuous-flow mixing of non-Newtonian fluids. *AIChE J.* 60 (1), 315.

Patel, D., Ein-Mozaffari, F., Mehrvar, M., 2014b. Using tomography to visualize the continuous-flow mixing of biopolymer solutions inside a stirred tank reactor. *Chem. Eng. J.* 239, 257.

Patwardhan, A.W., Joshi J.B., 1999. Relation between flow pattern and blending in stirred tanks. *Ind. Eng. Chem. Res.* 38, 3131-3143.

Paul, E.L., Atiemo-Obeng, V., Keresta, S.M., 2004. *Handbook of Industrial Mixing: Science and Practice.* Wiley-Interscience, USA.

Paulson, K., Breckon, W., Pidcock, M., 1992. Electrode modeling in electrical impedance tomography. *J. Appl. Math* 52, 1012-1022.

Peters, D.C., Smith, J.M., 1969. Mixing in anchor agitated vessels. *Can. J. Chem. Eng.* 47 (3), 268–271.

Pinheiro, P.A.T., Loh, W.W., Dickin, F.J., 1998. Optimal sized electrodes for electrical resistance tomography. *Electron. Lett.* 34, 69-70.

Prajapati, P., Ein-Mozaffari, F., 2009. CFD investigation of the mixing of yield-pseudoplastic fluids with anchor impeller. *Chem. Eng. Technol.* 32, 1211-1218.

Ranade, V.V., 1997. An efficient computational model for simulating flow in stirred vessels: a case of Rushton turbine. *Chem. Eng. Sci.* 52, 4473- 4484.

Ranade, V.V., 2002. *Computational Flow Modeling for Chemical Reactor Engineering.* ACADEMIC PRESS, San Diego.

Ranade, V.V., Bourne, J.R., Joshi, J.B., 1991. Fluid mechanics and blending in agitated tanks. *Chem. Eng. Sci.* 46, 1883-1893.

Rao, M.A., 1999. *Rheology of Fluid and Semisolid Foods Principles and Applications.* Aspen, Inc., Maryland.

Rewatkar, V.B., Joshi, J.B., 1991. Effect of impeller design on liquid phase mixing in mechanically agitated reactors. *Chem. Eng. Commun.* 91, 322-353.

Ricard, F., Brechtelsbauer, C., Xu, X.Y., Lawrence, C.J., 2005. Monitoring of multiphase pharmaceutical processes using electrical resistance tomography. *Trans IChem E.* 83, 794-805.

Rivera, C., Foucault, S., Heniche, M., Espinosa-Slares, T., Tanguy, P.A., 2009. Finite element modeling of the laminar and transition flow of the superbblend dual shaft coaxial mixer on parallel computers. *Chem. Eng. Sci.* 64, 4442-4456.

Roussinova, V., Kresta, S.M. Comparison of continuous blend time and residence time distribution models for a stirred tank. *Ind. Eng. Chem. Res.* 2008, 47(10), 3532-3539.

Rudolph, L., Schaefer, M., Atiemo-Obeng, V., Kraume, M., 2007. Experimental and numerical analysis of power consumption for mixing of high viscosity fluids with a coaxial mixer. *Chem. Eng. Res. Des.* 85, 568-572.

Saeed, S., 2007. Dynamic and CFD modeling of a continuous-flow mixer using fluids with yield stress. MAsc thesis, Ryerson University, Toronto, ON, Canada.

Saeed, S., Ein-Mozaffari, F., 2008. Using dynamic tests to study the continuous mixing of xanthan gum solutions. *J. Chem. Technol. Biotechnol.* 83, 559.

Saeed, S., Ein-Mozaffari, F., Upreti, S.R., 2007. Using computational fluid dynamics and ultrasonic Doppler velocimetry to study pulp suspension mixing. *Ind. Eng. Chem. Res.* 46, 2172-2179.

Saeed, S., Ein-Mozaffari, F., Upreti, S.R., 2008. Using computational fluid dynamics to study the dynamic behavior of the continuous mixing of Herschel-Bulkley fluids. *Ind. Eng. Chem. Res.* 47, 7465-7475.

Sahu, A.K., Kummar, P., Patwardhan, A.W., Joshi, J.B., 1999. CFD modeling and mixing in stirred tanks. *Chem. Eng. Sci.* 54, 2285-2293.

Samaras, K., Mavros, P., Zamboulis, D., Effect of continuous stream and agitator type on CFSTR mixing state. *Ind. Eng. Chem. Res.* 2006, 45, 4805-4815.

Seagar, A.D., Barber, D.C., Brown, B.H., 1987. Theoretical limits to sensitivity and resolution in impedance imaging. *Clin. Phys. Physiol. Meas.* 8, 13-31.

Seborg, D.E., Edgar, T.F., Mellichamp, D.A., 1989. *Process Dynamics and Control*. Wiley, New York.

Shekhar, S.M., Jayanti, S., 2003. Mixing of power-law fluids using anchors: Metzner-Otto concept revisited. *AIChE J.* 49, 30-40.

Shervin, C.R., Raughley, D.A., Romaszewski, R.A. 1991. Flow visualization scaleup studies for the mixing of viscoelastic fluids. *Chem. Eng. Sci.* 46 (11), 2867-2873.

Shyy, W., Thakur, S.S., Ouyang, H., Liu, J., Blosch, E., 1997. *Computational Techniques for Complex Transport Phenomena*. Cambridge University Press, New York.

Skelland, A.H.P., 1967. *Non-Newtonian Flow and Heat Transfer*. Wiley, New York.

Solomon, J., Elson, T.P., Nienow, A.W., 1981. Cavern sizes in agitated fluids with a yield stress. *Chem. Eng. Commun.* 11, 143-164.

Tahvildarian, P., Ng, H., D'Amato, M., Drappel, S.F., Ein-Mozaffari, F., Upreti, S.R., 2011. Using electrical resistance tomography images to characterize the mixing of micron-sized polymeric particles in a slurry reactor. *Chem. Eng. J.* 172, 517-525.

Takahashi, K., Horiguchi, H., Mishima, M., Yatomi, R., 2006b. Mixing characteristics in a vessel agitated by large paddle impeller Maxblend. *Proc. 12th Eur. Conf. on Mixing*, Bologna, Italy.

Takahashi, K., Yokota T., Konno, H., 1988. Mixing of pseudoplastic liquid in a vessel equipped with a variety of helical ribbon impellers. *J. Chem. Eng. Japan.* 21(1), 63-68.

Takahashi, T., Tagawa, A., Atsumi, N., Dohi, N., Kawase, Y., 2006a. Liquid-phase mixing time in boiling stirred tank reactors with large cross-section impellers. *Chem. Eng. Process.* 45, 303-311.

Tapp, H.S., Williams, R.A., 2000. Status and applications of microelectrical resistance tomography. *Chem. Eng. Sci.* 77, 119-125.

Tatterson, G.B., 1991. *Fluid Mixing and Gas Dispersion in Agitated Tanks*. McGraw-Hill, New York.

Uhl, V.W., Gray, J.B., 1966. *Mixing, Theory and Practice (Vol 1)*. Academic Press, New York, NY.

Upreti, S.R., Ein-Mozaffari, F., 2006. Identification of dynamic characterization parameters of agitated pulp chests using hybrid genetic algorithm. *Chem. Eng. Res. Des.*, 84(A3), 221-230.

Vakili, M.H., Nasr, M., Esfahani, M. N., 2009. CFD analysis of turbulence in a baffled stirred tank, a three-compartment model. *Chem. Eng. Sci.* 64, 351-362.

Van Doormal, J.P., Raithby, G.D., 1984. Enhancements of the simple method for predicting incompressible fluid flows. *Num. Heat Transfer*, 7, 147-163.

Versteeg, H.K., Malalasekera, W., 1995. *An Introduction to Computational Fluid Dynamics the Finite Volume Method*. 1st ed. Longman Group Ltd., London.

Versteeg, H.K., Malalasekera, W., 2007. *An Introduction to Computational Fluid Dynamics the Finite Volume Method*. 2nd ed. Longman Group Ltd., London.

Vlaev, D., Wang, M., Dyakowski, T., Mann, R., Grieve, B.D., 2000. Detecting filter-cake pathologies in solid-liquid filtration: semi-tech scale demonstrations using electrical resistance tomography (ERT). *Chem. Eng. J.* 77, 87-91.

Wang, M., Jia, X., Bennet, M., Williams, R.A., 2001. Flow regime identification and optimum interfacial area control of bubble columns using electrical impedance imaging. *Proc. 2nd World Cong. on Ind. Process Tomography*, Hannover Germany, 726-734.

Weetman, R.J., Oldshue, J.Y., 1988. Power, flow and shear characteristics of mixing impellers. In the Proceedings of the 6th European Conference on Mixing, Italy, AIDIC/BHR Group, Cranfield, UK, 43-50.

Wichterle, K., Wein, O., 1975. Agitation of concentrated suspensions. Presented in CHISA 75, Paper B4.6, Prague, Czechoslovakia.

Wichterle, K., Wein, O., 1981. Threshold of mixing of non-Newtonian liquids. *Inter. Chem. Eng.* 21, 116-120.

Wilkins, R.J., Miller, J.D., Dietz, D.C., Myers, K.J., 2005. New technique for measuring and modeling cavern dimensions in a Bingham plastic fluid. *Chem. Eng. Sci.* 60, 5269-5275.

Williams, R.A., Beck, M.S., 1995. *Process Tomography: Principles, Techniques, and Applications*. Butterworth-Heineman, Oxford.

Williams, R.A., Jia, X., West, R.M., Wang, M., Cullivan, J.C., Bond, J., Faulks, I., Dyakowski, T., Wang, S.J., Climpson, N., Kostuch, J.A., Payton, D., 1999. Industrial monitoring of hydrocyclone operation using electrical resistance tomography. *Minerals Eng.* 12, 1245-1252.

Yao, W., Mishima, M., Takahashi, K., 2001. Numerical investigation on dispersive mixing characteristics of MAXBLEND and double helical ribbons. *Chem. Eng. J.* 84, 565-571.

Yokoi, H., Koga, J., Yamamura, K., Seike, Y., Tanaka, H., 1993. High density cultivation of plant cells in a new aeration-agitation type fermentor, maxblend fermentor. *J. Ferment. Bioeng.* 75 (1), 48-52.

Zadghafari, R., Moghadas, J.S., Revstedt, J., 2009. A mixing study in a double –Rushton stirred tank. *Comp. Chem. Eng.* 33, 1240-1246.

Zannoud, N., Guiraud, P., Costes, J., Bertrand, J., 1991. Local laser measurements of velocities and concentrations in two continuous systems: A tubular jet-stirred reactor and a stirred vessel. *Proceedings of 7th European Conference on Mixing, Brugge, Belgium, K-VIV, Antwerpen, 173-180.*

Zhao, Z.F., Mehrvar, M., Ein-Mozaffari, F., 2008. Mixing time in an agitated multi-lamp cylindrical photoreactor using electrical resistance tomography. *J. Chem. Technol. Biotechnol.* 83, 1676-1688.

Zlokarnik, M., 2001. *Stirring: Theory and Practice*. Wiley-VCH: Germany, Weinheim.